Selective growth of Cu2O and metallic Cu by atomic layer deposition on ZnO and their application in optoelectronics

Claudia de Melo Sánchez

THÈSE

Pour l'obtention du titre de

DOCTEUR de L'UNIVERSITÉ DE LORRAINE

Spécialité : Science des Matériaux

Présentée par

Claudia de MELO SÁNCHEZ

Croissance sélective de Cu_2O et Cu métallique par dépôt par couche atomique sur ZnO et leur application en optoélectronique

Soutenue publiquement le 15 Mai 2019 à Nancy devant le jury composé de :

Fabrice GOURBILLEAU	Président	Directeur de recherche, Centre de recherche sur les Ions, les Matériaux et la Photonique (CIMAP), Caen
Naoufal BAHLAWANE	Rapporteur	Chercheur, Luxembourg Institute of Science and Technology (LIST), Luxembourg
David MUÑOZ-ROJAS	Rapporteur	Chargé de recherche, Laboratoire des Matériaux et du Génie Physique (LMGP, CNRS/Grenoble INP), Grenoble
Christian MOTZ	Examinateur	Professeur, Lehrstuhl für Experimentelle Methodik der Werkstoffwissenschaften, Universität des Saarlandes, Saarbrücken
Nathanaelle SCHNEIDER	Examinateur	Chargée de recherche, Institut Photovoltaïque d'Ile-de-France (IPVF)/CNRS, Région de Paris
David HORWAT	Directeur de thèse	Professeur, Institut Jean Lamour, Université de Lorraine – CNRS, Nancy
Maud JULLIEN	Co-directeur de thèse	Ingénieur de recherche, Institut Jean Lamour, Université de Lorraine – CNRS, Nancy
Frank MÜCKLICH	Co-directeur de thèse	Professeur, Lehrstuhl für Funktionswerkstoffe, Universität des Saarlandes, Saarbrücken

Institut Jean Lamour, UMR 7198, ARTEM - CS 50840-54011 Nancy Cedex
Université de Lorraine – Ecole doctorale : Chimie - Mécanique - Matériaux- Physique (C2MP)

Abstract

In this work we present the results on the selective growth of Cu_2O and metallic Cu by atomic layer deposition (ALD) on ZnO, Al-doped ZnO (AZO) and α-Al_2O_3 substrates. It was possible to tune the deposited material (Cu or Cu_2O) by controlling the deposition temperature, and the substrate conductivity/density of donor defects. An area-selective atomic layer deposition (AS-ALD) process was demonstrated on a patterned bi-layer structure composed of low-conductive ZnO, and highly-conductive AZO regions. Furthermore, the AS-ALD allows the fabrication of Cu_2O/ZnO/AZO/Cu-back-electrode microjunctions, as confirmed by conductive atomic force microscopy (C-AFM). The mechanism behind the temperature and spatial selectivities is discussed. In a second part of this thesis, Cu nanoparticles (NP) were deposited by ALD on ZnO thin films. The Cu NP exhibit a localized surface plasmon resonance, tunable from the visible to the near-infrared regions, as confirmed by spectroscopic ellipsometry. An enhanced visible photo-response was observed in the Cu NP/ZnO device thanks to the hot-electron generation at the surface of the plasmonic Cu NP and transfer into the conduction band of ZnO. Finally, semi-transparent Cu_2O/ZnO heterojunctions were fabricated by ALD and reactive magnetron sputtering. The heterojunctions present a stable self-powered photo-response under 1 Sun illumination, fast response times and high transparency in the visible region, which is promising for all-oxide transparent electronics, photodetection and photovoltaics.

Résumé

Dans ce travail, après l'état de l'art et la présentation de méthodes de synthèse et d'analyse, nous présentons des résultats sur la croissance sélective de Cu_2O et Cu métallique par dépôt par couche atomique (ALD) sur ZnO, ZnO dopé à l'Al (AZO) et α-Al_2O_3. Nous mettons en évidence la possibilité de déposer de façon sélective Cu métallique ou Cu_2O, en contrôlant la température de dépôt et la conductivité ou la densité des défauts ponctuels au sein du substrat. Un procédé sélectif local de dépôt par couche atomique (AS-ALD) a été mis en évidence sur une bicouche à motifs composée de zones de ZnO de faible conductivité et de régions d'AZO de forte conductivité. De plus, l'AS-ALD permet la fabrication de nano-jonctions à base de Cu_2O/ZnO /AZO/Cu, dont le comportement de jonction p-n a été confirmé par microscopie à force atomique à pointe conductrice (C-AFM). Les mécanismes liés à la croissance sélective locale sont également discutés. Dans la seconde partie de cette thèse, des nanoparticules de Cu (NP) ont été déposées par ALD sur des couches minces de ZnO. Les NP de Cu présentent une résonance plasmon de surface localisée caractérisée par ellipsométrie. La position de la bande de résonance plasmon est ajustable entre les régions visible et infrarouge du spectre électromagnétique en gérant la taille des particules et leur espacement par l'intermédiaire du temps de dépôt. Le système Cu NP/ZnO montre une photo-réponse dans le visible grâce à la génération d'électrons chauds à la surface des NP de Cu et l'injection dans la bande de conduction de ZnO. Finalement, des hétérojonctions Cu_2O/ZnO semi-transparentes ont été fabriquées par ALD et pulvérisation cathodique. Les hétérojonctions présentent une photo-réponse autoalimentée sous éclairement, des temps de réponse rapides et une transparence élevée dans le visible, ce qui est prometteur pour des applications dans les domaines de l'électronique transparente, la photo-détection et le photovoltaïque.

Zusammenfassung

In dieser Arbeit präsentieren wir die Ergebnisse zum selektiven Wachstum von Cu_2O und metallischem Cu durch Atomlagenabscheidung (ALD) auf ZnO-, Al-dotierten ZnO- (AZO) und α-Al_2O_3-Substraten. Es war möglich, das abgeschiedene Material durch Steuern der Temperatur, der Leitfähigkeit und der Dichte von Donatordefekten des Substrats abzustimmen. Ein flächenselektiver Atomlagenabscheidungsprozess (AS-ALD) wurde auf einer Zweischichtstruktur aus schwach leitfähigen ZnO- und hochleitfähigen AZO-Bereichen gezeigt. Des weiteren ermöglicht AS-ALD die Herstellung von Cu_2O/ZnO/AZO/Cu-Rückelektroden-Nano-Übergängen, was durch leitfähige Rasterkraftmikroskopie (C-AFM) bestätigt wurde. Der Mechanismus hinter den Temperatur- und Ortsselektivität wird diskutiert. In einem zweiten Teil der Arbeit wurden Cu-Nanopartikel (NP) durch ALD auf ZnO-Dünnschichten abgeschieden. Die Cu-NP weisen eine lokalisierte Oberflächenplasmonresonanz auf, die vom sichtbaren Bereich bis zum nahen Infrarotbereich eingestellt werden kann, was durch spektroskopische Ellipsometrie bestätigt wurde. Eine Verstärkung der Fotoantwort im sichtbaren Bereich durch die Erzeugung heißer Elektronen wurde in einem Cu-NP/ZnO Schaltelement beobachtet. Schließlich wurden semitransparente Cu_2O/ZnO-Heteroübergänge durch ALD und reaktives Magnetron-Sputtern hergestellt. Die Heteroübergänge bieten eine stabile selbstangetriebene Fotoantwort unter Sonnen-Beleuchtung, schnelle Reaktionszeiten und hohe Transparenz im sichtbaren Bereich.

Résumé étendu

Le dépôt sélectif par couche atomique a beaucoup attiré l'attention ces dernières années en raison de la possibilité de réaliser des motifs précis à l'échelle nanométrique même pour les nanostructures 2D et 3D. La croissance sélective locale est obtenue dans la plupart des cas en désactivant une partie du substrat par certaines molécules ou par des monocouches auto-assemblées, avant le dépôt par couche atomique (ALD, pour son acronyme en anglais). Ceci entraîne la croissance localisée du matériau souhaité dans des zones spécifiques du substrat. Du fait de la réduction des dimensions en microélectronique, il est essentiel de développer des nouvelles méthodes permettant de réaliser simultanément un dépôt sélectif local de différents matériaux sur différentes surfaces au moyen des approches ascendantes, dites « Bottom-up ». Dans cette thèse, nous proposons une nouvelle approche pour réaliser des dépôts sélectifs, basée sur la modulation des propriétés du substrat (dans ce cas, la conductivité / la densité des défauts ponctuels des films de ZnO), qui permet la croissance sélective locale de couches minces de Cu_2O et Cu.

Les nanoparticules métalliques, telles que Au, Ag et Cu, ont attiré l'attention pour de nombreux domaines d'applications en raison de leurs propriétés optiques et électriques remarquables. Elles présentent une résonance plasmon de surface localisée, qui provient du couplage entre un champ électromagnétique et les oscillations collectives des électrons de conduction à la surface des nanoparticules. Avec un contrôle précis de la taille, de la forme, et de l'environnement diélectrique, la lumière peut être manipulée et contrôlée de manière exceptionnelle. C'est la raison pour laquelle les nanoparticules suscitent un intérêt scientifique et technologique intense dans des domaines divers tels que les capteurs chimiques, la catalyse, la photonique et le photovoltaïque. Les nanoparticules de cuivre ont l'avantage de présenter un faible coût par rapport à l'or et l'argent. De plus, le cuivre est un matériau largement utilisé dans le domaine de la microélectronique, avec une conductivité électrique et une photosensibilité élevées. Ceci rend les nanoparticules de cuivre prometteuses dans des applications liées à la nanoélectronique et à l'optoélectronique. Dans cette thèse, nous présentons les potentialités pour la photo-détection visible de nanoparticules plasmoniques de cuivre déposées par ALD sur ZnO.

Parmi les défis auxquels fait face la technologie photovoltaïque (PV), on compte la nécessité d'évoluer vers l'utilisation de matériaux abondants, non toxiques et peu coûteux. Le PV basé sur les oxydes semi-conducteurs est une solution prometteuse pour relever ce défi.

L'oxyde de cuivre de type cuprite, Cu_2O, est l'un des matériaux les plus étudiés, notamment pour ses propriétés optiques et électriques singulières. Il s'agit d'un semi-conducteur de type p avec un coefficient d'absorption élevé dans une partie du spectre visible et une largeur de bande interdite de 2.1 eV. Une efficacité théorique de 20 % a été calculée pour la conversion de lumière en électricité des cellules solaires à base de Cu_2O utilisé comme couche absorbante. Cependant, jusqu'à présent, le record d'efficacité expérimentale n'est que 8.1 %, encore loin de la valeur théorique, du fait d'un défaut d'optimisation des matériaux constitutifs et de l'architecture des jonctions. ZnO est un semi-conducteur de type n intéressant pour un interfaçage avec Cu_2O. En effet, il présente une large bande interdite de 3.37 eV et une mobilité électronique élevée à température ambiante. De plus, les dispositifs basés sur des jonctions Cu_2O / ZnO peuvent être utilisés dans plusieurs domaines tels que le photovoltaïque tout oxyde, l'électronique semi-transparente, la photodétection, entre autres.

Globalement, dans cette thèse nous montrons les résultats du dépôt sélectif de Cu_2O et de Cu métallique par dépôt par couche atomique sur des substrats de ZnO et leurs applications dans l'optoélectronique. Le manuscrit est organisé en 5 chapitres, suivis de Conclusions et Perspectives.

Dans le premier chapitre sont présentés certains éléments clés concernant les principaux résultats obtenus dans cette thèse. Les propriétés de base (structure, défauts, propriétés électriques et optiques, etc.) des couches minces de Cu_2O et de ZnO sont présentées, ainsi que les méthodes de dépôt utilisées pour leur fabrication. Ceci est suivi par une description des applications des oxydes semi-conducteurs dans les systèmes photovoltaïques et, en particulier, les hétérojonctions à base de Cu_2O/ZnO. La deuxième partie de ce chapitre est consacrée aux nanoparticules plasmoniques et aux mécanismes de photo-détection. Premièrement, les applications principales des nanostructures plasmoniques sont présentées, particulièrement celles liées à la résonance plasmon de surface localisée. En second lieu, quelques principes de base de la photo-détection sont présentés en tant que préambule pour l'introduction des photo-détecteurs plasmoniques à porteurs chauds.

Dans le deuxième chapitre sont décrites les méthodes de dépôt par couche atomique et de pulvérisation cathodique utilisées pour la croissance des films minces de Cu_2O, Cu métallique, ZnO, ZnO dopé à l'Al et de nanoparticules de Cu. Les principes de base des principales méthodes de caractérisation utilisées dans cette thèse sont également présentés, ainsi que les paramètres spécifiques utilisés pour l'analyse des échantillons.

Dans le chapitre 3, nous décrivons la fabrication de films minces de Cu_2O et de Cu métallique par dépôt par couche atomique en utilisant $Cu(hfac)_2$ et H_2O comme précurseurs.

L’analyse par microscopie électronique en transmission à haute résolution (HR-TEM, pour son acronyme en anglais) montre la haute qualité cristalline des films déposés. Une croissance sélective des deux matériaux a été obtenue sur différents types de substrats (ZnO, AZO et α-Al_2O_3). La formation de films Cu_2O et de Cu métallique monophasés a été obtenue sur des substrats monocristallins d'α-Al_2O_3, ZnO et AZO en modifiant la température de dépôt entre 230 - 300 °C. D'ailleurs, une étude détaillée sur des substrats de ZnO et AZO démontre la possibilité de réaliser un dépôt sélectif locale. Un diagramme de phases montrant la formation des différents matériaux en fonction de la température de dépôt et de la conductivité du substrat (ZnO, AZO) est présenté.

À titre de preuve de concept, une bicouche composée d'une couche de ZnO (de faible conductivité) et d’une couche d’AZO (de forte conductivité) a été fabriquée, structurée et fonctionnalisée. L’HR-TEM et la spectroscopie de pertes d'énergie d'électrons (EELS, pour son acronyme en anglais) confirment le dépôt sélectif local de Cu métallique sur les zones de forte conductivité et de Cu_2O sur les zones de faible conductivité. Dans cette approche, le dépôt de différents matériaux est obtenu, mais la sélectivité « traditionnelle » (déposition versus non-déposition) est conservée en utilisant simplement des films de ZnO de très forte résistivité comme substrat pour empêcher la croissance locale. Après l’étude de la croissance des films sur différents substrats et l’analyse de l’évolution des défauts ponctuels dans la couche de ZnO par photoluminescence, nous concluons que la sélectivité locale est le résultat de la sélectivité inhérente du précurseur de $Cu(hfac)_2$ envers les différentes surfaces de ZnO présentant différentes conductivités / densités de défauts ponctuels. En outre, l’étude de la croissance de Cu_2O sur des substrats de ZnO avec des orientations cristallines différentes et de substrats monocristallins d'α-Al_2O_3 indiquent que la relation d'orientation cristalline entre le film et le substrat joue un rôle fondamental dans dépôt sélectif de Cu_2O. Sur la base du processus de dépôt sélectif local, des nano-jonctions Cu_2O/ZnO/AZO ont été fabriquées. Des caractéristiques I-V mesurées par microscopie à force atomique à pointe conductrice (C-AFM pour son acronyme en anglais) montrent un comportement redresseur typique d'une jonction p-n. Ce résultat est d’intérêt pour la microélectronique transparente. De plus, le dépôt de plusieurs nano-jonctions Cu_2O / ZnO par cette méthode sur un substrat transparent produirait une architecture photovoltaïque segmentée, prometteuse pour le photovoltaïque intégré au bâtiment. Cette configuration est une première approche parmi les nombreuses architectures possibles. En définissant autrement les zones de conductivité, différentes interfaces pourraient être générées, permettant la formation d'architectures différentes.

Dans le chapitre 4, est décrit le dépôt de nanoparticules (NP) et de films minces de cuivre par ALD sur des substrats de ZnO. L'obtention de NP de cuivre par ALD a été possible grâce au mode de croissance *Volmer–Weber*. La taille, la densité et la couverture surfacique des NP de Cu sur ZnO ont été contrôlées par le nombre de cycles ALD. Une évolution de la morphologie depuis des NP de cuivre vers une couche continue a été observée avec l'augmentation du nombre de cycles ALD. Le dépôt de Cu métallique a été réalisé par une voie simple, sans qu'il soit nécessaire d'incorporer une étape supplémentaire avec un agent réducteur (hydrogène, méthanol, isopropanol, etc.) dans le procédé ALD, comme habituellement requis.

Les NP de cuivre possèdent une résonance plasmon de surface localisée, mesurée par ellipsométrie. Par ailleurs, la longueur d'onde de la bande plasmon peut être réglée en continu entre les régions visible et infrarouge du spectre électromagnétique en modifiant la taille et la séparation des nanoparticules, paramètres contrôlés par le nombre de cycles ALD.

Un photo-détecteur de lumière visible a été fabriqué à partir des NP de cuivre déposées sur ZnO. Comparé à une jonction Schottky traditionnelle (film de Cu / ZnO), le dispositif Cu NP/ZnO montre une amélioration considérable du photo-courant qui peut être attribuée à l'effet des NP de Cu. Nous proposons que le mécanisme à l'origine de photo-détection est la génération d'électrons chauds à la surface des Cu NP, après la désexcitation non radiative de l'état plasmon, et l'injection des électrons dans la bande de conduction de ZnO à travers la barrière de Schottky à l'interface entre les deux matériaux.

La photo-réponse significative du dispositif Cu NP / ZnO ainsi que la possibilité d'accorder la bande de résonance plasmon entre les régions visible et infrarouge du spectre électromagnétique ouvrent la voie au développement de nouveaux systèmes pour augmenter l'efficacité de photo-détecteurs et dispositifs photovoltaïques.

Des résultats préliminaires sur le dépôt de NP de Cu sur des nanostructures de ZnO par ALD sont présentés à la fin de ce chapitre. Les résultats présentés sont prometteurs étant donnée la possibilité de couvrir des structures à facteur de forme élevé et des surfaces tridimensionnelles complexes, qui sont fortement demandées pour des applications liées à la détection de gaz, la catalyse et le photovoltaïque, entre autres.

Dans le chapitre 5, sont présentés les résultats de la fabrication d'hétérojonctions semi-transparentes p-Cu_2O / n-ZnO. La morphologie et la structure des films ont été étudiées par microscopie électronique à balayage, diffraction des rayons X et microscopie électronique en transmission. La largeur de la bande interdite des films a été déterminée par des mesures d'ellipsométrie et de transmittance optique, ce qui a donné une valeur de 2,42 eV pour le gap de Cu_2O et de 3,16 eV pour celui du ZnO. La caractérisation électrique des films de Cu_2O

montre une concentration relativement élevée de porteurs de $\sim 10^{16}$ cm^{-3}, une résistivité très faible de 9 à 150 Ωcm et des valeurs de mobilité élevées de 19 cm^2/Vs. Dans une première partie de l'étude, les hétérojonctions ont été fabriqués à partir d'un film de Cu_2O de 40 nm (par ALD) et d'un film de ZnO (par pulvérisation cathodique) déposés sur un substrat d'oxyde d'indium dopé à l'étain (ITO) / verre. Les caractéristiques I-V montrent un comportement redresseur typique d'une jonction p-n. Une photo-réponse autoalimentée a été observée sous éclairement. En autre, les hétérojonctions montrent une transmittance moyenne élevée de 73%.

Dans une seconde partie de l'étude, les propriétés électriques des hétérojonctions ont été considérablement améliorées par l'incorporation d'un film de Cu_2O de 200 nm d'épaisseur déposé par pulvérisation cathodique sur le film de Cu_2O de 40 nm déposé par ALD. L'hétérojonction montre une photo-réponse stable sous plusieurs cycles d'obscurité / lumière de 20 s sous tension de polarisation de 0 V. En particulier, grâce aux bonnes propriétés électriques des films de Cu_2O, des valeurs de V_{OC} relativement élevées ont été atteintes, compte tenu de la faible épaisseur du film.

Un temps de réponse rapide de 0,10 s a été déterminé à partir de la courbe de densité de courant en fonction du temps, en comparaison avec des autres photo-détecteurs visibles à base d'oxydes. Cette réponse rapide est due à la faible épaisseur de la couche de déplétion et à la possibilité de développer la totalité du potentiel de barrière, en fournissant un champ électrique puissant à l'interface de l'hétérojonction qui permet une séparation plus rapide des charges et, par conséquent, une réponse rapide du dispositif.

En fin de chapitre, sont présentés des résultats préliminaires sur le dépôt de Cu_2O sur des nanofils de ZnO, ce qui est prometteur pour des dispositifs photovoltaïques et photo-détecteurs. En effet, cela représente un moyen d'améliorer l'absorption de la lumière en raison de l'augmentation du rapport surface-volume dans les hétérojonctions nanostructurées et par des effets de piégeage de la lumière à l'intérieur des nanofils de ZnO. D'autre part, cette architecture permet d'améliorer l'efficacité de la collecte des porteurs en raison de la faible distance que les porteurs photo-générés ont à parcourir avant d'être collectés.

La transmittance élevée ainsi que la photo-réponse des hétérojonctions présentées ici sont prometteuses dans les domaines de l'électronique transparente tout oxyde, du photovoltaïque semi-transparent et de la photo-détection. Même si l'ALD est un processus lent qui ne convient pas à la croissance de couches épaisses, il peut servir à la croissance de couches tampons de haute qualité. D'ailleurs, il pourrait être intéressant pour la croissance de Cu_2O dans des cellules solaires nanostructurées ne nécessitant pas l'utilization d'une couche épaisse de Cu_2O en raison du rapport surface-volume élevé.

Acknowledgements

This thesis, the result of more than three years of research, would not have been possible without the contribution of many people.

In first place, I would like to thank my supervisor David Horwat for his support, guidance, motivation, and knowledge. This thesis would have not been possible without his major contribution, always bringing a lot of new and excellent ideas. For me have been a great pleasure to work with him, I have learned a lot during these years and I hope we can keep the collaboration in the future. I am grateful for all the time he dedicates to me and for all his help not only in the scientific aspects but in my professional and personal life. I could haven't asked for a better supervisor!

Special thanks to my co-supervisor Maud Jullien, for all her support and enthusiasm, for teaching me how to use the ALD and for our fruitful discussions. I really appreciate all the time she dedicates to this work and all the help and support she provides me during these years. I really enjoyed working with her.

I would also like to thanks my co-supervisor Prof. Frank Mücklich, for his significant contribution to this work and for his support during my stays at Saarbrücken.

My sincere thanks to Jean-François Pierson, head of Department 2 at Institut Jean Lamour, that was involved in my project from the beginning, always with insightful suggestions and ideas that contribute in a great deal to improve my work.

I would like to thank Jaafar Ghanbaja for his contribution with the TEM and EELS measurements, and for his expert advice in the structural characterization of the samples. I also want to thank Pascal Boulet for his help with XRD and especially with the Phi-scan and texture analysis, Alexandre Boucher for help with the XPS, Sylvie Migot for the preparation of TEM lamella using FIB, Laurent Badie for his help with the deposition of the Al contacts, Patrice Miska for the PL measurements, Denis Mangin for the SIMS profiles, Julian Ledieu and Vincent Fournée for the measurements at the SCAN, Sandrine Mathieu for the metallization process, Thomas Gries for his contribution with the ZnO nanowires, and François Montagne for the help with the patterning of the samples by lithography, and for his advices and recommendations, that contribute to the improvement of this work. A special thanks to Stéphane Andrieu and Sébastien Petit-Watelot for offering me the post-doc position in the 101 team before the thesis defense.

This thesis has also been the result of collaboration with other research partners. Special thanks to Yann Battie and Aotmane En Naciri (from LCP-A2MC, University of Lorraine) for their contribution with ellipsometry measurements and modeling, and to Federica Rigoni, Alberto Vomiero and Nils Almqvist (from Luleå University of Technology) for their collaboration with the C-AFM and electrical characterization of the samples. Thanks to all of them for the welcoming they gave me when I visited their laboratories and for their valuable suggestions to this work.

I would like to thank Valérie Frank, Chistine Sartori, Valérie Madeline, Martine Tailleur, and Anne-Marie Airault, for all their help with the administrative aspect during these years.

A special thanks to all my colleagues of team 202. I would like to mention my formers colleagues: Fahad, William, Martin, Manu, and Yong, I really enjoy sharing office with them, and I appreciate all their help at the beginning of my thesis, and to their successors: Christophe, Joseph, Benjamin, Daria, Agatha, Christy, and Osama. Special mention to Nicole that started and finished the PhD with me, thanks for your help and friendship during these years. I want also express my gratitude with the other members of the team 202: David Pilloud, Silvère Barrat, Stéphanie Bruyere, Fabien Capon, and Valérie Brien. Thanks to all of you for the good moments we spent together.

I would like to thank all my colleges from Department of Materials Science and Engineering at Saarland University: Jiaqi, Lucia, Kathy, Leandro, Jenny, Pranau …. for the time we spent together. I would like to express my gratitude to Flavio Soldera for the preparation of the TEM lamella by FIB and in general for all his help and support during my stays at Saarbrücken.

I would like to specially thank the Mojo's team: Alexis, Mariana, Magali, and Vitalis for the funny times we have shared together, and for their friendship.

I am grateful to the European Commission for financing this project through the "Erasmus Mundus" Ph.D. fellowship within the DocMASE project and the Université franco-allemande (UFA) for its financial support within the PhD track "German/French Graduate School in Materials Science and Engineering" (PhD02−14). The Daυm competence center of IJL is deeply acknowledged for giving me access to the ALD deposition facility.

Finally, I would like to thank my family and my parents in low for their support.

Specially, I would like to thank my parents for instilling in me their passion for science. Without their support and love during my whole life this would not be possible.

A very special thanks to my husband for sharing this adventure with me, for all his love and for the much he cares for me.

Contents

Motivation

Area-selective atomic layer deposition has attracted much attention in recent years due the possibility of achieving accurate patterning with nanoscale precision, even for 2D and 3D nanostructures [1]. The area-selective growth is achieved in most cases by deactivating part of the substrate by certain molecules or by self-assembly monolayers (SAMs)[2], prior to atomic layer deposition (ALD), which results in the localized growth of the desired material in specific areas of the substrate. With the continuous downscaling of electronic devices, it is critical to develop new methods for achieving simultaneously selective deposition of different materials on different surfaces through bottom-up procedures. In this thesis we propose a novel approach to achieve area-selective deposition, that is based on the modulation of the substrate properties (in this case the conductivity/density of majority point defects in ZnO and Al-doped ZnO films) to allow local growth of different materials (Cu and Cu_2O).

Plasmonic metallic nanostructures have also gained a lot of attention in recent years, due to the strong coupling between light and the free conduction electrons at the metallic nanostructures. By controlling the nanostructure size, shape and dielectric environment, light can be manipulated, focused and guided in exceptional manners. Plasmonic devices can serve as antennas to create strong localized electric fields, as waveguide to guide the light with nanoscale precision, as resonant light scatterers, as biosensor, among others. In combination with semiconductor materials, they can work as light trapping centers, enhancing considerably the photogeneration of carriers or they can directly inject carriers into the semiconductor band gap by hot-carrier generation at the nanostructure surface and transfer to the semiconductor. This phenomenon has been exploited for the fabrication of multiple optoelectronic devices, such as photodetectors, photocatalysts, optical antennas and solar cells [3–5]. Particularly, in this thesis we will show the potentialities of plasmonic Cu nanoparticles deposited by ALD on ZnO for visible photodetection.

Cu_2O has sparked renewed interest in the scientific community due to its p-type conductivity and high absorption combined with the abundance of constitutive elements in the earth crust, non-toxicity, and low-cost, which makes it compatible with low-cost all-oxide photovoltaics. Furthermore, theoretical power conversion efficiencies of ~20 % have been predicted for Cu_2O-based solar cells [6]. Maximum efficiency achieved so far is of 8.1 % [7], which means that there is still plenty of room for improvement. Among the possible n-type materials for partner layer, ZnO seems to be a suitable candidate regarding its wide band gap,

good electrical properties, and the compatibility with low-cost applications in combination with Cu_2O. Furthermore, Cu_2O/ZnO devices can find application in multiple fields such as all-oxide photovoltaics, semi-transparent electronics, photodetection, among others [8,9]. In the last chapter of this thesis, we will present the results on the fabrication of semi-transparent Cu_2O/ZnO heterojunctions by ALD and reactive magnetron sputtering.

Overall, this thesis deals with the selective deposition of Cu_2O, and metallic Cu by atomic layer deposition on ZnO substrates for applications in optoelectronics. The manuscript is organized in 5 Chapters, followed by the Conclusions and Outlook section.

Chapter 1 is a general introduction, where the basic properties of Cu_2O and ZnO are presented, followed by their applications in all-oxide photovoltaics. The second part of this chapter is devoted to the metallic plasmonic nanoparticles and their applications, as a preamble for the introduction of hot-carrier photodetectors.

Chapter 2 is dedicated to the basic principles of atomic layer deposition (ALD) and reactive magnetron sputtering methods, employed for the deposition of Cu_2O, metallic Cu, ZnO, and Al-doped ZnO (AZO) films, together with the structural, optical, electronic and electrical characterization methods employed through this thesis.

Chapter 3 is devoted to the selective deposition of Cu and Cu_2O thin films on ZnO, AZO, and α-Al_2O_3 substrates. Both temperature-driven and substrate-driven selectivities are reported, and the mechanisms behind are discussed. Particularly, for Cu_2O films, the influence of the substrate crystallographic orientation on the film growth is analyzed. Finally, Cu_2O/ZnO/AZO microjunctions were fabricated thanks to the area-selective atomic layer deposition process, and the electrical characterization of the junction is presented.

Chapter 4 is dedicated to the results on the fabrication of plasmonic Cu nanoparticles and Cu thin films by atomic layer deposition on ZnO substrates. An evolution from Cu nanoparticles at lower number of ALD cycles to Cu films at higher number is reported. The optical characterization of the Cu nanoparticles was performed by spectroscopic ellipsometry, allowing to identify the existence of a localized surface plasmon resonance (LSPR) band. The causes of the LSPR red-shift observed for Cu NP obtained at different number of ALD cycles are discussed. Finally, the electrical properties of Cu NP/ZnO device are investigated by conductive atomic force microscopy, and the mechanism responsible for the visible photoresponse of the device is discussed.

Chapter 5 is dedicated to the fabrication and characterization of semi-transparent heterojunctions based on Cu_2O and ZnO thin films. The optical characterization of the films was performed by UV-visible spectroscopy and ellipsometry, and the electrical characterization

was done through 4-point probe and Hall-effect methods. The heterojunction performance was studied by macroscopic electrical measurement in dark and under 1 Sun illumination, and the average transmittance was calculated from the transmittance spectrum in the visible region.

Chapter 1

General Introduction

In this chapter, some key elements regarding the main results obtained in this thesis are presented. The basic properties (structure, defects, electrical and optical properties, etc.) of Cu_2O and ZnO thin films are discussed, together with the deposition methods employed for their fabrication. This is followed by a description of the applications of metal oxide semiconductors in all-oxide photovoltaics, and particularly the Cu_2O/ZnO-based heterojunctions. The second part of this chapter is devoted to plasmonic nanoparticles and photodetection mechanisms. First, the main applications of plasmonic nanostructures are presented, emphasizing those related with localized surface plasmon resonance (LSPR). Secondly, some basic ideas of photodetection are discussed as a preamble for the introduction of the hot-carrier plasmonic photodetectors.

Contents

1.1 Basic Properties of Cu_2O

Copper I oxide (Cu_2O) is a stable binary copper compound that crystalizes in a cubic structure (cuprite, space group Pn-3m) with lattice constant of 4.269 Å. The unit cell contains 4 copper atoms and 2 oxygen atoms. The copper atoms (blue balls) are arranged forming a face-centered-cubic sublattice and the 2 oxygen atoms (red balls) are forming a body-centered-cubic sublattice, as is depicted in Figure 1.1. Each oxygen atom is 4-fold coordinated with oxygen atoms and each copper atom is linearly coordinated with the two oxygen atoms, the bond lengths are indicated in Figure 1.1 [10].

Cu_2O is a direct forbidden band gap semiconductor ($E_g = 2.1$ at $4.2\ K$) with large exciton binding energy of 150 meV [11]. In recent years, there has been a renewed interest in Cu_2O due to the experimental observation of Rydberg excitons with a principal quantum number of 25 [12], which has opened the research on giant Rydberg interaction that is of potential interest for fundamental research in condensed matter physics, and of potential impact in quantum information technologies [13].

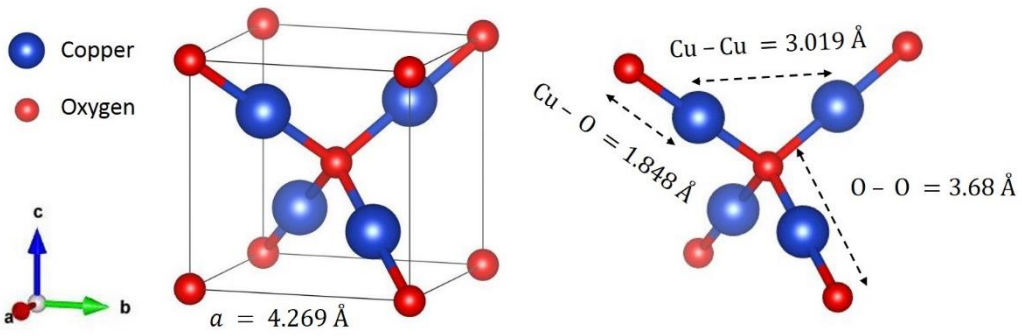

Figure 1.1. Crystal structure of cuprite Cu_2O (space group Pn-3m). The bond lengths are indicated.

A schematic of the Cu_2O band structure at the Γ-point of the Brillouin zone is shown in Figure 1.2. The highest valence band (Γ_7^+) has a d-like character since it originates from the 3d-Cu orbital, while the lowest conduction band (Γ_6^+) presents a 4s-like character and originates from the 4s-Cu orbital. The transitions from the valence band to the conduction band are represented in Figure 1.2, and, from their associated emission wavelength, they are named: yellow ($\Gamma_7^+ \rightarrow \Gamma_6^+,\ E = 2.173\ eV$), green ($\Gamma_8^+ \rightarrow \Gamma_6^+,\ E = 2.304\ eV$), blue ($\Gamma_7^+ \rightarrow \Gamma_8^-,\ E = 2.625\ eV$) and indigo ($\Gamma_8^+ \rightarrow \Gamma_8^-, E = 2.756\ eV$) [14,15]. The lowest fundamental transition is dipole-forbidden, since the parity of the lower conduction band and the highest valence band is the same. In consequence, the yellow and green series, can only occur by a phonon-assisted process, and the lowest allowed optical transition are the blue and the indigo series. This is the

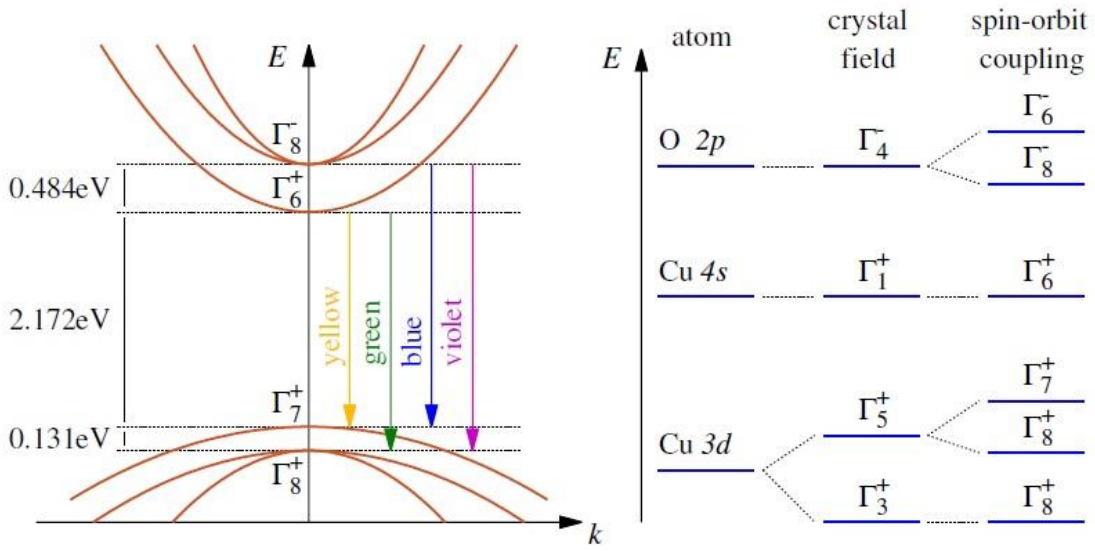

Figure 1.2. Schematic of the Cu_2O band structure at the **Γ**-point of the Brillouin zone, the different electronic transitions leading to the four excitonic series are indicated. Origin of conduction and valence bands from the atomic orbitals and the band splitting considering crystal-field and spin-orbit interaction are depicted on the right **[17]**.

reason why experimentally optical bandgap values ranging from 2.4 to 2.7 eV have been reported for Cu_2O [16].

Regarding the electrical properties, Cu_2O films exhibit intrinsic p-type conductivity. From theoretical studies and by deep-level transient spectroscopy analysis, it has been determined that the possible defects contributing to p-type conductivity in Cu_2O are: single Cu vacancies, V_{Cu}, copper vacancies in the split configuration, V_{Cu}^{split} (a copper interstitial, Cu_i, between two V_{Cu}) [18], and oxygen interstitials O_i in tetrahedral (O_i^{tet}) or octahedral (O_i^{oct}) coordination (Figure 1.3). Among them, the single V_{Cu} and the V_{Cu}^{split} configuration have the lowest formation energy under both, Cu-rich and Cu-poor conditions (see Figure 1.3), with transitions levels $\epsilon(0/-)$ at 0.22 and 0.47 eV above the valence band maximum, respectively [19], in agreement with the experimental values of 0.2 and 0.5 eV, obtained by deep-level transient spectroscopy [20]. On the other hand, O_i defects have much higher formation energies and are located deeper in the bandgap. Therefore, O_i defects don't contribute to the p-type conductivity, which arises mainly from V_{Cu} and V_{Cu}^{split}.

The influence of extrinsic defects in Cu_2O has also been studied. For example, nitrogen doping results in the formation of a shallow acceptor level associated to the molecular N_2 substituting Cu, $(N_2)_{Cu}$, that enhances hole carrier concentration and Cu_2O conductivity [21]. H-related defects have also been analyzed, and the complex H-V_{Cu} (that results from the

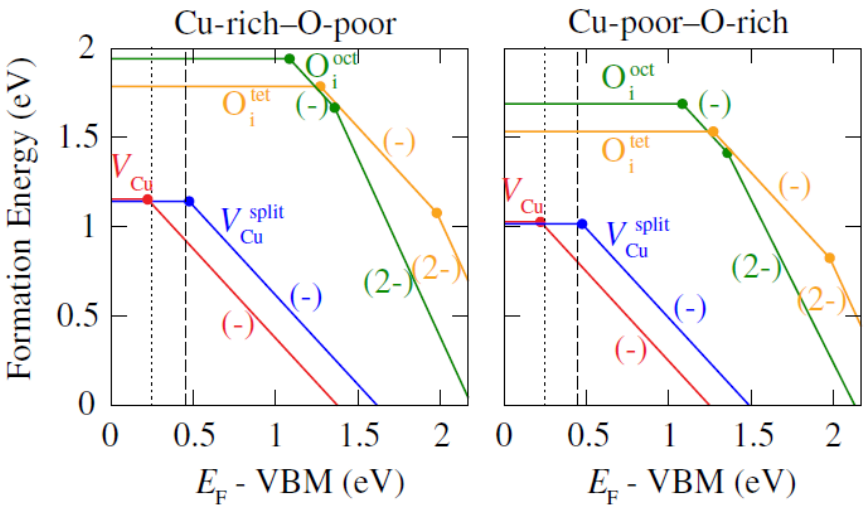

Figure 1.3. Theoretical calculations of the formation energy for the different acceptor levels in Cu_2O, under Cu-rich (left) and Cu-poor (right) conditions (color lines). The vertical dashed lines represent experimental values obtained from deep-level transient spectroscopy measurements **[19]**.

interaction between an hydrogen atom and a V_{Cu} presents low formation energy (0.17 eV), with transitions levels $\epsilon(0/-)$ at $\sim 1.15\ eV$, very deep inside the band gap. Therefore, this type of defect mainly works as hole killer, affecting p-type conductivity in Cu_2O [22].

Several techniques have been used for the deposition of Cu_2O like sputtering [23], pulsed laser deposition [24,25], electrochemical deposition [26], molecular beam epitaxy, chemical vapor deposition, and atomic layer deposition (ALD) [27,28]. The electrical properties of Cu_2O are very sensitive to deposition method, since the Cu_2O stoichiometry and point defect densities evolve from one technique to other. In fact, the resistivity, carrier concentration and carrier mobility reported in the literature, change widely depending on the growth conditions. Cu_2O films deposited by thermal oxidation show resistivity values ranging from $10^2 - 10^4\ \Omega$ cm [29]. For electrodeposited films, even higher values have been reported around $10^4 - 10^6\ \Omega$ cm, with low hole carrier concentrations of $10^{13} - 10^{14}\ cm^{-3}$, and mobilities of $\sim 1\ cm^2/Vs$ [29,30]. Lower resistivity values have been reported for sputtered Cu_2O films ranging from 10 to $10^3\ \Omega$ cm, with higher hole concentrations of $10^{16} - 10^{17}\ cm^{-3}$, and carrier mobilities of $1 - 62\ cm^2/Vs$ [16,31], which make this technique effective for the fabrication of Cu_2O films, with good electrical performance. Recently, ALD has emerged as a successful approach to deposit high quality Cu_2O thin films, with the additional advantage of producing highly uniform and conformal films. D. Muñoz-Rojas *et al.* reported the fabrication of low resistivity (125 Ω cm) Cu_2O thin films (~100 nm) deposited at relatively low temperature (225 °C) by atmospheric pressure spatial ALD, with hole mobilities and carriers concentrations of 5 cm^2/Vs and $10^{16}\ cm^{-3}$, respectively [28]. High carrier mobility of 8.05 $cm^2/V\ s$ has

also been reported for Cu_2O thin films deposited by thermal ALD, however the films presented lower carrier concentrations of $5.88 \times 10^{14}\ cm^{-3}$ [27].

High mobility and carrier concentrations of at least $10^{16}\ cm^{-3}$, are required for the applications in the TCO industry, and also to achieve good performance in photovoltaics. In this sense, sputtering and ALD appear to be promising for the fabrication of Cu_2O-based devices.

1.1.1 Atomic Layer Deposition of Copper Oxide Thin Films

Atomic layer deposition has emerged as a successful technique for the growth of high quality thin films, with high uniformity and high degree of conformability. The self-limiting growth mechanism in which ALD is based allows a very precise thickness control and a conformal deposition on high aspect-ratio structures, which is highly demanded in the microelectronics industry due to the continuous miniaturization trend in semiconductor devices. ALD found its first application in the thin film electroluminescent displays (TFEL) industry, since high-quality luminescence films deposited on large area substrates were required [32], and where it is widely used to the present days. Furthermore, ALD is commercially used in the semiconductor industry for the fabrication of high-k dielectrics like Al_2O_3, ZrO_2, and HfO_2 for metal–oxide semiconductor field-effect transistors (MOSFET), capacitors for dynamic random access memory (DRAM), and, in general, for complementary metal-oxide semiconductor (CMOS) technology [33]. ALD processes have been developed for the fabrication of metal and nitrides for electrodes and interconnects [32]. Recently, ALD has also been applied in photovoltaic technology for the fabrication of electrodes, transparent conductive oxides, thin-film semiconducting layers, passivation layers, and moisture diffusion barrier in organic solar cells [33–35].

There are many reports regarding the deposition of metallic Cu film by ALD [36–40], mainly for applications in microelectronics interconnection. In contrast, the deposition of copper oxides by ALD has been considerably less studied, and it started to gain interest in recent years due to the potentialities of Cu_2O for all-oxides photovoltaic applications.

Different approaches have been employed for the deposition of Cu_2O films. T. Törndahl reported the deposition of Cu_2O thin films on amorphous SiO_2 and single crystalline α-Al_2O_3 substrates by a high-temperature thermal ALD process (from 350 to 700 °C), using copper (I) chloride and water as precursors [41]. The films deposited were polycrystalline on SiO_2 and showed a (110) texture in α-Al_2O_3, more pronounced at higher temperatures. However, they present a small amount of metallic Cu, due to instability of the CuCl precursor, that increases

at higher deposition temperatures. They also reported a lower temperature ALD process (210 - 300°C) when using a different precursor, copper (II) hexafluoroacetylacetonate, $Cu(hfac)_2$. This precursor was employed for the growth of Cu_3N films in a six-steps ALD process, using water and ammonia as reactants [42], and Cu_2O films were formed when the ammonia pulse was removed. A two-step process was reported by Kwon *et al.*, consisting on the growth of metallic Cu using hexafluoroacetylacetonate Cu(I) (3,3-dimethyl-1-butene) and a H_2 plasma followed by oxidation in an O_2 plasma. This method allows the selective deposition of Cu, CuO and Cu_2O by changing the number of Cu deposition steps [43]. Highly-conformal Cu_2O films were also deposited by bis(1–dimethylamino–2–methyl–2–butoxy) copper ($C_{14}H_{32}N_2O_2Cu$), and H_2O in an ALD temperature window ranging from 120 to 240 °C [27]. Copper acetylacetonate, $Cu(acac_2)$, was employed as copper precursor in combination with ozone (O_3) from depositing the tenorite phase of copper (II) oxide films [44]. Muñoz-Rojas *et al.* obtained high mobility Cu_2O film by atmospheric pressure spatial ALD, using (Trimethylvinylsilyl) hexafluoroacetylacetonato Copper(I), Cu(I)(hfac)(TMVS), as copper precursor and water as oxidizer [28].

In this thesis we will demonstrate the deposition of high quality Cu_2O thin films by thermal ALD, using $Cu(hfac)_2$ as copper precursor and water as oxidizer. The films grown by this method present excellent electrical properties with high mobility and low resistivity. Furthermore, temperature-driven and conductivity-driven selective deposition processes will be demonstrated on different substrates, which allow the deposition of both metallic Cu and Cu_2O thin films.

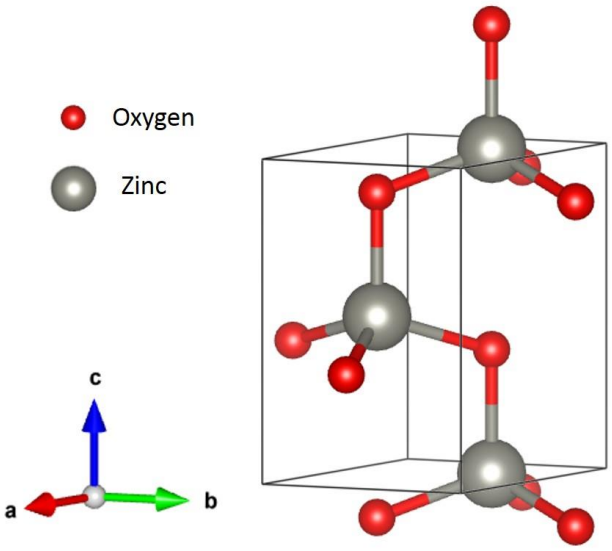

Figure 1.4. Schematic of the wurtzite crystal structure of ZnO.

1.2 Basic Properties of ZnO

ZnO is a n-type transparent conductive oxide (TCO) with a wide band gap of 3.37 eV, large exciton binding energy of 60 meV, high electron mobility, high thermal conductivity, and strong piezoelectric responses [45]. Furthermore, it is available as high-quality single crystal, and can be easily fabricated in different nanostructured architectures [46]. These properties make it an ideal candidate for UV photodetection, light emitting diodes, transparent thin film transistors, sensors, and window layers in solar cells [47–50].

At ambient conditions ZnO crystalizes in the wurtzite hexagonal crystal structure (space group $P6_3mc$), with lattice parameter $a = 3.25$ Å and $c = 5.21$ Å (see schematic in Figure 1.4). This structure is the superposition of two hexagonal-close-packed (hcp) sublattices of Zn and O. The zinc atoms are connected with oxygen atoms in tetrahedral coordination and vice versa.

Due to its large band gap of 3.37 eV, ZnO is transparent in the visible range of the electromagnetic spectrum. It is a direct band gap semiconductor since the valence band maximum and the conduction band minimum are located at the same k-point (Γ-point of the Brillouin zone), as can be seen in Figure 1.5 A. The conduction band arises mainly from the empty 4s states of Zn^{2+}, meanwhile the highest valence band arises from the occupied 2p states of O^{2-} [51].

Several native point defects have been identified in ZnO crystals: oxygen vacancies (V_O), zinc vacancies (V_{Zn}), oxygen interstitials (O_i), and zinc interstitials (Zn_i), among others. Most of the calculations agree that V_O has the lowest formation energy among all the ZnO defects (~ 1 eV under oxygen-poor conditions) [52]. On the other hand, V_{Zn} have shown its lowest formation energy under oxygen-rich conditions, particularly for n-type ZnO [45]. O_i and V_{Zn} have been considered acceptor defects in ZnO. Particularly, V_{Zn} are considered as the main compensating centers in n-type ZnO; this was corroborated experimentally by positron annihilation spectroscopy [45]. On the contrary, V_o and Zn_i are both donor defects, Zn_i being a shallow donor (~ 0.05 eV below the conduction band), and V_O a deep donor [45,52]. In n-type ZnO, Zn_i has a very high formation energy, however it has been suggested that this type of defect can still be formed under out-of-stable-equilibrium conditions [53]. The intrinsic n-type conductivity of ZnO can be explained by the presence of native donor defects, however this topic is still under debate, and some authors claim that it is the result of the existence of impurities in the ZnO acting as extrinsic donor defects. In particular, interstitial hydrogen (H_i)

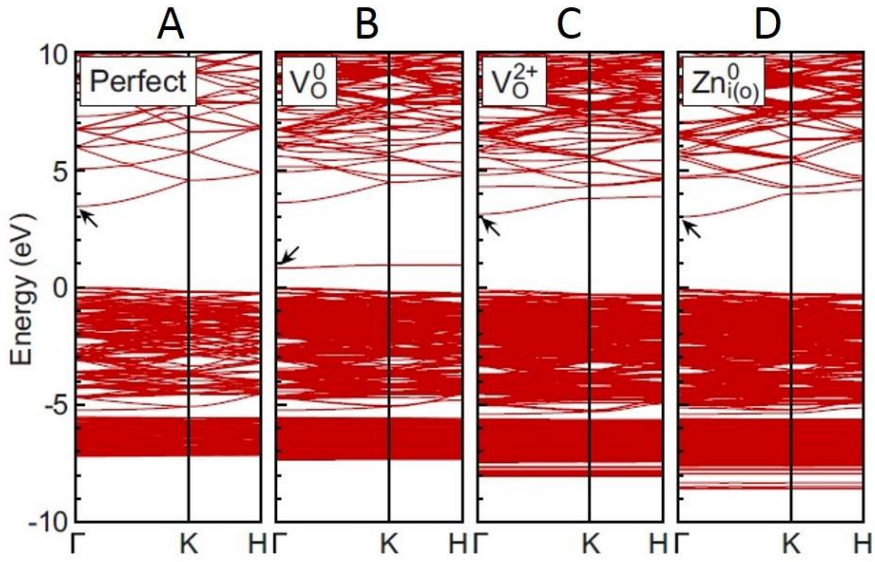

Figure 1.5. Band structure of a ZnO perfect crystal (A), and considering different types of defects: oxygen vacancies in the neutral state (B) and 2+ charge states (C), and Zn interstitial at the octahedral site in the neutral state **[52]**.

and substitutional hydrogen at the oxygen site (H_O) have been identified as shallow donors, with low formation energies, which means that they can exist in large amount in ZnO [45,52].

There is also the possibility of intentionally doping ZnO in order to increase the carrier concentration. Potential candidates for n-doping are the elements of group III B, that substitute the Zn cation site, such as Al, Ga, B or In. These elements have one additional valence electron compared to Zn, and therefore they introduce an extra electron into the ZnO conduction band [54,55]. The elements of group VII like Cl, F or I, can also act as donor dopants, in this case by substituting the oxygen atom, and providing also an extra electron into the conduction band [56]. Al has been the most commonly employed dopant for ZnO, improving considerably the ZnO conductivity [57,58]. Minami *et al.* reported resistivity values of $2 \times 10^{-4}\ \Omega cm$, and carrier concentration of $\sim 10^{21}\ cm^{-3}$, for AZO films fabricated by RF magnetron sputtering [59]. Resistivity of $\sim 10^{-4}\ \Omega cm$ and carrier concentration of $11 \times 10^{20}\ cm^{-3}$, were obtained for Al-doped ZnO (AZO) thin films deposited by high impulse magnetron sputtering [60], and Agura *et al.* reported resistivity and carriers concentration of $8.5 \times 10^{-5}\ \Omega cm$, and $1.5 \times 10^{21}\ cm^{-3}$, respectively for AZO films deposited by pulsed laser deposition (PLD) [61].

ZnO thin films can be grown by several techniques. Examples of the chemical routes most commonly employed are the sol-gel methods, electrochemical deposition, that has been widely employed for the growth of ZnO nanostructures [62], and chemical vapor deposition [63]. On

the other hand, among the physical vapor deposition methods there are: pulsed laser deposition [61], molecular beam epitaxy [64], and sputtering (DC, RF and HiPIMS) [60,65].

The sputtering technique is one of the most popular techniques employed for the deposition of ZnO thin films. It is a relatively simple method that allows the deposition of ZnO films with good electrical and optical properties, at low operating temperature, with the advantage of scalability to large-area substrates.

In this thesis we used the reactive magnetron sputtering method for the growth of ZnO and AZO films in $Ar+O_2$ atmosphere. By changing the O_2 partial pressure in the reaction chamber it is possible to tune the conductivity of the ZnO films in a large range.

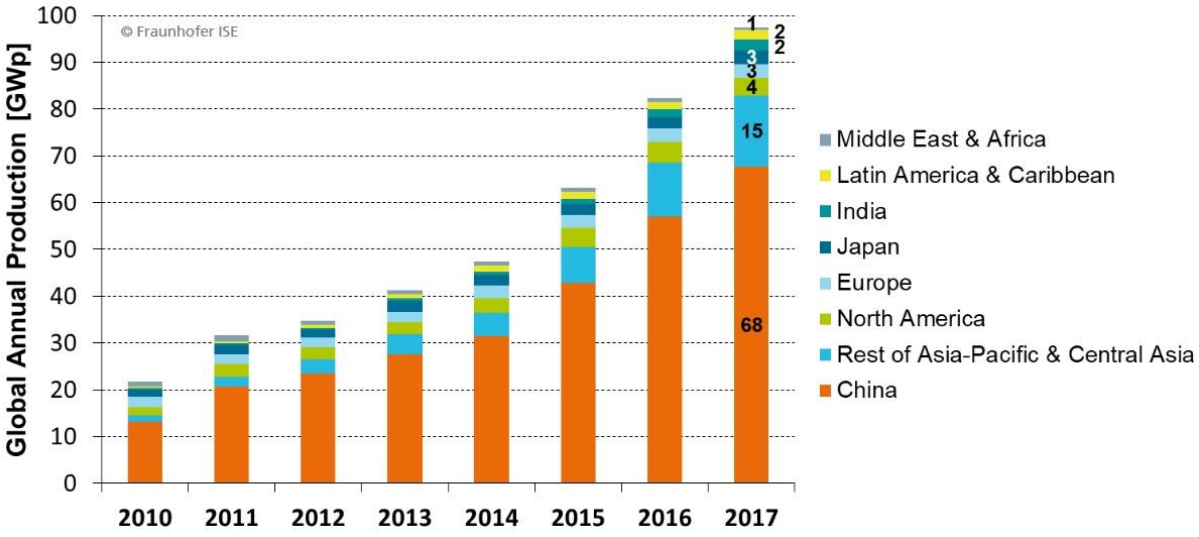

Figure 1.6. Evolution of the annual global photovoltaic production in the period 2010 - 2017 **[66]**.

1.3 All-oxides Photovoltaics

Metal oxide semiconductors have gained a lot of attention regarding their good chemical stability, abundance of constitutive elements in the earth crust, non-toxicity and low-fabrication cost. They can find application in a wide variety of fields like optoelectronics [45], photovoltaics [8,67], water splitting [26], and photodetection [9], among others. Furthermore, the fabrication of all-oxide based devices is emerging as a promising approach to reduce manufacturing costs and environmental impact.

The photovoltaic market has experienced a spectacular growth in the last decade (Figure 1.6). In 2017 the solar global market grew by 30% with respect to the previous year, reaching a global solar photovoltaic installed capacity of 99 GW, which leads to a cumulative installed capacity of more than 400 GW. However, even with this prosperity, further improvements need to be achieved in terms of efficiency and prize reduction to render PV competitive with

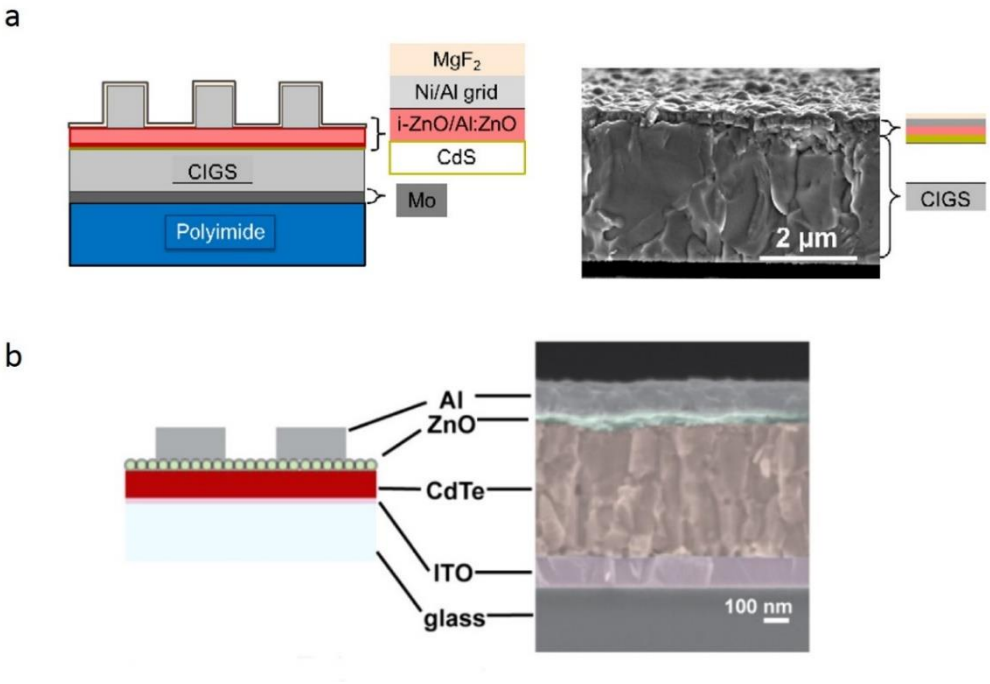

Figure 1.7. Schematic and cross-section SEM micrograph of a thin film CIGS solar cell on a flexible polyimide substrates, from **[74]** (a). Schematic and colored cross-section SEM micrograph of a CdTe solar cell, from **[75]** (b).

traditional electricity generation systems based on fossil fuels. In this sense, the use of low-cost, abundant and environmental-friendly materials is one of the challenges of PV technology. PV based on semiconductor oxides is a promising solution to accomplish this objective.

Metal oxide semiconductors have been already employed in solar cells technology, mainly as transparent conductor oxides (TCOs), such as indium tin oxide (ITO), fluorine-doped tin oxide (FTO), and ZnO-based materials [8]. TCOs have been widely used in the commercially available copper indium gallium diselenide (CIGS), and CdTe thin film technology [68–70], in copper indium selenide (CIS) solar cells [71] and in amorphous Si [72] technology. Two different solar cells configurations based on CdTe and CIGS absorber layers are depicted in Figure 1.7, with the use of different TCOs (ZnO, Al-doped ZnO, and ITO). The fabrication of textured or nanostructured TCOs has also been explored as a way of enhancing absorption, by light trapping and internal reflectance enhancement, and to increase carrier transport efficiency [8,73].

1.3.1 Cu_2O-based Solar Cells

Most of the applied TCOs are n-type materials, and achieving p-type doping is challenging. Therefore, for the progress of all-oxide photovoltaic industry entirely based on semiconductor oxides, p-type absorber materials with as good electrical properties as their n-type counterpart,

need to be developed. Among the p-type semiconductor oxides, Cu_2O is a suitable candidate due to its large absorption coefficient, high hole mobility, abundance of constitutive element in the earth crust, and non-toxicity. It has found application as p-type absorbed layer in combination with n-type wide bandgap semiconductor oxides such as ZnO, TiO_2, and Ga_2O_3 [76–78], as hole transporter layer in perovskite solar cells [79], and it has been investigated as constitutive of the top cell of Si-based tandem solar cells in combination with ZnO [80].

A theoretical power conversion efficiency (PCE) of 23% was predicted by the Shockley-Queisser theory [8] for Cu_2O as absorber layer in solar cells. However, so far, efficiencies reported for Cu_2O based devices remain far from the theoretical value (see Figure 1.8). The V_{OC}, I_{SC}, FF, and PCE of several Cu_2O-based solar cells are reported in Table 1.1, from 2004 up to the present. Cu_2O/TiO_2 heterojunctions have been fabricated on FTO/glass substrates by spray-pyrolysis. Maximum open circuit voltage (V_{OC}), and short-circuited current (I_{SC}) values for this device were of $350\ mV$, and $0.4\ mA/cm^2$, respectively. The authors claim that the small current density measured is not due to low absorption but to poor electrical quality of the Cu_2O films [78]. Cu_2O/ITO and Cu_2O/ZnO/ITO devices were fabricated by Mittiga *et al.* [81]. The Cu_2O thin films were grown by oxidation of Cu sheet at high temperatures, and the TCOs films (ITO and ZnO) were deposited by ion beam sputtering at room temperature. Higher V_{OC} and I_{SC} values of $575\ mV$ and $6.78\ mA/cm^2$, were obtained compared with the Cu_2O/TiO_2 heterojunctions. PCE of 1 and 2 % were reported for the Cu_2O/ITO and Cu_2O/ZnO/ITO, respectively. The authors point out that the factor limiting the device performance is the

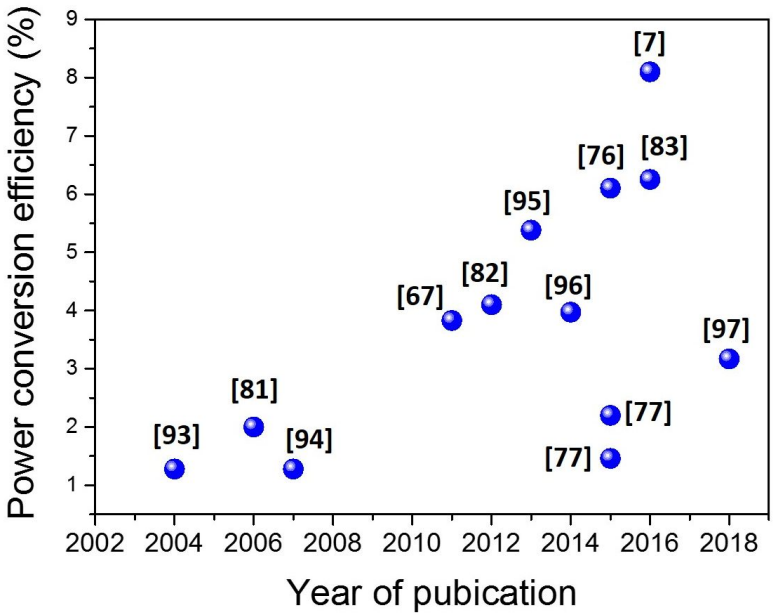

Figure 1.8. Power conversion efficiency in Cu_2O-based solar cells by year of publication.

presence of high series resistance, due to the high resistivity ($\sim 1000\ \Omega cm$) of the Cu_2O films. Nishi *et al.* reported an improvement of PCE by introducing a 50-nm ZnO buffer layer between a n-AZO and a p-Cu_2O films, reaching a PCE of 4.12 %, that is the highest value reported for a ZnO/Cu_2O-based solar cells [82].

A PCE of 6.25 % was reported by Minami *et al.*, in a MgF_2/AZO/ $(Ga_{0.975}Al_{0.025})_2O_3$/$Cu_2O$:Na device, with V_{OC} and I_{SC} values of $840\ mV$ and $10.8\ mA/cm^2$, respectively [83]. The improvement of the device performance was achieved in this case by optimization of the chemical composition of the n-type oxide and optimization of the Cu_2O film resistivity through Na-doping. Minami *et al.* also reported a higher PCE of 8.1 %, in a similar device by replacing the multi-component oxide $(Ga_{0.975}Al_{0.025})_2O_3$ by $Zn_{0.38}Ge_{0.62}O$. The authors claim that the improvement of the PCE in this device is the result of the lower electron affinity of the new multi-component oxide employed, that allows a reduction of the conduction band offset with Cu_2O.

1.3.2 Cu_2O/ZnO Heterojunctions

As can be seen in Table 1.1, the Cu_2O-ZnO system has been by far the most studied. Until now we have presented some examples of Cu_2O-based devices in which the thickness of the Cu_2O absorber layer ranged from 2 to 250 μm. However, there are several approaches where nanostructured devices have been fabricated to enhance the optical absorption without the need of thick absorbing layers as a way of improving charge collection, and reducing material use. Most of them consist in the deposition of Cu_2O thin films on ZnO nanostructures (nanowire, nanorods, or nanotubes), due to the versatility of ZnO to be produced in nanostructure architectures of different sizes and shapes [84–87]. Therefore, due to the high surface area of the nanostructured devices, lower thicknesses of Cu_2O are required. Additionally, the distance that carriers need to travel before reaching the junction is significantly reduced, increasing carrier collection efficiency.

Cu_2O/ZnO heterojunctions have also been studied for application in low-cost transparent electronics and transparent photovoltaics. In this type of devices, a compromise between transparency and electrical performance need to be reached. The relatively large band gap of Cu_2O (higher than the optimum value of 1.34 eV, predicted by the Shockley-Queisser theory [88]) makes it a promising candidate in this field in combination with ZnO [89–91]. Furthermore, Cu_2O/ZnO heterojunctions have been explored as possible candidates for photodetection [86], particularly in nanostructured architectures. High-performance in UV-VIS photodetection was reported in a device made of single-wall carbon nanotubes (SWNTs)/PET

Table 1.1. Cu_2O-based photovoltaic devices, electrical performance up to 2018.

Growth method	**Heterojunctions**	**V_{OC} (V)**	**J_{SC} (mA/cm^2)**	**FF (%)**	**PCE (%)**	**Ref.**
PLD / TO	AZO/Cu_2O	0.4	7.1	0.4	1.28	[93]
IBS / TO	ITO/ZnO/Cu_2O	0.59	6.78	50%	2	[81]
ECD	ZnO/Cu_2O	0.41	7.1	42	1.28	[94]
PLD / TO	AZO/ZnO/Cu_2O	0.69	10.1	55	3.83	[67]
PLD / TO	AZO/ZnO/Cu_2O	0.72	9.67	58	4.12	[82]
PLD / TO	AZO/Ga_2O_3/Cu_2O	0.8	9.99	67	5.38	[95]
ALD / ED	AZO/Ga_2O_3/Cu_2O	1.2	7.37	44.7	3.97	[96]
AALD / TO	ITO/$Zn_{0.79}Mg_{0.21}O$/Cu_2O	0.65	6.9	49.2	2.2	[77]
AALD / TO	ITO/ZnO/Cu_2O	0.49	7.5	40	1.46	[77]
PLD / TO	AZO/$Al_{0.025}Ga_{0.975}O$/ Cu_2O:Na	0.84	10.95	66	6.1	[76]
PLD / TO	AZO/$(Al_{0.025}Ga_{0.975})_2O_3$/ Cu_2O: Na	0.84	10.8	69	6.25	[83]
PLD / TO	AZO/$Zn_{0.38}Ge_{0.62}O$/ Cu_2O:Na	1.1	11.1	62	8.1	[7]
RO/RPE-CVD	ZnO/Cu_2O	0.557	11.42	49.8	3.17	[97]

TO, thermal oxidation; PLD, pulsed laser deposition; IBS, ion beam sputtering; ECD, electrochemical deposition; ALD, atomic layer deposition; AALD, atmospheric ALD; RO, radical oxidation; RPE-CVD, remote-plasma-enhanced chemical vapor deposition.

substrates covered by ZnO/Cu_2O hybrid nanofilm, deposited by RF magnetron sputtering [92], and recently, a fast response self-powered photodetector was reported in a ZnO/Cu_2O core-shell nanowires device [9].

In this thesis we will present the results on the fabrication of transparent thin film ZnO/Cu_2O heterojunctions. The Cu_2O films were deposited by ALD, since it allows achieving high mobility and low resistivity values which is essential to improve carriers transport properties. Furthermore, a good interface matching is obtained between the Cu_2O and ZnO films, which is particularly important to achieve an efficient charge separation and improve the device performance.

1.4 Noble Metal Nanoparticles

Noble metal nanoparticles have attracted lot of attention for mankind since prehistoric times, particularly gold and silver, which were used mainly for artistic and decorative purposes, for example, in the coloration of glasses, ceramics, fabric, etc. Today the comprehension of the atomic world, and the technological advances in nanofabrication techniques, have opened an avenue toward new applications that allow the precise control and manipulation of light, through the metal nanostructures that can be effectively used to focus and guide the light with nanoscale precision. By controlling the size, shape, chemical composition, and agglomeration of the nanoparticles, their chemical, optical and electrical properties can be manipulated, finding application in multidisciplinary fields such as, catalysis, optoelectronics, bio-sensing, photovoltaics, among others [98–101].

1.4.1 Localized Surface Plasmon Resonance

Metallic nanoparticles exhibit localized surface plasmon resonance (LSPR), that is the collective oscillation of the valence electrons at the metallic nanoparticle that enters in resonance with an external electromagnetic field, resulting in a selective absorption of light at the resonance plasmon frequency, and the enhancement of the electromagnetic field at the particle surface (see Figure 1.9).

Gustave Mie was the first to provide a theoretical background for explaining the plasmon resonance phenomenon observed in noble metal nanoparticles, by solving Maxwell equations on a metallic sphere of radius R, under the action of an electromagnetic field [102]. When the wavelength (λ) of the incident light is much higher that the particle radius ($R/\lambda < 0.1$), only

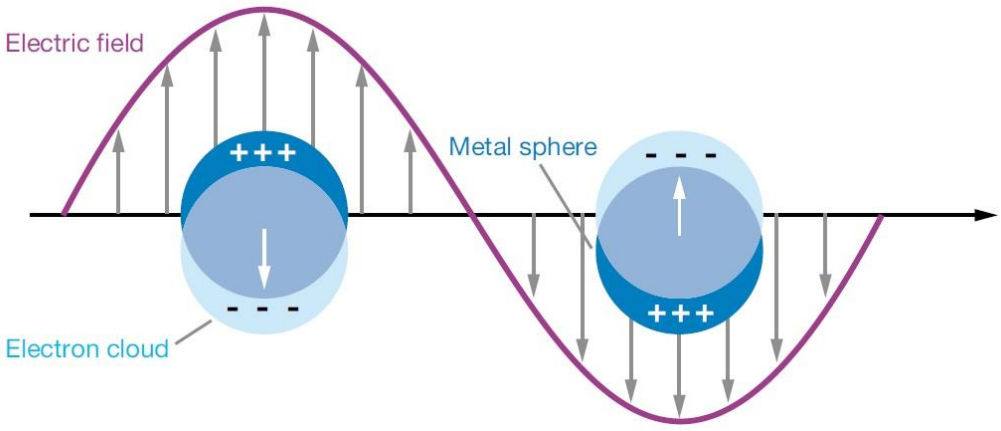

Figure 1.9. Schematic of localized surface plasmon resonance at the metallic nanoparticles **[98]**.

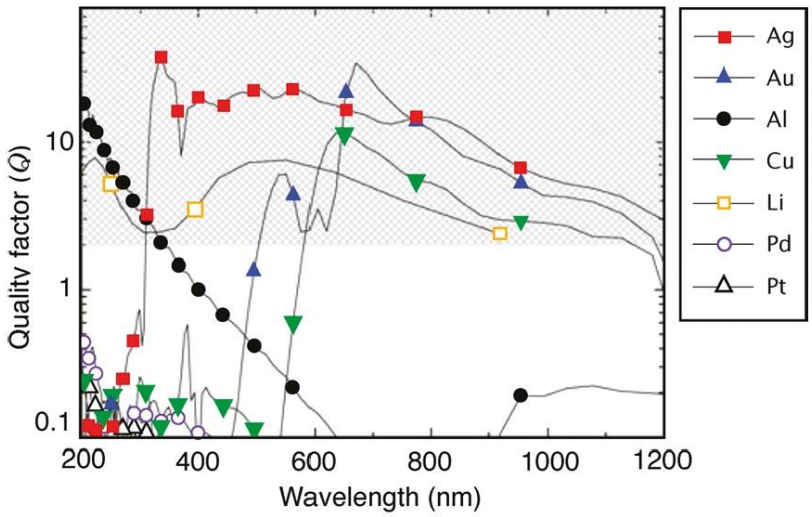

Figure 1.10. Quality factor of the localized surface plasmon resonance for several metals surrounded by air. The shaded area corresponds to the region of interest for most plasmonic applications **[103]**.

the electric dipole term contributes to the total extinction cross-section (σ_{ext}), which can be determined by:

$$\sigma_{ext} = \frac{12\,\pi\,w\,R^3{\varepsilon_m}^{3/2}}{c}\left[\frac{\varepsilon_i}{(\varepsilon_r + 2\,\varepsilon_m)^2 + {\varepsilon_i}^2}\right] \qquad \textbf{(1.1)}$$

where ε_r, and ε_i are the real and imaginary parts of the dielectric function of the metallic nanoparticle, respectively, ε_m is the dielectric function of the medium surrounding the nanoparticle, c is the speed of light, and w is the angular frequency of the light.

From equation (1.1), resonance is reached when $\varepsilon_r = -2\,\varepsilon_m$, that results in strong enhancement of the extinction cross-section. This condition cannot be fulfilled by most of dielectrics and nonmetals since they typically have $\varepsilon_r > 1$. Moreover, ε_i needs to be small, or weakly-dependent on w, to obtain strong plasmonic response. In fact, ε_i is a measure of the sharpness of the LSPR band (lower ε_i indicating a sharper resonance response).

A quality factor (Q) can be defined, that is directly proportional to the strength of the plasmon resonance and is given by [103],

$$Q = \frac{w\,(d\varepsilon_r/dw)}{2\,{\varepsilon_i}^2} \qquad \textbf{(1.2)}$$

The quality factor for several metals in contact with air is reported in Figure 1.10. The shaded region corresponds to materials with suitable quality factors for plasmonic applications. Aluminum is a suitable plasmonic material in the UV range, meanwhile Au, Ag and Cu are

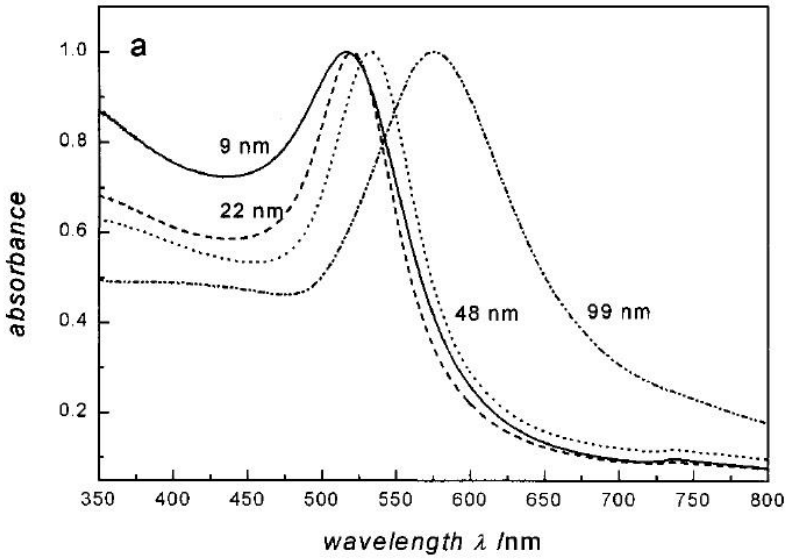

Figure 1.11. Absorption spectra of gold nanoparticles with sizes ranging from 9 to 99 nm **[105]**.

appropriate for application in the visible range. Lithium possesses also a suitable quality factor, however due to its reactivity and difficult handling is rarely considered.

1.4.2 Effects of Size, Shape and Interparticle Distance on the LSPR Signal

Mie theory is valid for particles of sizes smaller than the wavelength of the incident light, but doesn't take into account the specific particles dimension and therefore doesn't predict the LSPR shift with particles size. An example of the LSPR band red-shift with the increasing of gold NP size from 9 to 99 nm, is depicted in Figure 1.11. In the case of larger particles (usually R > 20 nm), the dependence of LSPR position with size becomes even more important, and the contribution of quadrupole and higher order multipole modes cannot be neglected [104]. In fact, in Figure 1.11 it can be seen that a small red-shift is observed between the 9 and 48 nm Au nanoparticles, meanwhile a considerable red-shift is observed between the 48 and 99 nm nanoparticles.

It is possible to obtain an analytical expression by solving the Maxwell equations for spherical particles (Mie theory), and for spheroidal particles (in this case, the analytical expression is far more complicated), however particles with other geometries need to be solved by numerical methods such the discrete dipole approximation (DDA) or the finite-difference time-domain (FDTD) method [106]. The LSPR band depends strongly on the geometry of the particles. For example, as nanoparticle shape becomes more oblate, the longitudinal and transversal polarization modes produce resonance at different wavelengths, and two LSPR bands appear (see Figure 1.12). One band is observed at higher energy (transverse mode), which is associated to electron oscillations perpendicular to the major axis of the particle, and the other

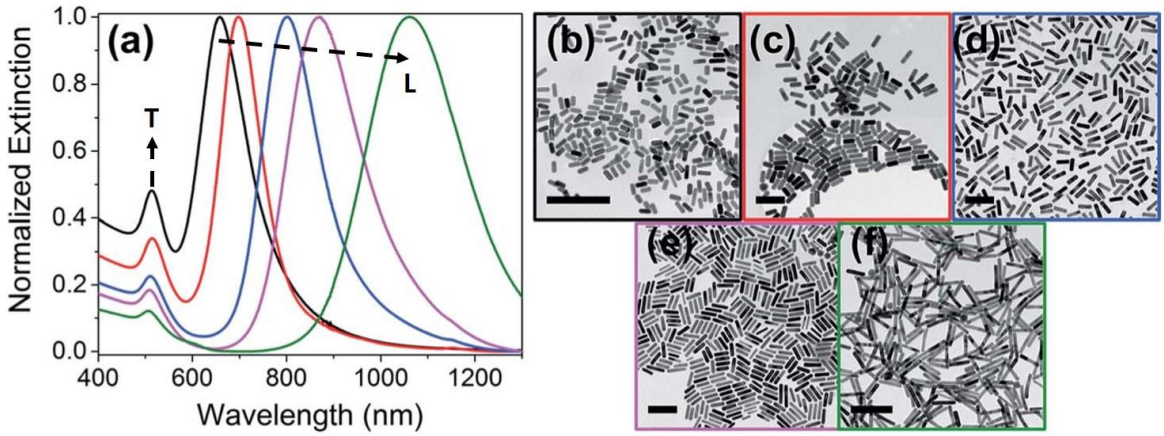

Figure 1.12. Evolution of the extinction spectra of Au nanorods by changing the aspect ratio. The longitudinal (L) and transverse (T) plasmon modes are indicated (modified from **[109]**).

band is observed at lower energy (longitudinal mode), and is associated to electron oscillations along the particles major axis. The separation between these bands increases with particles aspect ratio, as can be seen from the extinction spectra of Au nanorods of different aspect-ratio, in Figure 1.12. Multiple resonance modes are also observed for other nanoparticle geometries as triangular prims, cubes, rods, cylinders, etc.

Another factor influencing the position and width of the LSPR band is the agglomeration of particles. When the particles are closely packed an electromagnetic coupling is produced, the resulting extinction spectrum is composed of the single particles LSPR and that related with particle-particle interactions [107,108]. This phenomenon becomes important when the distance between adjacent particles is lower than five-time the particle radius, and results in a significant red-shift and broadening of the LSPR band. The red-shift produced by particle agglomeration can be considerably higher than the one produced by increasing particle size [108].

1.4.3 Hot-electron Generation

As was described in the previous section the LSPR band appears at different energies for different metallic nanoparticles, and can be tuned by controlling the particle size, shape, density, etc. Therefore, it is possible to fabricate plasmonic nanostructures with LSPR resonance covering the electromagnetic spectra from the UV to the infrared. This together with the enhancement of the electric field around the particle surface can be exploited for energy harvesting. In fact, the integration of plasmonic nanostructures into semiconductor and photovoltaic devices has been proposed as a way of improving device efficiency. Particularly,

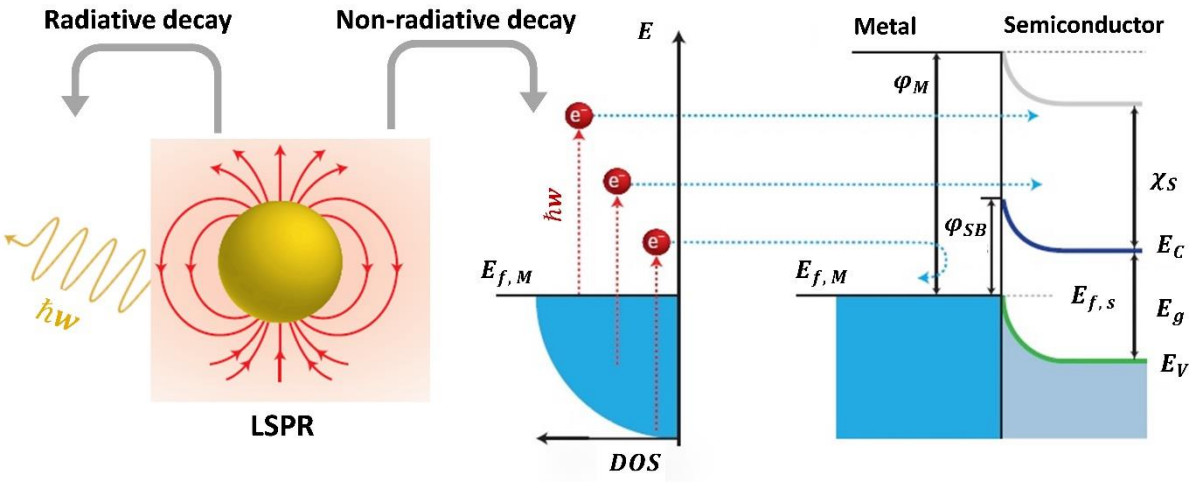

Figure 1.13. Schematic of the LSPR decay (left), and the hot-electron generation at the metallic nanoparticle and injection into the semiconductor (modified from **[3]**).

the LSPR allows direct conversion of light into electricity through hot-electron generation, as will be discussed in the following.

After LSPR excitation, surface plasmons decay radiatively, by re-emission of photons, or non-radiatively through emission of hot-electrons. These electrons can be excited above the Fermi level, as is shown in the schematic of Figure 1.13. If the particle is in contact with a semiconductor material (forming a Schottky junction), these electrons can be injected into the semiconductor if their energy is higher than the Schottky barrier, $\varphi_{SB} = \varphi_M - \chi_s$, where φ_M is the work function of the metallic particle, and χ_s is the electron affinity of the semiconductor. Therefore, plasmonic nanoparticles, with LSPR in the visible or near-infrared (lower than the semiconductor bandgap) can be excited by the low energy photons of the solar spectrum, and produce hot-electrons (E ~ 1 - 4 eV) that can be injected into the conduction band of the semiconductor. Hence, the low energy portion of the absorption spectrum of the semiconductor material is enhanced (by itself, the semiconductor can only absorb photons of energy higher than its band gap). This effect has been exploited for the fabrication of optical antennas for photodetection, for photocatalysis and photovoltaic applications [3,110].

The LSPR gives place to a highly localized electric field at the nanoparticle surface, that can be 10^3 times higher than the electric field of the incoming light [111]. Electron-hole pairs generation in a semiconductor, in close proximity with the plasmonic nanoparticle, is increased by few orders of magnitude, since it depends on $|E^2|$. This mechanism has been used for increasing the surface enhanced Raman scattering (SERS) signal, in the detection of certain molecules [112] and photocurrent enhancement of 20% have been reported in Si nanowires

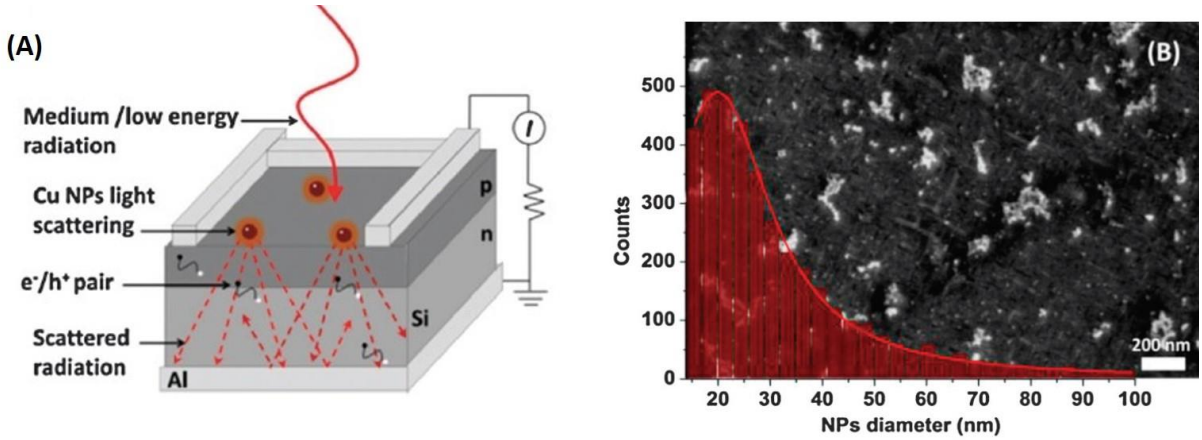

Figure 1.14. Schematic illustrating the light scattering in a Si solar cell due to the Cu nanoparticles at the surface (A). Top-view SEM micrograph of the devices showing the Cu nanoparticles at the surface (B) (modified from **[114]**).

decorated with Au nanoparticles, studied through variable-wavelength scanning photocurrent microscopy [113].

In systems composed of larger particles ($2R > 50$ nm) or aggregates, in addition to the LSPR there is an increase of the light scattering by the plasmonic nanostructures. Due to the strong scattering of the resonant photons, the optical photon path inside the device is increased and, in consequence, the generation of electron-hole pairs is boosted. This mechanism is depicted in Figure 1.14, where Cu nanoparticles are used to enhance the photocurrent in a Si photovoltaic device, by scattering and trapping light inside the device [114].

1.5 Photodetectors

Photodetectors are optoelectronic devices that convert light into an electrical signal, hence, working as a light sensor. Different than solar cells, which are intended to provide the maximum power yield, photodetectors are designed to achieve high sensitivity and fast response. Therefore, as in a solar cell we are interested in the power conversion efficiency, in a photodetector the important parameter is the external quantum efficiency (number of photogenerated carriers divided by the number of incident photons in the device). A figure of merit for photodectectors, directly related with the external quantum efficiency, is the responsivity, R (A/W), that is expressed in terms of the photogenerated current (photocurrent), I_{ph}, divided by the incident optical power, P_{inc} equation (1.3).

$$R = \frac{I_{ph}}{P_{inc}} \qquad \textbf{(1.3)}$$

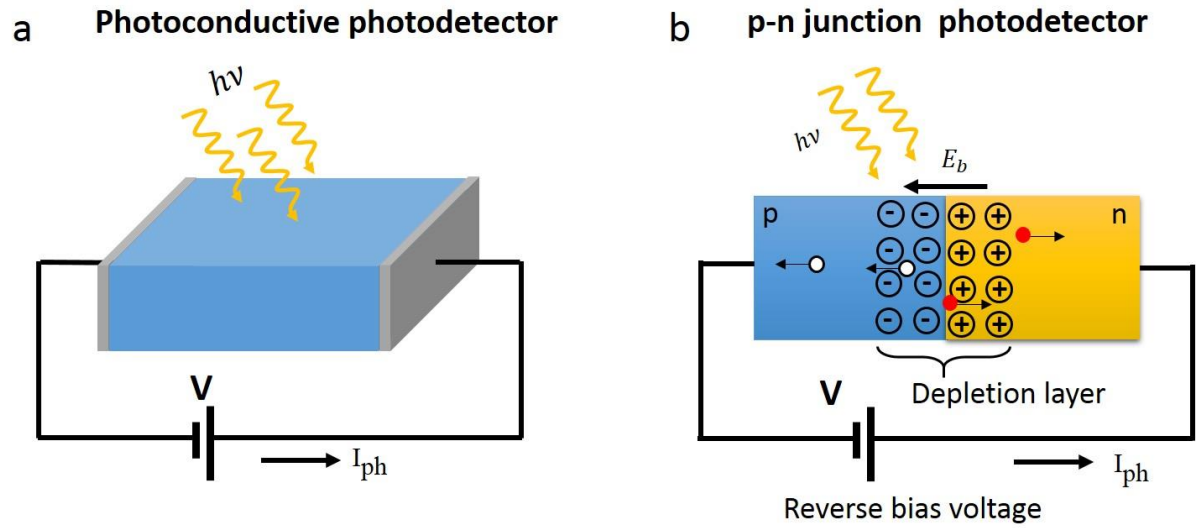

Figure 1.15. Schematic of a photoconductive (a) and a p-n junction (b) photodetectors.

The responsivity is affected by the optical absorption coefficient of the material that the photodetector is made of, the recombination rates, and the carrier's lifetime. Another key parameter in a photodetector is the response time (τ_r), that is defined as the time that the current takes to rise from 10 to 90 % of its final value, when the incident optical power changes abruptly.

Photodetectors can be classified in different categories based on the photodetection mechanism [115]. The simplest ones are the photoconductive photodetectors, that consist of a semiconductor material with ohmic contacts at its edges. When light hits the semiconductor, electron-hole pairs are generated which results in an increase of the conductivity. Hence, when a voltage is applied to the semiconductor, an electrical current is detected (see schematic in Figure 1.15 a). This type of photodetectors has the inconvenient of high dark currents and high noise levels.

Most efficient photodetectors are based on p-n junctions. When light shines into the p-n junction, electron-hole pairs are generated, and they are separated by the internal built-in electric field at the junction, as is shown in Figure 1.15 b (electrons to the n-side and holes to the p-side). This type of photodetectors can be operated without an external bias (self-powered photoresponse), but and external reverse bias can be applied to reinforce the internal built-in potential at the junction and improve the charge separation. This type of photodetectors is usually characterized by high responsivity values. The response time depends not only on the carrier drift transit time at the depletion layer, but also on the time that carriers (photogenerated one diffusion length away from the depletion layer) take to reach this region before being separated. This limits the response time of the photodetectors since the diffusion is a slow

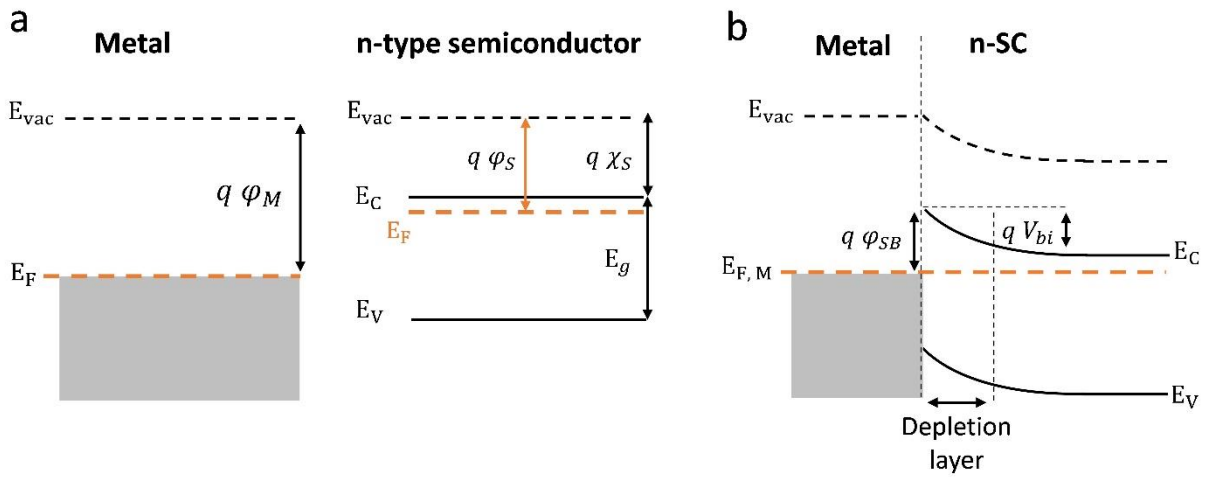

Figure 1.16. Band energy diagram of a metal and a n-type semiconductor, isolated (a) and when both materials are brought together, forming a Schottky junction (b).

process. Therefore, it is desirable that the absorption and photogeneration of carriers occur only at the depletion layer. This is achieved in the p-i-n photodetectors, where an intrinsic semiconductor is sandwiched between the n-type and p-type semiconductors. Since the i-region possesses a high resistivity, most of the applied voltage drops at this region. The width of the depletion layer is then controlled by the thickness of the i-region. In this configuration the diffusion contribution to the photocurrent is completely overtaken by the drift current, since most of the carriers are generated at the depletion layer. Furthermore, the semiconductor at the n and p regions can be chosen with higher bandgap than the energy intended to be absorbed, and the i-region with lower bandgap. In this way, n and p types regions are transparent and absorption only occurs at the i-region.

Another type of photodetector is the Schottky diode photodetector. Let's consider a metal that is brought in contact with a n- type semiconductor. If the work function of the metal (φ_M) is higher than the work function of the semiconductor (φ_S), electrons will pass from the metal to the semiconductor, a depletion region is created at the semiconductor side, and an electric field appears at the junction, analogously to the case of the p-n junction. A barrier is produced between the metal and the semiconductor, called Schottky barrier (see schematic in Figure 1.16).

When light shines into the Schottky junction, the internal electric field of the junction is exploited to allow the charge separation as in the case of the p-n junction. Connecting the device in reverse-bias conditions (positive to the n-type semiconductor and negative to the metal), both the barrier height and the depletion layer thickness increase, favoring the charge separation, and

the photocurrent. Usually, this type of photodetectors allows high speed operation, considerably faster than p-n junction photodetectors.

1.5.1 Hot-carrier Photodetectors

The LSPR phenomena observed in some metallic nanostructures that was described in section 1.4.1, has been widely exploited for photodection. There are two main photodetection mechanisms for devices based on plasmonic metallic nanostructures. First, through the enhanced electric field created at the nanoparticle surface that, when it is in contact with a semiconductor, can serve to increase the hole-carrier generation and the photocurrent, and secondly, the generation of hot-carriers at the plasmonic nanostructure and injection into the semiconductor. Here, we will focus on the hot-carrier plasmonic photodetectors, that is the main interest for this thesis.

As was already explained before, when a plasmonic metallic nanostructure is brought in contact with a semiconductor material and a Schottky junction is formed, thanks to LSPR, hot-carriers are generated at the metallic nanostructure and if they possess enough energy they can be transferred to the semiconductor. In a traditional Schottky photodetector, the photodetection mechanism is based on the generation of hole-electron pairs at the semiconductor and separation at the depletion layer. If the metallic film is replaced by plasmonic metallic nanoparticles, the photocurrent can be increased considerably by the injection of electron from the nanoparticle to the conduction band of the semiconductor, in addition to the electron generated in the semiconductor from band-to-band transitions. Furthermore, the spectral response of the device can be extended by combining the absorption spectra of the semiconductor with that of the metallic nanostructure.

Liu *et al.* reported the integration of Ag nanoplates into a flexible Si-nanowire-based photovoltaic device that allows a considerable enhancement of the external quantum efficiency of 59 % in the near-infrared, by LSPR in the Ag nanoplates and hot-electron injection into the n-type Si nanowire [116]. Luo *et al.* presented a photodetector made of Au nanoparticles deposited on CdTe nanowires. The Au nanoparticles improved the device responsivity by 100 times, and extended the device sensitivity to larger wavelengths, to which the virgin CdTe nanowires were blind. Furthermore, the response time of the device was considerably reduced with the incorporation of the nanoparticles from 6 to 2 seconds, approximately [117]. They also reported the fabrication of a plasmonic photodetector based on hollow gold nanoparticles (HGNs) deposited on CdSe nanoribbons (NR). All the figures of merit of the photodetector were improved by the inclusion of the HGNs. The experimental results, together with

theoretical calculations show that the enhanced performance observed in the device is due to the increase of the photocurrent due to localized field enhancement at the particle surface and to direct carrier injection into the CdSe nanoribbons [118].

Knight *et al*. showed that embedding the plasmonic structures into the semiconductor material enhances the hot-electron transfer since more Schottky interfaces are created. As a proof of concept Au nanobelts were embedded in a Si substrate. The efficiency in the embedded architecture was 25 times higher compared with the planar structure [119].

A hybrid device made of Au nanorods – ZnO nanowires was fabricated by Pescaglini *et al.* (see Figure 1.17 a). The photocurrent measured in the near-infrared, for the hybrid device was two order of magnitude higher that for the uncovered ZnO nanowires, due to the hot-electron injection from the plasmonic Au nanorods to the wide bandgap ZnO nanowires. Furthermore, the response time of the hybrid device was 40 times faster compared with the response of the uncovered ZnO nanowires [5].

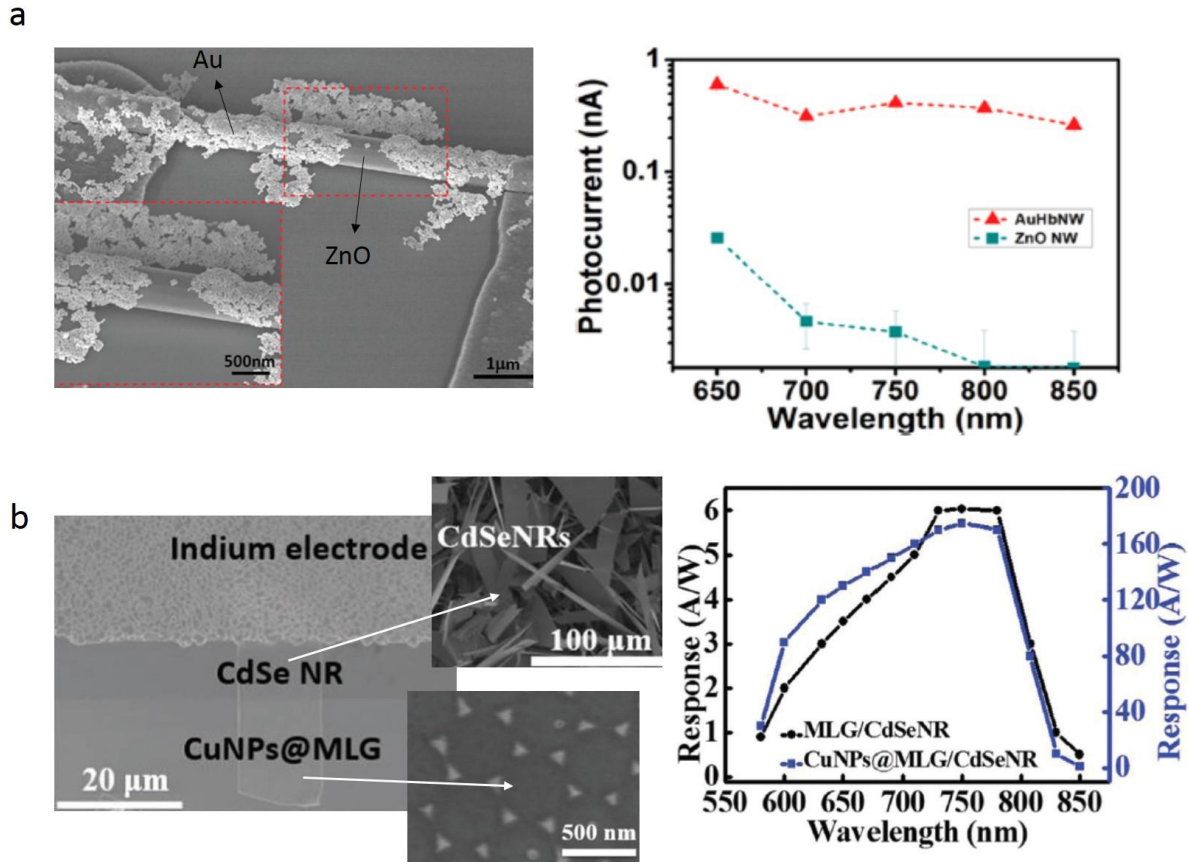

Figure 1.17. SEM micrograph of an hybrid photodetector made of Au nanorods on ZnO nanowires (left), the photocurrent of the hybrid device (red) and of the virgin ZnO nanowires (blue) as a function of the wavelength (right), modified from **[5]** (a). SEM micrograph of a MLG – CdSe nanoribbons Schottky diode, with Cu nanoparticles deposited on the MLG (left), the responsivity of the Schottky diode with (blue) and without (black) the Cu nanoparticles, modified from **[120]** (b).

Contrary to Au and Ag plasmonic nanostructures that have been widely investigated as plasmonic material to boost the performance not only for photodetectors but for several optoelectronic devices, Cu has been much less investigated. Cu has the advantage over Au and Ag of its low cost, abundance in the earth crust, and the fact that is a material already widely employed in microelectronics. Recently Wang *et al.* reported the fabrication of a nano-photodetector made of multi-layer graphene (MLG) – CdSe nanoribbons, decorated with Cu nanoparticles (see Figure 1.17 b). The incorporation of Cu nanoparticles on the surface of the multi-layer graphene results in an increase of the photocurrent by 24 times [120]. These results show the potentiality of Cu nanoparticles to boost the performance of Schottky junction photodetectors through hot-electron generation.

In this thesis we will present a simple device made of plasmonic Cu nanoparticles deposited by ALD on ZnO thin films, that shows a broadband visible photoresponse and fast response times, thanks to the hot-electron generation at the Cu nanoparticles and injection into the ZnO.

Chapter 2

Experimental Techniques

This chapter describes the atomic layer deposition and reactive magnetron sputtering methods employed for the growth of Cu_2O, metallic Cu, ZnO, Al-doped ZnO, and Cu nanoparticles through this thesis. The basic principles of the main characterization methods used in this thesis are also given, together with the specific parameters used for the analysis of the samples.

Contents

2.1 Introduction

Cu_2O, metallic Cu films and Cu nanoparticles (NP) were grown by atomic layer deposition, and ZnO and Al-doped ZnO (AZO) films were grown by reactive magnetron sputtering. The structure and microstructure of the films were studied by X-ray diffraction (XRD), scanning electron microscopy (SEM), energy dispersive spectroscopy (EDS), transmission electron microscopy (TEM) and atomic force microscopy (AFM). The electrical characterization was performed by means of the four-point probe method, Hall effect measurements and conductive-atomic force microscopy (C-AFM). The optical properties were investigated by spectroscopic ellipsometry and UV-visible spectrophotometry, and the electronic structures by X-ray photoemission spectroscopy (XPS), and electron energy loss spectroscopy (EELS). In this chapter we present the general features of atomic layer deposition and reactive magnetron sputtering as well as the main characteristics of the experimental techniques used throughout this thesis.

2.2 Atomic Layer Deposition

2.2.1 Basic Principles

Atomic layer deposition (ALD) is a vapor phase technique that has emerged as an important tool for depositing high quality thin films due to the sequential and self-limiting gas-solid surface reaction mechanism which allows an excellent surface coverage and conformal deposition with a very precise control of deposited thickness. The continuous downscaling in semiconductor and electronics industry and the miniaturization of semiconductor devices leads to the formation of high aspect-ratio structures, which impose atomic level control and requires highly conformal deposition. In this sense ALD is the most suitable approach, since no other deposition technique can achieve the degree of conformability of ALD.

In contrast with chemical vapor deposition (CVD), in which the precursors are delivered continuously, in ALD they are dosed in a cyclic manner, with purge or evacuation steps after every exposure. Growth parameters like substrate temperature, reactant exposure time, purge or evacuation time and reactant pressure are controlled and adjusted to guarantee that all the chemical reactions are completed and all the by-products are exhausted. Under these conditions, ALD proceeds through self-limiting saturated surface reactions, which means that the reaction is terminated when all the available reactive sites at the surface are occupied by the precursor molecules. After the surface is completely covered no further adsorption takes place and the growth stops until the next half cycle begins to enable cumulative deposition [121].

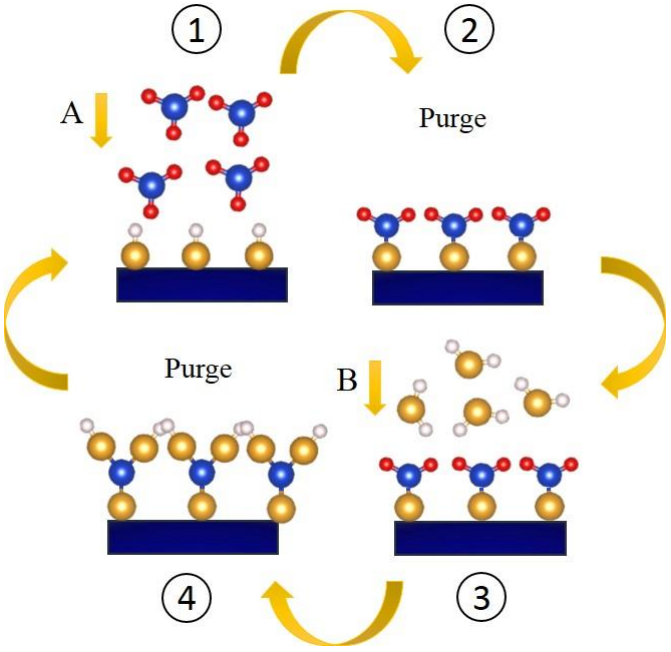

Figure 2.1. Schematic of an ALD four-step process: (1) exposure to the first precursor A, (2) purge step, (3) exposure to the second precursors B, and (4) final purge step.

In the simplest case, ALD deposition consists of four steps (see Figure 2.1). In the first step the substrate surface is exposed to the first precursor (a metal precursor, for example) which is chemisorbed onto the surface until it is completely covered with ideally one monolayer of the precursor molecules (1). This is followed by a purge step with an inert gas, in which the weakly-bound molecules deposited on top of the chemisorbed monolayer are removed (2). Furthermore, this purge step avoids the cross-contamination of the different precursors by removing the residual precursor remaining in the gas phase. The third step consists in the introduction of the second precursor into the reaction chamber which will react with the already chemisorbed monolayer to form the desired compound (3). Finally, the excess of the second precursor, together with the reaction by-products are removed from the chamber in a final purge step (4). This process is repeated cyclically until the desired thickness is achieved.

The self-limiting or self-terminated reactions make ALD a surface-controlled process were parameters others than nature of the substrate, precursor and temperature have practically no influence in the growth process. Due to the self-limiting film growth, the amount of material deposited during each ALD cycle is the same and it is the reason why the term “growth per cycle (GPC)” (deposited thickness during each ALD cycle) is preferred to design the rate of deposition.

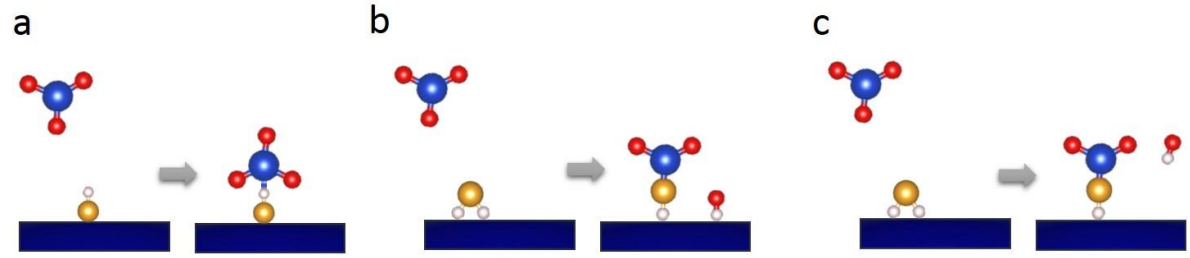

Figure 2.2. Schematic of the chemisorption mechanisms in ALD: association (a), dissociation (b), and ligand exchange (c).

2.2.2 Chemisorption Mechanisms and Self-limiting Reactions

Three main chemisorption mechanisms have been identified for the self-limiting ALD reactions: association, dissociation and ligand exchange reaction (see a schematic in Figure 2.2). When association occurs, the precursors molecule is completely adsorbed on a reactive site of the surface without any ligand release (a). In dissociation, the precursor molecule is split, a fragment is chemisorbed at the surface and the ligand released is bound to another reactive site at the surface (b). Finally, for the ligand exchange reaction, the precursor is also split, but the released ligand is bound with a surface group forming a volatile compound that is released as a gaseous reaction by-product (c) [121].

The factors causing the saturation of the surface in the self-limiting ALD reactions are the steric hindrance effect and the limitation in the number of reactive sites available at the surface (see Figure 2.3). In the case of steric hindrance of the ligands, some reactive sites at the surface can be shielded by the large precursor molecules already attached at neighboring sites, as is schematically represented in Figure 2.3 a. Under this condition, there is no space available for the new incoming precursor molecules, therefore the surface is considered full and saturation is reached. In the second case, when all the reactive sites at the surface are occupied by the precursor molecules, saturation is achieved because there are no more suited bonding sites available for new incoming molecules, even if there is still plenty of space at the surface (see Figure 2.3 b). Steric hindrance effect dominates when precursor formed by large molecules are employed. Regardless of the mechanism causing saturation of the surface reactions most of the ALD processes lead to the growth of less than one monolayer per cycles. Even if saturative conditions are achieved, in both cases, the chemisorbed layer doesn't necessarily contain enough atoms to form a full monolayer of the desired compound [121], and rarely GPC reach values higher than 50 % of a monolayer. Typical values of GPC range from 0.01 to 0.3 nm/cycle [122].

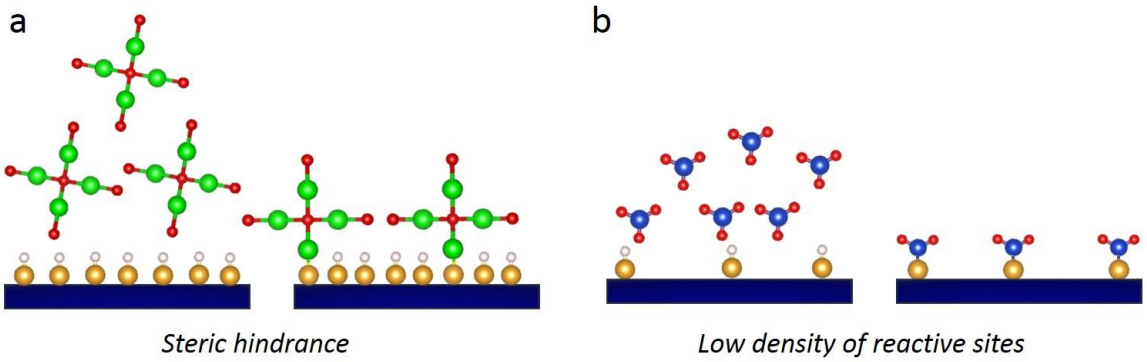

Figure 2.3. Simplified representation of the mechanism that lead to less than one monolayer deposition: steric hindrance (a) and low density of reactive sites (b).

The main advantages of this method are the high conformability, the straightforward scalability of the process and the possibility to keep a good homogeneity on large surfaces. However, it is worth to note that this is a technique mostly suitable for ultra-thin films (1 nm - 50 nm) due to the slowness of the deposition process.

2.2.3 ALD Temperature Window

Typical ALD processes are conducted at modest temperature (210-350°C) compared to the equivalent CVD processes. The temperature range, in which the conditions of self-limiting surface reactions are fulfilled, is called *ALD temperature window*. This temperature range is dependent on the specific ALD process (precursor employed, nature of the substrate, and reactions taking place). Figure 2.4 shows a schematic of the different possibilities for the GPC evolution as a function of the substrate temperature. The central region (orange) corresponds to the *ALD window,* in which the GPC is constant, independently of substrate temperature. Outside the ALD window, the self-limiting reaction mechanism is lost and there is a dependency of the GPC on the temperature.

For lower substrate temperatures, the self-limiting conditions are not reached because of slow reaction kinetics (Figure 2.4, curve A) or precursor condensation (Figure 2.4, curve B). In case A, the temperature is not high enough to efficiently activate the involved chemical reactions and complete saturation of the surface reaction sites is not achieved, which results in slow reaction kinetics. Therefore, the GPC increases with substrate temperature, until temperature is high enough to achieve complete saturation. In case B, the low substrate temperature results in the condensation of the reactants or the by-products, which produces more than one monolayer per cycle [123]. The reduction of condensation by increasing the substrate temperature produces the decrease in GPC observed in Figure 2.4, curve B.

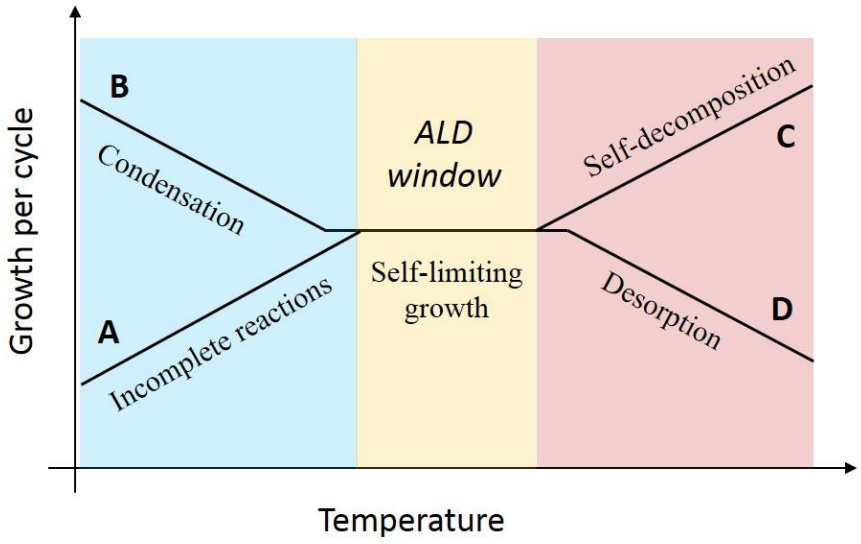

Figure 2.4. Schematic of ALD process, showing the GPC evolution versus substrate temperature.

On the other hand, for substrate temperatures above the *ALD window*, thermally activated self-decomposition of the precursor (Figure 2.4, curve C) or desorption of the chemisorbed precursor molecules (Figure 2.4, curve D) could occur [35]. In case C, precursor self-decomposition results in the deposition of the decomposition products on the surface producing an increase of the GPC with substrate temperature. In case D, the already chemisorbed precursor molecules can re-evaporate, due to elevated temperatures, resulting in a decrease of the GPC with substrate temperature.

In order to benefit from the advantages of ALD, i.e. conformability and accurate thickness control, it is required to work within the *ALD window*. Nevertheless, small deviations from this self-limiting conditions can be accepted in some cases in order to reduce the process time, as long as the reaction taking place proceeds in a surface-controlled manner. For example, when particularly long pulses are required to reach complete saturation of the surface, sometimes shorter pulse times can be employed [41,122].

The evolution of the GPC with time or with the number of cycles is another factor to take into consideration. Even if the GPC is expected to be independent of the number of ALD cycles when self-limiting conditions are fulfilled, a dependency has been observed, particularly at the beginning of the growth process. This dependence is understandable since the ALD process is dependent on the nature of the surface which evolves as the film grows. At the beginning, the precursor is exposed to the substrate surface while, after a few cycles it is exposed to both the substrate surface (partially uncovered at this stage) and the ALD-grown material. At larger number of cycles, a continuous film is formed, and the precursor is exposed to the ALD-grown

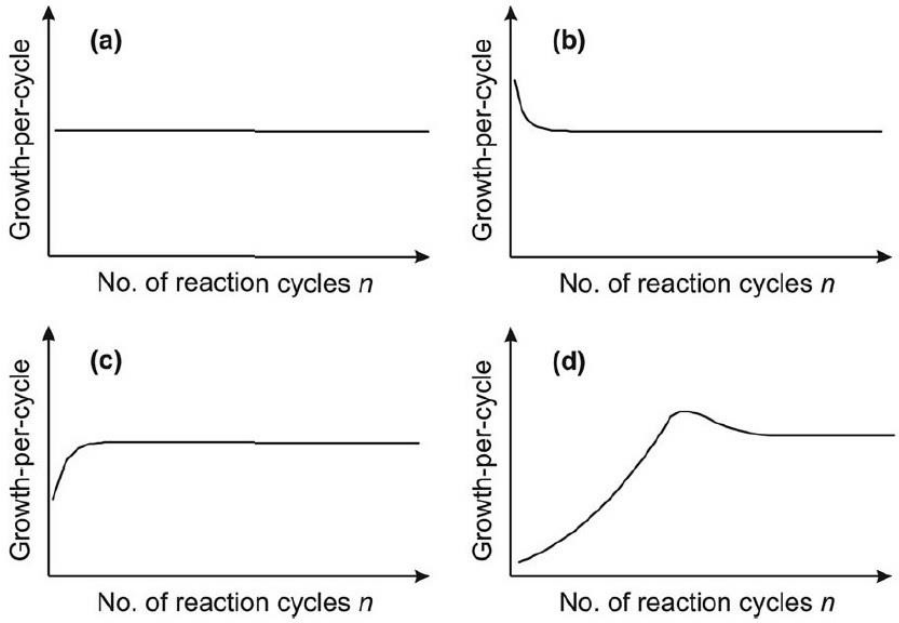

Figure 2.5. Evolution of the GPC with the number of ALD cycles. Linear growth (a), substrate-enhanced growth (b), substrate-inhibited growth type I, and substrate-inhibited growth type II (d) **[121]**.

material alone. The difference in chemical composition, bound type and reactivity of the different surfaces is expected to influence the GPC [121].

The evolution of the GPC with the number of ALD cycles can be divided in four categories, as depicted in Figure 2.5: linear growth (a), substrate-enhanced growth (b), substrate-inhibited growth of type I (c), and substrate-inhibited growth of type II (d). In the linear growth regime, the film thickness increases linearly with the number of ALD cycles, which corresponds with a GPC constant over time (Figure 2.5 a). This regime is the most commonly reported in the literature, some examples are the growth of Al_2O_3 by trimethylaluminum (TMA) and H_2O [124], ZnO on glass by diethylzinc (DEZn) and H_2O precursors [125], Cu_3N on SiO_2 by $Cu(hfac)_2$, H_2O and NH_3 precursors [42], and metallic Cu deposited on α-Al_2O_3 and SiO_2 substrates by CuCl, H_2O and H_2 precursors [41].

In the substrate-enhanced growth regime (Figure 2.5 b), the GPC is higher at the beginning of the film growth, and decreases with the increase of the number of ALD cycles before stabilization at a constant value in the steady regime. The reason of this behavior is the existence of a higher number of reactive sites at the substrate surface than in the ALD-grown film [35]. This regime has been observed, for example, for the thermal ALD of Al_2O_3 films on Si_3N_4 surfaces, by TMA and H_2O precursors [126], and for the plasma-enhanced ALD (PE-ALD) of Ti films on Pt substrates by $TiCl_4$ and H_2 precursors [127].

In the case of the inhibited-enhanced growth of type I (Figure 2.5 c), the GPC is lower at the beginning of the growth than at the steady regime; due to a lower number of reactive sites at the substrate surface than at the ALD-grown film. Examples of this growth mode are the deposition of TaN film on single crystalline Si, and the PE-ALD of Pd on Si [128].

Finally, substrate-inhibited growth of type II (Figure 2.5 d) differs from type I in that the GPC, instead of increasing gradually until reaching the steady regime, increases to a maximum value and then decreases just before stabilization. This growth mode has been observed, for example, by Satta *et al.* for the deposition of TiN on SiO_2 substrates, and has been associated with a lower number of reactive sites at the substrate (as in type I) combined with an island growth mode for the ALD growing film [121,129].

2.2.4 Experimental Setup and Deposition Parameters

For the deposition of the metallic Cu thin films, Cu NP and Cu_2O thin films an ALD PICOSUN™ R-200 Advanced reactor was employed (see Figure 2.6 a, b). This ALD reactor is composed of a dual chamber structure: an exterior chamber (the vacuum chamber) and an interior one which houses the substrate holder and where deposition takes place. Copper (II) hexafluoro acetyl acetonate, known as $Cu(hfac)_2$, was used as Cu precursor (99.99+%-Cu, Stream Chemicals) and deionized water was used as reactant. The precursor choice for this study was done on the basis of the versatility of $Cu(hfac)_2$ for the growth of metallic copper and copper oxide films, based on several CVD processes reported in the literature [130–132] and in a few ALD studies [38,41]. Both precursors were introduced into the reaction chamber by separate gas lines (see schematic in Figure 2.6 b). Nitrogen was used as carrier gas to transport the precursor into the reaction chamber, and as purge gas to evacuate the reactor between precursor pulses. The N_2 flow rate of each line was controlled by a mass flow controller and the pressure was measured by a pressure transducer. For the $Cu(hfac)_2$ and H_2O lines, N_2 flow rates of 120 and 150 sccm were used, respectively. In order to enhance the vapor pressure of $Cu(hfac)_2$ the boosting mode was used with N_2 flow rate of 300 sccm. The Cu and Cu_2O films were deposited on sputtered ZnO, Al-doped ZnO thin films, monocrystalline α-Al_2O_3 (CrystTec) and monocrystalline ZnO (PI-KEM) substrates.

The procedure followed for the deposition is described below:

- Cleaning the substrates with ethanol and distilled water.
- Introducing the substrates in the sample holder inside the reaction chamber.
- Pumping down the ALD reactor to 10 hPa.

- Heating the reaction chamber and the $Cu(hfac)_2$ bottle to the selected temperature (see Table 2.1).
- When temperature is stabilized, the 4-step ALD deposition process starts as described in Figure 2.1 (just before starting the deposition of the films the substrate was exposed to a remote-plasma of O_2 for 2 min, in order to prepare the surface for the deposition).

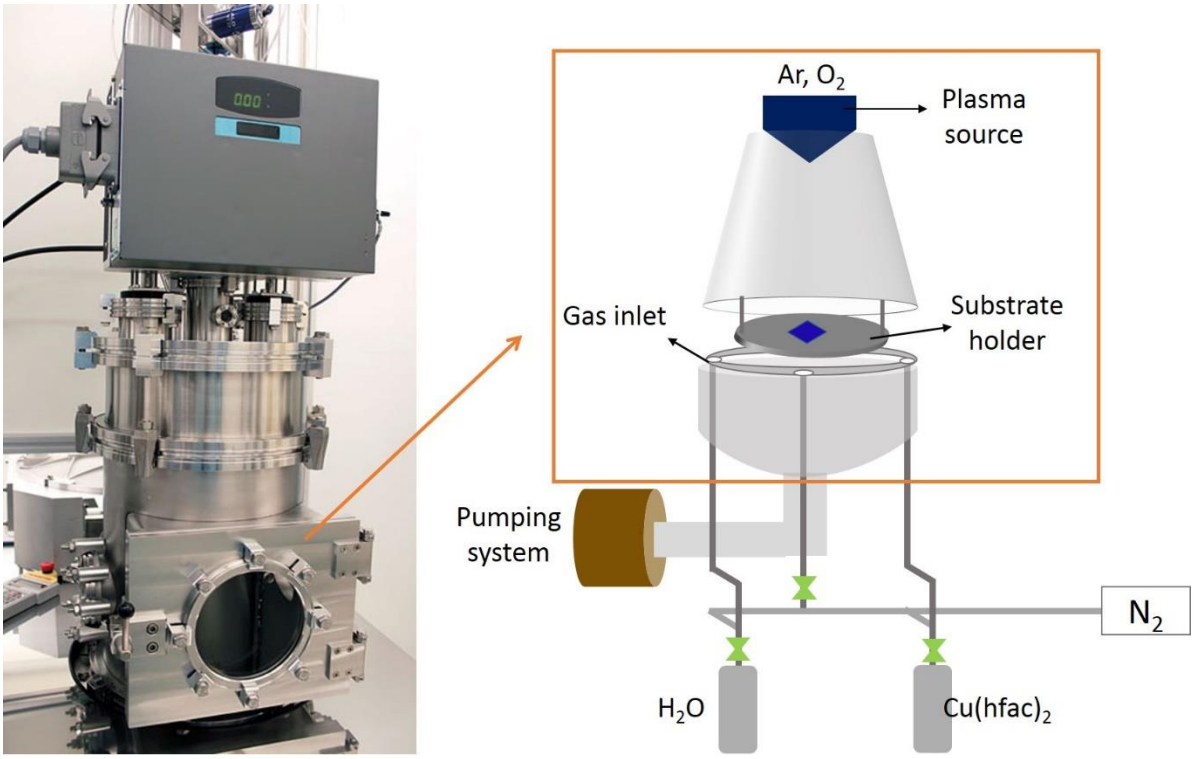

Figure 2.6. Picture of the ALD PICOSUN™ R-200 Advanced reactor (a). Simplified schematic of the ALD reactor, showing the reaction chamber, the plasma source at the top, and the precursor bottle and connections with the camber at the bottom (b).

Due to the small thickness of the films deposited by ALD, determining the film thickness is a difficult task. In consequence, we used the X-ray diffraction intensities as a tool to compare the deposition rate of different samples, assuming that crystalline quality was the same, and X-ray absorption varies little with the deposited thickness. An optimization of the pulses time was done by varying the length of the $Cu(hfac)_2$ and H_2O pulses in a wide range. Figure 2.7 a shows the evolution of the (110) and (220) diffraction peaks of Cu_2O (JCPDS 04-007-9767), when the H_2O pulse length is increased from 0.1 to 4 s. The $Cu(hfac)_2$ pulse was fixed at 3 s, the temperature of the reaction chamber was kept at 280 °C, and the number of cycles was 5000 for all the samples. It can be seen that even at 0.1 s of H_2O there is some Cu_2O deposited since a small (220) peak can be observed at the X-ray diffractogram. As the H_2O pulse length increases the intensity of the (110) and (220) is increased. It is assumed that saturation is

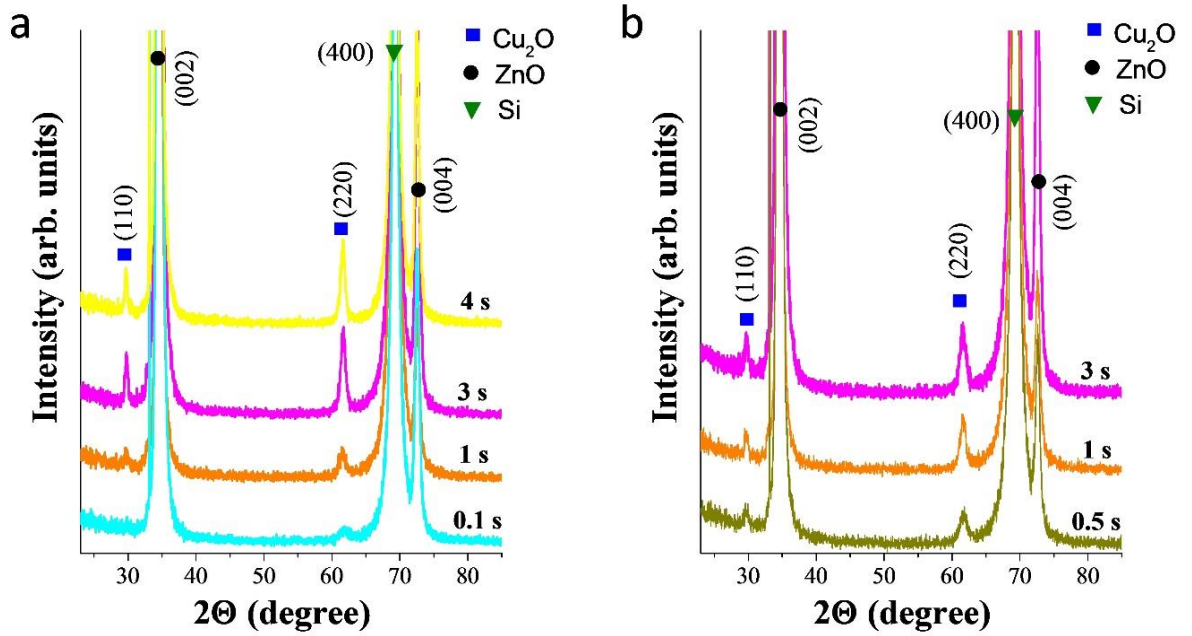

Figure 2.7. Optimization of the precursors pulse length: H_2O (a) and $Cu(hfac)_2$ (b) for the deposition of Cu_2O on ZnO substrates. The substrate temperature and the number of cycles were fixed at 280 °C and 5000, respectively.

achieved for 3s of H_2O since there is no further increase of the peak intensity for 4s. In Figure 2.7 b the same type of analysis was done but in this case the H_2O pulse length was fixed at 3 s and the $Cu(hfac)_2$ pulse length was varied from 0.5 to 3 s. The intensity of the (110) and (220) peaks increases as the $Cu(hfac)_2$ pulse length increases. However, the difference between samples obtained at 1 and 3 s is very small. Therefore, when higher thickness is desired it is convenient to use 1 s of $Cu(hfac)_2$ instead of 3 s in order to reduce the total deposition time.

Metallic Cu thin films were also deposited on ZnO substrates with the same conditions as described for the Cu_2O thin films. The possibility of obtaining both types of films is due to the selectivity of the $Cu(hfac)_2$ precursor towards different substrates with different conductivities/ defect densities. Cu NP were also grown by ALD due to the Volmer–Weber island growth mode at early stages of deposition. When a low number of cycles were used (200-5000) Cu NP were obtained and at higher number we obtained a continuous metallic film (as will be shown in Chapter 4). In Table 2.1 are reported the growth parameters explored for the deposition of Cu_2O, metallic Cu and Cu NP during this thesis.

Table 2.1 Deposition parameters used for the deposition of metallic Cu, Cu_2O thin films and Cu NP.

	Precursors			Reaction chamber		# cycles
	t_{pulse} (s)	t_{purge} (s)	Temp. (°C)	Temp. (°C)	Pressure(hPa)	
Cu(hfac)$_2$	0.5 – 3	6	70	210 - 350	10	200 – 10000
H_2O	0.1 – 4	6	18			

In general, the deposition of Cu_2O and Cu film was also tested on metallic substrates (e.g. W, Zr and Au), on semiconductors (e.g. Si, ZnO, and AZO) and on insulating substrates (e.g. glass and α-Al_2O_3). All these tests were done to understand the influence of the conductivity and structure of the different substrates on the selectivity of the Cu(hfac)$_2$ precursor towards the different surfaces. The influence of temperature on the selectivity was also investigated. Details on the selectivity aspects are discussed in Chapter 3.

2.3 Sputtering Deposition Process

2.3.1 Basic Principles

Sputtering is a well-established physical vapor deposition technique widely used for the fabrication of thin films for industrial applications and scientific research. The sputtering process consists in the extraction of atoms from the surface of an electrode (target) due to the moment exchange with ions from a plasma gas. The atoms ejected from the target are then deposited onto a substrate forming a film of the target material. In Figure 2.8 a is shown a schematic of the sputtering process. A negative potential is applied to the target in the presence of an inert gas (typically Ar) at low pressure (~ 0.1 - 10 Pa). Thereby, an electric discharge is produced between the target (cathode) and the reactor chamber walls (anode) which produces the ionization of the Ar atoms. The Ar^+ ions are accelerated towards the target due to the electric potential difference. When impacting the target they can eject atoms from its surface (1), promote the emission of secondary electrons that help to maintain the plasma discharge (2), be implanted into the target (3), and be reflected by the target surface after neutralization by secondary electrons (4), as is schematically represented in Figure 2.8b. The sputtering yield (Y) that describes the number of sputtered atoms per incident ion is given by:

$$Y = \frac{3\,\alpha_{MR}}{\pi^2}\frac{M_1 M_2}{(M_1+M_2)^2}\frac{E}{U_S} \qquad \textbf{(2.1)}$$

where, M_1 and M_2, are the atomic masses of the ion and the target, respectively, α_{MR} is a dimensionless parameter depending on the mass ratio of the incident ion and the target atom, E is the energy of the incident ion and U_S the surface binding energy [133].

It is important to note that the sputtering phenomenon is only possible if the energy of the incident ion is higher than a certain threshold energy, since the energy transferred to the target needs to be higher than the binding energy of the material. This threshold energy is between 15-30 eV for most of the metals. The process of emission of secondary electrons is characterized by a parameter called secondary electron yield (γ_{SE}) corresponding to the number of emitted electron per incident ion. Typical values of γ_{SE} are around 0.1 for most of the metals but can be considerably higher for many oxides and nitrides [134].

2.3.2 Magnetron Sputtering

So far we have described the traditional sputtering mechanism (diode sputtering). In this type of sputtering process, the low ionization rate of the discharge obliges to work at high pressures (~ 10 Pa) to sustain the plasma. This results in very low deposition rates and porous films, since the sputtered atoms encounter many collisions with atoms in the gas phase, before reaching the substrate. To overcome these problems, the cathode is equipped with a magnetron device formed by two concentric magnets of inverted polarities, as is depicted in Figure 2.9 a. Under the presence of an electric and magnetic fields, electrons emitted by the target describe a trajectory perpendicular to both fields, creating a current (Hall current) in the vicinity of the target. This produces an intense plasma in this region, increasing considerably the ionization rate and in consequence the growth rate. It also permits growing at lower pressure enabling the deposition of dense films.

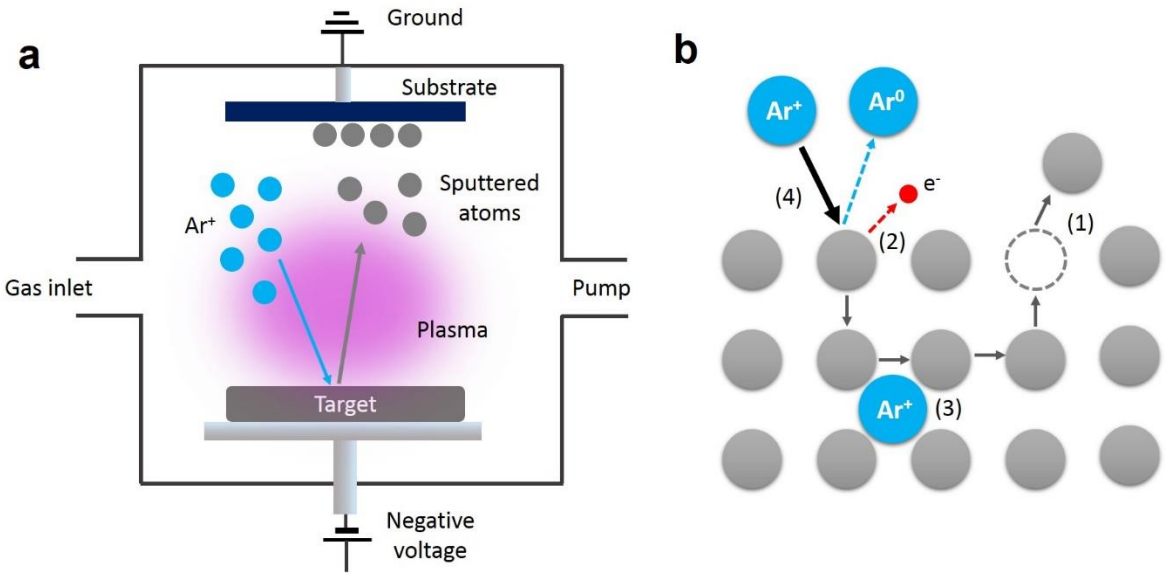

Figure 2.8 Schematic of the sputtering process (a) and the different interaction between the Ar ions and the target atoms (b).

2.3.3 Reactive Magnetron Sputtering

So far we have described the sputtering of a metallic target to deposit a metallic film of the same material. There is also the possibility of depositing compound films such as oxides, nitrides or carbides. One possibility is the use of a ceramic target; however, this requires working in radiofrequency (RF) mode due to the insulating character of this type of targets to avoid the charge accumulation at the surface and the occurrence of arcs. RF power supplies are more expensive than DC generators, and also ceramic target are usually more expensive that metallic ones. Moreover, the growth rate with RF sputtering is considerably smaller compared with DC power supplies working at the same power. Finally, it is difficult to control and monitor individually voltage and current. Another possibility for depositing a compound is the use of reactive magnetron sputtering. It consists in the sputtering of a metallic target, like in traditional sputtering, but in a reactive gas mixture formed by Ar and reactive species (e.g. O_2, N_2, CH_4….). The reactive gas reacts at the film surface with the metallic atoms to form the desired compound. The amount of the reactive gas is controlled in order to produce a fully reacted compound.

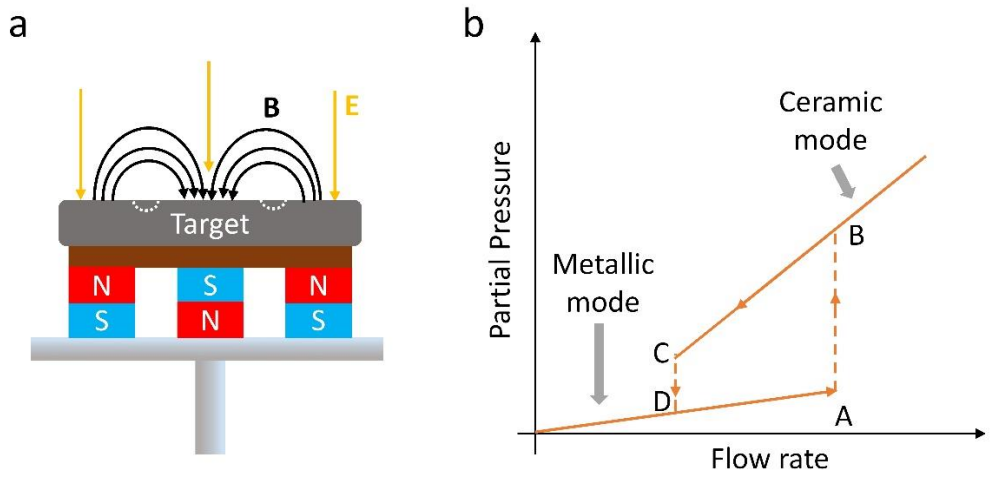

Figure 2.9. Schematic of the magnetron source (a). Schematic of the characteristic curve of reactive gas partial pressure vs. flow rate in the reactive magnetron sputtering process (b).

The reactive ions react not only with the metallic atoms at the substrate but with all the surface it encounters, including the target. We can find two extreme behaviors in reactive sputtering depending on the reactive gas flow rate in the reactor chamber. For low flow rates, metallic mode is observed. In this regime, most of the reactive species are trapped by getter effect in the reactor walls and there is small poisoning of the target [135]. Therefore, it remains in metallic mode and high deposition rates are usually achieved. The partial pressure of the reactive gas is small and it varies smoothly with the reactive gas flow rate as is shown in Figure 2.9 b. After the reactive gas flow rate reaches the critical point (A, in Figure 2.9 b), the reactor walls are saturated and a small increase of the reactive gas flow rate leads to a considerable increase in the pressure (dashed line A-B in Figure 2.9 b). For higher flow rates, the compound or ceramic sputtering mode is achieved since the target is completely poisoned by the reactive gas and a compound is formed at its surface. In this regime the sputtering yield decreases considerably since the binding energy of the target material increases when it is transformed from a metallic material to the compound (except for few cases: WO_3, MoO_3). An hysteresis behavior is observed when changing the flow rate, as is depicted in Figure 2.9 b. It can be seen that when the flow rate is decreased below a second critical point, starting from the ceramic mode, there is an unstable transition of the same type of A-B, but in opposite direction since it is related with the decontamination of the target (dashed line C-D) [134]. This hysteresis, that is highly undesirable, can be avoided by increasing the pumping speed to allow a fast evacuation of the reactive gases from the reaction chamber [136]. Also working with systems of low

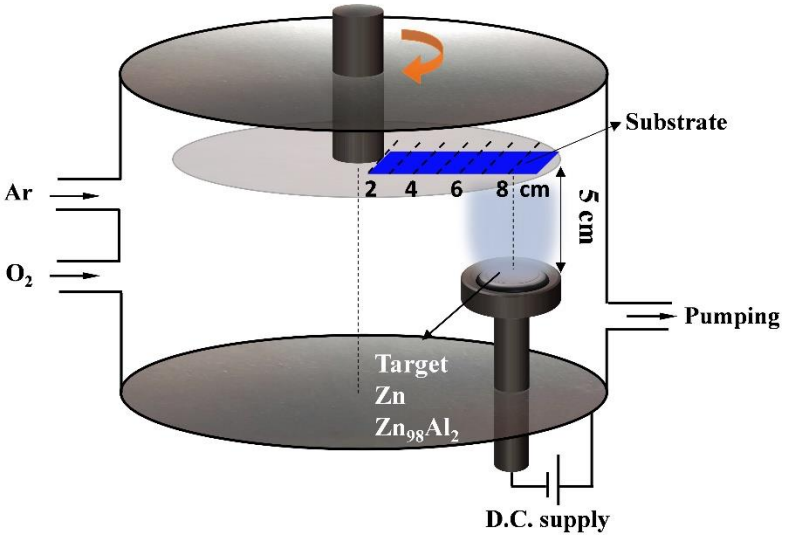

Figure 2.10. Schematic of the sputtering chamber used for the deposition of ZnO and AZO films.

reactivity can help to suppress the hysteresis, since it has been typically observed for sputtering processes where the target elements are highly reactive toward the gas species.

2.3.4 ZnO and Al-doped ZnO Thin Films Deposition

ZnO and AZO films have been deposited on (100) Si and glass substrates by reactive magnetron sputtering of Zn target with 99.995 % purity (HMW Hauner GmbH & Co KG) in a 40-L sputtering chamber pumped down via a mechanical and a turbo-molecular pump, allowing a base vacuum of 10^{-4} Pa. The procedure followed for the deposition of the films is described below:

- Cleaning the substrate with ethanol and distilled water
- Introducing the substrate on the rotating substrate holder facing the magnetron axis at a distance of 5 cm from the target (see schematic in Figure 2.10 a)
- Pumping down the chamber to 10^{-4} Pa
- Introducing Ar into the chamber to etch and clean the substrate surface using a RF power supply (70 W, 2 min)
- Introducing oxygen into the chamber, switching on the DC generator and switching off the RF power supply.

An advanced Energy MDX 1.5 kW DC generator was used to sputter the Zn target. The current applied to the target was fixed at 0.07 A. The Ar flow rate was fixed at 50 sccm for all the depositions and the O flow rate was varied between 6 - 15 sccm, based on the previous work of Chamorro *et al.* [65]. The samples were deposited at a total pressure of 0.5 Pa and no

intentional heating was used during the deposition process. During the deposition, the substrate holder was in rotation mode to obtain a good homogeneity of the films.

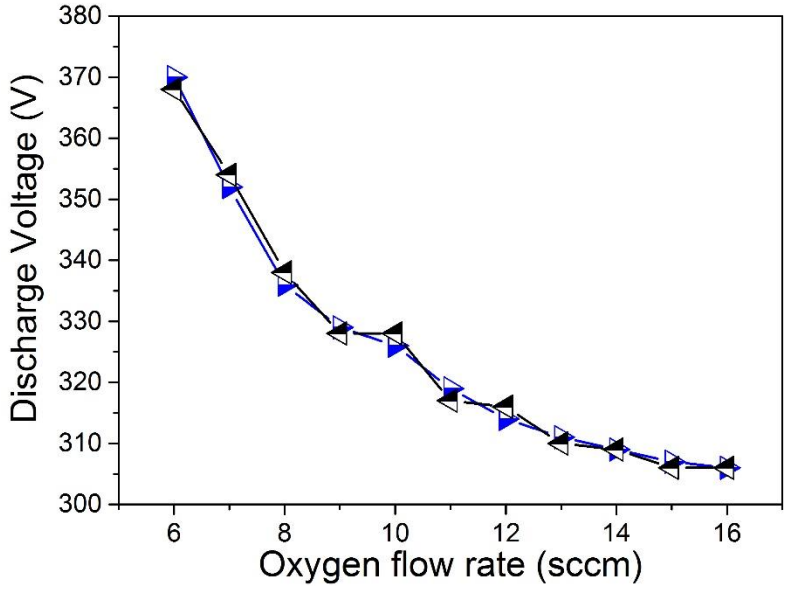

Figure 2.11. Evolution of the discharge voltage as a function of the oxygen partial pressure.

The evolution of the discharge voltage vs. the oxygen flow rate is depicted in Figure 2.11. Changes in the oxygen partial pressures affect the discharge voltage due to changes in the secondary electron emission yield upon oxidation (an increase on the partial pressure produces a decrease of the discharge voltage and vice versa). Therefore, the hysteresis behavior can be detected in a plot of discharge voltage vs. oxygen flow rates, analogous to the plot of oxygen partial pressure vs. oxygen flow rate. Figure 2.11 shows a progressive transition from the metallic to the compound mode and no hysteresis loop, in our case.

All the films deposited were c-axis oriented, in agreement with the self-texturing effect observed on ZnO and AZO films [65,137]. The film thickness ranged from 200 to 330 nm depending on the oxygen flow rate and the position of the substrates with respect to the target axis.

2.3.5 Cu_2O Thin Film Deposition

For the deposition of thicker Cu_2O films we used the reactive magnetron sputtering method, since ALD is a very slow process, not suitable for films thicker than 50 nm. Cu_2O films were deposited on silicon and glass substrates using a Cu metallic target (99.99 %, Ampere Industry) in various Ar-O_2 reactive mixtures. The samples were deposited at a total pressure of 0.5 Pa, and the Ar flow rate was fixed at 25 sccm, based on the previous work of Wang *et al.* [138]. Depending on the oxygen flow rate it is possible to obtain CuO, Cu_2O, Cu_4O_3, or a mixture of these phases [138]. Therefore, the O_2 flow rate was optimized to obtain single phase Cu_2O. For

all the sample deposited in this work we use an O_2 flow of 6 sccm, which results in the deposition of single phase Cu_2O. A pulsed-DC supply (Pinnacle + Advanced Energy) was used to sputter the Cu target. The current applied to the target was 0.3 A and the distance between the substrates and the target was 60 mm. During the deposition, the substrate holder was in rotation mode to obtain a good homogeneity of the films. The Cu_2O growth rate was of 80 nm/min, and the sample showed a preferential orientation in the [111] direction.

2.4 X-ray Diffraction

X-ray diffraction is one of the most used techniques for the study of crystalline solids. The phenomenon of diffraction can be observed in a crystal when the wavelength of the incident radiation is of the same order than the interatomic distances, this is the reason why X-rays with wavelengths in the range of 0.5-2.5 Å are employed. When X-rays are incident in a crystalline solid they are scattered by the atoms constituting the solid. The resulting scattering waves can interfere in a constructive of destructive manner, producing a diffraction pattern. The position, intensity and shape of the multiple Bragg reflections (peaks in the diffraction pattern) provide structural information about the sample. The position of the peaks allows to perform qualitative phase analysis, to identify the crystalline structure of these phases, and the parameters of the unit cell. The shape of the peaks gives information about the microstructure of the material and is associated with defects present in the structure (dislocations, vacancies, twins, etc.), non-uniform deformations and crystallite size (<1μm) [139]. The distance d_{hkl} between crystallographic planes can be obtained through the Bragg's law as a function of the position of the diffraction peaks (θ), and the wavelength of the incident radiation (λ) [139]:

$$2d_{hkl} \sin \theta_{hkl} = m\lambda \qquad \textbf{(2.2)}$$

Knowing the wavelength of the X-rays (the most commonly used is Cu Kα, $\lambda = 1.5406$ Å) the d_{hkl} can be determined for each peak observed in the diffraction pattern.

There exist different geometries employed in X-ray diffraction, θ-2θ or Bragg Brentano being the most commonly used. A schematic of this configuration is shown in Figure 2.12 a. The sample is rotated by an angle θ and the detector by an angle 2θ, in a synchronized way. Under these conditions only the diffraction peaks corresponding with the crystallographic planes parallel to the sample surface are observed. In the case of monocrystalline or textured films only few peaks are observed in the X-ray diffractograms, because the planes that are parallel to the surface belong to the same family. In the case of non-textured-polycrystalline films, several peaks are observed since the grains are oriented in many different directions

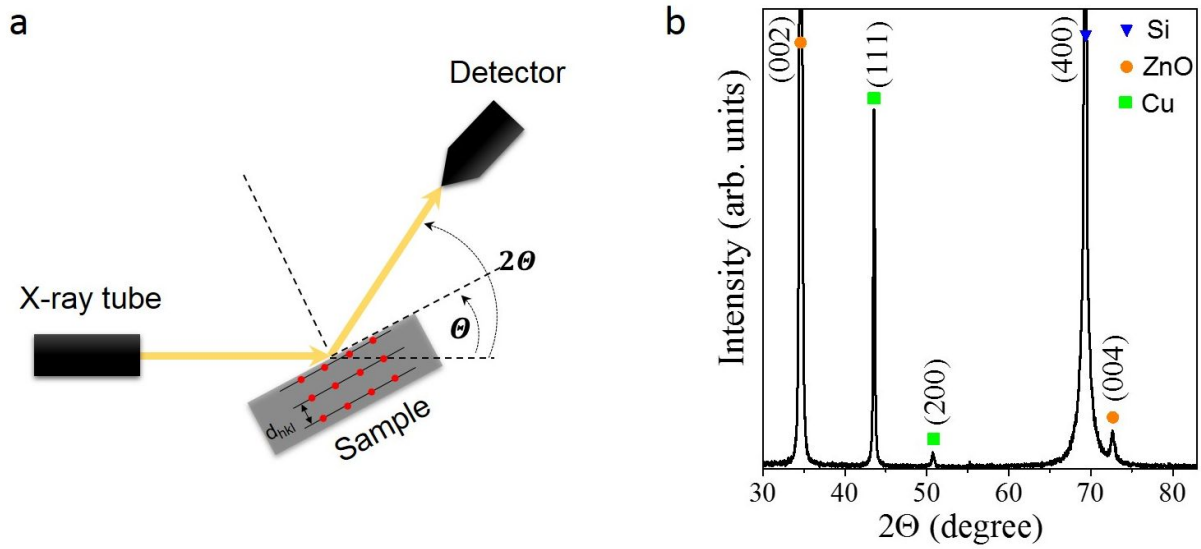

Figure 2.12. Schematic of the Bragg-Brentano geometry used in XRD (a). X-ray diffractogram of Cu/ZnO/Si sample (b).

through the film. A diffractogram of a Cu/ZnO/Si sample is presented in Figure 2.12 b. The Cu film is polycrystalline, showing the (111) and (200) Bragg reflections. The ZnO is also polycrystalline but texture in the [001] direction, since only the (00l) peaks are observed. Finally, the Si substrates is monocrystalline, and only the (004) peaks is observed.

In the particular case of crystalline structures belonging to the cubic and hexagonal systems, corresponding to the materials studied in this thesis, the relation between the interplanar distance of a set of planes (hkl) and the lattice constants (a, c) is given by equations (2.3) and (2.4), respectively.

$$\frac{1}{{d_{hkl}}^2} = \frac{h^2 + k^2 + l^2}{a^2} \tag{2.3}$$

$$\frac{1}{{d_{hkl}}^2} = \frac{4}{3}\frac{[h^2 + hk + k^2]}{a^2} + \left(\frac{l}{c}\right)^2 \tag{2.4}$$

As was mentioned before, the peak broadening gives information on the microstructure of the material to be analyzed. An estimation of the length of the coherent diffraction domains in the direction perpendicular to the sample surface (see Figure 2.12) can be obtained using Scherrer's equation:

$$D_V = \frac{K\,\lambda}{\beta\,\cos\theta} \tag{2.5}$$

where D_V is the length of coherent diffraction domains, β is the full width at half maximum (FWHM) and K is a constant that has different values depending on the particle geometry. In general, for spherical particles $K = 0.829$ should be used [140]. It is important to note that this expression doesn't take into consideration that part of the broadening of the peaks can be related with non-uniform micro-strain, in consequence it provides only a lower bound for D_V. This expression is particularly useful in the case of spherical nanoparticles. In fact, we employed this expression to obtain an estimation of the height of Cu nanoparticles obtained by ALD.

In this thesis, X-rays diffractograms in the Bragg-Brentano configuration were collected using a Bruker D8 Advanced diffractometer with Cu $K_{\alpha 1}$ radiation (λ=1.5406 Å). The crystalline structure was determined using the JCPDS and the DIFFRAC.EVA software, provided by Brucker. To obtain information regarding the texture and epitaxial relation between the Cu_2O films and the ZnO and sapphire substrates, pole figure and φ scan measurements were performed in a Bruker D8 Discover diffractometer with Co $K_{\alpha 1}$ radiation (λ = 1.7912 Å).

2.5 UV Visible Near-Infra Red (UV-VIS-NIR) Spectroscopy

UV-VIS-NIR spectroscopy is a very useful non-destructive optical characterization technique based on the analysis of the intensity of the light reflected or transmitted by a solid to obtain information on the optical and electronic properties of the material. When electromagnetic radiation reaches a solid, a fraction is reflected by the surface; the reflectance (R) of a material is defined as the ratio of the reflected and incident light intensities (I_R/I_0). Another part of the light is transmitted through the material and the transmittance (T) is defined as the ratio of the transmitted to incident light intensities (I_T/I_0). Finally, a part of the light is absorbed by the film, and the absorbance (A) is defined in analogy with the previous cases. From the law of conservation of energy:

$$I_0 = I_R + I_T + I_A \quad \textbf{(2.6)}$$

And therefore,

$$R + T + A = 1 \quad \textbf{(2.7)}$$

Both transmittance and reflectance can be determined from the UV-VIS-NIR spectrophotometer. The most common setup is the double beam system. In this configuration two beams are employed, one is directed into the sample and the second is used as a reference. For specular reflectance measurement the second beam is directed to a reference mirror. For transmittance measurements several methods are commonly employed. In this work we use the simplest one, where the substrates (usually glass) is used as reference, and the measured transmittance is directly the transmittance of the film. In this method, possible effects at the interface film-substrate are neglected, but this didn't affect our results in a significant manner. Typical transmittance and reflectance spectra of a Cu_2O film deposited on a α-Al_2O_3 substrate are presented in Figure 2.13 a, b as example.

In the reflectance and transmittance spectra of thin films, the appearance of a modulation of the intensity in the form of maxima and minima is commonly observed [141]. This interference phenomenon is due to the discontinuity of the refractive index at the air-layer and layer-substrate boundaries, observed in transparent enough thin films, in a specific range of thicknesses and wavelengths. From the position of the intensity maxima and minima, it is possible to obtain an estimate of the film thickness [142].

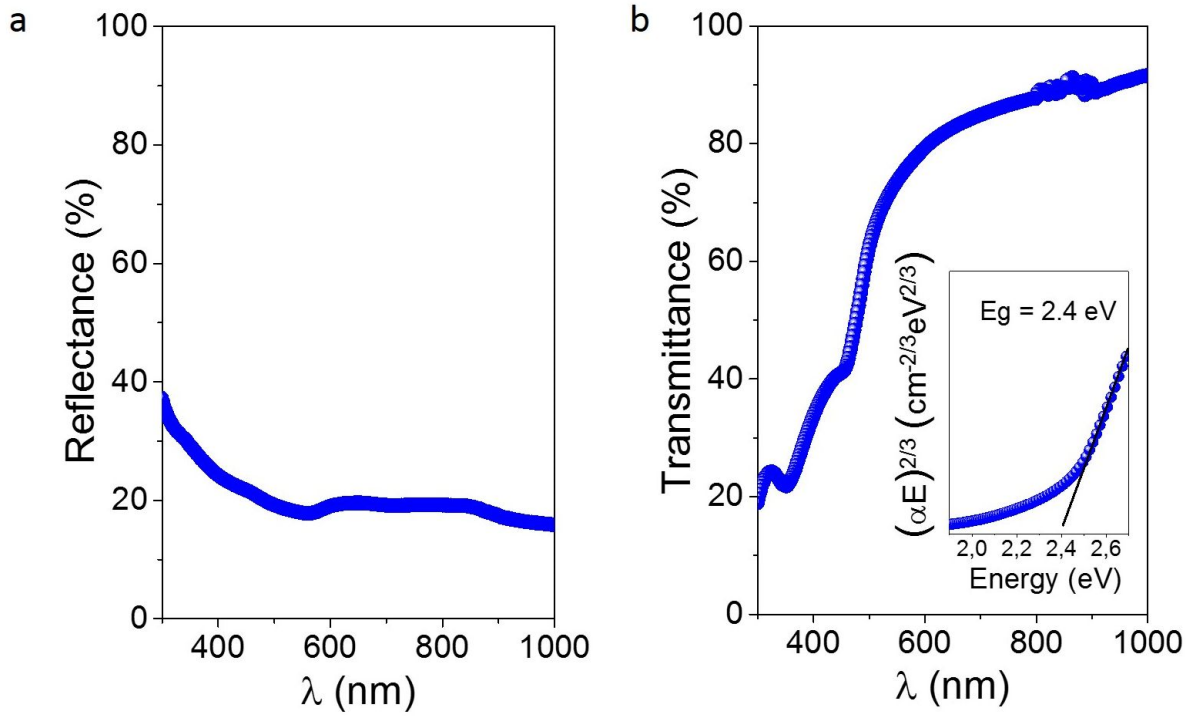

Figure 2.13. Reflectance (a) and transmittance (b) spectra of a Cu_2O film deposited on α-Al_2O_3. The Tauc Plot for this sample is presented as inset.

The absorption coefficient (α) can be determined from the transmittance spectra by the Lambert-Beer's law [143]:

$$T = \frac{I}{I_0} = e^{-\alpha t} \tag{2.8}$$

$$\alpha = \frac{1}{t}\ln\left(\frac{1}{T}\right) \tag{2.9}$$

Where I is the intensity of the transmitted light, I_0, the intensity of the incident light, and t the thickness of the sample. If part of the light is reflected at the sample surface, equation (2.9) is transformed to:

$$\alpha = \frac{1}{t}\ln\left(\frac{1-R}{T}\right) \tag{2.10}$$

When working with semiconductor materials, the band gap (E_g) can be determined from the transmittance spectra using the Tauc plot [144]. This method considers that the absorption coefficient and the band gap are related by the following expression:

$$(\alpha h\nu)^n = C\left(h\nu - E_g\right) \tag{2.11}$$

Where h is the Plank constant, ν is the frequency of the light, C a proportionality constant and n is a coefficient equal to 2 for direct allowed transitions, $2/3$ for direct forbidden transitions and $1/2$ for indirect transitions. The Tauc Plot of a Cu_2O film is presented at the inset of Figure 2.13 b. Since Cu_2O presents a direct forbidden bandgap an exponent of 2/3 was employed for the band gap determination.

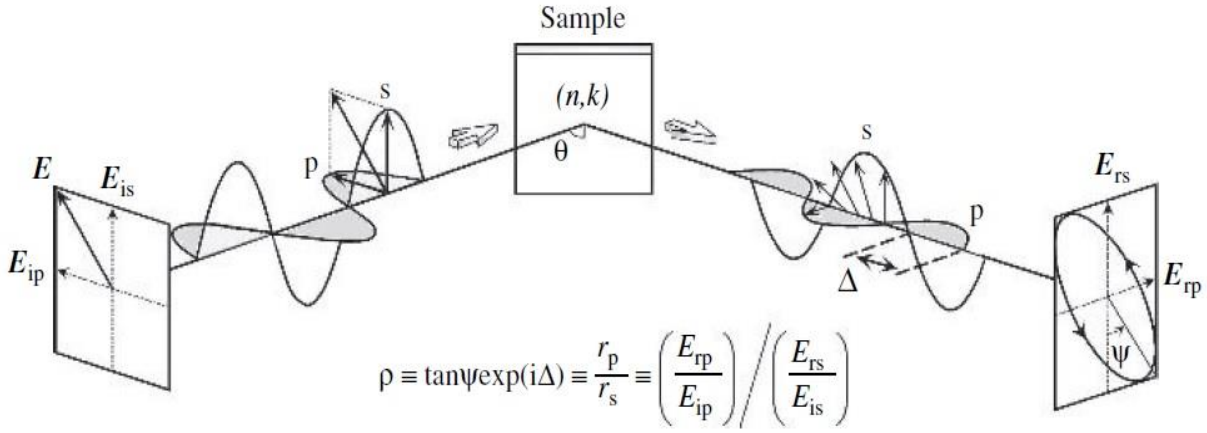

Figure 2.14. Configuration for spectroscopic ellipsometry measurements **[143]**.

2.6 Ellipsometry

Ellipsometry is an optical characterization method that measures the change in polarization of the light upon light reflection on a material (or transmission through a material). The polarization changes are described by two parameters: Ψ and Δ. These parameters represent the amplitude ratio (Ψ) and the phase difference (Δ) between the parallel and perpendicular components of the electric field of the light after the interaction with the sample (see Figure 2.14). In particular, when spectroscopic ellipsometry is employed, the changes in polarization of the light after interaction with the material is studied as a function of the wavelength of the light. The measured response depends on the optical properties of the analyzed material. From this technique the thickness and optical constants of the samples can be determined.

In this thesis ellipsometric measurements were carried out using a phase-modulated ellipsometer (UVISEL, Horiba) in the spectral range 0.6 eV - 4.6 eV at two angles of incidence (60° and 70°). The ellipsometer measures the parameters I_s and I_c which are related with the ellipsometric angles Ψ and Δ by the following equations:

$$I_s = sin2\Psi sin\Delta \tag{2.12}$$

$$I_c = sin2\Psi cos\Delta \tag{2.13}$$

In order to obtain accurate values from the ellipsometry data appropriate models need to be used, taking into consideration the optical properties of the sample under analysis. Some optical models are the Drude model (for free carriers), the Cauchy model (in the transparent region, where the imaginary part of the dielectric function is zero or close to zero), the Lorentz and Tauc-Lorentz models, that have been employed for semiconductor materials, among others.

In heterogeneous systems, which are composed by more than one phase, the effective medium approximation is employed, where the optical response of the system is analyzed from the response of each of the components, by taking into account the dielectric constant of the different phases and its volume fraction to obtain the effective dielectric constant of the system. Depending on the fraction of each phase and the way in which they are distributed in the sample, different models are considered. The Bruggeman's effective medium model is one of the most employed. In this model, the general equation considering the coexistence of two different phases a and b is given by:

$$f_a \frac{\varepsilon_a - \varepsilon_{eff}}{\varepsilon_a + 2\,\varepsilon_{eff}} + (1 - f_a) \frac{\varepsilon_b - \varepsilon_{eff}}{\varepsilon_b + 2\,\varepsilon_{eff}} \tag{2.14}$$

Where ε_a and ε_b are the dielectric constant of a and b phases, respectively, ε_{eff} is the effective dielectric constant of the medium and f_a and $(1 - f_a)$ are the volume fraction of the a and b phases, respectively.

The Bruggeman's effective medium model has been widely employed to account for the roughness of the films [143]. The sample is divided in a bulk and an uppermost layer, composed of a mixture between the film material and air (see Figure 2.15). For the uppermost layer, ε_a and f_a are the dielectric contacts and the volume fraction of air, and ε_b the dielectric constant of the film material.

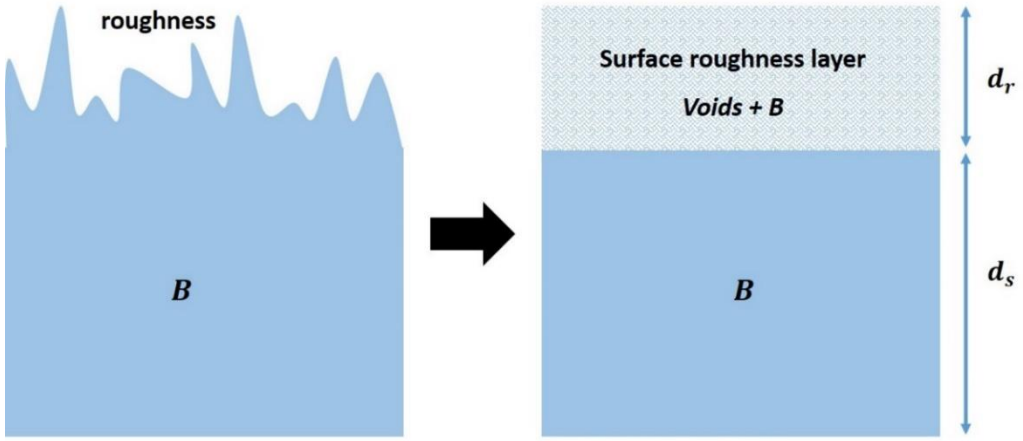

Figure 2.15. Schematic of the optical model employed to simulate the surface roughness (b).

2.7 Photoluminescence spectroscopy

Photoluminescence (PL) spectroscopy is a nondestructive and versatile characterization technique that is widely employed to study the electronic structure and defect levels in semiconductor materials. In this technique light is shined onto the material under analysis and electrons are excited to higher energy levels. When the electrons return to their equilibrium state, the excess energy is emitted in the form of light if the process is radiative. The energy emitted by these electrons is given by the difference between the states involved in the transition, so the wavelength emitted by the material gives us information of its electronic structure.

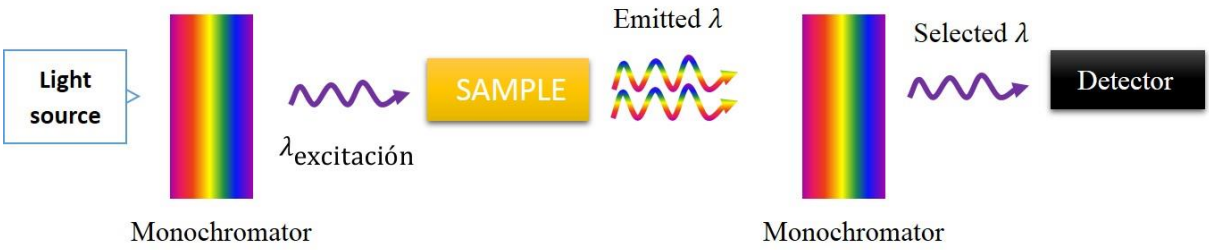

Figure 2.16. Schematic principle of the photoluminescence spectroscopy set-up.

A schematic of a typical PL set-up is depicted in Figure 2.16. It consists of an optical source (a laser beam or a lamp), a monocromator placed after the light source that allows selecting the excitation wavelength, a second monocromator at the output of the system that selects one by one the emitted wavelengths, and a detector.

In the particular case of semiconductor materials, which are the interest of this work, the excitation energy must be greater than the band gap to excite the electrons from the valence to the conduction band. A study of the emitted wavelengths allows determining parameters such as: band gap energy, existence of defect levels within the semiconductor and the energy of these levels. A typical PL spectrum of a ZnO film is shown in Figure 2.17. The first peak in the UV range is associated with the near band edge emission and the broad band that appears in the visible is due to defect levels within the band gap.

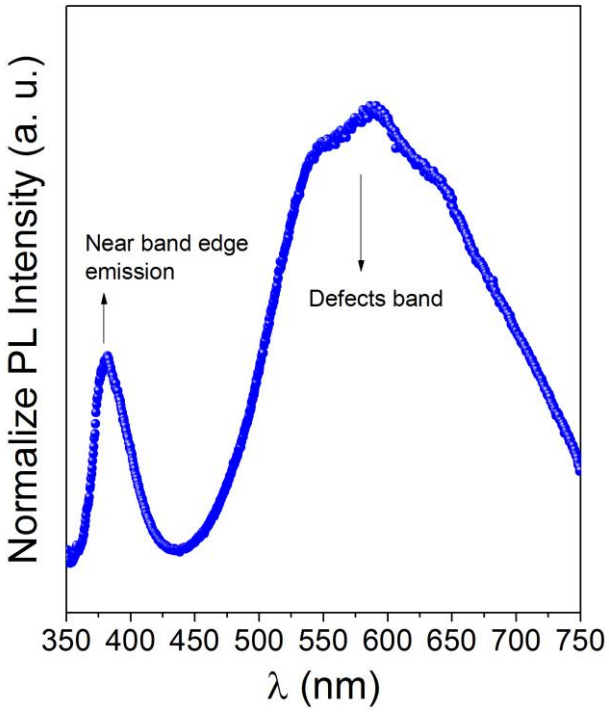

Figure 2.17. Photoluminescence spectrum of a typical ZnO film.

In this thesis, PL measurements were performed to study the evolution of defect levels in the ZnO films deposited by reactive magnetron sputtering at different P_{O_2}. The measurements were performed at room temperature using an excitation wavelength of 325 nm.

2.8 Scanning Electron Microscopy

Scanning electron microscopy (SEM) is a technique used for the acquisition of high resolution topographic images of the samples. A high-energy electron beam is accelerated by a voltage of a few kV and focused on the sample surface by a system of magnetic lenses. The electron beam scans the sample surface by moving along a path of parallel lines [145]. Due to the interactions of the electron beam with the sample, different signals are produced such as: secondary electrons, backscattered electrons, characteristic X-rays, visible light, among others (Figure 2.18 a). Secondary electrons (SE) originate due to inelastic interactions between the primary electron beam and the sample atoms. Since they are emitted with low energy, only those originated close to the sample surface can escape form the sample, which allows the acquisition of high resolution images. Backscattered electrons (BE) are a part of the primary electrons that have been reflected by the sample surface due to elastic collisions with the sample atoms. They originate from a wider region within the interaction volume compared with SE. The signal produced by BE can also be used to obtain images, although the SE are better for obtaining topographic images and the BE to show differences in the composition of the sample through chemical contrast.

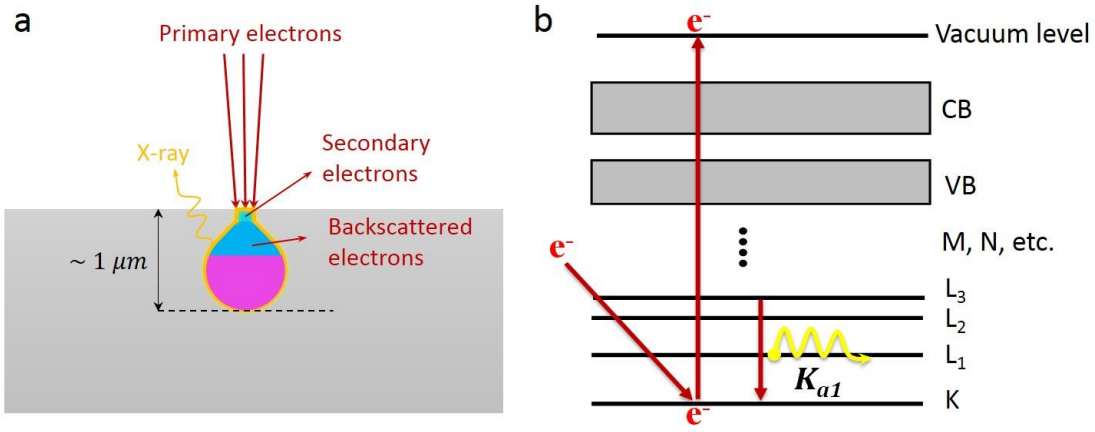

Figure 2.18. Schematic of the interaction between the electron beam and the sample surface (a). Schematic of the generation of X-ray by electron bombardment at the sample surface (b).

The scanning electron microscope can also be used to perform chemical semi-quantitative analyzes and composition mapping if it has an energy-dispersive spectroscopy (EDS) system embedded. The EDS makes use of the X-ray emitted by the sample to perform chemical analysis. The incident electrons excite the atoms of the sample and cause the emission of X-rays whose wavelengths are element specific (Figure 2.18 b). The energy of the incident electrons, E_0 (of the order of the keV), has to exceed the energy of the core shell level, E_c (energy needed to remove an electron from the inner shells of the atom, K, L, M, etc.). From the cross section for inner-shell ionization by electron impact it is known that, in order to produce an efficient excitation, E_0 need to be 2.3 - 3 eV higher than E_c [147]. Figure 2.19 show the ionization cross-section for the K shell as a function of the overvoltage ($U = E_0/E_c$) calculated by the DWBA (distorted-wave first-order Born approximation) method from [146].

In this work top-view and cross-section scanning electron micrographs were taken in a Philips XL-30 S-FEG SEM at 5 kV to analyze the microstructure of the samples.

2.9 Transmission Electron Microscopy and Electron Energy Loss Spectroscopy

Transmission electron microscopy (TEM) is a powerful high resolution microscopy technique. A high energy electron beam is accelerated with voltages of 200 - 300 kV onto a very thin sample (10 - 100 nm) and the transmitted electrons are used to obtain an image. A system of magnetic lenses allows controlling the region of the sample to be analyzed.

In a TEM there are two basic modes of operation: diffraction and imaging (see schematic in Figure 2.18). In diffraction mode, an image of the back focal plane of the objective lens is projected on the screen. The electrons scattered by the sample in the same direction are collected

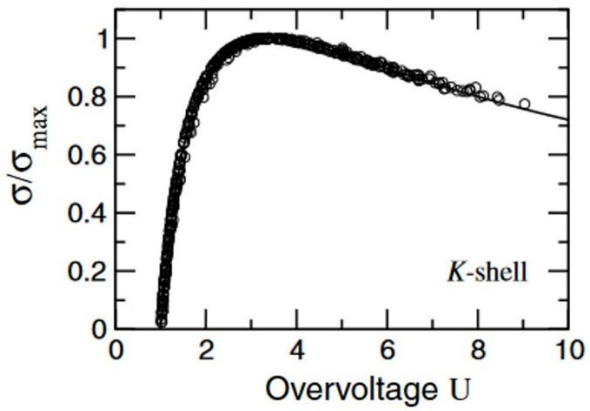

Figure 2.19. Normalized ionization cross-section of the K shell vs. overvoltage from **[146]**. The circle represent the DWBA calculation from several elements and the continuous line an analytical expression proposed by Campos *et al.*

into a single point in the back focal plane of the objective lens. For crystalline samples, each spot corresponds to a crystallographic plane (hkl) in the direct space. Crystallographic information can be also obtained from the Fourier transform patterns taken from high-resolution TEM (HR-TEM) micrographs of the samples.

In image mode, the image plane of the objective lens is projected on the screen. Bright field (BF) and dark field (DF) images can be obtained as is schematically represented in Figure 2.21. In BF mode, the image is constructed by the electrons that are transmitted through the sample without much deflection (direct beam) as is depicted in Figure 2.21 a. Therefore, the areas of the sample that scatter or absorb the electrons appears in dark (heavy elements) and the areas that transmit the electron beam without much scattering appear brighter (lighter elements); no diffraction contrast is observed in this type of images. DF images are created by blocking the direct beam and selecting one or more diffracted beams (Figure 2.21 b). Therefore, the image is formed by the scattered electrons. In this case, bright regions correspond to heavy elements and also to crystallites that are under the selected diffraction conditions. Example of BF and DF images of a Cu_2O/ZnO sample are shown in Figure 2.21 c and d, respectively. Information on the microstructure and types of defects present in the samples, grain size, orientation, epitaxy, etc. can be obtained from these types of images.

The inelastic collision of the electron beam with the sample leads to the generation of characteristic X-rays, which allow to performed chemical analysis through EDS, as in SEM. Another technique associated with TEM is the electron energy loss spectroscopy. It consists in the analysis of the electron energy distribution after they undergo inelastic scattering with the sample. The amount of energy lost is related with the inelastic interactions with the sample, which permits to obtain relevant information regarding the chemical state, bonding, electronic structure, etc. In general, this technique provides similar information to X-ray absorption spectrometry (XAS).

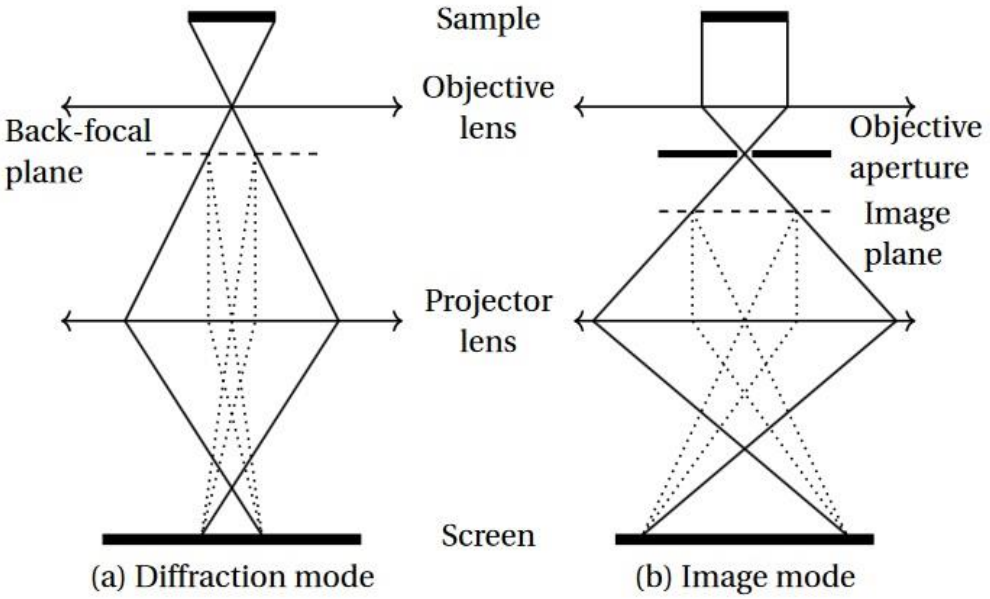

Figure 2.20. Simplified schematic of the configuration for the diffraction and imaging mode in TEM from **[60]**.

Particularly important features in the EELS spectra are the ionization edges (K, L, M, …) that appear when the energy loss equals E_C (ionization energy of a certain core shell). The intensity fluctuations observed few tens of eV beyond the ionization edge is called energy-loss near-edge structure (ELNES) and arises from the energy distribution of the unfilled electronic states (DOS) above the Fermi level. After the ionization process, the core electron can receive enough energy to be ejected form the core shell, but not to escape into the vacuum level. Therefore, it will occupy one of the available levels above the Fermi level. In this way, the energy lost by the incident electron will reflect the unfilled DOS.

The analysis of the ELNES spectrum gives valuable information on valence state, bonding and electronic structure in general [148,149]. More than 50 eV beyond the ionization edge appear the extended energy-loss fine structure (EXELFS), in form of very weak oscillations of the EELS intensity, that are the result of interference phenomenon between the wave associated to the ejected electron after the ionization process, with the backscattered wave from the surrounding atoms. The analysis of this oscillation provides information on the local atomic environment, the nearest neighbor distances, and coordination number [150].

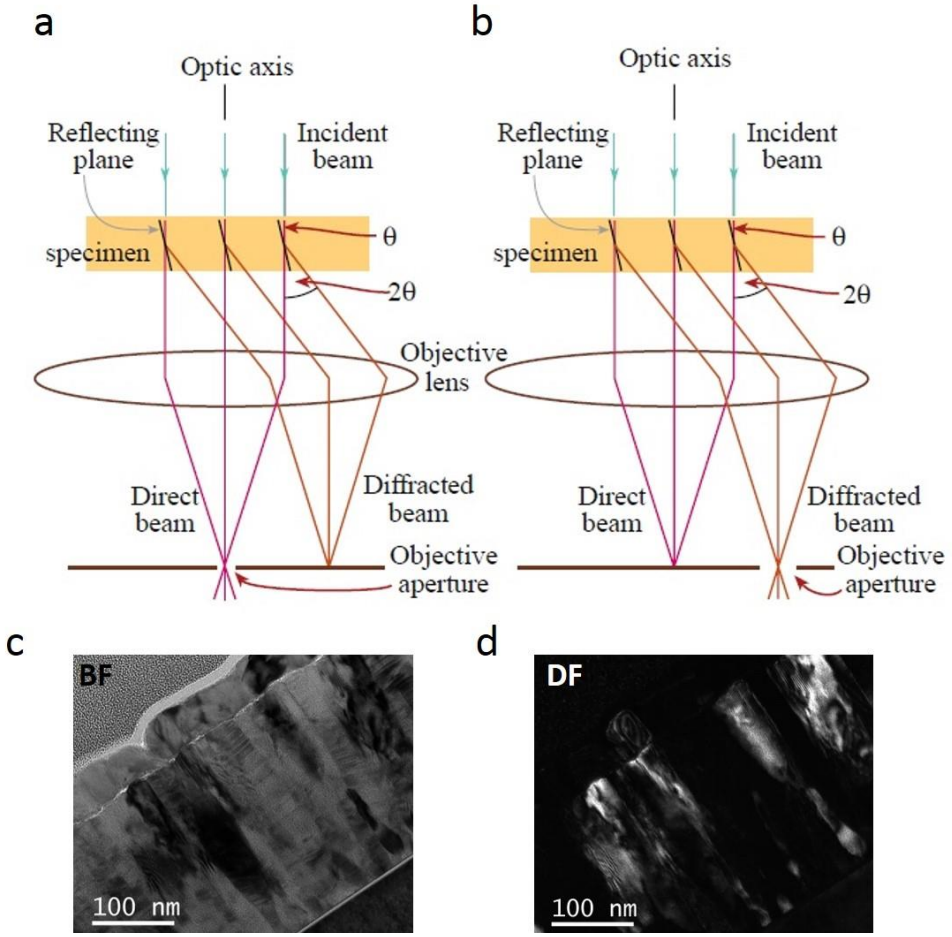

Figure 2.21. Schematic of the configuration in the TEM for obtaining BF (a) and DF (b) images **[150]**. BF (c) and DF (d) for a Cu film deposited by ALD on a ZnO film.

A particular important feature of ELNES spectra is the presence of "white lines" that are sharp and intense peaks present at the onset of certain ionization edges, where the core electron are excited to well-defined levels and not into a broad continuum ($L_{2,3}$ edges for transition metals, and $M_{4,5}$ edges in the rare-earth elements, for example) [150]. In the case of the 3d transition metals, the "white lines" observed at the $L_{2,3}$ edges arise from the transition of electrons from 2p core shells to the unoccupied d shells above the Fermi level. Therefore, its presence is a signature of the unoccupied 3d DOS. In Figure 2.22 a typical EELS spectra from a Cu_2O film is presented. The spectra are taken at the O K edge (black) and at the $L_{2,3}$ edges (blue), where the "white lines" are clearly observed.

In this work TEM was performed using a JEOL ARM 200-Cold FEG (point resolution 0.19 nm). Cross-section TEM samples of films were prepared using a focused ion beam (FIB) scanning electron microscope (SEM) dual beam system (FEI Helios 600). The samples were obtained with the lift-out technique. Preparation and thinning of the foil were done with an acceleration voltage of 30 kV. However, the last step of the thinning was done with an

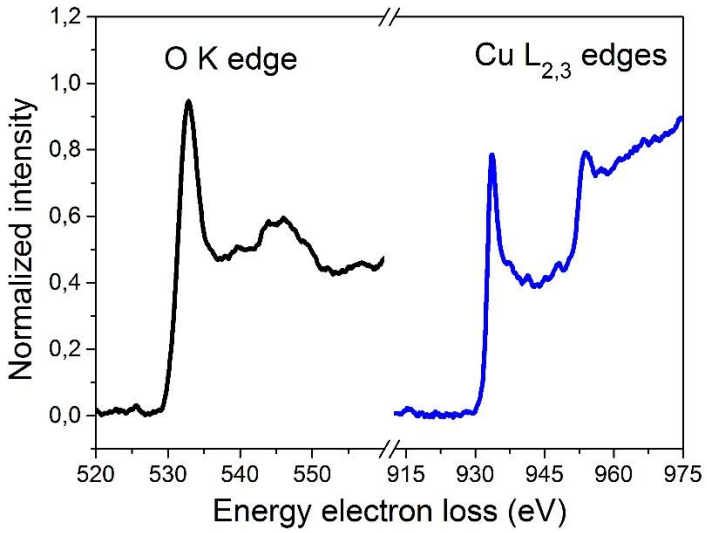

Figure 2.22. Typical EELS spectrum from a Cu_2O film, at the high energy loss region.

acceleration voltage of 5kV, in order to minimize any possible artifact like amorphization or ion implantation. Composition profiles were obtained by EDS in scanning transmission electron microscopy (STEM) mode. EELS experiments were performed in diffraction mode. The spectrometer was set to an energy dispersion of 0.05 eV/channel. The condenser aperture, spectrometer entrance and camera length were 150 µm, 2.5 mm and 4 cm, respectively, leading to a collection half angle of 20 mrad and an energy resolution of 0.5 eV, measured at full width at half maximum (FWHM) of the zero loss peak.

2.10 X-ray Photoelectron Spectroscopy

X-ray photoelectron spectroscopy is a surface analysis technique that allows the identification of the chemical composition and chemical bonding of elements in a sample. In this technique the sample is irradiated by X-rays that induce the electron emission from the sample surface by the photoelectric effect (see schematic in Figure 2.23 a). The kinetic energy (K_e) of the emitted electron is given by:

$$K_e = h\nu - E_B \qquad \textbf{(2.15)}$$

Where $h\nu$ is the energy of the incident photons and E_B is the binding energy of the electron to the atomic orbital from which it originates. Typically $Mg\ K\alpha$ ($\lambda = 1253.6\ eV$) and $Al\ K\alpha$ ($\lambda = 1486.6\ eV$) X-rays are employed for exciting the sample. Only electrons coming from a few nm below the film surface can escape from the surface without energy loss, and these electrons are the responsible for the different peaks in the XPS spectra; the background is formed by all the electrons that undergo inelastic energy losses before emerging from the sample surface

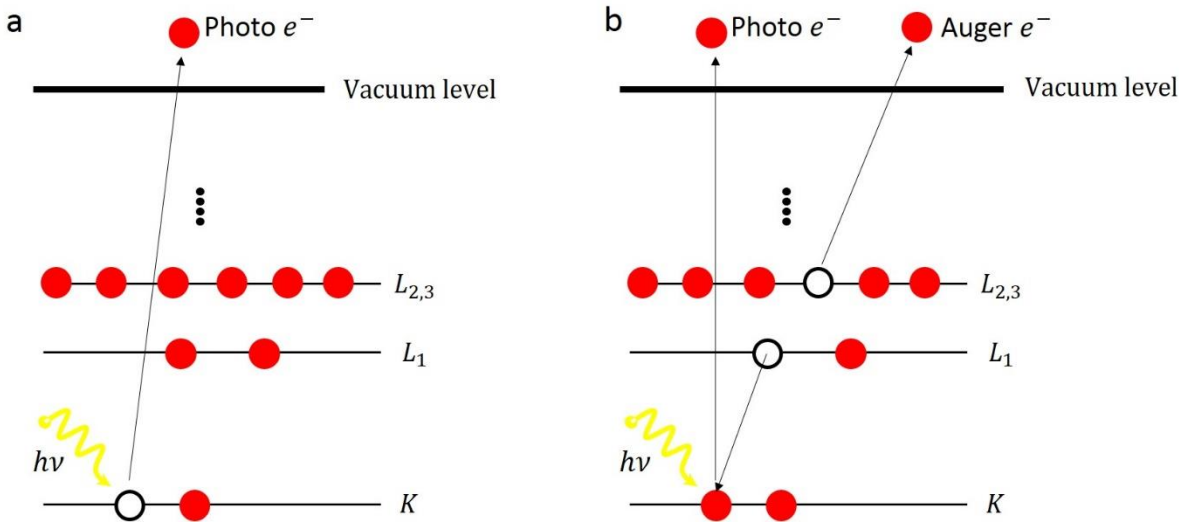

Figure 2.23. Schematic representation of photoelectron emission in XPS process (a) and Auger electron emission at result of relaxation process (b).

[151]. Figure 2.24 shows a XPS survey spectrum from a Cu_2O/ZnO sample, together with a high-resolution spectrum in the Cu 2p region, as example.

In addition to photoelectron emission, there are some peaks in the XPS spectra related to Auger emission that occurs as a result of the relaxation process after photoelectron emission. After the ejection of the photoelectron from a core shell (e.g. K shell) and the creation of a vacancy, the atom is left in an unstable state. Therefore, an electron from an outer shell (e.g. L_1 shell) will fill this hole and the energy lost can be transferred to a third one from an outer shell (eg. $L_{2,3}$) that can be ejected from the atom if the energy is higher than the binding energy of this electron to its corresponding shell. The process is schematically represented in Figure 2.23 b. The transition is indicated using the spectroscopic notation $KL_1L_{2,3}$, where K represents the core shell where the vacancy is created, L_1 the initial state of the electron filling the vacancy and $L_{2,3}$ the shell of the final ejected electron (auger electron). The kinetic energy (K_e) of the auger electron is given by equation (2.16).

$$K_e = (E_{L_1} - E_k) - E_{L_{2,3}} \qquad \textbf{(2.16)}$$

Where E_k, E_{L_1} and $E_{L_{2,3}}$ are the binding energy of the levels involved in the process. The auger emission process occurs approximately 10^{-14} s after the photoelectron release and most typical auger series observed in XPS spectra are the KLL and the KMM.

Since each element has a unique set of binding energies, XPS can be used to determine the chemical composition and the relative concentration of the different elements present in the

sample. Moreover, variations of the binding energies (chemical shifts) can be used to determine the oxidation states and chemical environments of the atoms in the compound.

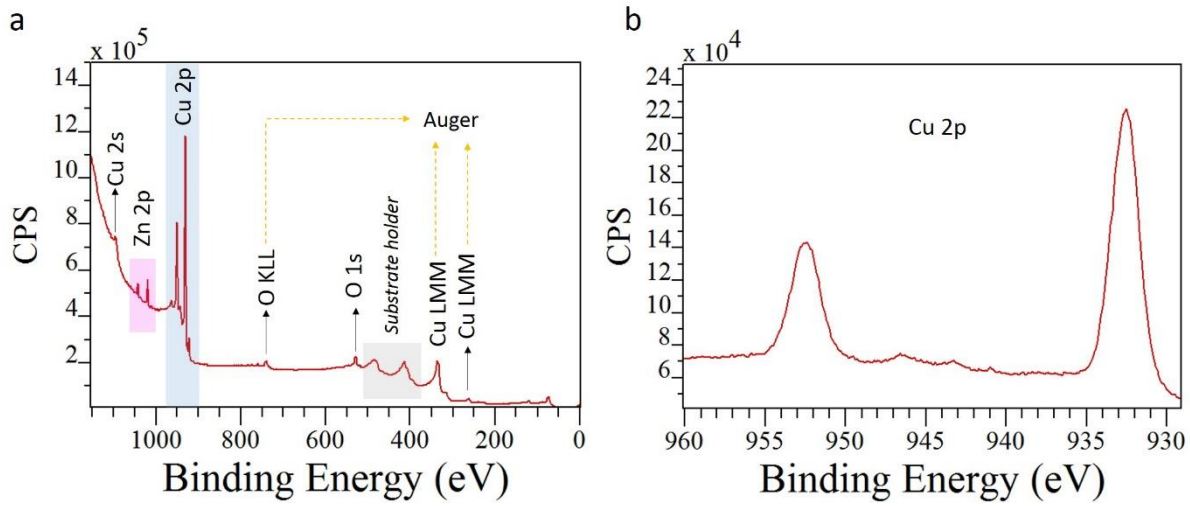

Figure 2.24. XPS survey spectrum (a) and Cu 2p spectra (b) from a Cu_2O film.

In this work, XPS measurements were performed to the samples using Mg Kα radiation. Before the analysis, a 2 min Ar-etching at 5 keV was done to remove the contamination at the sample surface.

2.11 Hall Effect and 4-point Probe Method

A four-point probe is a simple technique to measure the resistivity of a material. The sample is contacted by four probes in a linear configuration (Figure 2.25 a). Then, a current is passed through the two outer probes and a voltage is measured through the two inner probes. From the current (I) and voltage (V) values the sheet resistance is calculated by $R_S = C * (V\ /\ I)$, where C is a constant depending on the geometry of the contact that equals $\pi/\ln 2$ for the linear configuration. Then, if the thickness (t) of the film is known, the resistivity (ρ) can be easily determined by $R_S * t$. Another configuration, also used to measure the sample resistivity is the Van der Pauw configuration. In this case, the four probes are in the perimeter of the sample as is shown in Figure 2.25 b.

Hall effect measurement are very useful for the electrical characterization of semiconductors. A magnetic field B is applied perpendicular to the film surface while and electrical current is circulating in the longitudinal direction (x), as is depicted in Figure 2.25 c. The charge carriers experience the Lorentz force and are deflected in the transverse direction (y). As a result of the charge accumulation at one side of the film, a transverse voltage is detected, called Hall voltage (V_H) and is described as:

$$V_H = \frac{I\,B}{n\,t\,e} \tag{2.17}$$

Where I is the current in the longitudinal direction, t is the film thickness, n the charge carrier concentration and e the electron charge. Since V_H has different polarity for different types of charge carriers, this technique is useful for determining the type of conductivity (p or n) for a semiconductor. Moreover, carrier concentration, electrical resistivity and carrier mobility can be also determined by this technique.

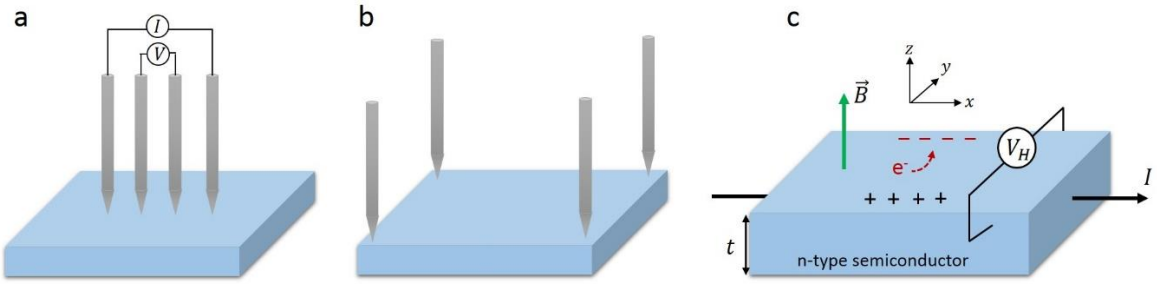

Figure 2.25. Contact configuration for 4-point probe measurements: linear (a) and Van der Pauw (b). Schematic of Hall effect measurements (c).

The electrical characterization of the samples analyzed in this work was done by the four-point probe method in the linear configuration and by a Hall measurement system in the Van der Pauw geometry (Ecopia, HMS-5000) with a DC magnetic field of 0.57 T.

2.12 Conductive Atomic Force Microscopy

Atomic force microscopy (AFM) is a powerful imaging technique that provides 3-dimensional topography images of the sample surface. It has the advantages that almost any type of material can be analyzed: conductive, non-conductive, soft or hard, ceramics, polymers and biological samples [152]. There are different operating modes in AFM, namely, contact mode, non-contact mode and tapping mode. The working mode is selected depending on the sample characteristics, the contact mode being the simplest and most commonly employed.

In contact mode, a cantilever with a sharp tip scans the sample surface and the topography is measured by detecting the deflection of the cantilever, that is controlled by an optical system formed by a laser and a photodiode (see schematic in Figure 2.26 a). The laser beam is focused at the cantilever flat surface and reflected to the photodiode. Any deflection of the cantilever as a result of the interaction between the tip and the sample surface produces a displacement of the reflected beam position at the photodiode. This deflection is sensed and compared in a

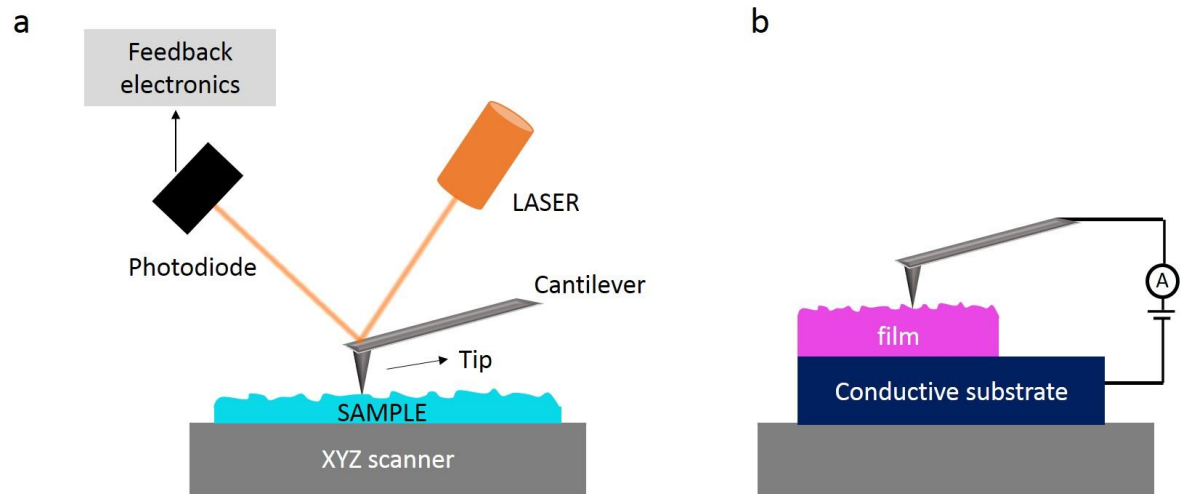

Figure 2.26. Schematic of the AFM system in contact mode (a). Schematic of one of the standard geometries for the C-AFM measurements.

feedback loop with a previously selected deflection value to control the force and tip position, which allows to monitor the height of the features at the sample surface, displayed as a function of the lateral position of the sample.

The force applied to the sample is not measured directly but can be calculated by Hooke's law from the deflection of the cantilever by:

$$F = -k\,z \tag{2.18}$$

Where z is the deflection and k is the spring constant of the probe.

Usually, the AFM operates at ambient condition. However some systems allow to work in a controlled atmosphere using different gases, liquids, or under high vacuum conditions [153,154]. Additional functionalities have been implemented in AFM systems to link sample morphology to the mechanical properties like young modulus and surface energy. Conductive AFM (C-AFM) is an additional feature incorporated to AFM that permits to measure simultaneously the topography of the sample surface and the electrical current flowing from the sample surface to the tip. For this type of measurements, conductive tips are needed (usually metal-coated tips are used) and the system operates in contact mode. A voltage is applied between the tip and a counter electrode and the current is measured. With this mode it is possible to perform current maps by moving the AFM tip over the sample surface at a fixed voltage or measuring the current-voltage characteristics of the sample by recording current as a function of the voltage keeping the tip at a fix position on the sample surface [155]. A schematic of the geometry employed for C-AFM measurements is presented in Figure 2.26 b.

This technique allows the electrical characterization of nanostructured materials like nanowires or nanorods, [156–158], nanoparticles [159], and in general for materials where changes in charge-transport properties occur at the macro or nano-scales and for which traditional macroscopic electrical measurements are not suitable or too difficult to performed [152,160].

The C-AFM measurements in this work were performed at ambient conditions with a NTEGRA AFM (NT-MDT) system in contact mode using a N-doped diamond coated probe (DCP20 series) with a tip height of 10 μm, nominal tip radius of 100 nm and nominal spring constant of 48 N/m.

2.13 Current-density Characteristics

Current-voltage (I-V) characteristic curves show the relationship between the current flowing through a device and the voltage applied across its terminals. P-n junctions are the "building block" of several semiconductor devices such as transistors, diodes, solar cells, LEDs, lasers, etc. They show non-linear I-V characteristics, as opposed to resistors where a linear relation between the voltage and the current is observed following Ohm's law.

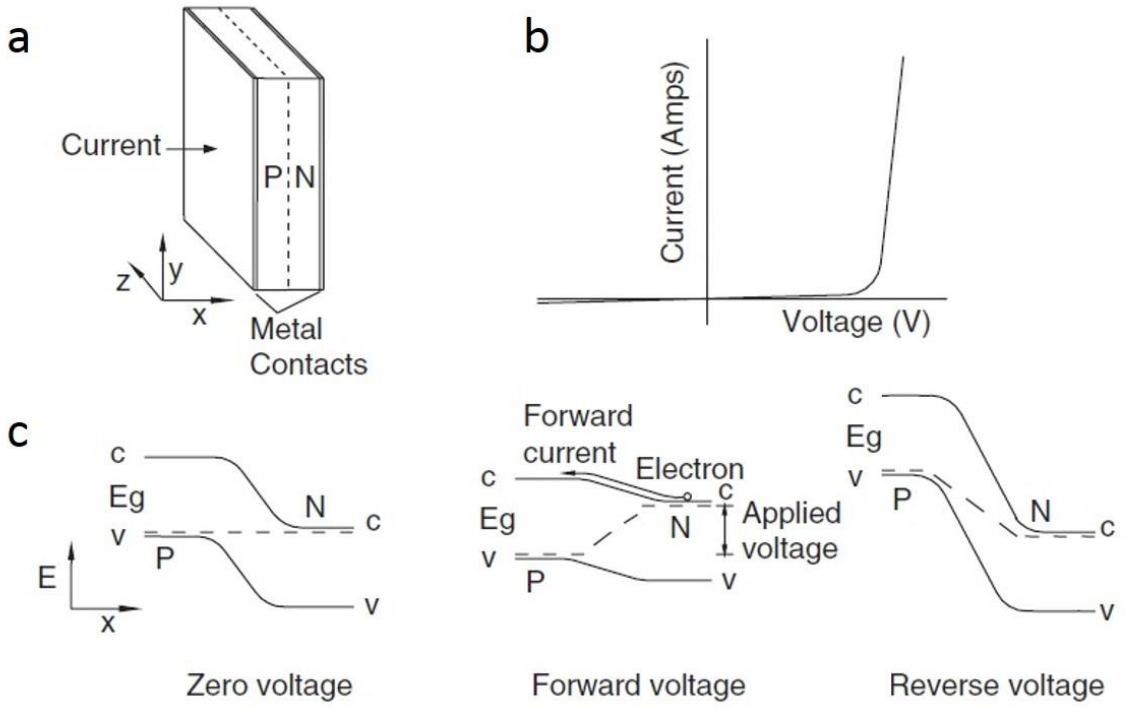

Figure 2.27. Schematic of a p-n junction (a). I-V characteristics of the junction (b). Energy diagrams diagrams for the different operation modes of the p-n junction: zero voltage (left), forward bias (center), reverse bias (right) (c) **[161]**.

For p-n junctions the I-V characteristics show a rectifying behavior allowing the flow of the current only in one direction (see Figure 2.27 a, b). At zero bias voltage (no external voltage applied) the current flowing through the device is zero, since there is an equilibrium between generation, recombination, diffusion and drift of carriers at the junction [161]. Under forward bias (the voltage connected positive to the p-type semiconductor and negative to the n-type semiconductor) an electric field opposite to the electric field across the depletion layer is created reducing the net electric field at the junction (Figure 2.27 c, center). Therefore, the carriers can more easily diffuse (electron from the n to the p-side, and hole from the p to the n-side), increasing the current flowing through the device (first quadrant of Figure 2.27 b). Under reverse bias conditions (the voltage connected negative to the p-type semiconductor and positive to the n-type semiconductor), the net electric field at the junction is increased (Figure 2.27 c, right) reducing the probability of carrier diffusion and therefore preventing the current from flowing in the device (third quadrant in Figure 2.27 b). A very small current circulates through the device on reverse bias conditions (leakage current), which is due to the drift of minority carriers (electron from the p to the n-side and holes from the n to the p side).

The equation describing the diode behavior is given by:

$$I = I_0 \left(e^{\frac{q\,V}{n\,k\,T}} - 1 \right) \qquad \textbf{(2.19)}$$

Where I_0 is the dark saturation current (leakage current), q is the electron charge, k the Boltzmann's constant, T the temperature, and n the ideality factor (equals to one for an ideal diode).

When the p-n junction is illuminated with photon energies higher than the semiconductors band gap, carriers are generated, and separated by the electric field at the junction, producing a photocurrent through the device. This results in a shift of the I-V curve toward the fourth quadrant. The diode equation is modified in consequence as:

$$I = I_0 \left(e^{\frac{q\,V}{n\,k\,T}} - 1 \right) - I_L \qquad \textbf{(2.20)}$$

where I_L is the photogenerated current.

Figure 2.28 shows the I-V characteristics of an ideal solar cell in the dark, and under illumination. The analysis of I-V curves under illumination allows determining several parameters useful for the device characterization such as: short circuit current, open circuit voltage, fill Factor, and efficiency. The short circuit current (I_{SC}) is the current circulating through the device when the voltage across the solar cell is zero, and the open circuit voltage

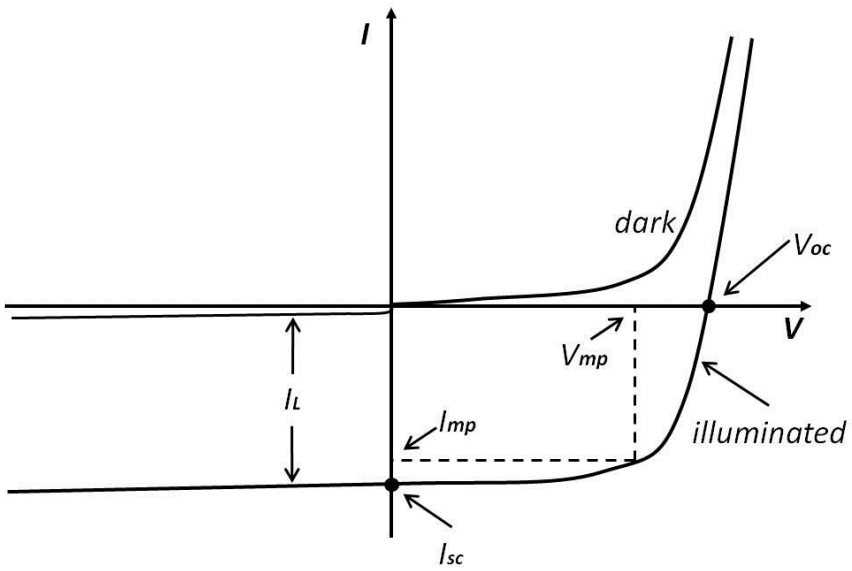

Figure 2.28. I-V characteristics of a p-Cu_2O/n-ZnO heterojunction on dark and under 1 Sun illumination **[162]**.

(V_{OC}) is the voltage across the device when the current is zero. I_{SC} and V_{OC} are the maximum current and voltage, respectively, that can be extracted from a solar cell. However, at these points either the current or the voltage is zero and in consequence no power can be extracted from the device. In this sense, it is interesting to determine the point of maximum power (V_{mp}, I_{mp}). The Fill Factor is a figure of merit for solar cell devices that measures the maximum power that can be extracted from the solar cell. It is calculated from the maximum power divided by the product of I_{SC} and V_{OC}:

$$FF = \frac{I_{mp} \times V_{mp}}{I_{SC} \times V_{OC}} \quad \textbf{(2.21)}$$

Finally, the power conversion efficiency of the solar cell is defined as the fraction of incident power (P_{inc}) from the sun that can be converted into electricity, and is given by:

$$\eta = \frac{I_{SC} \times V_{OC} \times FF}{P_{inc}} \quad \textbf{(2.22)}$$

In this thesis, I-V characteristics were performed to the p-Cu_2O/n-ZnO micro-junctions by C-AFM. I-V curves were also measured on the Cu nanoparticles/ZnO samples. In this case, the measurements under illumination were collected employing a Thorlabs white LED with 5700 K color temperature, emission spectra from 400 nm to 800 nm and maximum output power of 4.6 W. Finally, for the thin films p-Cu_2O/n-ZnO heterojunctions, I-V curves were obtained using a source picometer (Keithley 2401). For the measurement under 1 Sun illumination a

solar simulator was employed, consisting in a xenon arc lamp with a AM 1.5G filter (1000 W/m^2).

Chapter 3

Local Structure and Point-Defect-Dependent Area-Selective Atomic Layer Deposition of Copper Oxide and Metallic Copper Thin Films

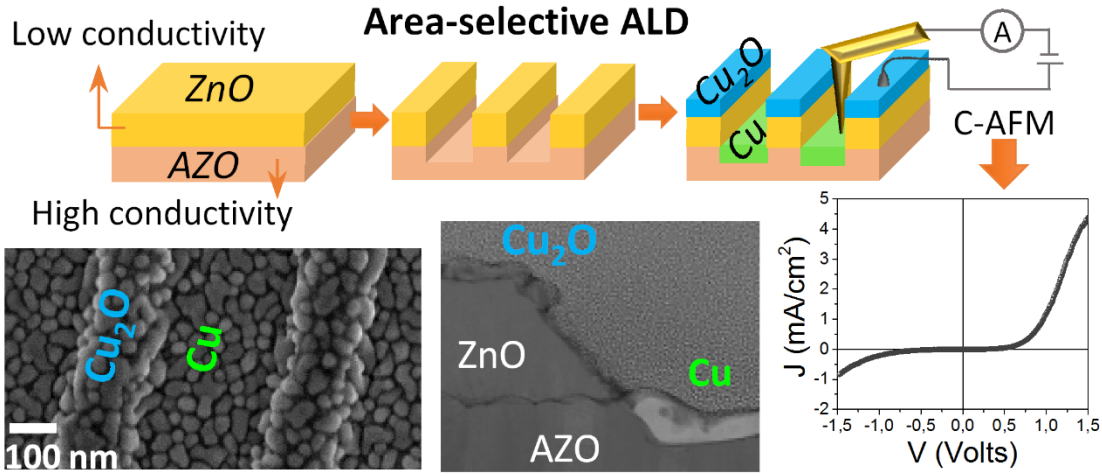

ABSTRACT: In this chapter we present the selective deposition of Cu_2O and Cu thin films by atomic layer deposition (ALD) on ZnO, Al-doped ZnO, and α-Al_2O_3 substrates, using $Cu(hfac)_2$ and water as precursors. We were able to tune the deposited material (Cu or Cu_2O) by changing the temperature and substrate conductivity/density of point defects. Generally, the growth selectivity is achieved by starting from different materials and results (ideally) in localized growth of a single material. We propose here a new concept, in which a property of the substrate is modulated to achieve localized growth of different materials. This concept is demonstrated by selective growth of high quality metallic Cu, and semiconducting Cu_2O thin films achieved by changing the type of majority point defects in the ZnO underneath film exposed to the reactive species, using a patterned bi-layer structure composed of highly conductive and highly resistive areas, as confirmed by transmission electron microscopy (TEM) and electron energy loss spectroscopy (EELS). The selective growth of these materials in a patterned ZnO/Al-doped ZnO substrate allows the fabrication of p-Cu_2O/n-ZnO micro-junctions showing a non-linear rectifying behavior typical of a p-n junction, as confirmed by conductive atomic force microscopy (C-AFM).

Contents

3.1 Introduction

The continuous trend of miniaturization in microelectronics makes conventional patterning techniques challenging due to the extremely small features that are required. Conventional patterning is achieved by a top-down process consisting of the patterning of a resist film by lithography (photolithography, e-beam lithography, soft lithography, etc.) and a subsequent etching step. With technology approaching to the sub-10 nm scale, conventional pattering is reaching its limit due to the difficulty in achieving a precise pattern, in particular when it comes to 2D and 3D nanostructures. In conventional lithography, multiple patterning steps (E.g. double exposure, spacer-defined double patterning or spacer-defined quadruple patterning [1]) are introduced as a way of improving the final resolution. However, the many step involved in the process can result on mask misalignment issues or edge placement errors which is critical for device performance [163]. Moreover, there are also some compatibility issues of certain materials with the developer or resist film, and the etching step could be difficult when working with organic semiconductors and carbon-based materials [1]. These are the reasons why area-selective deposition has gained a lot of attention. It limits the deposition of the material to the areas where it is desired, eliminating, or at least reducing, the number of lithography steps.

On the other hand, atomic layer deposition (ALD) has emerged as an important technique for depositing high-quality thin films due to the self-limiting growth mechanism, which enables an excellent surface coverage and conformal deposition on high-aspect-ratio structures. The fact that it depends strongly on the surface chemistry makes it a technique of choice for achieving area-selective deposition. One approach for achieving area-selective atomic layer deposition (AS-ALD) is based on the different nucleation times of a material grown by ALD on different surfaces. However, by this method, selective growth is restricted to a few nanometers [164]. An alternative that allows the growth of thicker films and to improve the selectivity is combining the previous approach with a periodically etching step to remove the deposited material from the undesired areas. An example is the AS-ALD of TiO_2 and Ta_2O_5 films reported by R. Vallat et *al.* on TiN vs. SiO_2/Si surfaces by incorporating a NF_3 plasma etching step to a standard plasma-enhanced ALD process [160,161]. Another AS-ALD approach widely employed relies on the deactivation of part of the substrate by certain molecules or by self-assembly monolayers (SAMs), prior to ALD [165–170]. A schematic of the AS-ALD process by SAMs is presented in Figure 3.1 a. The SAMs are absorbed in the areas of the substrate where deposition is to be prevented, blocking the adsorption of the precursor molecules. Therefore, during the ALD process the precursor is adsorbed selectively in the

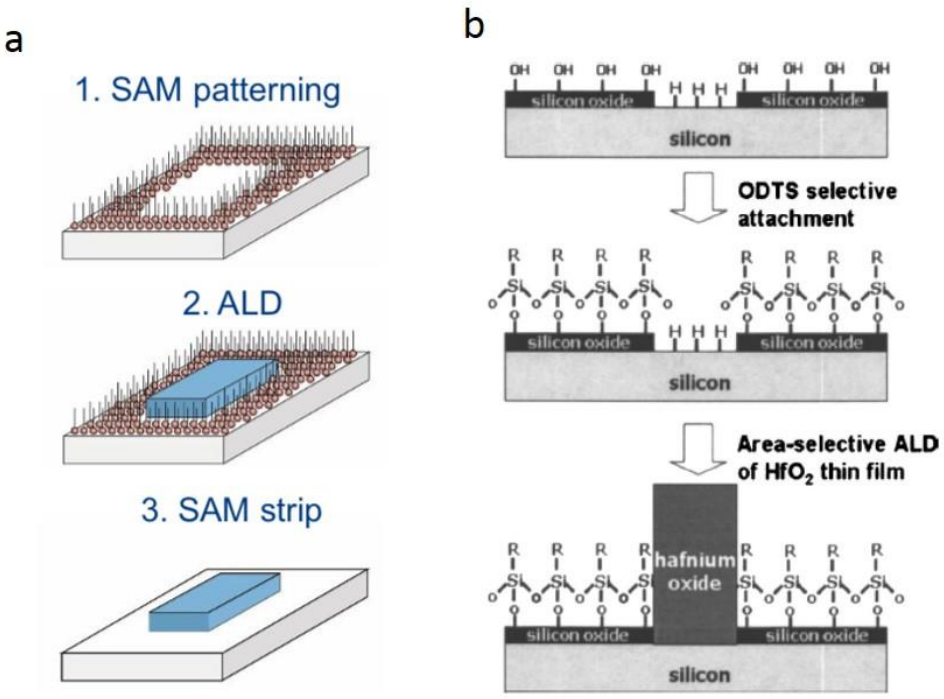

Figure 3.1. Schematic of the AS-ALD process by deactivation of the surface using SAMs [1] (a). Schematic of the AS-ALD process for the fabrication of HfO_2 using octadecyltrichlorosilanes (ODTS) SAMs to modify the surface **[165]**.

regions that are not covered by the SAMs. At the end of the deposition process the SAMs are removed and the AS-ALD process is completed. An example of the AS-ALD of HfO_2 on a patterned Si substrate by using octadecyltrichlorosilane (ODTS) SAMs is shown in Figure 3.1 b. The substrate patterning was achieved by thermal oxide growth and photolithography resulting in a surface formed by OH-terminated SiO_2 regions and H-terminated Si areas. The ODTS SAMs were selectively adsorbed on the OH-terminated SiO_2 regions, and the HfO_2 AS-ALD process occurs in the H-terminated Si surface [165], as can be seen in Figure 3.1 b.

Successful deposition of ZnO and TiO_2 has been accomplished on Cu/Si-patterned substrates by blocking the Cu surface using SAMs [168]. The selective growth of high-k gate dielectrics HfO_2 and ZrO_2 was demonstrated by Chen *et al.* by using octadecyltrichlorosilane (ODTS) [170]. SiO_2 films were successfully grown on GeO_2 substrate with patterned Al_2O_3, using acetyl-acetonate as growth inhibitor molecule [166], and Al_2O_3 nanopatterns were selectively deposited on octadecylphosphonic acid (ODPA)-patterned Ti substrates [169]. AS-ALD of metallic films like Co, Ni, and Pt has been also successfully achieved by SAMs [171–173]. Nevertheless, the use of SAMs is not without challenges. High deposition temperatures in thermal ALD affect the thermal stability of the SAMs, causing the loss of selectivity.

Furthermore, SAMs are not compatible with plasma-assisted or ozone-based ALD [1], which limits the number of materials that can be deposited in a selective manner by this method.

In general, when referring to area-selective deposition, it comes to whether a certain material can be deposited on different surfaces or on the same surface but locally modified. However, for future nanoelectronic devices it is crucial to develop new approaches for simultaneous deposition of different materials in a selective manner on different surfaces in a straightforward way without adding new steps in the process.

In this work, we present the SAMs-free approach for the AS-ALD of Cu and Cu_2O on ZnO and Al-doped ZnO films of controlled electronic conductivity. Our selective deposition approach is based on the inherent selectivity of the $Cu(hfac)_2$ precursor toward different ZnO surfaces. Therefore, no inhibitor or blocking molecules are needed. Hence, the process is simpler than any other patterning approach and eliminates the problem of thermal stability related to SAMs. The modulation of the ZnO properties is achieved in this work by tuning the ZnO conductivity/type of majority point defects over a very large range (10^{-4} to 10^{3} S/cm) which, as we will demonstrate, will determine the final material deposited: Cu or Cu_2O. As already shown in the literature, the nature of the substrates can influence the growth and evolution of thin films [174,175]. Moreover, the charge exchange at the interface between thermally-resistant inorganic substrates and film has shown its potential to strongly influence the phase formation in a selective way [176]. The area-selective deposition approach proposed here is very promising, since the combination of metallic Cu films with semiconductor oxides (ZnO, Cu_2O, or both) has many applications in different fields related with optoelectronics [177], catalysis [178], gas sensing [179], and photovoltaics [180].

3.2 Microstructure and Morphology of the Cu_2O and Cu Thin Films

ZnO and Al-doped ZnO (AZO) films were deposited on a (100) Si substrate by reactive magnetron sputtering of Zn and $Zn_{98}Al_2$ targets, respectively, in different Ar-O_2 reactive mixtures (see the details of the deposition process in Chapter 2). Figure 3.2 displays the conductivity of the films as a function of the position in the chamber together with a schematic of the configuration used for deposition. The conductivity of the ZnO and AZO films was determined by the 4-point probe technique. It shows a minimum facing the magnetron axis (at 8 cm) and monotonously increases off-axis (see schematic of the target-substrates geometry in Figure 3.2a). This is in line with a higher flux of energetic O atoms and O^- ions in front of the target axis [181] (see schematic in Figure 3.2b), which results in the incorporation of oxygen interstitial into the film, that is a well know acceptor defect in ZnO. Therefore, the films

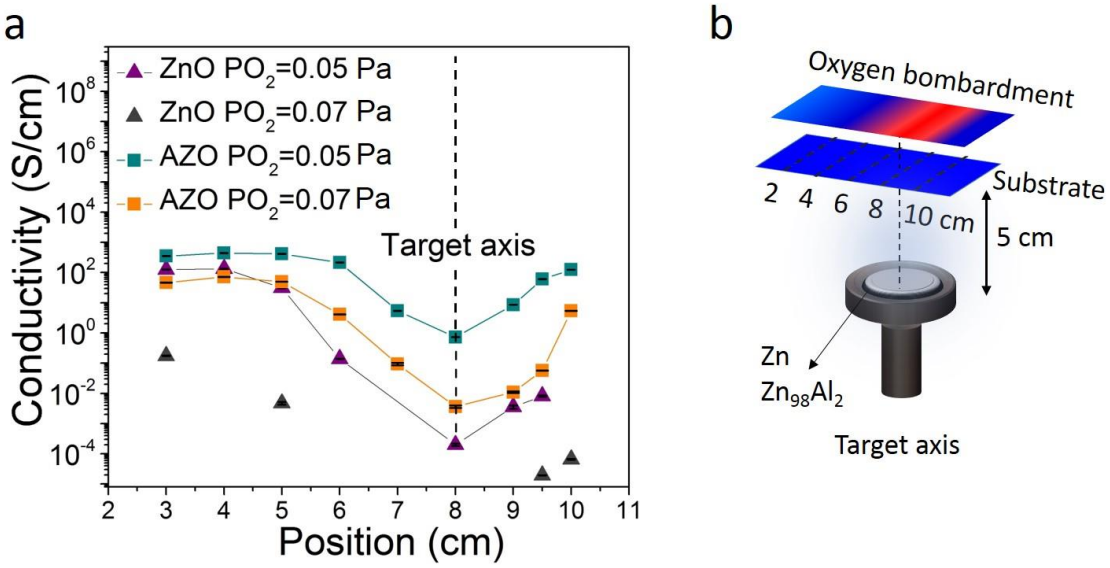

Figure 3.2. Conductivity of the ZnO and AZO films as a function of the position in the sputtering chamber and O_2 partial pressure (a). Schematic of the configuration used for the deposition and of the flux of high energetic O atoms and O^- ions (b). Remark: the conductivity of sample deposited using $\boldsymbol{P_{O_2}}$ = 0.07 Pa was too high to be measured near the target axis, explaining why symbols were selected instead of connecting lines in (a) for this condition.

deposited at this position present a lower density of donor defects and, in consequence, lower conductivity compared with those deposited farther away from the target axis. This effect is enhanced if the O_2 partial pressures (P_{O_2}) in the chamber is increased, which explains the decrease in conductivity for samples deposited at higher P_{O_2} (see Figure 3.2a). In addition, an efficient n-doping of ZnO by Al was achieved as evident from Figure 3.2a. The sputtered Al atoms substitutes the Zn site in the ZnO crystal lattice forming an Al_{Zn}^{x} structure element, which is a shallow donor that can release an electron upon ionization: $Al_{Zn}^{x} \Leftrightarrow Al_{Zn}^{o} + e'$ [182], resulting in the increase of the films conductivity.

Cu and Cu_2O films were grown on top of the ZnO and AZO films by atomic layer deposition, using $Cu(hfac)_2$ as the Cu precursor and water as the reactant (see more details on the deposition process at Chapter 2). Typical X-ray diffractograms of the samples obtained at a substrate temperature of 280 °C are shown in Figure 3.3 a (the substrates used for the samples whose reported data appear in the figure are indicated by arrows in Figure 3.2). Pure metallic Cu (green line), Cu_2O (blue line), and a mixture of both phases (red line) were obtained depending on substrate conductivity. Some details about their structure, microstructure and synthesis conditions are given in the following before demonstrating their spatially-selective growth and discussing the mechanisms behind the formation of the different phases.

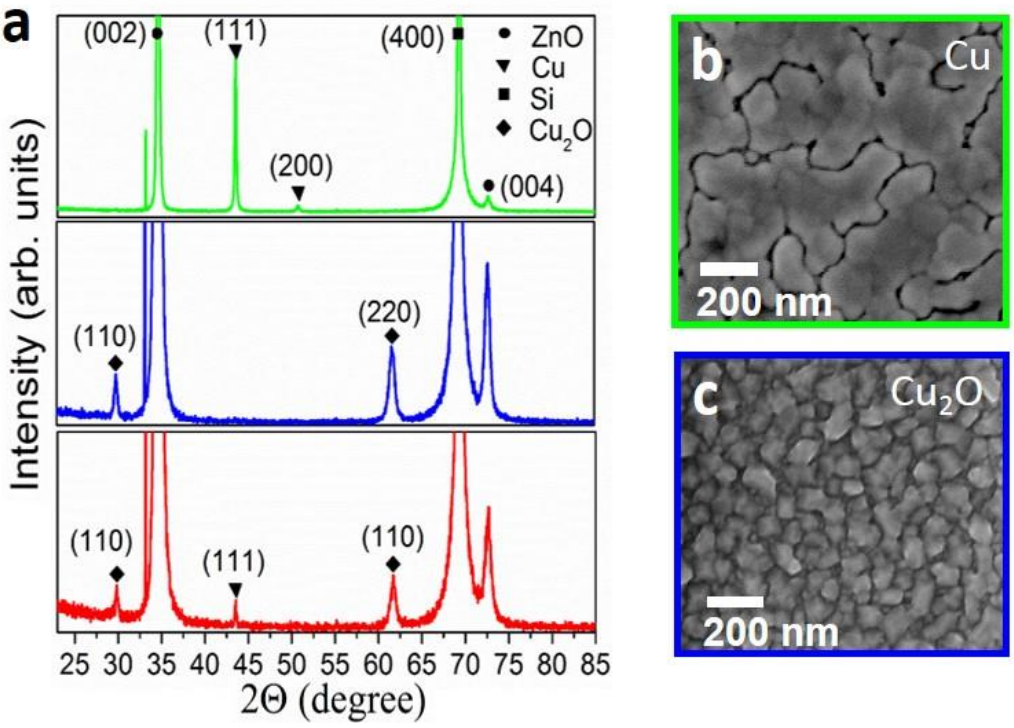

Figure 3.3. X - ray diffractograms of the samples after the ALD deposition at 280°C (a). Top-view SEM micrographs of the Cu film (b) and the Cu_2O film (c).

A top view SEM micrograph of a typical metallic Cu film (obtained after 10000 ALD cycles) is shown in Figure 3.3 b. The film covers the entire substrate surface, except some discontinuities between crystallites, and consists of nanocrystalline Cu grains preferentially oriented in the [111] direction, as shown by the X-ray diffractogram of Figure 3.3 a (green line). The length of the coherent diffraction domains was determined from the integral breadth of the (111) diffraction peak, using Scherrer's equation. A value of 44 nm was obtained in good agreement with a film thickness of 48.9 nm, measured directly form the cross-section TEM micrograph of Figure 3.4 a. A high-resolution TEM (HRTEM) micrograph of this sample, with the corresponding fast Fourier transform pattern (FFT), is shown in Figure 3.4 b. The interplanar spacing of the (111) planes was measured to be 0.211 nm, in good agreement with the value reported for cubic Cu (JCPDS 00-004-0836). For these samples, a systematic study of the film morphology for different ALD cycles indicates a Volmer-Weber or island growth mode at early stages (this will be discussed in more details in Chapter 4).

Figure 3.3 c shows a top-view SEM micrograph of a typical Cu_2O film (10000 ALD cycles). In general, all the Cu_2O samples deposited were textured with (110) planes parallel to the c-axis of ZnO, since only (110) and (220) peaks are observed in the X-ray diffractogram (Figure 3.3 a, blue line). A thickness of around 40 nm was measured from the cross-section

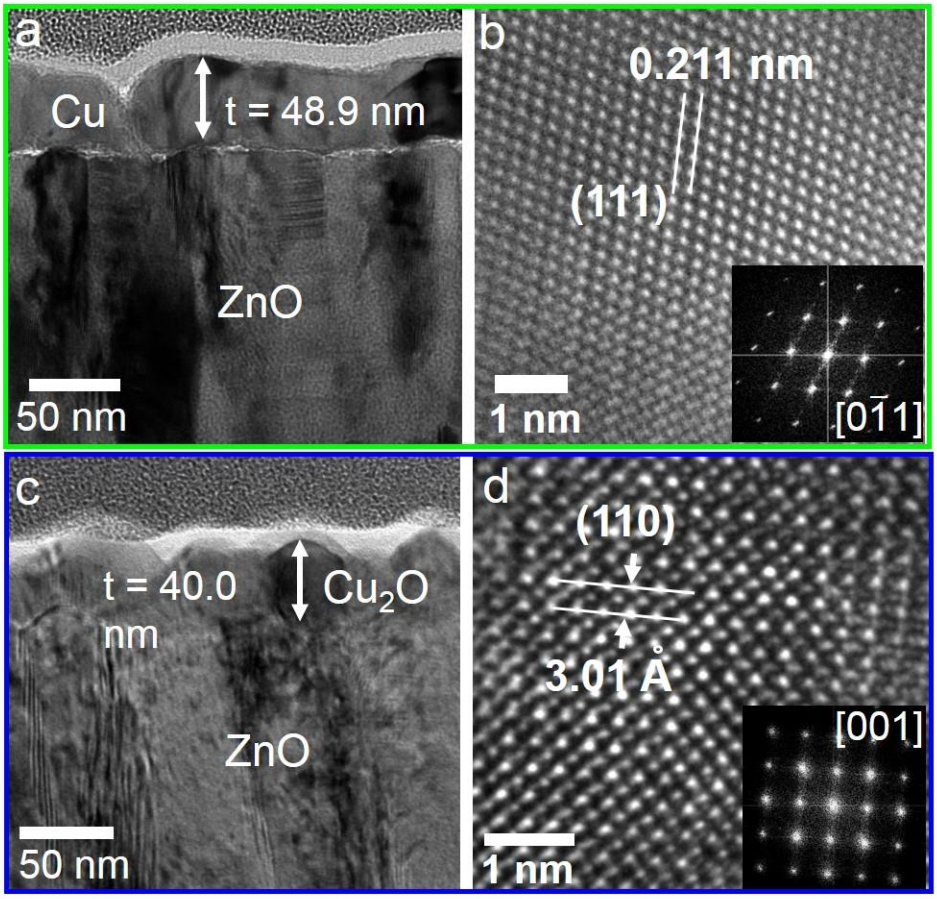

Figure 3.4. Cross-section TEM micrographs of the Cu (a) and the Cu_2O (c) films. HRTEM micrographs of the Cu (b) and the Cu_2O (d) films; the corresponding FFT patterns are shown at the inset.

TEM micrograph shown in Figure 3.4 c. A HRTEM micrograph of this sample is shown in Figure 3.4 d, where the distance between (110) planes is measured to be 0.301 nm, in agreement with the values reported for cubic Cu_2O (JCPDS 04-007-9767). The texture of the Cu_2O film on ZnO, with (110) Cu_2O || (001) ZnO, observed in the X-ray diffractogram is different from that typically-reported. Yet, it has already been obtained for Cu_2O films grown by MOCVD using also $Cu(hfac)_2$ as precursor [130], and in Cu_2O films grown by sputtering of a ceramic target [183]. This texture suggests the possibility of a local epitaxy between the Cu_2O and ZnO films. In order to verify the latter, HR-TEM images were taken at the interface between Cu_2O and ZnO. The continuity of the lattice planes in the TEM micrograph (Figure 3.5 a) and the fast Fourier transform patterns taken at the interface between both films (Figure 3.5 b - d) indicate a local epitaxial relationship where [110] Cu_2O || [001] ZnO, and [001] Cu_2O || [010] ZnO films.

A schematic model of this epitaxial relationship is shown in Figure 3.5 e - f. The oxygen atoms at (001) planes of ZnO form a rectangular unit cells with sides of 3.250 Å and 5.629 Å and the copper atoms at the (110) planes of Cu_2O form a rectangular unit cells with cell edges

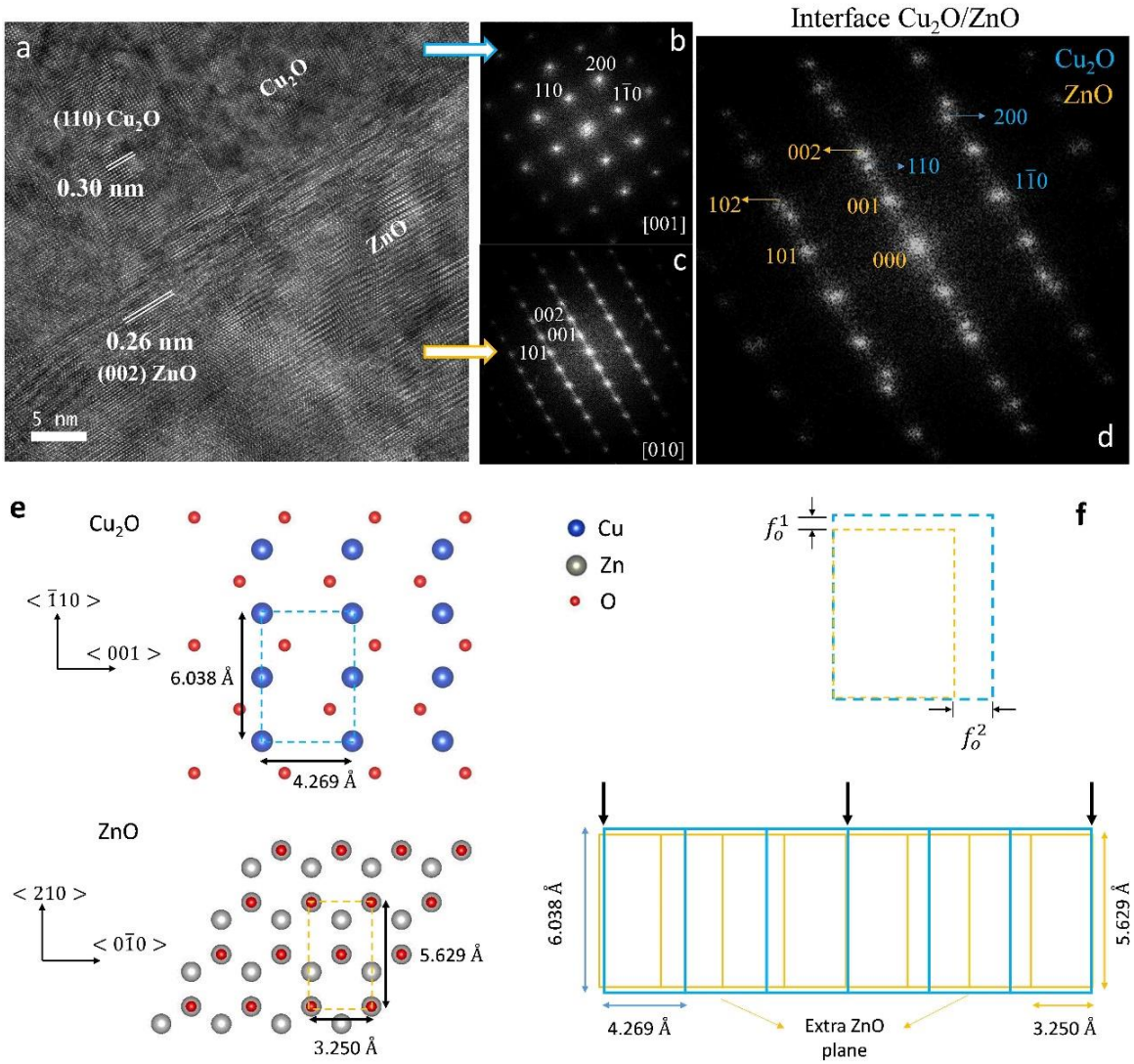

Figure 3.5. TEM micrograph taken at the Cu_2O/ZnO interface (a). FFT patterns of the TEM image in the region of Cu_2O (b), ZnO (c), and at the interface (d). Schematic model for the atomic arrangement of the (110) planes of Cu_2O (top) along the [110] zone axis and the (001) planes of ZnO along the [001] zone axis (bottom)(e). Top view schematic of the rectangular unit cells for Cu_2O and ZnO, indicating the lattice mismatch (top) (f). Schematic model of the epitaxial relationship between the (110) Cu_2O and the (001) ZnO surfaces (bottom) (f).

of 4.269 Å and 6.037 Å (see dotted lines in Figure 3.5 e). Under this configuration, the lattice mismatch f_o^1 corresponding to the [$\bar{1}$10] Cu_2O direction, that is between the ($\bar{1}$10) Cu_2O and (100) ZnO planes, is 7.3 % and the f_o^2 corresponding to the [001] Cu_2O direction, i.e. between (001) Cu_2O and (1$\bar{2}$0) ZnO planes, is as high as 31%. Nevertheless, epitaxy is still possible in a system with such a large lattice misfit thanks to domain matching epitaxy (DME), that occurs when integer multiples of lattice planes match at the interface of the films [184].

In fact, since $a_{Cu_2O}/a_{ZnO} = 1.31 \approx (n+1)/n$ with $n = 3$, a perfect coincidence occurs every 3 rectangular unit cells of Cu_2O and 4 of ZnO, as schematically depicted in Figure 3.5 f (black arrows indicate the coincidence sites). Looking at the coincidence lattice, the f_o^2 natural misfit of 31 % is significantly reduced to:

$$f_o^2 = (3a_{Cu_2O} - 4a_{ZnO})/4a_{ZnO} = 1.46\% \quad \textbf{(3.1)}$$

As can be seen from Figure 3.5 f there is an extra ZnO plane for each unit cell of the coincidence lattice. The formation of a geometrical misfit dislocation at the interface relieves the lattice misfit strain, allowing lattice fitting and hetero-epitaxial growth [130,185].

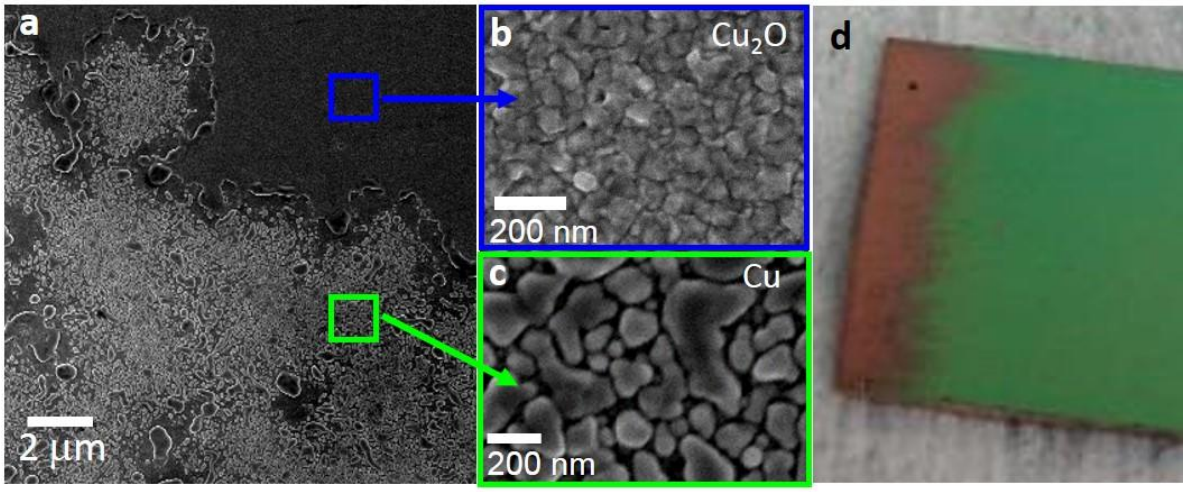

Figure 3.6. Top-view SEM micrographs of the sample composed of a mixture between Cu and Cu_2O (a). Amplified micrograph at the Cu_2O (b) and Cu (c) regions. Picture of the sample, where the interface between the Cu (orange) and the Cu_2O (green) can be observed (d).

Finally, the diffractogram of the sample composed of a mixture of Cu_2O and Cu is presented in Figure 3.3 a (red line). The microstructure is confirmed by the presence of several peaks associated with (111) planes of Cu and (110) and (220) planes of Cu_2O. Figure 3.6 a shows a top-view SEM micrograph of this sample. Two different morphologies are identified, one associated with Cu_2O (Figure 3.6 b) and the other with metallic Cu (Figure 3.6 c), in agreement with obtained X-ray diffractograms. A picture of this sample is shown in Figure 3.6 d. It can be observed with naked eye a clear difference between both regions, Cu presenting an orange-metallic color and Cu_2O a green coloration.

It is worth mentioning that all these samples were grown simultaneously; hence, the deposition conditions were exactly the same for all of them, except the nature of the substrate used. Hence, the phase change is driven by the nature of the substrates used. On highly-conductive ZnO or AZO substrates ($\sigma > 10$ S/cm), Cu films are obtained, while on substrates

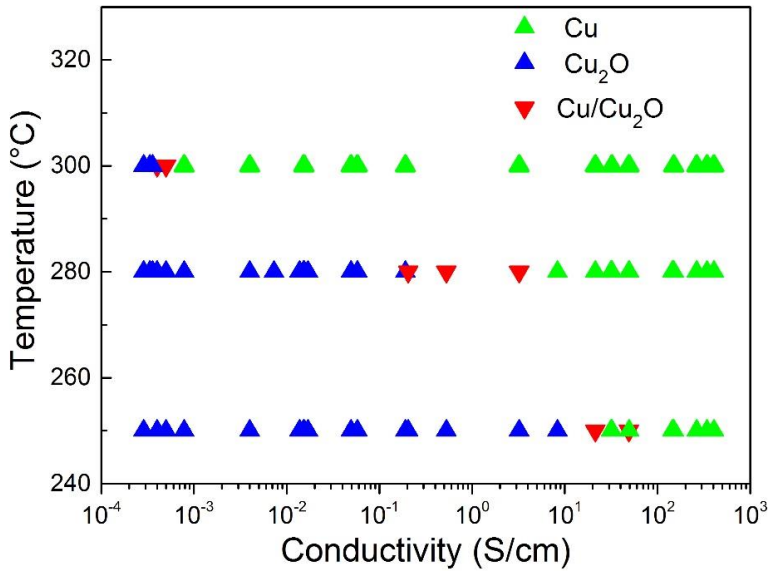

Figure 3.7. Diagram of the different phases deposited (Cu, Cu_2O or mixture) depending on the temperature and the substrate conductivity.

with lower conductivity values ($\sigma < 10^{-2}$ S/cm), Cu_2O is obtained, and for intermediate values, a mixture of both phases is obtained. Additionally, on highly-resistive ZnO substrates ($\sigma << 10^{-4}$ S/cm), neither Cu nor Cu_2O deposition was observed. Therefore, it is possible to tune the deposited material or avoid deposition by simply changing the substrate conductivity.

The same study was repeated at 250 and 300 °C in order to analyze the influence of the growth temperature on the deposition process. Figure 3.7 summarizes all the results; the different phases obtained are plotted as a function of the ALD reaction chamber temperature and the substrate conductivity. No distinction was made between ZnO and AZO substrates; they were simply arranged in the figure depending on their electronic conductivity. For all the temperatures studied, Cu, Cu_2O, and a mixture of Cu and Cu_2O could be obtained. However, the range of conductivity at which those phases appear is shifted depending on the substrate temperature. Higher temperatures favor the reduction of Cu into the precursor from Cu^{2+} to metallic Cu^0. This is the reason why at 300 °C, the window for deposition of Cu_2O becomes smaller, and metallic Cu is obtained even for $\sigma < 10^{-2}$ S/cm. In contrast, at low temperature, the reduction of Cu^{2+} into Cu^{1+} to form Cu_2O is extended to more conductive substrates.

3.3 Temperature-driven Selective Deposition of Cu and Cu_2O on α-Al_2O_3

Cu_2O and Cu thin film were also deposited on (001) α-Al_2O_3 substrates. The growth conditions were the same as those used for the deposition on ZnO and AZO substrates, except for the temperature that was varied in a wider range, from 210 to 350 °C. Figure 3.8 shows the X-ray diffractograms of Cu_2O and Cu films obtained at different temperatures and at 5000 ALD

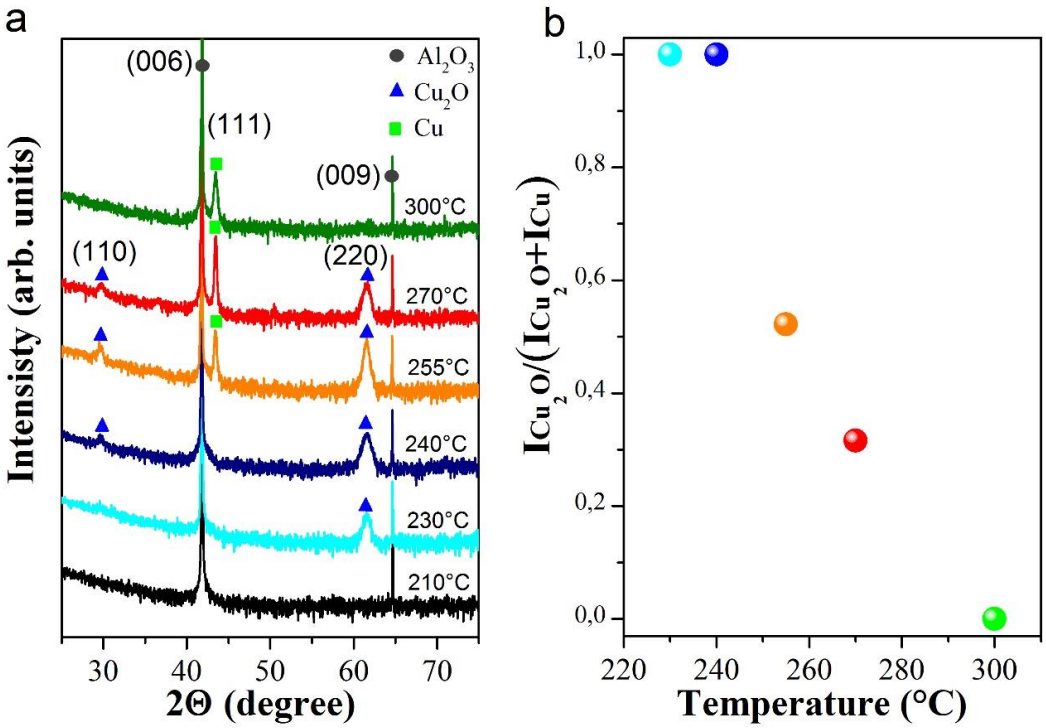

Figure 3.8. X-ray diffractograms Cu_2O and Cu films on sapphire substrates, showing the temperature-dependent selectivity (a). Evolution of the Cu and Cu_2O XRD intensity with deposition temperature (b).

cycles. As can be seen, at lower temperatures (below 250 °C) Cu_2O is formed, for temperatures between 255 °C and 300 °C a mixture of Cu/Cu_2O was obtained, and above 300 °C only metallic Cu was deposited. This evolution from Cu_2O to Cu can be better appreciated in Figure 3.8 were the relation of intensity between the (220) Cu_2O peak and the (111) Cu peak is represented as the ratio $I_{Cu_2O}/(I_{Cu} + I_{Cu_2O})$ vs. substrate temperature, where I_{Cu_2O} and I_{Cu} are the XRD intensities of the (220) Cu_2O and the (111) Cu planes, respectively. A ratio equal to one, which corresponds with the deposition of single phase Cu_2O was obtained for low temperatures, between 230 and 250 °C. For temperatures above 250 °C the ratio decreases monotonously until it reaches zero at 300 °C, where single phase metallic Cu is formed. This temperature-dependent deposition process was observed in the deposition on ZnO and AZO substrates. However, in that case we had the influence of the substrate conductivity, that is not changing in the case of sapphire. These results suggest that the activation energy of the reactions involved in the ALD deposition of metallic Cu are higher than those involved in the Cu_2O formation.

The Cu_2O films are textured with the (110) crystallographic planes parallel to the (001) α-Al_2O_3, since only the (110) and (220) peaks are observed in the diffractograms. The Cu_2O films deposited on ZnO substrates, showed also a (110) texture, and a local epitaxial relationship was already demonstrated. Since the α-Al_2O_3 substrates are monocrystalline we could expect the

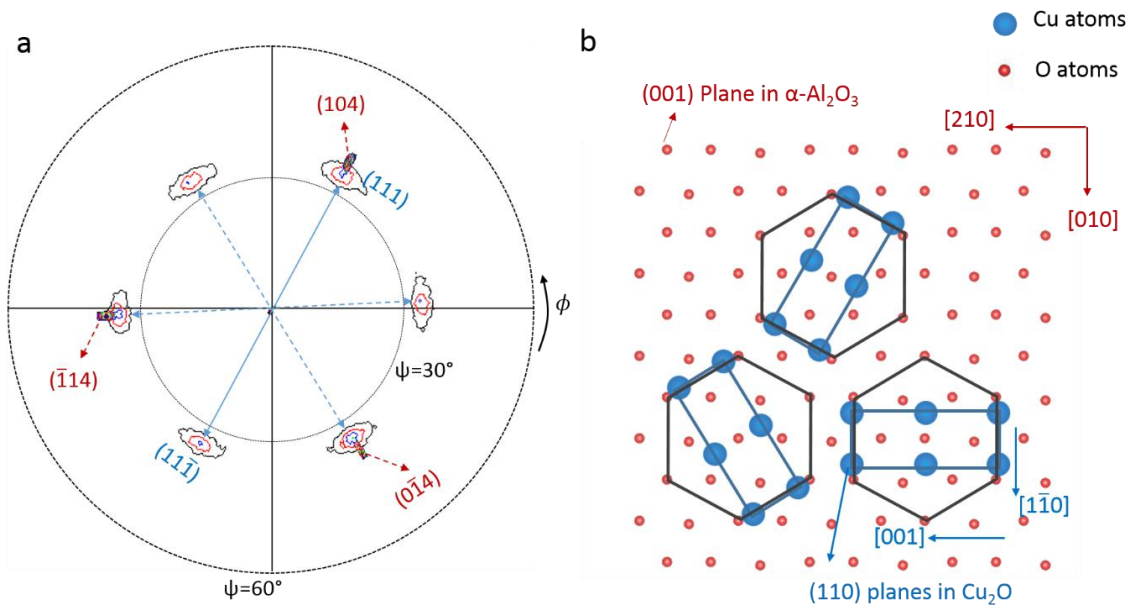

Figure 3.9. Pole figure of a Cu_2O film deposited on α-Al_2O_3 at 2θ=36.42°, the {111} and {104} family of planes for Cu_2O and α-Al_2O_3, respectively, are indicated (a). Schematic of the epitaxial relationship between the Cu_2O films and the α-Al_2O_3 substrate, the different configuration, associated with the three Cu_2O domains are indicated (b).

epitaxial growth of the Cu_2O film. In order to verify the later, pole figures where performed to the Cu_2O film deposited at 240°C. The pole figures were performed at 2θ = 36.42 °, which corresponds to the {111} crystallographic planes of Cu_2O (see Figure 3.9). Six symmetric peaks can be observed at ψ = 34.7 °, separated by an angle of 60°. The ψ angle at which these peaks appear is very close to the angle between the (110) and (111) crystallographic planes in Cu_2O (35.26°), which is in agreement with the texture of the films with the [110] direction perpendicular to the sample surface. The presence of six peaks would indicate a six-fold symmetry that is surprising since Cu_2O has a cubic crystal structure, and the [110] direction is a 2-fold rotational symmetry axis. The presence of six peaks is probably related with the existence of 3 different Cu_2O domains in the film, as will be discussed later.

In addition to the Cu_2O peaks other three peaks are observed at ψ = 37.3 °. These peaks are considerably narrower than those of Cu_2O, and correspond to the (104), ($\bar{1}$14), and (0$\bar{1}$4) planes of α-Al_2O_3. It is possible to observe this family of planes, since they appear at 2θ = 35.16°, closer to angle 2θ at which the {111} crystallographic planes of Cu_2O are located. The ψ angle at which these planes are located is closer to the angle between the (001) and (104) crystallographic planes of α-Al_2O_3 (38.24 °), in agreement with c-axis orientation of the α-Al_2O_3 substrates.

The superposition of both family of planes in the pole figure allows the determination of the in-plane epitaxial relationship between the Cu_2O film and the α-Al_2O_3 substrate. Three of the Cu_2O peaks share the same azimuth with the three peaks of α-Al_2O_3, which means that the (111) planes in Cu_2O grow along the same direction that the (104) planes of α-Al_2O_3 Furthermore, the (104), ($\bar{1}$14), and (0$\bar{1}$4) planes of α-Al_2O_3 share the same azimuth with the (100), ($\bar{1}$10), and (0$\bar{1}$0) planes, respectively, which form an angle of 90° with the (001) planes of α-Al_2O_3. Analogously, the (111) and (11$\bar{1}$) planes of Cu_2O share the same azimuth with the (002), and (00$\bar{2}$) planes, respectively, which form an angle of 90° with the (110) surface plane of Cu_2O. Hence, the Cu_2O film is oriented with the [001] direction along the [210], [$\bar{1}$10] and [$\bar{1}\bar{2}$0] of α-Al_2O_3, giving place to the three different Cu_2O domains represented in Figure 3.9 b. The rectangular unit cell formed by the Cu atoms at the (110) planes in Cu_2O (blue rectangle) can be oriented in the hexagonal unit cell defined by the oxygen atoms at the (001) planes of α-Al_2O_3 (black hexagon) in three different directions: [210], [$\bar{1}$10], and [$\bar{1}\bar{2}$0], rotated by 60° from each other, which explains the apparent six-fold rotational symmetry observed in Figure 3.9 a. Overall, the pole figure demonstrates the epitaxial growth of Cu_2O film on α-Al_2O_3 substrates, with [110] Cu_2O || [001] α-Al_2O_3, out of plane, and [001] Cu_2O || [210] α-Al_2O_3, in-plane.

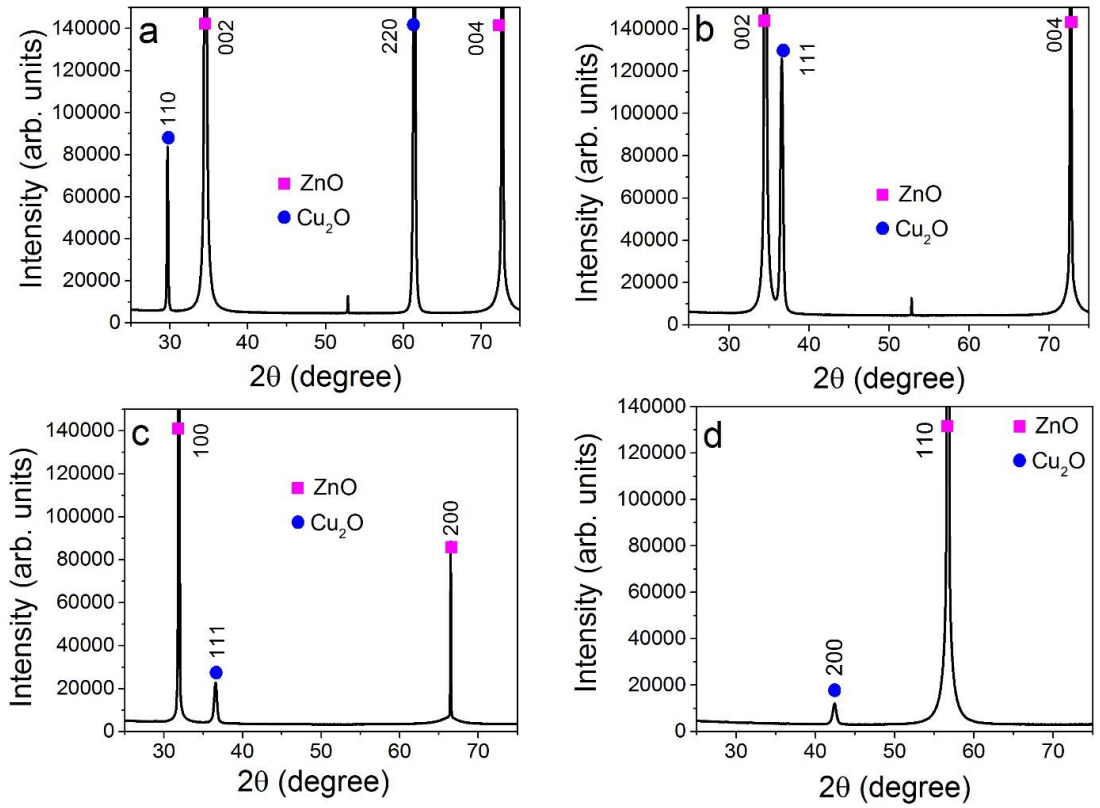

Figure 3.10. X-ray diffractograms of the Cu_2O films deposited on c-plane oriented O-terminated ZnO (a), c-plane oriented Zn-terminated ZnO (b), a-plane ZnO (c), and m-plane ZnO (d) substrates.

3.4 Cu_2O Deposition on Monocrystalline ZnO Substrates

So far, Cu_2O films deposited on c-axis-oriented polycrystalline ZnO, and (001)-oriented monocrystalline α-Al_2O_3, have always shown a [110] texture. To analyze the influence of substrate orientation, Cu_2O films were deposited on four different monocrystalline substrates: the polar (001) O - terminated (a) and Zn - terminated ZnO (b) surfaces, and the non-polar (100) (c), and (110) ZnO surfaces (d), using the same conditions that for the deposition on polycrystalline ZnO substrates (280 °C, 10000 cycles).

Figure 3.10 shows the X-ray diffractograms of the samples. It is worth to note that all the samples were grown at the same time. Nevertheless, the Cu_2O films show different texture depending on the crystallographic orientation of the ZnO substrates. Moreover, the films grown on the (001) ZnO surfaces, showed different texture depending on whether the ZnO surface was terminated by oxygen or zinc planes (Figure 3.10 a – d). It is worth to note that the small peak observed at 52.8° in the diffractograms of the (001)-oriented monocrystalline ZnO substrates (Figure 3.10 a, b) corresponds to the ZnO 003-forbidden reflection, that is observed due to multiple diffraction (*Umweganregung*) [186].

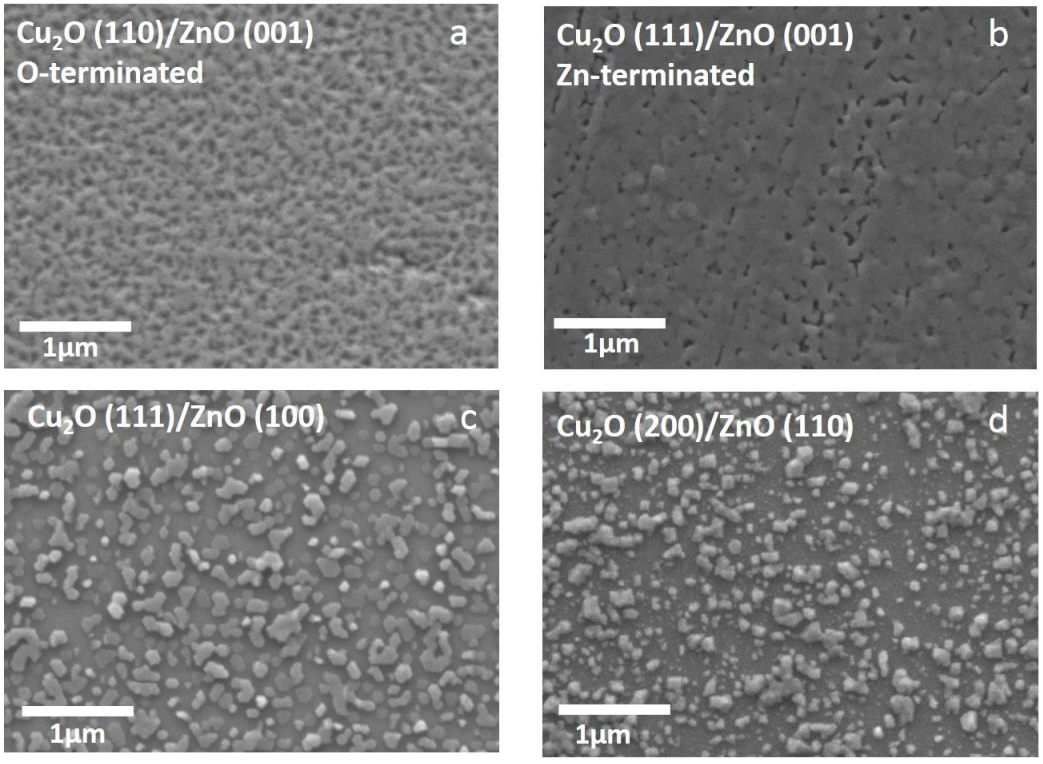

Figure 3.11. Top-view SEM micrographs of the Cu_2O films deposited on the c-plane O-terminated (a) and Zn-terminated (b) ZnO polar substrates, and the a-plane (c) and m-plane (d) ZnO non-polar substrates.

Figure 3.11 a – d shows top-view SEM micrographs of the Cu2O films on the different ZnO substrates. The morphology of the films changes from one substrate to another. Moreover, the surface coverage was considerably lower for the films deposited on the non-polar ZnO surfaces, where isolated Cu2O crystals are observed instead of the continuous films obtained on the polar surfaces.

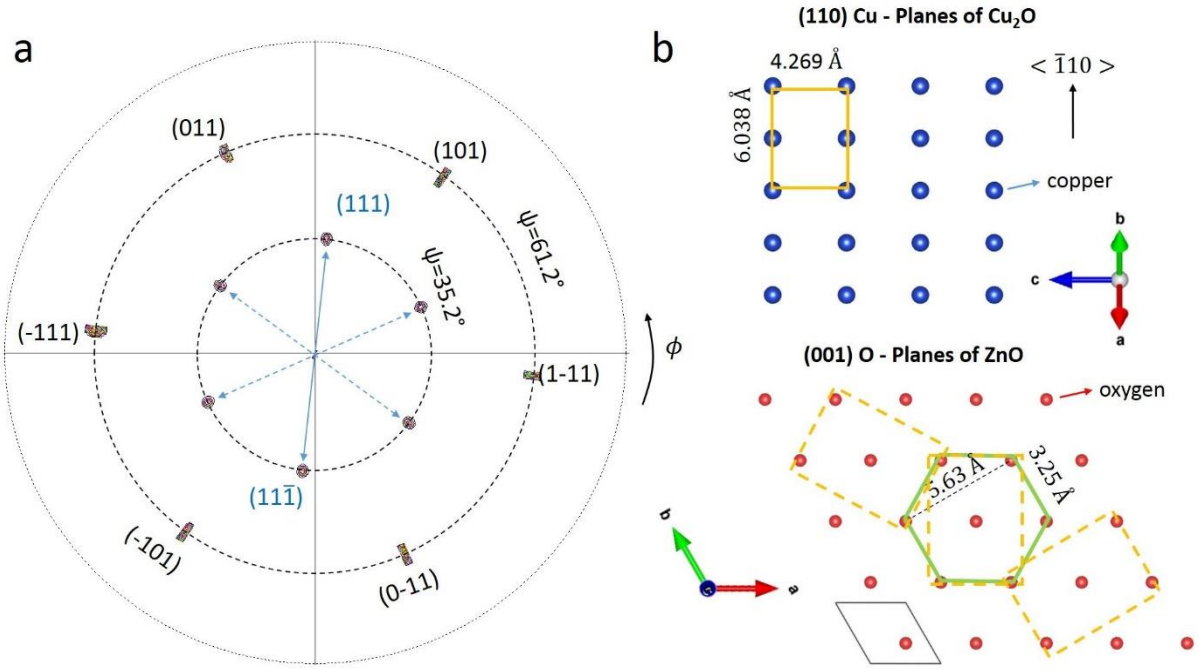

Figure 3.12. Pole figure of the Cu_2O film deposited on ZnO at 2θ=36.42°, the {111} and {101} family of planes for Cu_2O and ZnO, respectively, are observed (a). Schematic of the Cu atoms at the (110) planes of Cu_2O (top), and the oxygen atoms at the (001) planes of ZnO (bottom). The different configuration in which the Cu_2O domains can grow on top of the ZnO substrate (b).

3.4.1 ZnO Polar Surfaces

On the (001)-O-terminated ZnO substrates, the Cu_2O film grows with the [110] direction aligned with the [001] direction of ZnO (see Figure 3.10 a). A pole figure was performed to this sample in order to determine the in-plane orientation relationship. The pole figure was done at 2θ=36.42°, in order to observe the {111} crystallographic planes of Cu_2O. Six peaks appear at $\psi = 35.2\,°$, which correspond very well with the angle between the (111) and the (110) planes of Cu_2O, in agreement with the (110) orientation of the films. The presence of six peaks instead of the two that should be expected due to the symmetry of the [110] axis, can be explained by the existence of 3 domains rotated by 60°, identical to the deposition on α-Al_2O_3 substrates. Six other peaks appear at $\psi = 61.4\,°$, that correspond to the {101} family of planes of ZnO. It is possible to observe these peaks since they appear at 2θ=36.25°, very close to the {111} family

in Cu_2O. Furthermore, the $\psi = 61°$ at which they are located is the same angle formed between the {101} and the {001} planes in ZnO, in agreement with the c-axis orientation of the ZnO substrate. The angle ϕ between the (111) planes in Cu_2O and the (101) in ZnO is 30°. This corresponds to an in-plane orientation where the [001] direction in Cu_2O is aligned with the [100], [010], or [110] in ZnO, giving place to the three different domains shown in Figure 3.12 b, which explains the apparent six fold symmetry.

It is worth to note that the epitaxial relation observed for this sample is in agreement with the one obtained on the c-axis oriented ZnO polycrystalline substrates. In that case we obtained (110) Cu_2O|| (001) ZnO, and [001] Cu_2O || ZnO [010], which is the same orientation that one of the 3 domains observed here. The (111) planes in Cu_2O have the most suitable lattice coherence with the (001) planes in ZnO (lattice misfit strain ~7 %). However, as has been shown previously on the polycrystalline ZnO substrates, the [110] orientation can be favored due to domain matching epitaxy, that reduces considerably the lattice misfit strain to 1.4 %.

For the (001)-Zn-terminated ZnO substrates the Cu_2O film shows a different texture, with the [111] direction along the [001] direction in ZnO (Figure 3.10 b). This result can be understood by looking at the possible surface terminations of the (110) and (111) crystallographic planes in Cu_2O. The Cu_2O (111) planes are terminated either by Cu or O atoms,

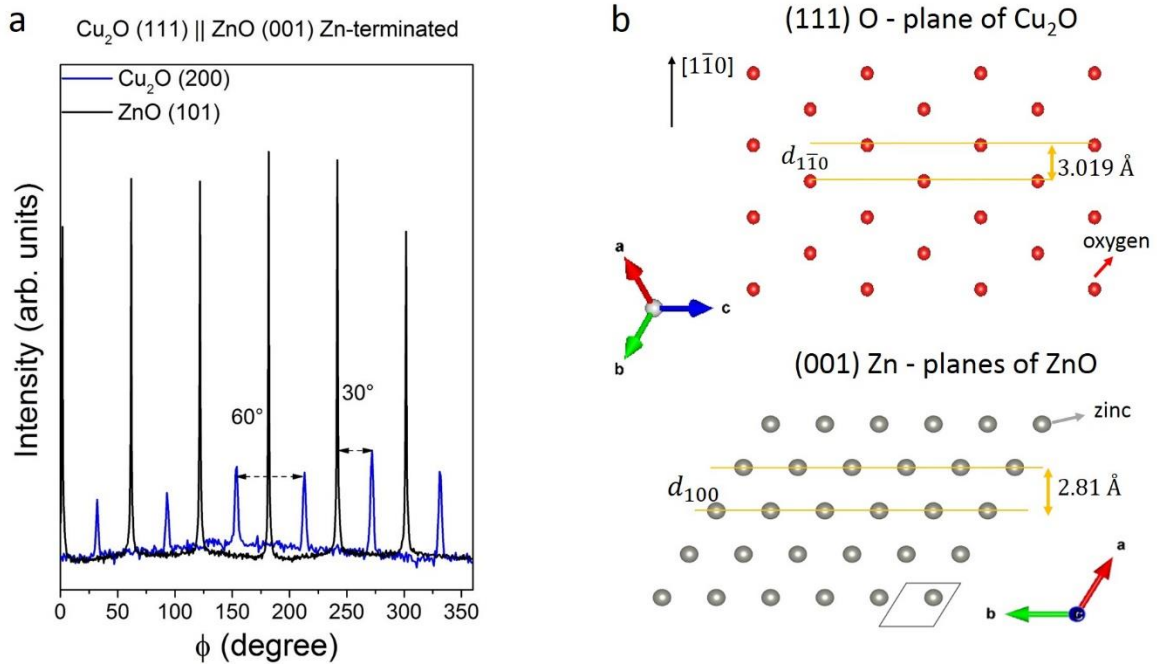

Figure 3.13. ϕ-scan of the Cu_2O (200) and the ZnO (101) crystallographic planes of the Cu_2O-(111)/ZnO-(001)-Zn terminated sample, in logarithmic scale (a). Schematic of the oxygen atoms at the (111) planes of Cu_2O (top) and the zinc atoms at the (001) plane in ZnO (bottom) (b).

meanwhile the Cu_2O (110) planes are formed by Cu atoms, or by a mixture of Cu + O atoms. The Zn atoms that form the polar [001] surface in the ZnO substrates may prefer to bond with oxygen atoms when the first monolayer of Cu_2O is growing, leading to the polar [111] orientation in Cu_2O, instead of the [110] orientation observed on O-terminated surfaces. XRD ϕ-scans of the (200) and (101) planes of Cu_2O and ZnO, respectively were performed (see Figure 3.13 a). Six peaks separated by 60° are observed for the (101) planes of ZnO (black line), as expected due to the six-fold symmetry of the [001] axis in ZnO. Six peaks of Cu_2O (blue line), are also observed, however the [111] direction is a three-fold symmetry axis. The existence of six peaks has already been observed for (111)-oriented Cu_2O films, deposited by sputtering on ZnO, due to epitaxial twinning, which means that the Cu_2O film grows in two domains rotated by 180° from the [111] common axis [183,187] (HR-TEM micrographs need to be performed to this sample in the future to confirm the later).

To summarize, the epitaxial relation for this sample is (111) Cu_2O || (001) ZnO, out of plane, and two different orientations are obtained in-plane: $(1\bar{1}0)$ Cu_2O || (100) ZnO, and $(\bar{1}10)$ Cu_2O || (100) ZnO. The epitaxial growth occurs thanks to the favorable periodic lattice coincidence between both materials at these planes, as is shown in Figure 3.13 b.

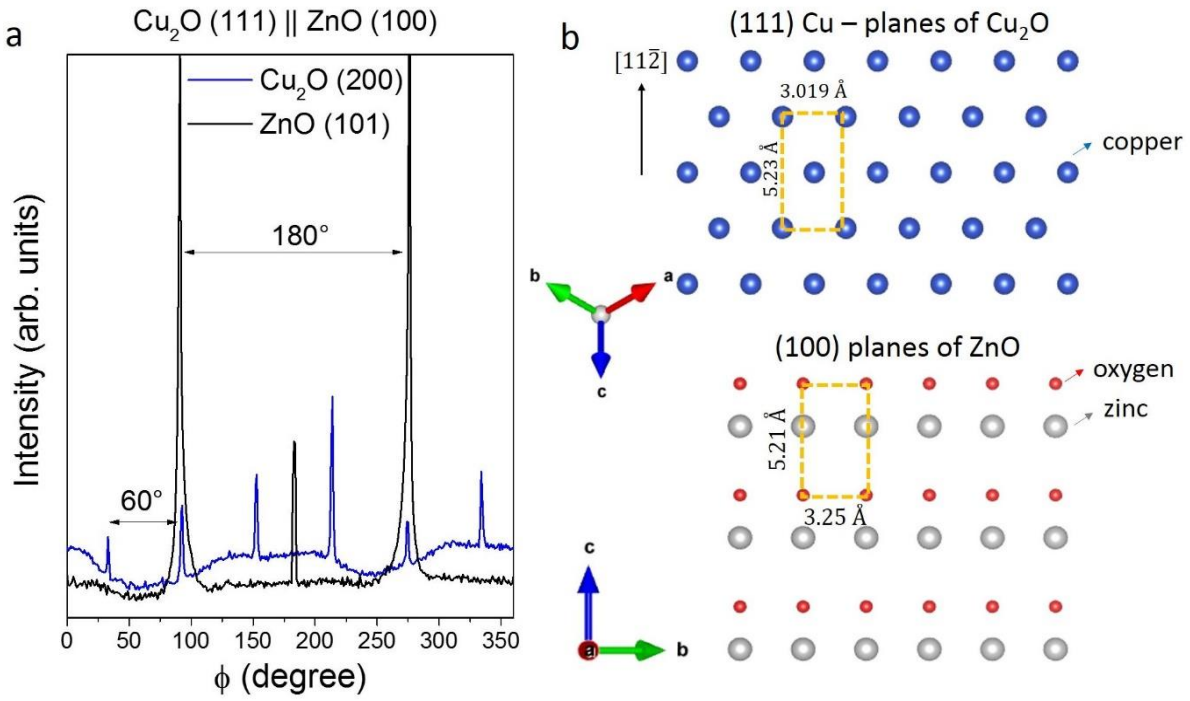

Figure 3.14. ϕ-scan of the Cu_2O (200) and the ZnO (101) crystallographic planes of the Cu_2O-(111)/ZnO-(100) sample, in logarithmic scale (a). Schematic of the Cu atoms at the (111) planes of Cu_2O (top) and the Zn atoms at the (100) plane in ZnO (bottom) (b).

3.4.1 ZnO Non-Polar Surfaces

Contrary to the deposition on c-plane polar ZnO substrates, were continuous films were obtained, on the a-plane and m-plane ZnO substrates, the film grows as isolated crystals as can be seen in Figure 3.11 c, d.

The Cu_2O film deposited on the (100) - ZnO substrates shows also the [111] texture (see Figure 3.10). As can be seen in Figure 3.11 c, Cu_2O crystals of different shapes (hexagons, trapezoids, and polyhedrons in general) and lateral sizes ranging from 30 to 350 nm are formed. XRD ϕ-scan of the (200) and (101) planes of Cu_2O and ZnO, respectively are depicted in Figure 3.14 a. Two peaks separated by 180° are observed, associated to the (101) planes of ZnO (black line), according to the two-fold symmetry of the [210] axis. There is an very small peak at ϕ =183°, that can be observed in Figure 3.14 because we used logarithmic scale. This peak was also observed in the measurement performed to the pristine ZnO substrate, and is probably related with an imperfection of the substrate. For Cu_2O (blue line) six peaks rotated by 60° are observed, which indicate that the Cu_2O crystal are not randomly oriented in-plane. The presence of six peaks instead of the three expected peaks is probably due to the existence of twin's domains as for the Cu_2O (111)/ZnO (001) sample.

Therefore, the orientation relationship for this sample is Cu_2O (111)/ZnO (100), out of plane; $(11\bar{2})$ Cu_2O || (001) ZnO, and $(\bar{1}\bar{1}2)$ Cu_2O || (001) ZnO in-plane. In Figure 3.14 b is shown a schematic of the atomic arrangement at the (111) Cu_2O (top) and (100) ZnO planes (bottom), showing that there is a favorable periodic lattice coincidence between both materials at this planes, and it is the reason why all the Cu_2O crystals (Figure 3.11) grow following the same orientation.

Finally, the Cu_2O film deposited on the (110) - ZnO substrates shows the [100] texture. XRD ϕ-scans of the (111) Cu_2O planes were noisy and extra peaks appeared, probably related with the fact that the Cu_2O grains are randomly oriented in-plane. The [100] texture of the Cu_2O grains, is probably related with the film trying to replicate the substrate, since the [110] axis in ZnO is a four-fold symmetry axis, equal to the [100] axis in Cu_2O.

Overall, these results indicate that the surface chemistry and structure of the underlying substrate strongly impact the growth of the Cu_2O films. A summary of these results is presented in Table 3.1. Cu_2O films easily grow on the c-axis-oriented polar surfaces of ZnO because, in this case, a continuous film was formed compared with the non-polar surfaces, were a lower surface coverage was observed and the film was not continuous but in form of isolated crystals. For the Cu_2O film deposited on polycrystalline c-axis-oriented ZnO substrates, the [110] Cu_2O

Table 3.1. Epitaxial relationship between the Cu_2O and the monocrystalline ZnO substrates.

Substrate	Cu_2O-orientation	Lattice mismatch	
		f_0^1	f_0^2
(001) - ZnO O- terminated	Out-of-plane: (110) || (001) In-plane: [100] Cu_2O || [100], [010], [110] ZnO.	7.3 %	31% →1.5% DME
(001) - ZnO Zn- terminated	Out-of-plane: (111) || (001) In-plane: $(1\bar{1}0)$ and $(\bar{1}10)$ Cu_2O || (100) ZnO	7.4 %	7.4 %
(100) - ZnO	Out-of-plane: (111) || (100) In-plane: $(11\bar{2})$ and $(\bar{1}\bar{1}2)$ Cu_2O || (001) ZnO	0.4 %	7.1 %
(110) - ZnO	Out-of-plane: (100) || (110) In-plane: random	-	-

f_0^1 and f_0^2 are the in-plane directions in which the lattice mismatch is calculated.

DME: domain matching epitaxy.

|| [001] ZnO orientation was always observed, suggesting that the ZnO films obtained by reactive sputtering under the conditions used in this thesis were oxygen-terminated.

3.5 Mechanism for the Area-Selective ALD of Cu_2O and Cu

Several studies have reported the chemical vapor deposition of metallic Cu using $Cu(hfac)_2$ as the Cu precursor. However, few reports concern atomic layer deposition of metallic Cu and even less concern Cu_2O deposition, using this precursor. In ALD, the precursors are pulsed separately, and therefore, the reactions taking place should be different from those in CVD, where precursors are injected simultaneously. The study of Cohen *et al.* concerning the mechanism of copper chemical vapor deposition evidenced that $Cu(hfac)_2$ dissociates on Ag substrates, as Cu(I)-hfac and hfac [174]. According to this study, H_2 or alcohol is required to serve as the proton source to allow the hfac ligand removal and Cu deposition. Lecohier *et al.* also studied the mechanism of Cu deposition using $Cu(hfac)_2$ and water in the presence of He or H_2 carrier gases [131]. Their results suggest that H_2 is not indispensable as a reducing agent, since they were able to obtain clean metallic Cu films when He was used instead of H_2. A different mechanism was proposed by Awaya and Arita, who suggested that $Cu(hfac)_2$ in the presence of water, when adsorbed on the substrate, dissociates in Hhfac and CuO, which is

further reduced by H_2 to metallic Cu [132]. Our results dismiss the idea of the formation of an intermediate oxide (CuO) further reduced into metallic Cu, since we do not use any reducing agent after the water pulse, and nevertheless, metallic Cu films are obtained. Moreover, XPS measurement does not indicate the presence of Cu^{2+}, neither in the case of metallic Cu nor for Cu_2O films. The survey spectra in Figure 3.15 a were obtained for Cu (green) and Cu_2O (blue) films grown by ALD at 280 °C for 5000 cycles on ZnO substrates of different conductivities. The spectra were performed after 2 min of Ar etching at 5 keV to eliminate the contamination at the surface of the films. Both spectra confirm the good quality of the films since neither C nor F contamination was detected. This means that there was no undesired decomposition of the $Cu(hfac)_2$ during the ALD deposition. Cu 2p spectra presented in Figure 3.15 b are the typical ones observed for Cu_2O and Cu [188]. Even if it is not possible to differentiate between Cu and Cu_2O from the Cu 2p spectra, the presence of CuO is ruled out in both cases.

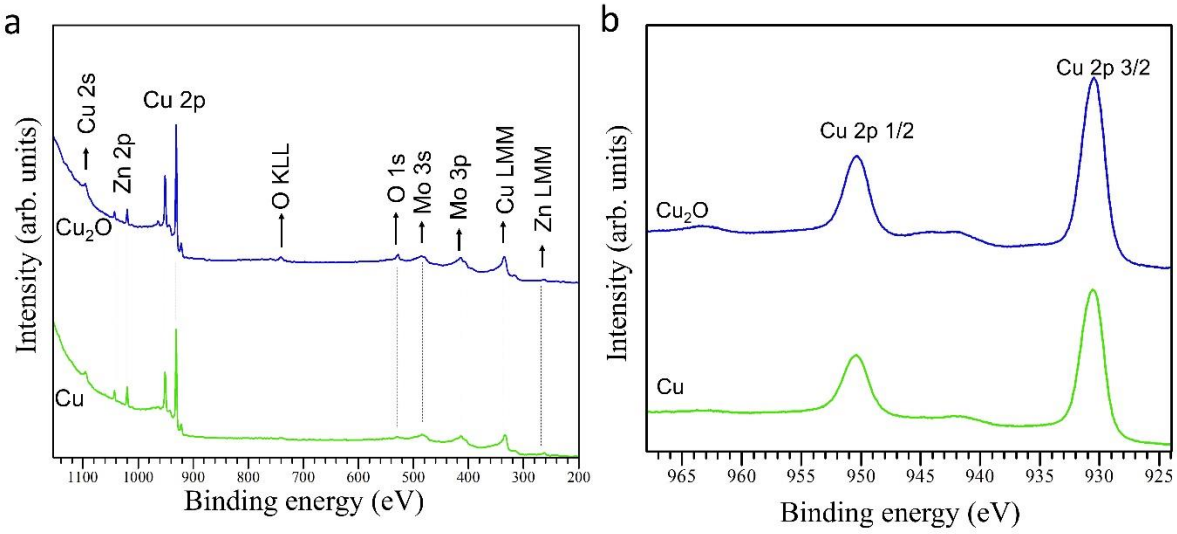

Figure 3.15. XPS survey scan (a) and Cu 2p spectra (b) for a Cu_2O (blue) and a Cu (green) film.

The results presented above indicate undoubtedly a correlation between conductivity and area-selective deposition. However, the possibility of achieving a temperature-selectivity process on non-conductive α-Al_2O_3 substrates suggests that the selectivity observed on ZnO and AZO films is correlated but probably not directly related to the level of conductivity. It is more likely related with local chemistry and/or structure that, in turn, influence the conductivity. Photoluminescence (PL) measurements were performed on the ZnO substrates obtained at different P_{O_2} (Figure 3.16 a) to identify emitting defects present in the films. The peak at 380 nm is attributed to the near band edge emission of ZnO. The broad band that appears between 450 and 750 nm can be deconvoluted (from multiple-peak Gaussian fitting) into three bands: P1, P2, and P3 around 528 nm (green band), 564 nm (yellow band), and 660 nm (red band),

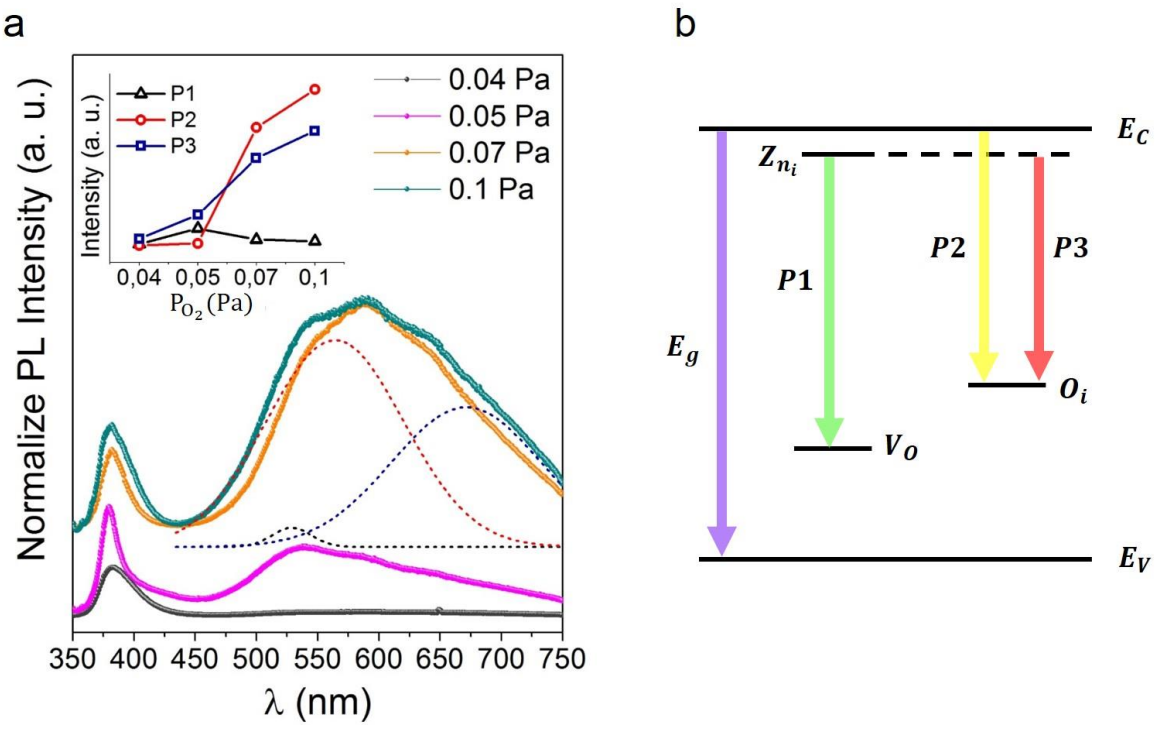

Figure 3.16. Normalized photoluminescence spectra of ZnO films deposited at different P_{O_2}, the evolution of the areal intensity of the defect bands with the oxygen partial pressure is presented at the inset (a). Energy level diagram illustrating the defect levels in ZnO and the transition observed in the photoluminescence spectra (b).

respectively. The P1 band has been ascribed to transitions between an Zn interstitial (Zn_i) shallow level and oxygen vacancy (V_O) level, the P2 band is associated with a transition between the conduction band and an oxygen interstitial (O_i) level, and the P3 band has been ascribed to a transition from the Zn_i level to the O_i level [189]. A schematic illustrating the different defects levels in ZnO and the transitions (P1, P2, and P3) observed in the PL spectra is depicted in Figure 3.16 b.

The evolution of the areal intensity of this three bands as a function of the P_{O_2} is shown at the inset of Figure 3.16 a. As can be seen, P1 decreases as P_{O_2} increases as a result of the decrease of V_O in more oxidative conditions. On the contrary, the P2 and P3 bands increase with P_{O_2}, since the generation of O_i defects occur in more oxidative conditions. It is worth noting that the remarkable difference between the signatures of the ZnO sample deposited at P_{O_2} of 0.05 and 0.07 Pa resulting from the evolution of the densities of the different point defects (higher density of Zn_i and V_O for deposition at 0.05 Pa and higher density of O_i defects for deposition at 0.07 Pa). In another study, this evolution in the PL signal with P_{O_2} was related to small, yet monotonous, changes in the oxygen content in the ZnO films [65]. V_O and Zn_i are

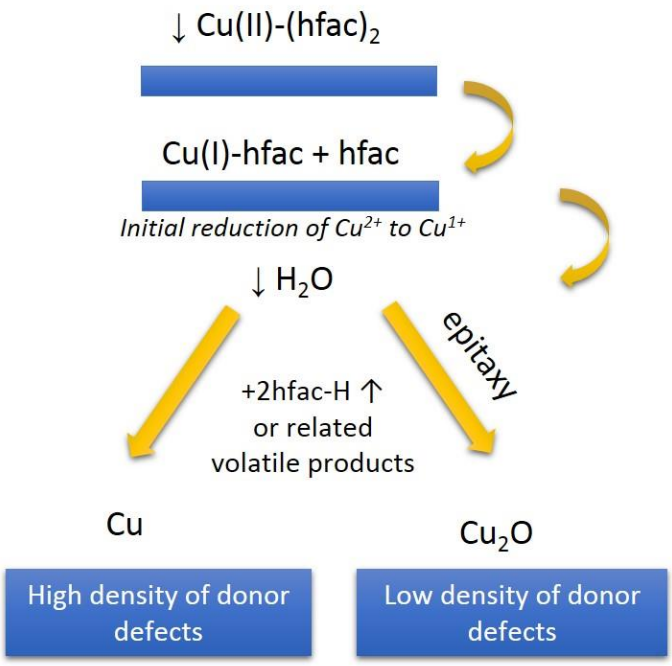

Figure 3.17. Schema illustrating the mechanism behind the selective deposition of Cu and Cu_2O.

considered as donor defects impacting the final n-type conductivity of the ZnO films. Furthermore, these donor defects can act as reducing agents for the $Cu(hfac)_2$ precursor, inducing the selectivity of Cu vs. Cu_2O. V_O defects, for example, are known as active catalytic sites and electronically active centers [190,191], that could play an important role in the $Cu(hfac)_2$ reduction.

We consider that the mechanism for $Cu(hfac)_2$ adsorption at the first ALD step is the same as proposed by Cohen *et al.* on Ag substrates: $Cu(hfac)_2$ is adsorbed as a Cu(I)-hfac intermediate and hfac. This first reduction of the precursor to Cu^{1+} is possibly due to the conductivity/density of donor defects (V_O and Zn_i) in the ZnO substrates, as shown in ecuation (3.1).

$$Cu^{+2} + Zn_i{}^{0} \Rightarrow Cu^{+1} + Zn_i{}^{+1} \quad \textbf{(3.1)}$$

In equation (3.1) we assums that Zn_i are the defects involved in the precursor reduction rather that V_O. Even if V_O defects have a low formation energy they are deep donors in ZnO, and therefore are less likely involved in the reduction of the $Cu(hfac)_2$ precursor. On the contrary, Zn_i is a shallow donor, that stabilizes in the +2 charge state (Zn_i^{2+}), donating two electrons into the conduction band, that can effectively help to the precursor reduction process.

When the conductivity of ZnO and density of donor defects are high enough, Cu^{1+} is further reduced into metallic Cu as follows:

$$Cu^{+1} + Zn_i{}^{+1} \Rightarrow Cu^{0} + Zn_i{}^{+2} \quad \textbf{(3.2)}$$

In this step, water is fundamental as a proton source to form a volatile compound and to remove the hfac ligands from the surface. On the contrary, when a ZnO of low conductivity/low-density-of-donor-defects is used as substrate, and water is pulsed into the chamber, Cu remains as Cu^{1+} to form Cu_2O (see the schematic of Figure 3.17). In the case of Cu_2O formation, the local epitaxial relation between the film and substrate seems to play also an important role in the film growth as will be shown later.

In the case of metallic substrates such as W and Zr films (see Figure 3.18 a, b) only metallic Cu could be obtained regardless of the deposition temperature used. In this case the high conductivity of the substrates favors the reduction of $Cu(hfac)_2$ to form metallic Cu. On the other hand, neither Cu nor Cu_2O has been deposited on glass, fused silica and Si substrates with this precursor. Several tests were performed varying substrates temperature (230 -300 °C), purge and precursor pulse length (1 - 6 s), and N_2 flow rate in the precursor lines, and no deposition was observed. Figure 3.18 c show a top-view SEM micrograph, as an example of the selectivity on a Si substrate. A ZnO patterned film was fabricated on top of the Si substrates by using a mask during the ZnO sputtering deposition. Cu_2O deposition was observed on the region where the ZnO film was deposited and no deposition occurred on the pristine-Si side.

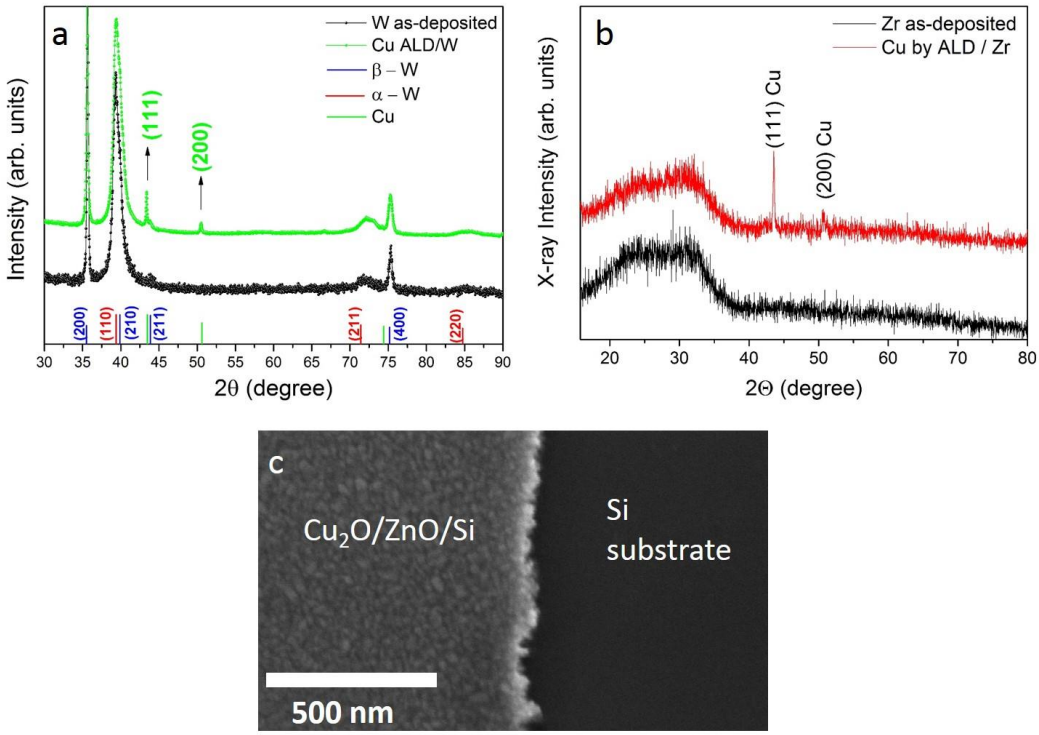

Figure 3.18. X-ray diffractometer of a Cu film deposited by ALD on a 200 nm W film (a) and on a 500 nm Zr film (b). Top view SEM micrograph for a $Cu_2O/ZnO/Si$ sample showing the area-selectivity of Cu_2O on ZnO vs. Si substrates (c).

The inhibition of Cu_2O on these substrates offers opportunities for area-selective deposition, by using for example metallic or ZnO patterns.

3.6 Fabrication of p-Cu_2O/n-ZnO Microjunctions

In order to take advantage of the selectivity of Cu and Cu_2O depending on the nature of the exposed surface, a bilayer system was fabricated, patterned, and functionalized. First, a low-conductive ZnO layer ($\sigma = 4.3 * 10^{-3}\ S/cm$) was deposited on top of a highly-conductive AZO film ($\sigma = 3.1 * 10^{2}\ S/cm$) with thicknesses of 145 and 323 nm, respectively, as is schematically represented in Figure 3.19 a. Then, a pattern was formed by removing some regions of the ZnO top layer, and consequently, part of the AZO underneath layer was exposed, as depicted in Figure 3.19 b. For the patterning of the bilayer structure we use the e-beam lithography and ion beam etching. First, polymethyl methacrylate (PMMA) 5% (ARP672.05) was coated at the surface of the bilayer and was heated at 180° for 5 min. Then, the surface was exposed to the electron beam using 20 kV with doses ranging from 80-160 µC/cm². This step was followed by an immersion of the film into a liquid developer formed by a mixture of Methyl Isobutyl Kethone (MIBK) and isopropyl alcohol (IPA) for 60 s and then the sample was rinsed in IPA solution for 30 s. This process allows to remove the part of the mask exposed to the e-beam. Then, ion beam etching (200 eV Ar ions) was used to etch the unmasked areas down to the AZO layer. Finally, O_2 plasma was used to remove any resist from the surface. Finally, the

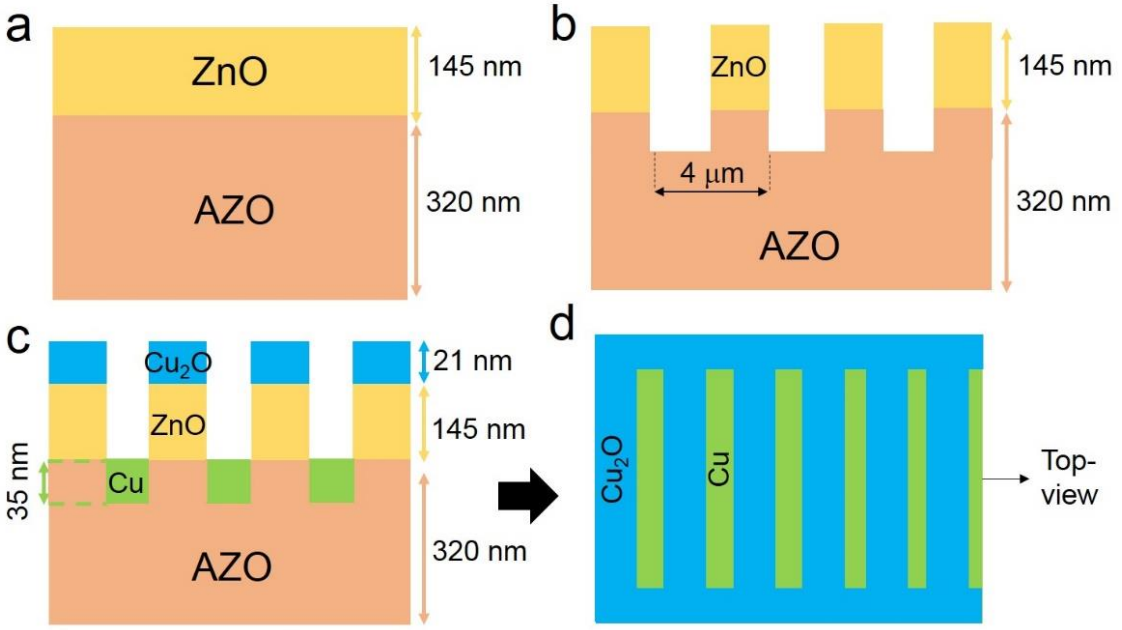

Figure 3.19. Schematic of the bilayer structure (a) as-deposited, (b) after etching, and after ALD deposition in (c) cross-section and (d) top-view.

samples were introduced into the ALD chamber for selective deposition of Cu and Cu_2O during 5000 ALD cycles. A temperature of 280 °C was used in order to obtain Cu_2O in the ZnO regions and metallic Cu in the exposed AZO regions (see Figure 3.19 c, d).

In Figure 3.20 a, a top-view SEM micrograph of the sample taken after ALD deposition illustrates the different morphologies between the material deposited at the bottom of the wells (Cu) and the material deposited on top (Cu_2O). In Figure 3.20 b, an annular dark field scanning transmission electron microscopy (ADF-STEM) micrograph at the well edge is displayed. The

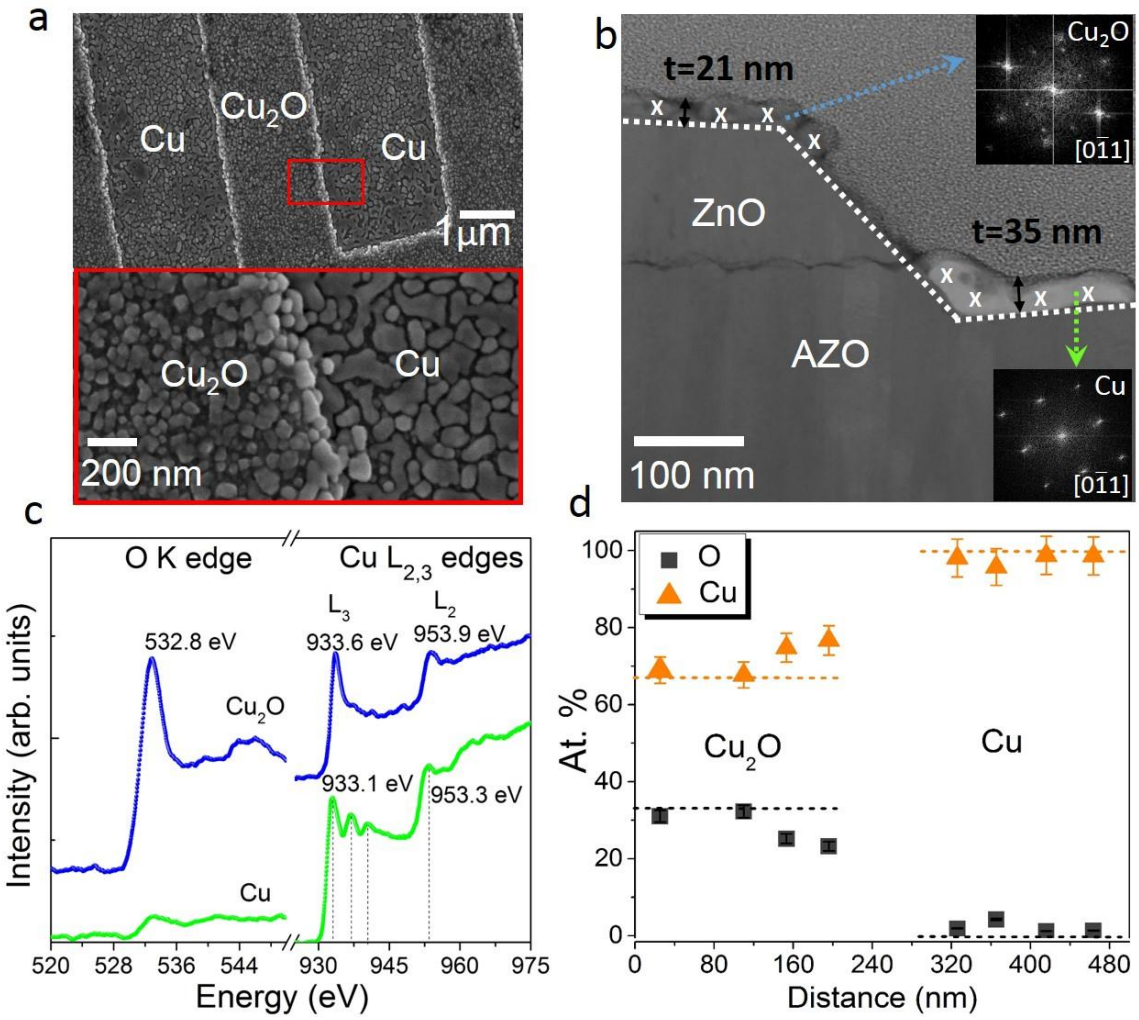

Figure 3.20. Top-view SEM micrograph of the bilayer and magnified micrograph at the Cu_2O/Cu interface highlighted by a red square (a). ADF-STEM micrograph of the bilayer (b) with FFT patterns obtained from HRTEM micrographs in the Cu region (bottom inset) and the Cu_2O region (top inset). EELS spectra at the O K and the Cu $L_{2,3}$ edges at the top (Cu_2O) and bottom (Cu) of the bilayer (c). EDS composition profiles in the regions of the sample indicated by crosses in b (dashed lines indicate the expected Cu and O concentrations for stoichiometric Cu_2O and for metallic Cu) (d).

FFT patterns taken from HRTEM micrographs in the Cu_2O (top inset) and Cu (bottom inset) regions, respectively, demonstrate the growth of metallic Cu on top of AZO and Cu_2O on top of ZnO. Electron energy loss spectroscopy (EELS) in transmission mode was performed in both regions. The energy loss near edge structure (ELNES) spectra at the O K and Cu $L_{2,3}$ edges are shown in Figure 3.20 c. The spectra obtained at the Cu $L_{2,3}$ edges in Cu and Cu_2O are in good agreement with those reported in the literature [192–194].

The Cu_2O ELNES spectrum is characterized by the $L_{2,3}$ white lines at 953.9 and 933.6 eV, respectively. At the Cu region the spectrum is formed by the L_3 line around 933.1 eV, followed by two less intense peaks around 937.1 and 940.4 eV, which have been identified in the literature as the 4p-4d hybridization structure [195]. The L_2 line appears at 953.3 eV, followed by a wide band that rises around 962.6 eV, which has been ascribed to a 4f band with some d character [195]. The features of the spectra and the peak position at the O K edge confirm that pure Cu_2O was deposited on top of ZnO [196]. In the case of Cu, a very small, poorly-defined edge is observed that we ascribe to the presence of some oxidized Cu in the form of CuO at the surface of the Cu film.

Composition profiles at the surface obtained by EDS analysis in STEM mode at the same region where the STEM micrograph was taken further confirm the deposition of Cu_2O on the ZnO layer and Cu on the AZO film (see Figure 3.20 d). The film deposited on top of ZnO contains 32 at. % O and 68 at. % Cu, very close to the stoichiometry of Cu_2O, even if slightly different values of 28 at. % O and 72 at. % Cu, are obtained close to the well edge. On the other hand, on top of the AZO films, values around 99% for the Cu and 1% for the O were obtained, confirming the deposition of metallic Cu in this region. The detection of some oxygen even in a minor quantity could be related to the presence of some CuO formed at the surface of the Cu film.

It is worth mentioning that the Cu layer stops exactly at the interface with the low-conductive ZnO film, as can be seen in Figure 3.20 b. In the case of the Cu_2O, deposition is somehow inhibited in the lateral walls of the ZnO films; with deposition on the corner. Noticeably, there is no Cu_2O deposition along the rest of the lateral wall. This result indicates that the local epitaxial relationship between Cu_2O films on ZnO substrates plays an important role in Cu_2O formation. Indeed, Cu_2O more easily grows epitaxially on (001) ZnO with [001] Cu_2O || [010] ZnO, and [110] Cu_2O || [001] ZnO films. We have shown in section 3.4 that the orientation relationship between the Cu_2O and the substrates, is an important parameter influencing the Cu_2O deposition. Since the ZnO film presents a different orientation at the lateral walls, Cu_2O deposition is blocked at the edge of the ZnO plateau, in contrast with the

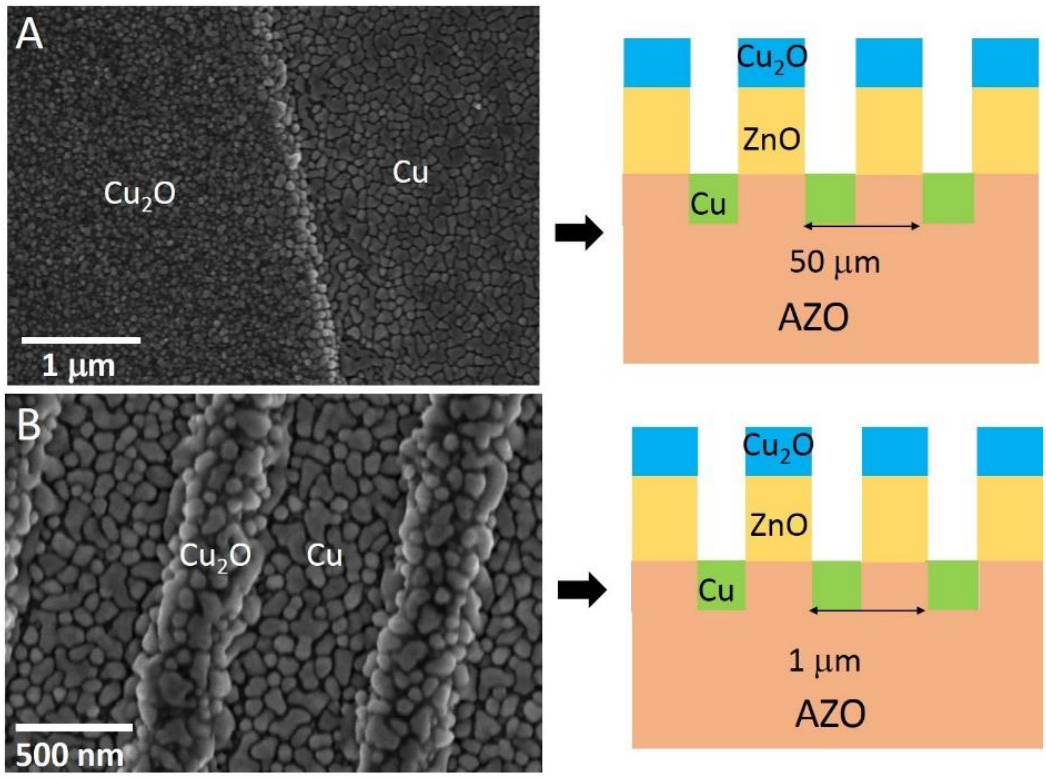

Figure 3.21. Cu_2O and Cu area-selective deposition on features of different sizes: 50 µm (a) and 1 µm (b).

deposition of metallic Cu that extends up to the AZO/ZnO interface regardless of the orientation relationship. This is in line with the possibility to deposit Cu_2O on the c-axis sapphire substrates (Figure 3.8), and with the low nucleation on a-plane and m-plane monocristalline ZnO substrates as was discussed previously (Figure 3.10).

Using this selective area deposition process, we have tested and achieved selective growth of Cu and Cu_2O features of lateral sizes from ca. 200 nm up to several centimeters. In Figure 3.21 top-view SEM micrographs of the two samples obtained with different separations between the wells are presented. In this case, lateral sizes for the Cu and Cu_2O features are of 25 μm (top) and 500 nm (bottom), respectively.

3.6.1 Electrical Characterization of the Microjunctions

This architecture achieved by this relatively simple method is interesting for the fabrication of segmented Cu_2O/ZnO/AZO microjunctions. The Cu film deposited on top of the AZO layer works as an electrical contact. The suppression of Cu_2O deposition observed on the ZnO side walls eliminates the risk of short circuit between Cu_2O on ZnO and Cu on AZO. Due to the extremely small features in this sample, traditional photovoltaic measurements are not suitable.

Figure 3.22. Picture of the chip used as substrate holder for the C-AFM measurements and the Al wire used as electrical contact on the Cu_2O film.

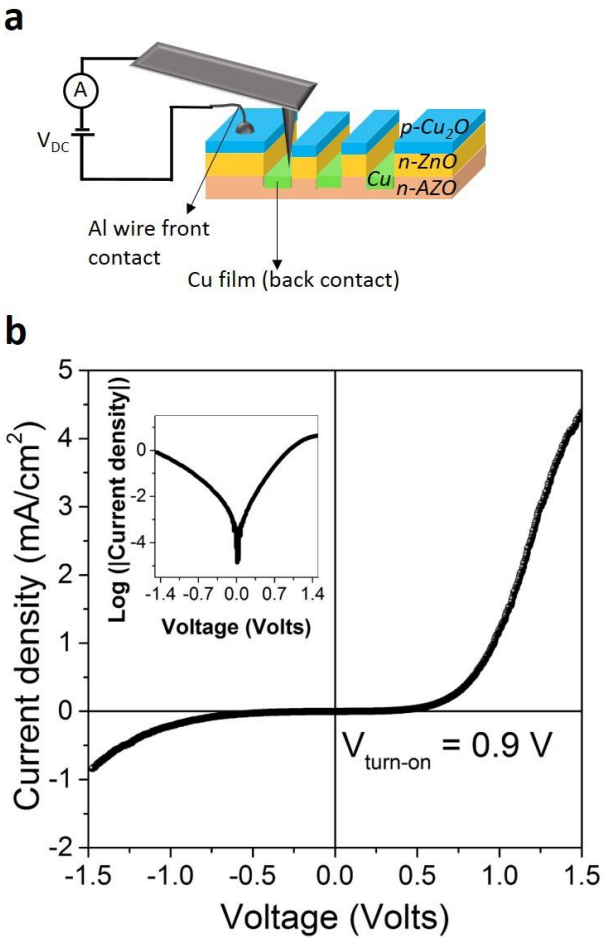

Figure 3.23. Schema of the sample configuration for the C-AFM measurements and the electrical contacts (a). Current density - voltage characteristics of the device in the dark at room temperature (b), the curve is also reported in semi-logarithmic scale as inset.

Therefore, in order to test the rectifying behavior of these microjunctions, conductive atomic force microscopy (C-AFM) was performed. The small chip of Figure 3.22 was used as the substrate-holder. An Al wire was attached on top of the Cu_2O region and weld to the exterior contact of this chip to work as a front contact (see amplified picture at the center of **Erreur ! Source du renvoi introuvable.**). Then, the AFM tip was put in contact with the Cu film, working as a back contact (see schematic in Figure 3.23 a).

Figure 3.23 b shows the current density - voltage (J-V) curve measured in the dark at room temperature by C-AFM. A nonlinear rectifying behavior characteristic of a p-n junction is observed, which confirms the formation of a heterojunction between Cu_2O and ZnO. A turn-on voltage of approximately 0.9 V was measured, which is in good agreement with the values reported by S. Jeong *et al.* (0.5 - 1.1 eV) on Cu_2O/ZnO heterojunction fabricated by metal-organic chemical vapor deposition [130].

The method we have reported here enables easy fabrication of segmented p-Cu_2O/n-ZnO microjunctions with simultaneous deposition of the p-Cu_2O layer and of the metallic Cu contact using AS-ALD on a patterned AZO/ZnO bilayer. It opens up new possibilities for the nanofabrication of semiconductor devices.

3.7 Chapter Conclusions

In this chapter we reported on the successful deposition of Cu_2O and metallic Cu thin films by atomic layer deposition, using $Cu(hfac)_2$ and H_2O, as precursors. High-resolution transmission electron micrographs showed the high crystalline quality of the deposited films. A selective growth of both materials was reported on different types of substrates (ZnO, AZO, and α-Al_2O_3). The formation of single phase Cu_2O and metallic Cu was tuned on monocrystalline α-Al_2O_3, ZnO, and AZO substrates by changing the deposition temperature in the range of 230 to 300 °C.

In addition, a detailed study on ZnO and AZO substrates demonstrate an area-selective deposition process. A phase diagram was presented showing the formation of the different phases as a function of the deposition temperature and substrate conductivity. As a proof of concept, a bilayer structure made of a low-conductive ZnO layer on top of a highly-conductive AZO film was fabricated, patterned, and functionalized. HRTEM, EELS, and EDS confirm that area-selective deposition of metallic Cu on highly conductive areas and Cu_2O on low-conductive areas was achieved. In this approach, deposition of different materials is obtained, but “traditional” selectivity is kept by simply using highly-resistive ZnO films as substrate to avoid local growth.

The mechanism behind the area-selective deposition process is discussed. After the study of the deposition on different substrates and the analysis of the point defects evolution in the ZnO films by photoluminescence spectroscopy, we conclude that the observed area-selectivity is the result of the inherent selectivity of the $Cu(hfac)_2$ precursor toward the different ZnO surfaces, with different conductivity/density of donor defects. In the case of Cu_2O films, the orientation relationship between film and substrates seem also to play a fundamental role in the selectivity, as was demonstrated on the monocrystalline ZnO substrates, and by TEM analysis at the lateral walls of the ZnO film at the bilayer, where the growth of the Cu_2O was inhibited. These results offer a novel approach for the AS-ALD where the properties of the substrate are modulated (in this case by tuning the substrate conductivity/density of donor defects and/or structure) in order to achieve the local deposition of different materials in different regions.

Finally, based on the AS-ALD process, Cu_2O/ZnO/AZO microjunctions were successfully fabricated. I-V characteristics measured to the samples show a rectifying behavior typical of a p-n junction, which is promising for low-cost all-oxide transparent microelectronics. Furthermore, the deposition of several Cu_2O/ZnO microjunctions by this method on a transparent substrate would produce a segmented photovoltaic architecture, promising for building-integrated photovoltaics. This configuration is a first approach of the many different ones than could be achieved. Defining otherwise the conductivity zones one would create different interfaces, allowing the formation of different architectures. All in all, this method provides an understanding of how AS-ALD can be further improved and extended to a wider range of materials.

Chapter 4

Tunable Localized Surface Plasmon Resonance and Broadband Visible Photoresponse of Cu Nanoparticles / ZnO Surfaces

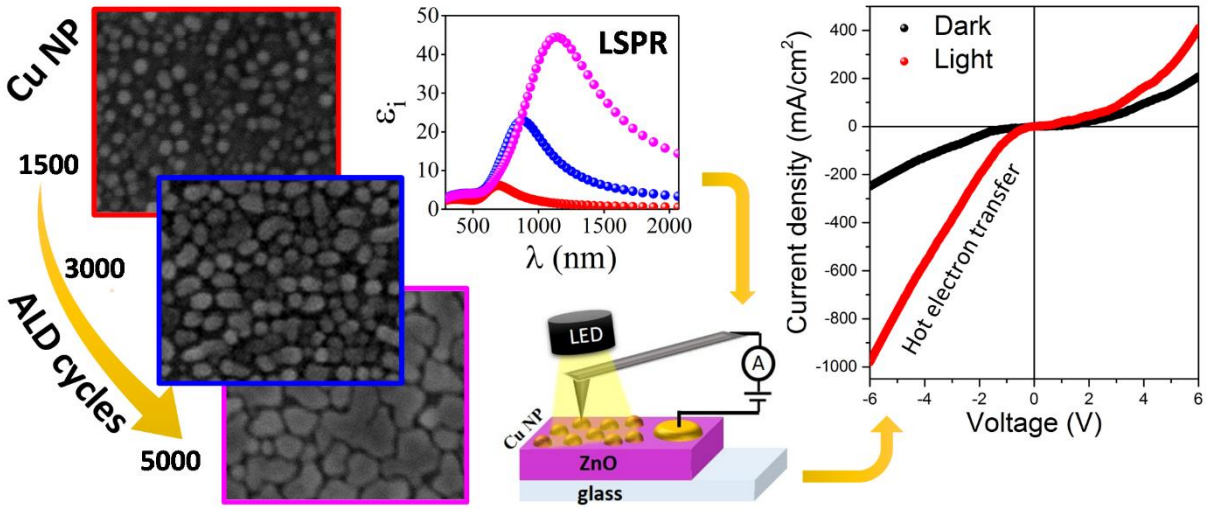

ABSTRACT: In this chapter we present the results on the successful deposition of Cu nanoparticles (NP) on ZnO substrates by atomic layer deposition (ALD), owing to the Volmer–Weber island growth mode, and their application as photodetectors. An evolution from Cu NP to continuous Cu films was observed with increasing the number of ALD cycles. Real and imaginary parts of the NP dielectric functions, determined by spectroscopic ellipsometry using an effective medium approach, evidence a localized surface plasmon resonance that can be tuned between the visible and near infrared ranges by controlling the interparticle spacing and size of the NP. The resulting Cu NP/ ZnO device shows an enhanced photo-response under white light illumination with good responsivity values, fast response times and stability under dark/light cycles. The significant photocurrent detected for this device is related with the hot electron generation at the NP surface and injection into the conduction band of the ZnO. The possibility to tune the plasmon resonance together with the photo-responsivity of the device is promising for applications related with photo-detection, photonics and photovoltaics.

Contents

4.1 Introduction

Metal nanoparticles, such as Au, Ag, and Cu, have gained a lot of attention in multiple fields due to their outstanding optical and electrical properties. They exhibit localized surface plasmon resonance (LSPR), which comes from the coupling between the electromagnetic field and the collective oscillations of the free conduction electrons at the nanoparticle surface. With precise control of the size, shape, density, and dielectric environment, light can be manipulated and controlled in an exceptional manner. This is the reason why nanoparticles (NP) have drawn intense scientific and technological interest in many fields, e.g. chemical sensing [197], catalysis [198], photonics [107], and photovoltaics [114,199]. Cu NP have the advantage of their low cost as compared with Au and Ag. Moreover, Cu is already a material widely used in microelectronics, with high electrical conductivity and photosensitivity [200], making Cu NP promising in applications related to nanoelectronics, optoelectronics, sensing, etc.

ZnO is a low-cost wide-bandgap semiconductor, with high exciton binding energy and high chemical stability [45], which has proven to be an excellent candidate for UV photodetection, light-emitting diodes (LED), and transparent thin-film transistors, among other applications. In particular, Cu NP grown on ZnO act as catalysts in methanol synthesis from CO_2 hydrogenation [178] and also for plasmonic energy conversion through hot-electron generation at the interface between Cu NP and ZnO films [3,201]. The plasmonic effect in Cu NP can boost the optoelectronic properties of ZnO by broadening the absorption band, enhancing the photocurrent and photocatalytic activity, and allowing wavelength-tunable photodetection in Cu/ZnO devices by controlling the NP size, shape, density, and agglomeration, for example [5,202].

Examples of some of the different routes used for the fabrication of Cu NP are nanosphere lithography [203], electrochemical deposition [204], laser ablation in liquid media [200], and chemical reduction [205]. Even if these methods enable the production of Cu NP, in some cases this is achieved on limited surface areas and/or using complex routes. In this paper, we propose a different approach to fabricate highly responsive Cu NP/ZnO photodetectors using a simple atomic layer deposition (ALD) route. In the previous chapter, we have already demonstrated the area-selective atomic layer deposition of Cu and Cu_2O on ZnO substrates [206]. In this chapter, the growth of Cu NP on ZnO thin films and nanowires is achieved at early stages of the deposition owing to the Volmer–Weber island growth mode. The optical responses of Cu NP and thin films, determined by spectroscopic ellipsometry using an effective medium approach, are given and analyzed. It is shown that the LSPR of Cu NP can be tuned between

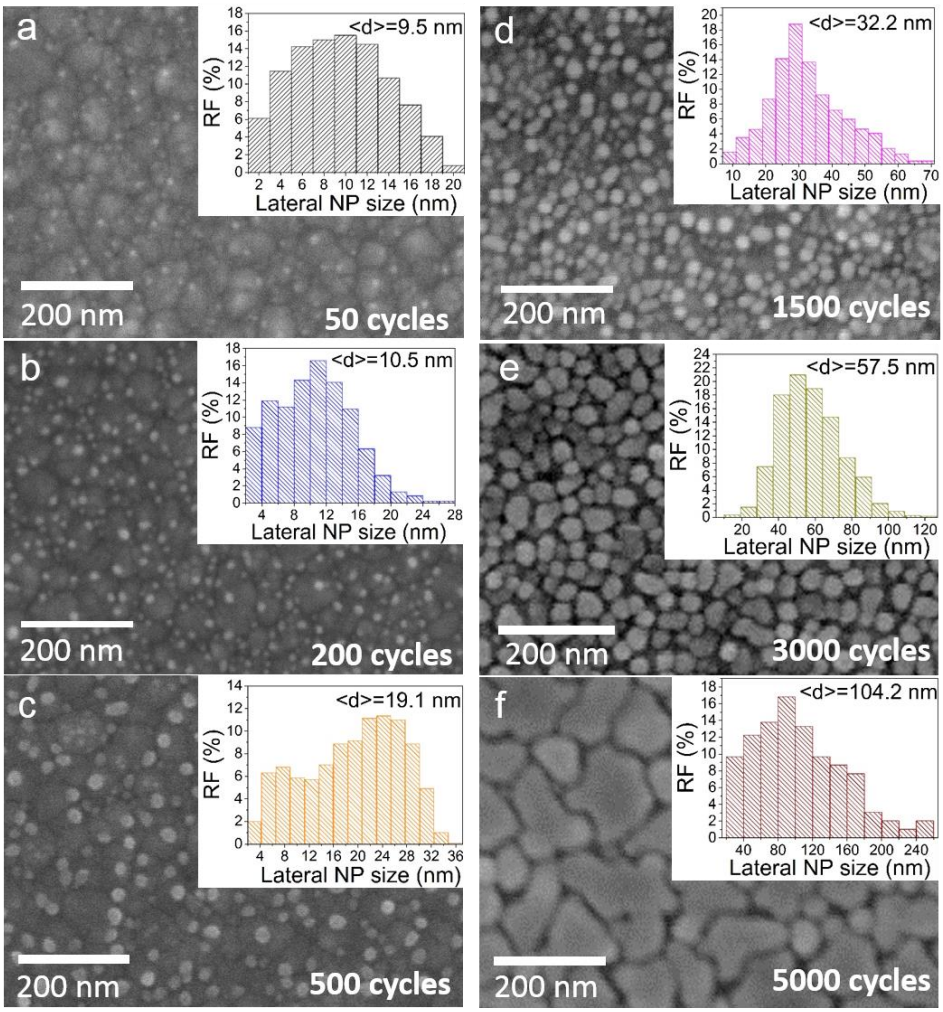

Figure 4.1. Top-view SEM micrographs of Cu NP at 50 (a), 200 (b), 500 (c), 1500 (d), 3000 (e), and 5000 (f) ALD cycles with the corresponding lateral NP size distributions in the inset (RF meaning relative frequency).

the visible and near infrared ranges by controlling the interparticle spacing and size of the NP. Finally, the enhanced photoresponse capability of the plasmonic Cu NP/ZnO device is demonstrated by conductive atomic force microcopy (C-AFM), showing the potentialities of ALD for the fabrication of photodetecting devices. Furthermore, the possibility of injecting electrons from the metallic particles to the ZnO semiconductor can be exploited in the future to boost the performance of Cu_2O/ZnO-based solar cells or photodetectors.

4.2 Evolution of the NP with the Number of ALD Cycles

Cu nanoparticles (NP) were grown on high conductivity ZnO thin films ($\sigma = 1.5 * 10^2\ S/cm$) by atomic layer deposition at 280 °C. Figure 4.1a-f show top-view scanning electron micrographs (SEM) of the Cu NP grown on ZnO films after 50 – 5000 ALD cycles; the lateral

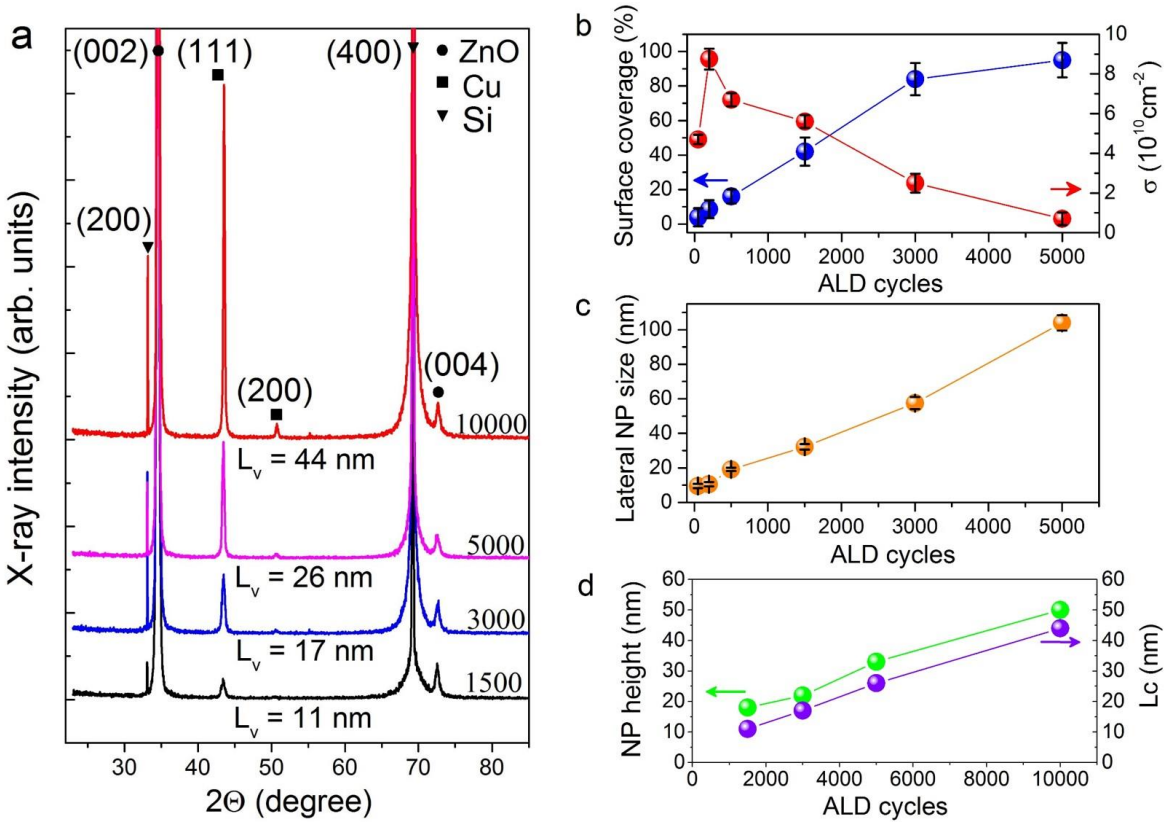

Figure 4.2. X-ray diffactrograms of the Cu NP after 1500 (black), 3000 (blue) and 5000 (magenta) ALD cycles and the Cu film (red) deposited at 10000 ALD cycles (a). Surface coverage, density (b) and average lateral NP size (c), versus the number of ALD cycles. Average NP height (green), and coherence length (violet), versus the number of ALD cycles (d).

NP size (NP_{LS}) distributions are shown at the inset. The average NP_{LS}, surface coverage, and density (particle/cm^2) was determined from SEM micrographs using Image J software (see Figure 4.2).

At early growth stages (50 cycles) we observe a random nucleation of Cu islands, with average NP_{LS} and density of 9.5 nm and 4.7×10^{10}cm^{-2}, respectively. The formation of these small Cu NP dispersed on the ZnO substrate indicate a Volmer–Weber island growth mode at the first stages of deposition [207,208]. On increasing the number of ALD cycles, the density is further increased as a result of the nucleation of new islands at "free" sites on the surface. However, after this first increase, the NP density tends to decrease monotonically with increasing the number of ALD cycles as a result of the coalescence between adjacent islands. More precisely, for samples obtained at 500 cycles or more, there is a competition between coalescence and nucleation as can be verified in the histogram of Figure 4.1c, which shows two NP populations, one with the most likely size around 7 nm (due to nucleation) and a second one with the most likely size around 24 nm (due to coalescence of smaller islands). For Cu NP obtained after 3000

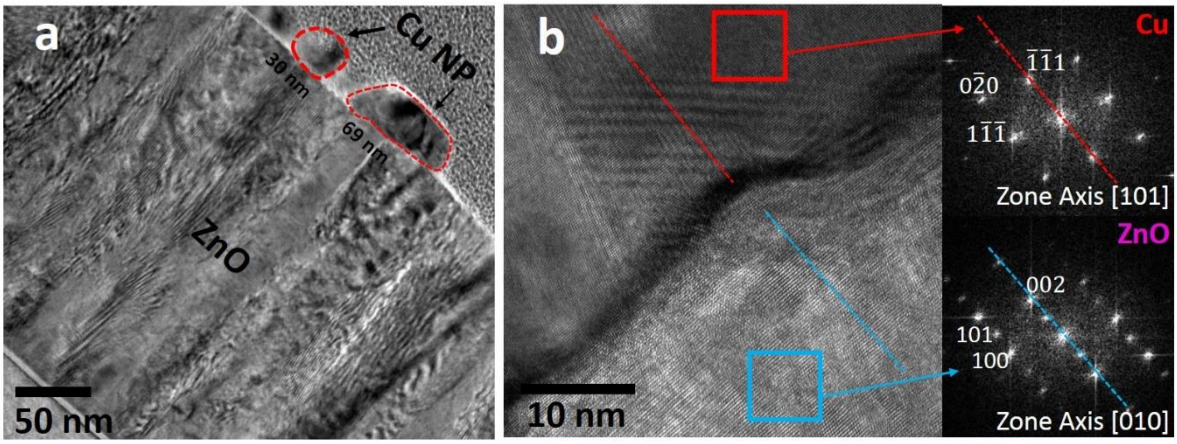

Figure 4.3. Bright-field-TEM micrograph of the CuNP/ZnO sample (a). High resolution TEM micrograph at the interface between the Cu NP and the ZnO film. FFT patterns taken at the Cu and ZnO regions are shown in the inset.

cycles, coalescence is clearly dominant and there is no secondary nucleation. This leads to a decrease in the density of particles (Figure 4.2b), while the surface coverage and average NP_{LS} increase as can be observed in Figure 4.2 b, c. In general, wide Cu NP_{LS} distributions were obtained as a result of different nucleation times [204].

At 5000 ALD cycles, most of the islands are interconnected due to the strong coalescence, which also leads to a much wider NP_{LS} distribution (NP sizes ranging from 20 to 257 nm). Moreover, at this point, as the surface is almost completely covered (surface coverage: 95%), the growth of smaller particles is limited by their proximity to neighboring particles, which also contributes to the broadening of the NP_{LS} distribution.

Figure 4.3 shows a cross-section TEM micrograph of the Cu NP deposited at 5000 ALD cycles. In Figure 4.3 (a) two nanoparticles are shown, with lateral sizes of 30 and 69 nm. The NP height was around 30 nm, in agreement with the values obtained by ellipsometry and X-ray diffraction (Figure 4.2 d). Figure 4.3 b shows a HR-TEM micrograph taken at the interface between the Cu NP and the ZnO film. The corresponding FFT patterns are shown as insets. The FFT confirms the formation of single phase metallic Cu on the ZnO films. The NP grows with the [111] direction parallel to the [001] direction of ZnO, as indicate the dotted lines in Figure 4.3 b, which is in agreement with the X-ray diffractograms that show a preferential orientation in the [111] direction for the Cu NP.

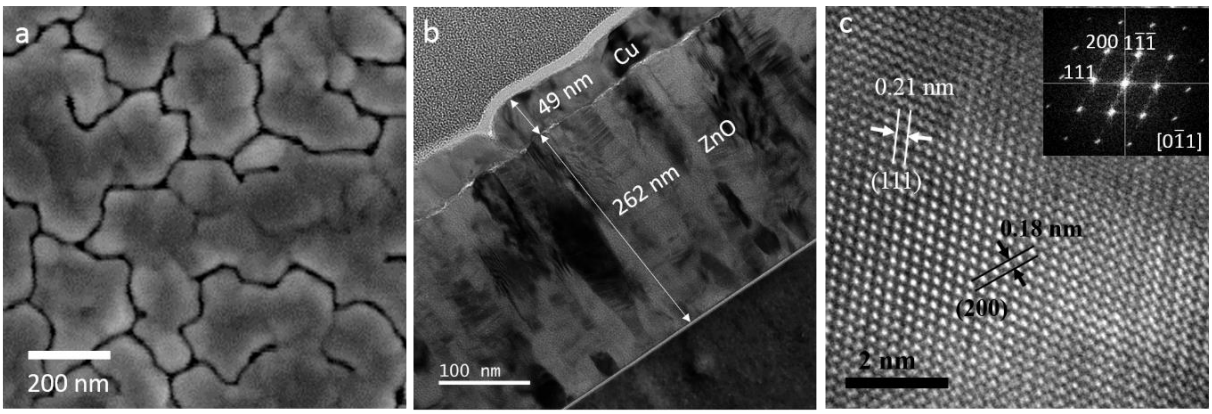

Figure 4.4. Top-view SEM micrographs of the Cu film after 10000 ALD cycles (a). TEM bright field micrograph taken from a cross-section of the Cu film (b). HRTEM micrograph taken to the Cu film (c) and the corresponding FFT pattern (inset).

4.3 Metallic Cu Thin Film

After 10000 ALD cycles, a continuous Cu film (Figure 4.4 a, b) is formed apart from some discontinuities between grains. The increase in NP_{LS} and surface coverage is also accompanied by an increase in thickness (NP height) from 18 nm at 1500 cycles to 50 nm for 10000 cycles (Figure 4.2d). The thickness measured from cross-section TEM micrographs (Figure 4.4b) is in the 45-50 nm range. Resistivity values for this sample are in the $8 - 10\ \mu\Omega\,\text{cm}$ range. These values are in relatively good agreement with the resistivity of bulk copper ($1.68\ \mu\Omega\,\text{cm}$) considering electron scattering at film interfaces [209] due to the small film thickness, which is comparable to the mean free path of conduction electron in Cu (40 nm) [210].

X-ray diffractograms of the samples obtained after various ALD cycles are shown in Figure 4.2 a. Cu grains are preferentially oriented in the [111] direction, as indicated by the very small peak associated with the (200) crystallographic planes compared with the (111) peak. The intensity of the (111) Cu peak increases with the number of ALD cycles as a result of the increase in thickness, size of Cu NP, and surface coverage. A cross-section HR-TEM micrograph of the sample obtained at 10000 ALD cycles is displayed in the inset of Figure 4.4c, with the corresponding FFT pattern. It is possible to identify the (111) and (200) planes of Cu. The interplanar distances were measured to be 0.21 and 0.18 nm for the (111) and (200) planes, respectively, in good agreement with those reported for face-centered cubic Cu (PDF 04-0836), evidencing the good crystalline quality of the metallic Cu grown by this ALD route. The metallic nature is also confirmed for Cu NP, as reported in Figure 4.3.

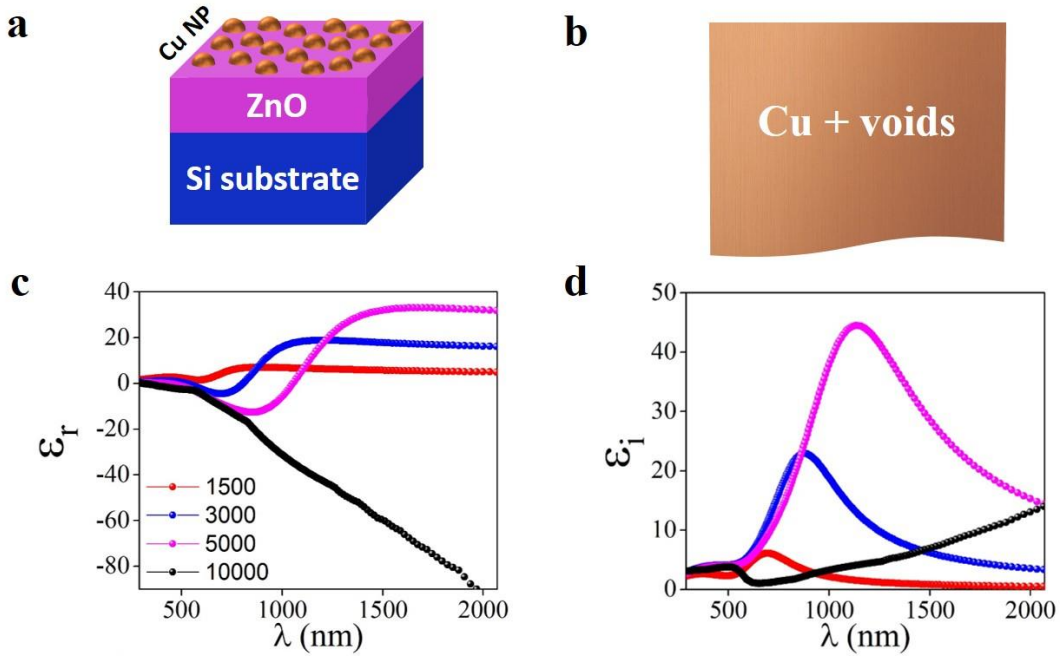

Figure 4.5. Schematic of the physical model used for fitting the ellipsometry data for the Cu NP (a) and the Cu film (b). Real (c) and imaginary (d) part of the dielectric function of the Cu NP and the Cu film (black line).

4.4 Localized Surface Plasmon Resonance

The samples obtained from 1500 to 10000 cycles were characterized by spectroscopic ellipsometry. For samples obtained at lower number of ALD cycles, it was not possible to perform this kind of measurement, due to the small signal obtained as a result of the very small size and low density of the NP.

The ZnO substrates were characterized by ellipsometry before the ALD deposition in order to generate appropriate models. The dielectric function of ZnO was modeled in the 0.6 eV-1.8 eV spectral range, by a constant independent of the wavelength making possible to determine the film thickness. Then, the spectra were fully modeled to determine the dielectric function of the ZnO. To that end, the thickness of the film was fixed to that obtained previously and the dielectric function of ZnO was determined by means of direct inversion wavelength-by-wavelength. Following this procedure, the spectra were fully reproduced (see Appendix 1).

The model employed for samples obtained after 1500, 3000 and 5000 ALD cycles is schematically represented in Figure 4.5 a. The film stack consists in Cu NP deposited on a ZnO film grown on the Si substrate. The effective dielectric function for the Cu NP was described by the sum of two terms as indicated below:

$$\varepsilon = \varepsilon_{\mathrm{TL}} + \varepsilon_{\mathrm{osc}} \quad \textbf{(4.1)}$$

The first term ($\varepsilon_{\mathrm{TL}}$) describes the inter-band transitions of Cu NP and was modeled using the Tauc-Lorentz dispersion law:

$$\varepsilon_{\mathrm{i}} = \frac{1}{\omega} \frac{A\,\omega_0\,C\,\left(\omega - \omega_{\mathrm{g}}\right)^2}{(\omega^2 - \omega_0^2)^2 + C^2\omega^2}\,\Theta\left(\omega - \omega_{\mathrm{g}}\right) \quad \textbf{(4.2)}$$

$$\varepsilon_{\mathrm{r}} = \varepsilon_{\infty} + \frac{2}{\pi} P \int_{\omega_{\mathrm{g}}}^{\infty} \frac{\Omega\,\varepsilon_{\mathrm{i}}(\Omega)}{\Omega^2 - \omega^2} d\Omega \quad \textbf{(4.3)}$$

Where the Heaviside distribution $\Theta(\omega - \omega_{\mathrm{g}})$ is zero when $\omega \leq \omega_{\mathrm{g}}$ and equal to 1 when $\omega > \omega_{\mathrm{g}}$, ε_{r} and ε_{i} are the real and imaginary part of the dielectric function, ε_{∞} is the high-frequency dielectric constant, ω_0 is the the energy of the first interband transition, ω_{g} is the threshold energy of the interband transitions of the NP, A is the transition matrix element, and C a broadening term.

The second term ($\varepsilon_{\mathrm{osc}}$) describing the plasmon resonance band of Cu nanostructures is given by:

$$\varepsilon_{\mathrm{osc}} = \frac{f\,\omega_1^2}{\omega_1^2 - \omega^2 + \mathrm{i}\,\omega\,\gamma} \quad \textbf{(4.4)}$$

Where f is the oscillator strength, ω_1 the resonance plasmon energy and γ the damping factor associated to the plasmon resonance band width.

In the case of the sample deposited at 10000 cycles, only a Cu film with a certain porosity was considered since this film was thick enough to be opaque (Figure 4.5 b). The effective dielectric function for the porous Cu ($\varepsilon_{\mathrm{eff}}$) was modeled using the Bruggeman's model:

$$0 = (1 - f_{\mathrm{Cu}}) \frac{1 - \varepsilon_{\mathrm{eff}}}{1 + 2\varepsilon_{\mathrm{eff}}} + f_{Cu} \frac{\varepsilon_{\mathrm{Cu}} - \varepsilon_{\mathrm{eff}}}{\varepsilon_{\mathrm{Cu}} + 2\varepsilon_{\mathrm{eff}}} \quad \textbf{(4.5)}$$

Where f_{Cu} is the Cu volume fraction and $\varepsilon_{\mathrm{Cu}}$ is the Cu dielectric function. The comparison between the ellipsometry data and the models for the Cu NP and the Cu films are reported in Appendix 1.

Figure 4.5 shows the real (b) and imaginary (c) parts of the effective dielectric function for the Cu NP and the Cu film obtained at 10000 ALD cycles. The imaginary part of the effective dielectric function (ε_i) for samples obtained at 1500 (black line), 3000 (blue line), and 5000 (violet line) cycles displays localized surface plasmon resonance (LSPR) bands located at 697 nm (1.78eV), 867 nm (1.43eV) and 1127 nm (1.10 eV), respectively, which is accompanied by a large variation in the real part of the dielectric function (ε_r). Moreover, the amplitude of this

variation in ε_r increases consistently with the LSPR peak intensity. LSPR bands are relatively wide, and the FWHM increases according to the broadening of Cu NP_{LS} distribution.

It is worth noting that ε_r presents ranges with negative values for samples obtained at 3000 cycles and above. In this case, ε_r becomes negative for energy values between 516 and 826 nm (1.5 - 2.4 eV) and this behavior is more pronounced for the sample obtained at 5000 cycles. The negative values of ε_r are the result of NP coalescence: with an increasing the number of cycles, Cu NP come in contact to form a compact layer (metallic behavior). However, they still support a plasmonic mode as confirmed by the presence of the LSPR band in ε_i. Therefore, this sample presents a hybrid behavior between a metallic and a plasmonic material [211]. For the sample obtained at 10000 cycles, ε_r is also negative, but no plasmonic band is observed, indicating a metallic behavior. This result is expected since, in this case, a continuous metallic Cu film was formed, as verified by TEM and SEM micrographs.

As shown in Figure 4.5 d, the LSPR band is red-shifted as the number of ALD cycles increases. This LSPR red-shift has already been observed for Cu NP with increasing particle sizes [203,204]. However, such a large shift cannot be explained solely by the increase in NP size. Theoretical and experimental studies have shown that reducing the distance between Au NP produces a red-shift in the LSPR spectra [104,212,213]. Additionally, the plasmon resonance depends strongly on the particle shape; for example changes in the geometry of the grains from circles to pentagons or triangles produce a significant shift in the plasmon signal [214] and a red-shift has been predicted when spherical particles become more oblate [106]. The formation of NP agglomerates, chain, or complex networks can also produce an important broadening and red-shift of the plasmon resonance [101,108,211,215].

In our case, the red-shift is obviously mostly related to NP coalescence and the decrease in the interparticular spacing, which strengthen the coupling between different NP as they get closer to each other. In the case of samples grown with 5000 cycles, where particles as large as 257 nm are observed, the NP size can also contribute to this red-shift. In any case, the effect of the NP shape cannot be completely ruled out, since an evolution in the geometry of Cu NP can be observed from samples grown at 1500 cycles to samples grown at 5000 cycles, and this could also influence the position and width of the LSPR band.

For all of the samples, the spectra in Figure 4.5 are dominated by interband transitions below 540 nm (above 2.3 eV) [216]. The values of the interband transition threshold are 571 nm (2.17 eV), 623 nm (1.99 eV) and 620 nm (2.00 eV), for the 1500, 3000, and 5000 cycles samples, respectively, in relatively good agreement with the value of 590 nm (2.1 eV) reported for bulk Cu.

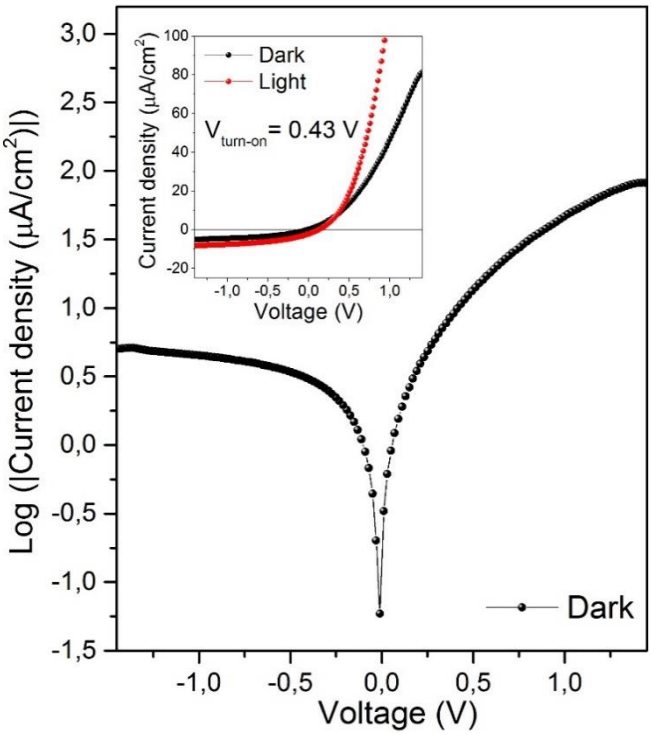

Figure 4.6. Current density characteristics (semi-log scale) for the Cu/ZnO Schottky junction, in the inset the I-V characteristics is shown in linear scale together with the J-V curve under illumination (red line).

4.5 Cu/ZnO Schottky Diode

Both ohmic contact or a Schottky junction have been reported in the literature between ZnO and metallic Cu. [217–219]. This is due to the similar work function values between Cu (4.59 – 4.98 eV) [220] and ZnO (4.3 - 4.71 eV) [221,222], and to the fact that they can vary largely depending on surface preparation, structure, morphology, and point defect densities [223]. Figure 4.6 shows the current density- voltage characteristics (J-V) of the Cu film/ZnO (10000 ALD cycles, T=280 °C). The non-linear rectifying behavior observed indicates that a Schottky junction is formed between the metallic Cu film and the semiconducting ZnO, in our case.

The current-voltage characteristic of a Schottky diode are described by the Richardson equation:

$$I = I_S\left(e^{\frac{q\,V}{n\,k\,T}} - 1\right) \tag{4.6}$$

$$I_S = A\,R^*T^2 e^{\frac{-q\,\phi_B}{k\,T}} \tag{4.7}$$

Where I_S is the reverse saturation current, A the junction area, R^* the modified Richardson constant (for ZnO this constant has a value of $32\,A\,cm^{-2}\,K^2$ [217]), T the temperature in

Kelvin, q the electronic charge, k the Boltzmann's constant and $q\,\phi_B$ the Schottky barrier height.

From the semi-log plot of the J-V curve the value of Is can be determined by extrapolating to zero volt the forward bias current and then the Schottky barrier height can be determined through equation (4.7). A value of $I_s = 7.5 * 10^{-9} A$ ($J_s = 3.2\ \mu A/cm^2$) and $q\,\phi_B = 0.7$ eV were determined. The Schottky barrier height value is in good agreement with those of 0.67 – 0.68 eV reported by A. Khan *et al.* in a Cu/ZnO nanorods Schottky diode [217].

J-V characteristics of the sample under white light illumination (white LED, 5700 K, spectra from 400 nm to 800 nm) are presented at the inset of Figure 4.6. As can be seen, only a small increase in current density is observed after illumination in reverse bias. The carriers contributing to it are the photoelectrons emitted from the Cu film and transferred to the ZnO through the Schottky barrier. This hot electron emission process from the Cu film to ZnO is not efficient under visible light excitation (due to the low energy of the photon involved), which could be the reason of the small current observed [3]. On the other hand, the current density increases considerably in forward bias after illumination, which is surprising since no photoelectron generation in the ZnO is expected with excitation below the bandgap energy. However, a similar photoconductive effect has been observed in doped Cu:ZnO systems in which a trap type-controlled space charge limited (SCL) transport mechanism has been considered to explain the photoconductive behavior [224].

4.6 Photo-response of Cu NP under Visible Light

To verify the photoresponse capability of the plasmonic Cu NP/ZnO device, conductive atomic force microscopy (C-AFM) measurements were performed in the dark and under illumination with a white-light LED (5700 K, spectra from 400 nm to 800 nm). A schematic of the sample configuration for the C-AFM measurement is presented in Figure 4.7 a. The AFM tip was in contact with the Cu NP and a gold back contact was sputtered on the ZnO film. Only the sample with Cu NP deposited at 1500 ALD cycles was tested since it has an LSPR band centered at 697 nm. For the other samples, with LSPR bands in the IR region of the electromagnetic spectrum, no excitation should be expected with the used LED.

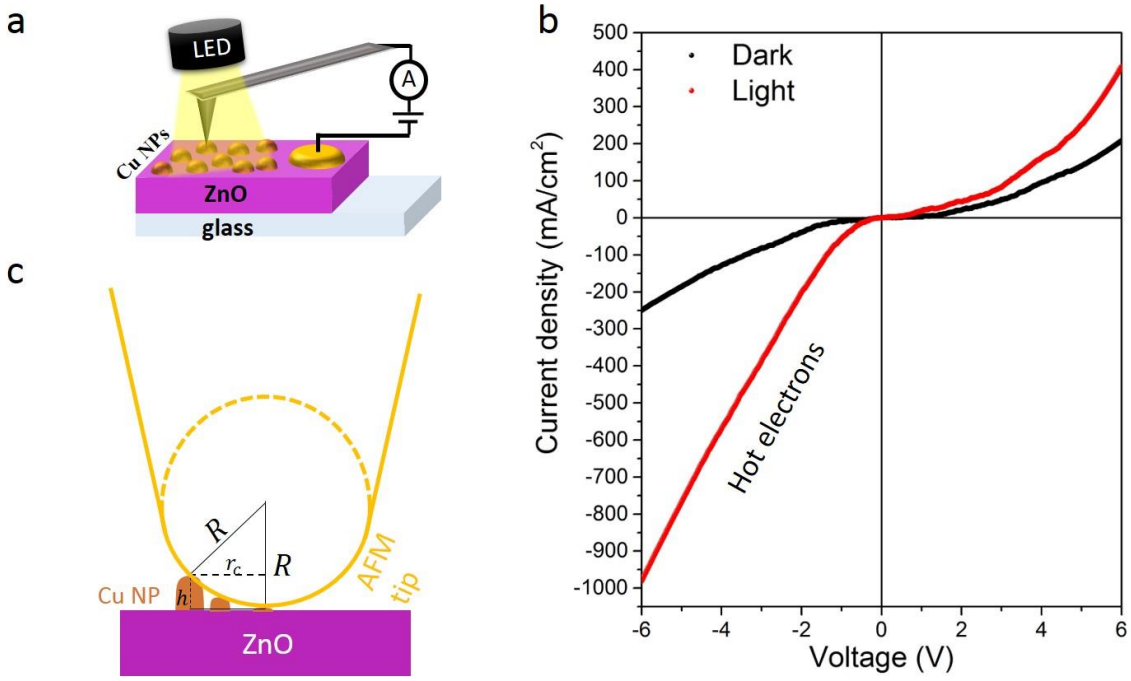

Figure 4.7. Photoresponse of Cu NP under visible light. Schematic of the C-AFM measurements (a). Current density characteristics of the Cu NP/ZnO device in the dark and under visible-light illumination, with an estimated contact area of 4.3×10^3 nm^2 (b). Schematic of the contact area between the AFM tip and the sample surface (c).

Current density-voltage (J-V) characteristics of the sample in the dark and under LED illumination are shown in Figure 4.7 b. In order to determine the current density, we estimate the contact area between the tip and the Cu NP considering that the tip is in contact with more than one NP at a time since its radius (R=100 nm) is higher than the average NP radius (~15 nm) and taking into consideration the surface coverage of the NP on the ZnO substrate. We consider the maximal contact area possible assuming that the NP that is in contact with the tip end is completely flattened by the tip, as is show in the schematic of Figure 4.7 c. The last NP in contact with the tip will have a height of 18 nm, that is the average NP height determined from ellipsometry for this sample (Figure 4.2 d). Therefore, considering $h = 18\,nm$ and $R = 100\,nm$ a contact radius of 57.2 nm is obtained from equation (4.8).

$$r_c{}^2 = h^2 + (R - h)^2 \qquad \textbf{(4.8)}$$

The maximum contact area will be the projected area of the spherical cap in contact with the NP and it is equal to 10.3×10^3 nm^2, from equation (4.9).

$$A_C = \pi\, r_c{}^2 \qquad \textbf{(4.9)}$$

As we are working with NP and not with a homogeneous film we need to consider the NP are not covering the whole surface. For this sample, the surface coverage determined from SEM

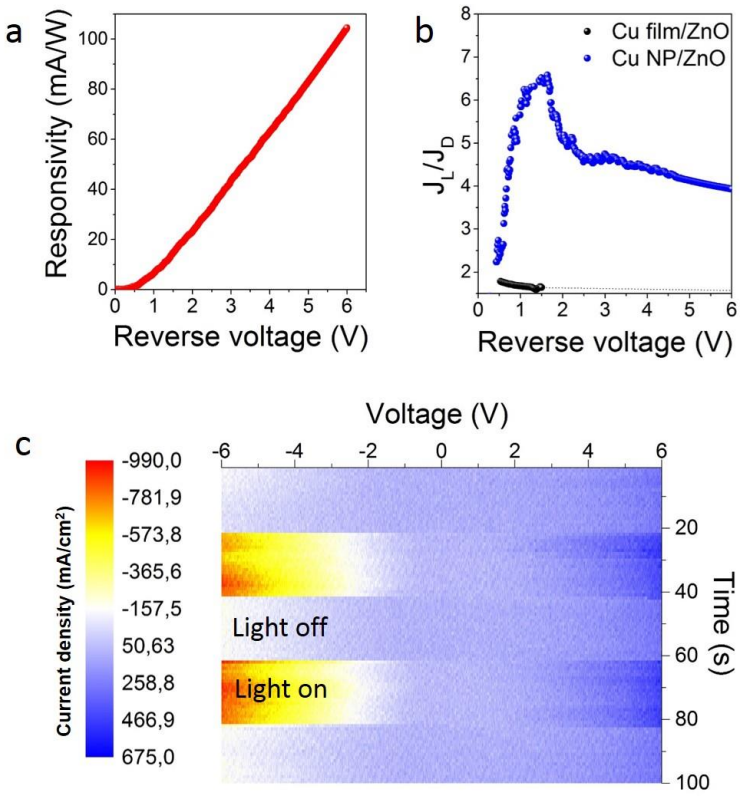

Figure 4.8. Responsivity (a) and J_L/J_D ratio (b) as a function of the reverse voltage. Current density evolution as a function of the applied bias voltage during dark/light cycles of 20 s (c).

micrographs was of 42% (Figure 4.2 b). Therefore, the contact area will be 42% of A_C, that is 4.3×10^3 nm^2. It is worth to note that this is approximation is an overestimation of the contact area, since actually the particle that is in contact with the tip end is not completely flattened by the tip because the force applied was relatively small of 130 nN (see Appendix 2).

The formation of a Schottky junction between Cu and ZnO was previously verified by macroscopic electrical measurements for the compact Cu film/ZnO. In case of the Cu NP/ZnO structure, an almost symmetric J-V curve was obtained by C-AFM. This result is due to the formation of two Schottky junctions at the Cu NP/ZnO and ZnO/Au (back contact) interfaces, as symmetrical J-V characteristics are typical of back-to-back Schottky devices [225–227]. The formation of the back contact between ZnO and Au is expected since the work function of Au (5.31-5.47 eV) [220,228], is much higher than that of ZnO [229].

The J-V curve under illumination with the white LED (red line) shows a significant increase in the current density, which confirms the photosensitivity of the device. Moreover, the current density under illumination gradually increases (almost linearly) with the increase of the reverse bias voltage from 0 to -6V. The current observed for reverse bias voltage on dark arises from thermionic emission [229].

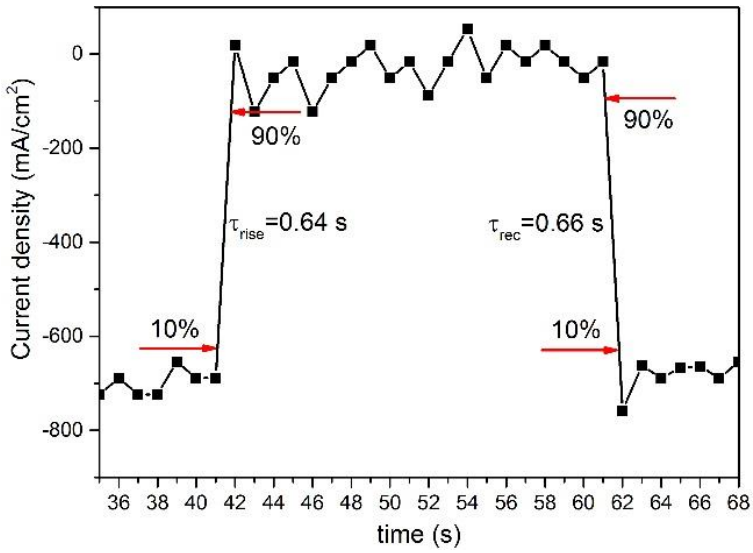

Figure 4.9. Current density vs. time for the Cu NP/ZnO deposited at 1500 ALD cycles, under dark/light cycles of 20 s.

The responsivity for the device (R) was calculated by the formula, $R = J_{ph}/P_{opt}$, where P_{opt} is the incident power density on the device and J_{ph} is the photocurrent calculated by subtracting the dark current (J_D) from the current under illumination (J_L) [230]. The sample responsivity is plotted in Figure 4.8 a as a function of the reverse bias voltage. The highest responsivity was of ~ 0.10 A/W, obtained at a bias voltage of -6 V ($\lambda = 400 - 800\ nm$, $P_{opt} = 7\ W/cm^2$), that is the same order as values reported for other Cu-ZnO-based visible photodetector at 10 V [224]. In Figure 4.8 b is compared the ratio between the current density under illumination, and the current density on dark (J_L/J_D) for the Cu NP/ZnO and the Cu film/ZnO. For the Cu film, the current density was measured only between -1 and 1 V, therefore only this region appears in Figure 4.8 b. However, it is enough to appreciate that the J_L/J_D ratio is considerably higher for the Cu NP/ZnO device compared to the Cu film/ZnO system.

Figure 4.8 c shows the evolution of the current as a function of the applied bias voltage during dark/light cycles of 20 s (during these measurements, the AFM tip was stationary on the NP). A photocurrent is detected whenever light is on, confirming that the device can be switched on/off, keeping a good stability.

To describe the response speed of the photodetector, the rise and recovery times were calculated from the current vs. time curves at different applied voltages under dark/light cycles of 20 s. The rise time, defined as the time difference between the 10 and 90% points of the maximum amplitude of the current pulse, was between 0.50 and 0.75 s, after measuring at different cycles and for different bias voltages (see Figure 4.9). The recovery time, defined as the time difference between the 90 and 10% points of the maximum amplitude of the current

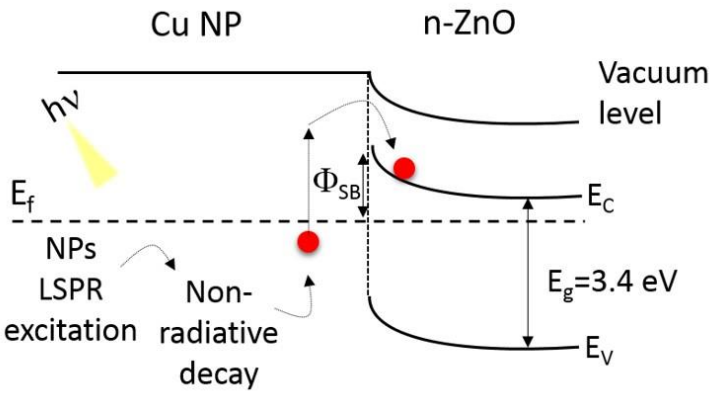

Figure 4.10. Schematic illustration of the energy band alignment at the Cu NP/ZnO interface together with the representation of hot electron generation at the Cu NP and the transfer to ZnO through the Schottky barrier.

pulse during the trailing edge of the pulse, was between 0.54 and 0.67 s. These response times are promising considering the values that have been reported for some Cu-ZnO-based visible photodetectors of 8 s and 17 - 23 s [224,231].

Since ZnO exhibits a wide band gap of 3.3 eV, there is no significant absorption (except for a weak one related to some defect levels within the bandgap) when illuminated with white light. Furthermore, for the traditional Schottky junction formed between Cu and ZnO thin films the ratio J_L/J_D was of 1.65 at -1V which represents less than 30 % of the ratio of 5.86 obtained for the Cu NP/ZnO at the same bias voltage (Figure 4.8 b). Therefore, the significant increase in the photocurrent observed here can be univocally attributed to the effect of the Cu NP. We propose that it is the result of hot-electron generation from Cu NP upon LSPR decay, and injection into the ZnO film. When white light illuminates the sample, LSPR excitation occurs in the Cu NP, in the case of nonradiative decay this energy is transferred to hot electrons that are excited above the Fermi level (see Figure 4.10). Electrons in the Cu NP having sufficient energy to overcome the Schottky barrier are injected into the ZnO semiconductor. A rough estimation of the Schottky barrier for the Cu/ZnO structure of 0.7 eV was made using the thermionic emission-theory [232] (see section 4.5). For noble metal nanoparticles, the hot-electron energies are usually in the range of 1 to 4 eV above the Fermi level [3,111]. Hence, they can easily overcome the Schottky barrier and be injected into the ZnO film, resulting in photocurrent generation. Since the electrons are injected into the semiconductor, the plasmonic NP are left positively charged; however, the charge is balanced as the device is connected to an external circuit. A reverse bias provides the necessary electrons to keep the charge balanced

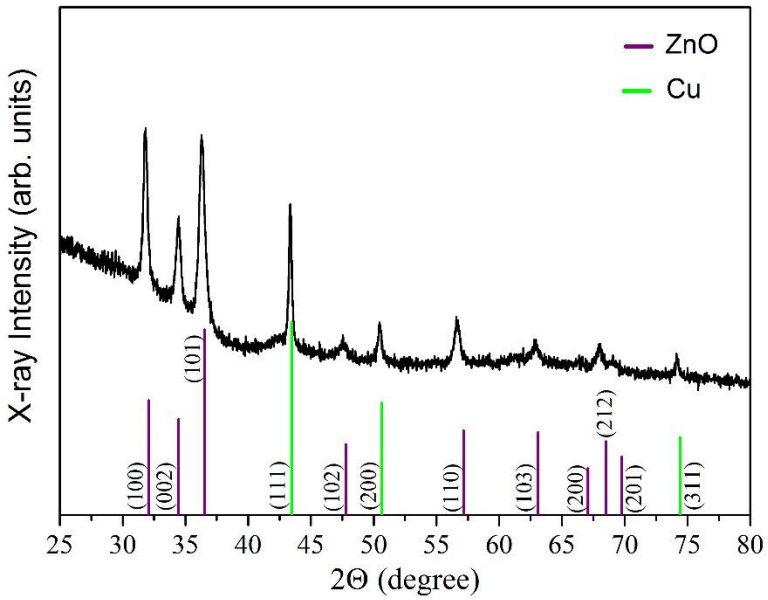

Figure 4.11. X-ray diffractograms of the Cu NP/ZnO nanowires sample.

and the current flowing in the device. Moreover, increasing the negative bias voltage favors electron injection form Cu NP to the conduction band of ZnO, increasing the photocurrent.

4.7 Preliminary Results on the Deposition of Cu NP on ZnO Nanowires

In order to test the possibility of depositing the Cu NP on high aspect ratio structures we employed a substrate formed by ZnO nanowires. The ZnO nanowires were obtained by a two step-process consisting on the deposition of a thick Zn film by DC magnetron sputtering and a subsequent oxidation by a flowing microwave afterglow [233]. For the deposition of the Cu NP by ALD, we used the same conditions described before for the NP on ZnO thin films, but increasing the exposure time of the $Cu(hfac)_2$ precursor to 3 s in order to favor its transport inside the nanostructure and achieving the deposition along all the surfaces of the nanowires.

Figure 4.11 show the X-ray diffractogram of the sample after the deposition of the Cu NP by ALD. The formation of single phase metallic Cu is confirmed by the presence of (111), (200) and (311) peaks in the diffractogram that correspond to the metallic Cu (JCPDS 00-004-0836). The others peaks observed in Figure 4.11 correspond to the ZnO nanoblets (purple line).

Figure 4.12 shows a top-view SEM micrograph of the as-grown nanowires (a) and after the deposition of the Cu NP (b). As can be seen, the NP are deposited all along the nanowires down to the bottom, forming a pearl-necklace arrangement.

The possibility of depositing Cu NP on the ZnO nanowires is a way to further enhance the photoresponse capabilities of the Cu NP/ZnO device, since the increase of surface to volume

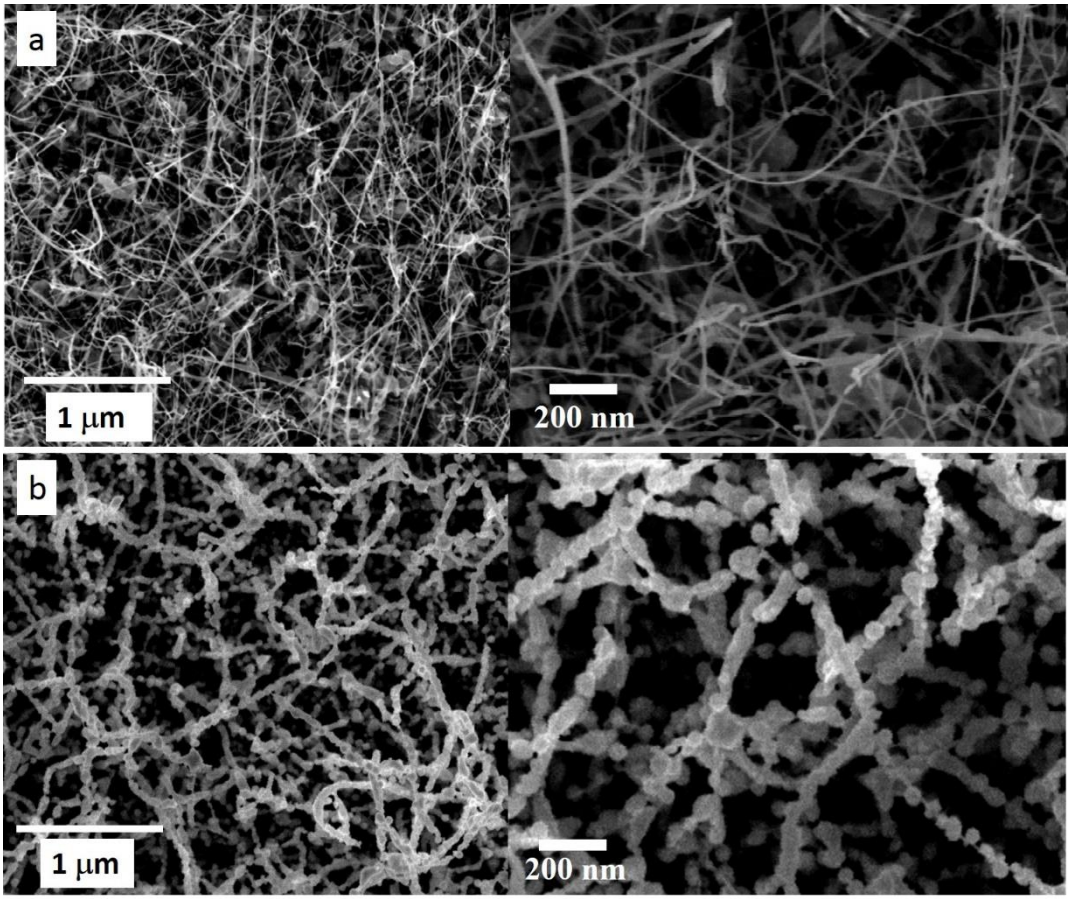

Figure 4.12. Top- view SEM micrographs of the as-grown ZnO nanowires (a) and after the deposition of the Cu NP by ALD (b). On the right, are presented magnified micrographs.

ratio in the ZnO nanowires will increase the absorption of light, increasing the probability of hot electron generation and transfer to the ZnO.

Unfortunately, we have not yet performed electrical characterization of this sample because we need to deposit appropriate contacts in order the measure the I-V characteristics of the device. This remains as a perspective work.

4.8 Chapter Conclusions

In this chapter we have reported the deposition of Cu NP and Cu thin films by atomic layer deposition on ZnO substrates. Obtaining Cu NP by ALD was possible thanks to the Volmer–Weber or island growth mode at early stages of deposition. The NP size, density and surface coverage was controlled by the number of ALD cycles, and an evolution from NP to a continuous Cu film was observed. We achieve the metallic Cu deposition, by a simple ALD route, without the need of incorporating an extra-step with a reducing agent (hydrogen, methanol, isopropanol, etc.) in the ALD process, as usually required.

The NP hold LSPR, as demonstrated by ellipsometric measurements. Furthermore, the plasmon wavelength was tuned continuously between the visible and near-infrared regions, by changing the NP size and separation, parameters that are controlled by the number of ALD cycles.

A highly responsive visible-light photodetector was fabricated based on hot electron injection from Cu NP exhibiting LSPR to ZnO thin films, as demonstrated by C-AFM measurements. The significant photoresponse of Cu NP/ZnO device together with the possibility of tuning the LSPR band between the visible and near-infrared regions of the electromagnetic spectrum open an avenue toward the development of new systems for plasmon-enhanced light-emitting and photovoltaic devices.

Finally, the deposition of Cu NP on ZnO nanostructures by ALD offers the possibility to cover high aspect ratio structures and complex three-dimensional surfaces, which is highly demanded for applications related to gas sensing, plasmon catalysis, and plasmonic energy conversion.

Chapter 5

Fabrication of Semi-Transparent p-Cu_2O/n-ZnO Thin Film Heterojunctions for Photovoltaics and Photo-detecting Applications

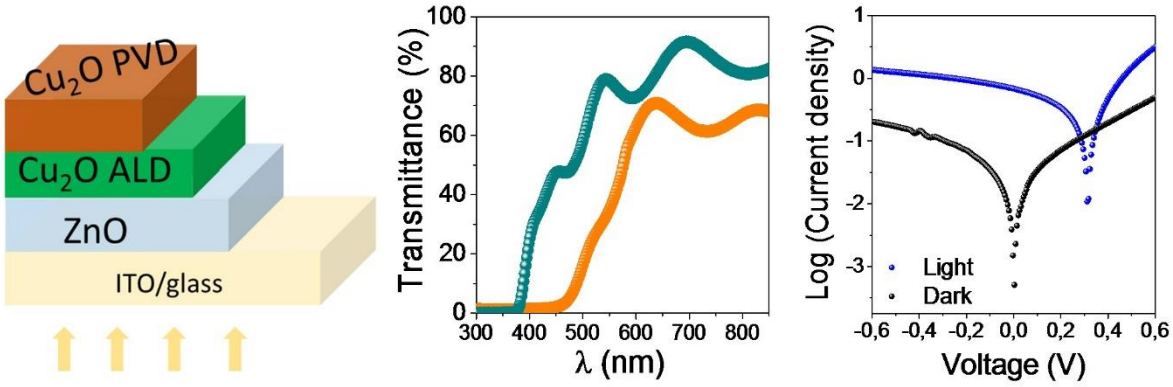

ABSTRACT: In this chapter we present results on the fabrication of semi-transparent heterojunctions based on Cu_2O and ZnO thin films by atomic layer deposition and reactive magnetron sputtering. High-resolution transmission electron micrographs show the high crystalline quality of the films deposited. Electrical measurements performed to the Cu_2O films show very low resistivity and high mobility values of 9 - 150 Ω cm and 19 cm^2 / Vs, respectively. The Cu_2O/ZnO heterojunctions exhibit a non-linear rectifying behavior characteristic of a p-n junction, self-powered photo-response under 1-Sun illumination and high transmittance in the visible region of the electromagnetic spectrum, which is promising for all-oxide transparent electronics, photodetection and photovoltaics applications.

Contents

5.1 Introduction

Among the present challenges faced by photovoltaic (PV) technology is the need to move towards the use of abundant, non-toxic and inexpensive materials. PV devices based on semiconductor oxides is a promising solution [8]. Cu_2O has gained a lot of interest due to its high absorption coefficient in the visible region, chemical stability and earth abundance. Oxide-based thin films solar cells with Cu_2O as absorber layer have a theoretical efficiency of 23% [8]. However, until now the efficiency record has only reached 8.1% in n-type multi-component oxide and p-type Na-doped Cu_2O sheet [76], remaining still far from the theoretical value (see details in Chapter 1).

The intrinsic p-type conductivity of Cu_2O makes difficult the creation of a n-p homo-junction and then achieving the maximum efficiency. Therefore, research has been focused on combining Cu_2O with n-type wide band gap oxides such as ZnO, TiO_2, In_2O_3, In_2O_3: Sn (ITO), and Ga_2O_3 [67,77,93,95,234]. Among these materials, ZnO is an attractive candidate due to its wide band gap and high electron mobility. Efficiencies around 1-4 % have been reached in ZnO/Cu_2O heterojunction, and an efficiency of 4.08 % has been reported in an AZO/ZnO/Cu_2O structure [235]. Nevertheless, the efficiency and the open circuit voltage vary widely depending on the synthesis method. Factors contributing to low efficiency include high surface recombination and poor charge collection [16]. Therefore, analysis and optimization of the interface between both oxides is a particularly important issue in order to improve the performance of the heterojunctions.

Nowadays, PV technology has been implemented mainly in solar farms and roof panels, but the entire area around the building offers opportunities to significantly increase the conversion of solar energy into electricity. Transparent and semi-transparent PV technology hold promising opportunities in the field of building-integrated PV, since transparent solar panels can be integrated into glass facades, windows, sun-breakers, etc [236]. The fabrication of transparent and semi-transparent solar cells based on semiconductor oxides has the advantage of reducing the costs of production, the environmental impact and promoting large scale incorporation. Cu_2O/ZnO heterojunctions are well suited for such applications considering the wide band gap of ZnO and the relatively large band gap of Cu_2O (2.4 - 2.5 eV) [16].

In this chapter we present the fabrication of semi-transparent Cu_2O/ZnO heterojunctions by atomic layer deposition of Cu_2O on ZnO deposited using reactive magnetron sputtering. The fabrication of the Cu_2O thin films by ALD results in high crystalline quality films and has the advantages of large scale scalability, on the one hand, and possible incorporation into

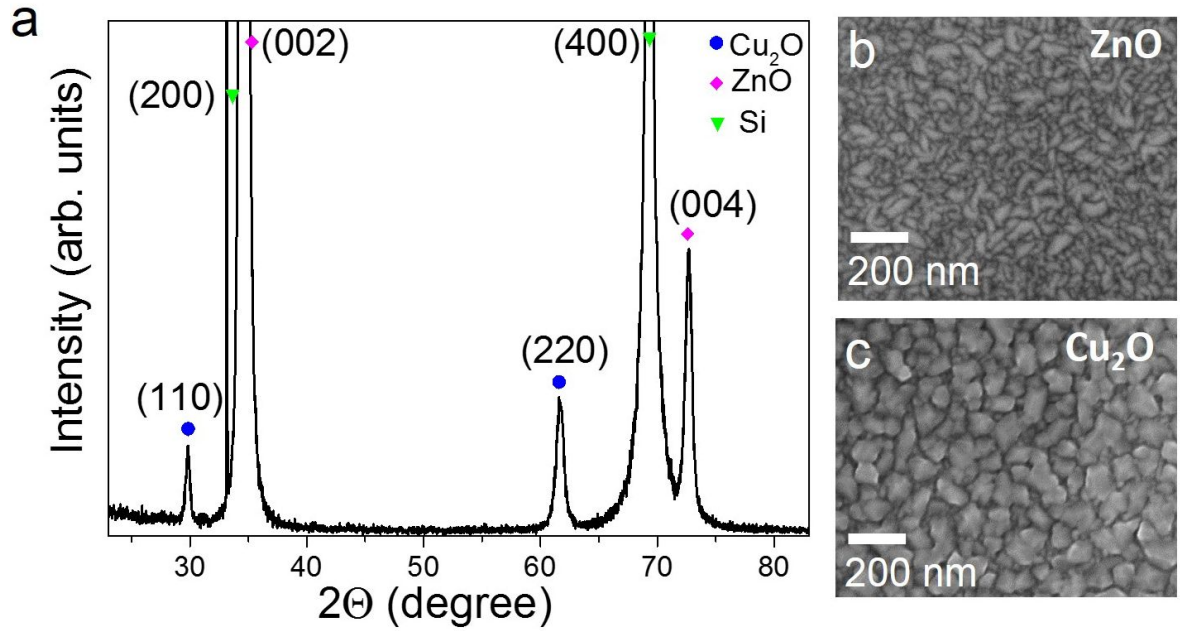

Figure 5.1. X-ray diffrcatogram of the Cu_2O/ZnO heterostructure (a). Top-view SEM micrograph of the as-grown ZnO film (b) and of the Cu_2O film deposited on top (c).

nanostructured devices in which conformability is a fundamental factor, on the other hand. The possibility of fabricating semi-transparent heterojunctions based on these materials is very promising not only in the field of semi-transparent PV but in the field of all-oxide transparent electronics, optoelectronic devices, transparent thin film transistors, among others.

5.2 Structural, Morphological and Chemical Characterization

In Chapter 3 we have reported the area-selective ALD growth of Cu_2O and metallic Cu thin films on ZnO substrates using $Cu(hfac)_2$ as precursor, in the temperature window 250-300 °C. In the present work we use the optimized conditions for the growth of single phase Cu_2O at 280 °C. ZnO thin films were grown by reactive magnetron sputtering at P_{O_2} of 0.07 Pa (see details in Chapter 2).

Figure 5.1 a shows the X-ray diffractogram of a typical Cu_2O/ZnO/Si sample. The ZnO films are c-axis oriented since only the (00l) diffraction lines were observed in the X-ray diffractograms. Cu_2O films are textured with the [110] direction parallel to the ZnO c-axis, since only the (110) and (220) diffraction planes are observed. The morphology of both films can be seen in the top-view SEM micrograph in Figure 5.1 b, c. In order to perform TEM analysis to the sample, TEM lamellas were prepared by FIB. Figure 5.2 a shows a HR-TEM micrograph of the ZnO film with the corresponding FFT taken in the region enclosed by the white rectangle (Figure 5.2). The ZnO film shows a c-axis oriented columnar structure, in

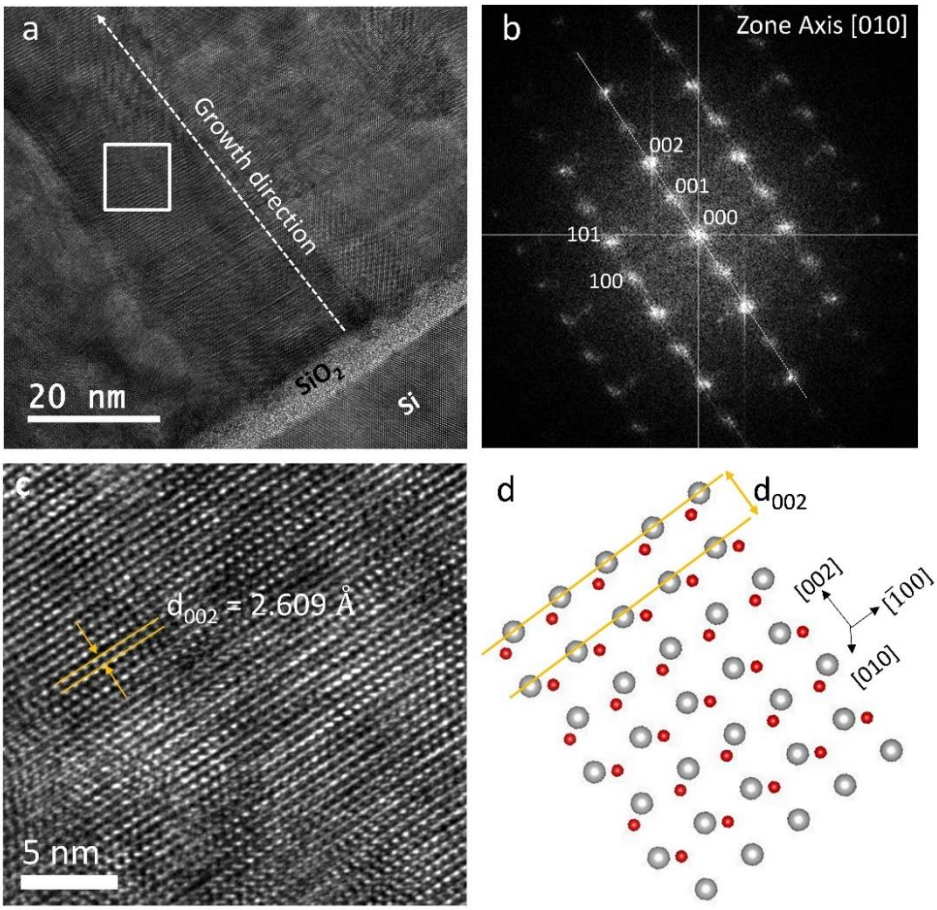

Figure 5.2. Cross-section HR-TEM micrograph of the ZnO film (a) with the corresponding FFT pattern (b). Amplified HR-TEM micrograph, the (002) planes are indicated (c). Schematic of the ZnO crystal structure, where the (002) planes are indicated (d).

agreement with the XRD results. A magnified micrograph is shown at Figure 5.2 c. A value 2.609 A was measured for the lattice spacing of the (002) crystallographic planes. As a comparison, in Figure 5.2 d is depicted a schematic of the atoms arrangement on the (002) planes; the red and gray circles correspond to oxygen and zinc atoms, respectively.

Figure 5.3 a shows a HR-TEM micrograph of one of the Cu_2O grains with the corresponding FFT pattern on the right (see Figure 5.3 b). The growth direction is indicated by a dotted line in the HR-TEM micrograph, and it corresponds to the [110] crystallographic direction, in agreement with XRD results that show a texture in this direction. Figure 5.3 c shows a magnified micrograph taken at the center of Figure 5.3 a. The (110) and (220) crystallographic planes are indicated and the lattice spacing was measured to be 0.30 nm and 0.15 nm, respectively, in agreement with the values reported for cubic Cu_2O (JCPDS 04-007-9767). On the right (Figure 5.3 d) a schematic of the 110 planes from the [001] zone axis is depicted for comparison with the amplified HR-TEM micrograph.

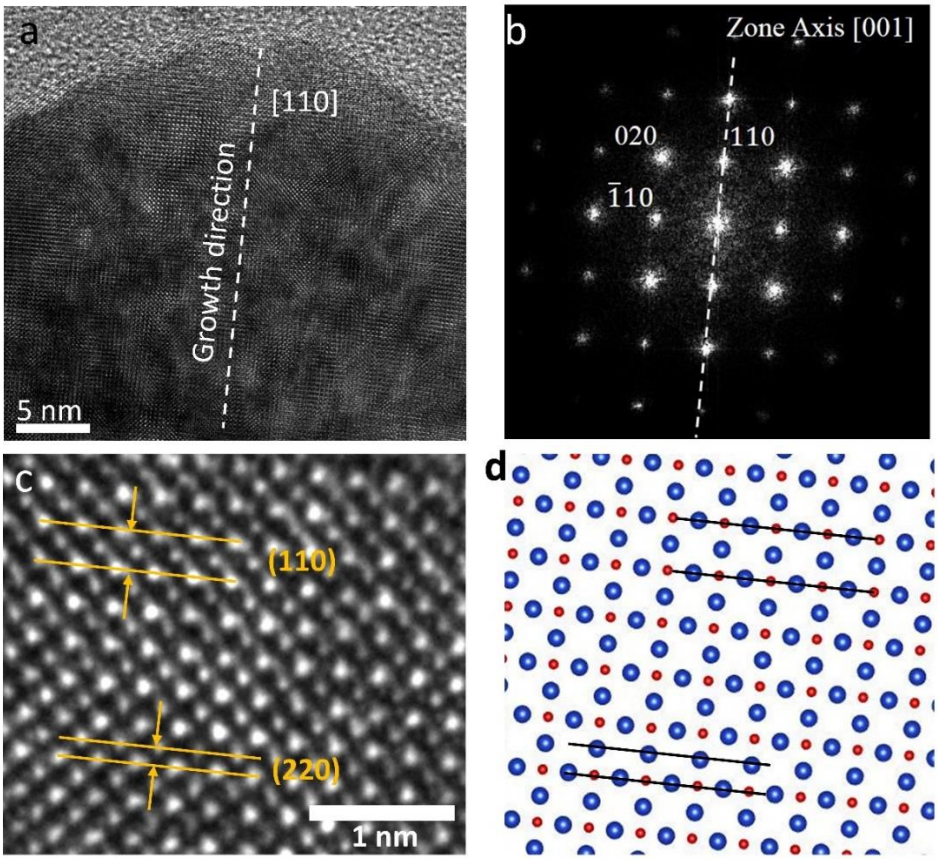

Figure 5.3. Cross-section HR-TEM micrograph of the Cu_2O film (a) with the corresponding FFT pattern (b). Amplified HR-TEM micrograph, the (110), and (220) planes are indicated (c). Schematic of the Cu_2O crystal structure (d).

The typical epitaxial relationship of (110) Cu_2O || (001) ZnO; [001] Cu_2O || [010] ZnO was observed between both layers (see details in Chapter 3). A bright-field STEM micrograph taken at the interface between Cu_2O and ZnO is presented in Figure 5.4 a. EDS analysis was performed to the sample in the region enclosed by a white rectangle, the compositional profiles for Cu (orange), Zn (violet) and O (black) are displayed in Figure 5.4 b (dashed lines indicate the expected concentration for stoichiometric Cu_2O and ZnO). For the Cu_2O film, the atomic concentration obtained for copper (~ 69 %) and oxygen (~ 31 %) are in relatively good agreement with those expected for the stoichiometric material, and just a very small oxygen sub-stoichiometry is observed. On the other hand, the ZnO film presents a high sub-stoichiometry in oxygen. The high transparency of the film (see section 5.5) together with the relatively high resistivity of 150 Ω cm (section 5.4) are in contradiction which such high oxygen sub-stoichiometry, which probably indicates that the oxygen content in the film have been underestimated.

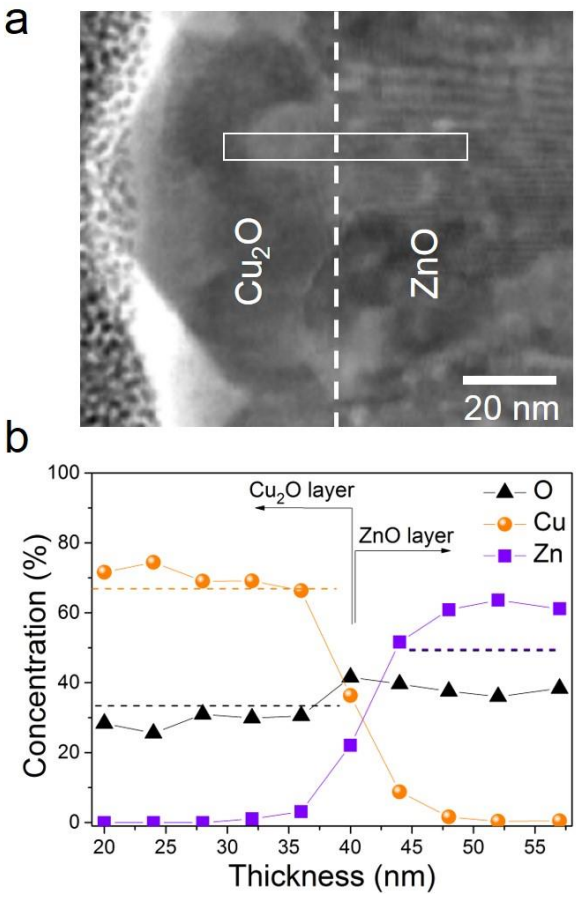

Figure 5.4. Bright field STEM micrograph taken at the interface between Cu_2O and ZnO films (a). Composition profiles obtained by EDS in the region enclosed by a rectangle in a (dashed lines indicate the expected Cu, Zn and O concentrations for the stoichiometric Cu_2O and ZnO) (b).

5.3 Optical Characterization of the Cu_2O and ZnO Films

Ellipsometric measurements were performed to the samples in the 0.6 eV - 4.5 eV spectral range. A schematic of the physical model employed is shown in Figure 5.5 b. The model consists of a three-layer structure on top of a Si substrate. For the Cu_2O layer, it was necessary to consider an uppermost layer composed of 50% Cu_2O and 50% voids in order to take into account the roughness at the surface.

The dielectric function of ZnO was determined before the Cu_2O deposition, as in the case of the Cu NP/ZnO sample (see Chapter 4). The dielectric function of the Cu_2O film (ε_{Cu_2O}) was modeled by the Tauc-Lorentz dispersion law:

$$\varepsilon_{\mathrm{i}} = \frac{1}{\omega}\frac{A\,\omega_0\,C\,(\omega-\omega_{\mathrm{g}})^2}{(\omega^2-\omega_0^2)^2+C^2\omega^2}\,\Theta(\omega-\omega_{\mathrm{g}}) \qquad \textbf{(5.1)}$$

$$\varepsilon_r = \varepsilon_\infty + \frac{2}{\pi} P \int_{\omega_g}^{\infty} \frac{\Omega\, \varepsilon_i(\Omega)}{\Omega^2 - \omega^2} d\Omega \qquad \textbf{(5.2)}$$

Where the Heaviside distribution $\Theta(\omega - \omega_g)$ is zero when $\omega \leq \omega_g$ and equal to 1 when $\omega > \omega_g$, ε_r and ε_i are the real and imaginary part of the Cu_2O dielectric function, ε_∞ is the high-frequency dielectric constant, ω_0 is the the energy of the first transition, ω_g is the energy gap of Cu_2O, A is the transition matrix element, and C a broadening term.

The effective dielectric function (ε_{eff}) of the uppermost layer that accounts for the roughness at the surface was described by the Bruggeman's effective medium model, considering 50% Cu_2O and 50% voids:

$$0 = \frac{1 - \varepsilon_{eff}}{1 + 2\,\varepsilon_{eff}} + \frac{\varepsilon_{Cu2O} - \varepsilon_{eff}}{\varepsilon_{Cu2O} + 2\,\varepsilon_{eff}} \qquad \textbf{(5.3)}$$

The thickness of the ZnO film and the thickness and roughness of the Cu_2O film, together with the parameters A, C, ε_∞, ω_0 and ω_g were determined by fitting the model to the ellipsometry data (see Appendix 1). The values obtained for the thickness of the Cu_2O and ZnO

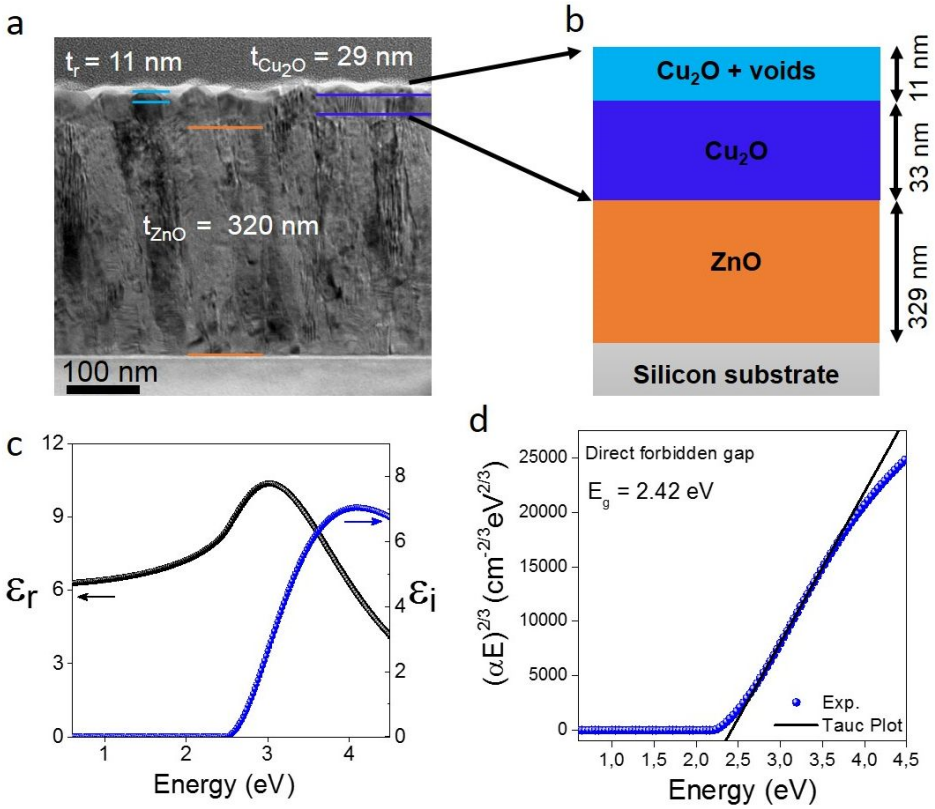

Figure 5.5. TEM micrograph of the Cu_2O/ZnO heterojunction (a). Schematic of the physical model used for fitting the ellipsometric data (b). Real and imaginary parts of the dielectric function of the Cu_2O film determined by ellipsometry (c). Tauc Plot for the Cu_2O film (d).

layers are shown in Figure 5.5 b. These values are in good agreement with those measured directly form the cross-section TEM micrograph presented in Figure 5.5 a. Real (ε_r) and imaginary (ε_i) parts of the dielectric function, extracted from the fitting of ellipsometry measurements are shown in Figure 5.5 c. The band gap of the Cu_2O film was determined from the Tauc Plot (see Figure 5.5 d). Cu_2O is a semiconductor with a direct forbidden band gap, which means that the direct transition from the highest valence band maximum to the lowest conduction band minimum is parity forbidden [10]. Therefore, an exponent of 3/2 was used for the Tauc plot in this case. Values around 2.42 - 2.55 eV were obtained for the Cu_2O films, in good agreement with the values reported in the literature for this material [16].

Transmittance and reflectance measurements were also performed to the Cu_2O and ZnO films growth on α-Al_2O_3 and glass substrates, respectively. In Figure 5.6, the absorption coefficient for the Cu_2O film deposited on α-Al_2O_3 is shown. The change in slope observed around 2.4 eV in the absorption spectrum (Figure 5.6 a) is the result of the contribution of the blue and violet excitonic series to the absorption of Cu_2O [14]. The contribution at 2.72 eV corresponds very well with the values reported for the violet excitonic serie [10]. A schematic of the Cu_2O electronic band diagram, with the four excitonic series (yellow, green, blue, and violet) that result from the transition from the conduction (E_C) to valence (E_V) bands are shown in Figure 5.6 b. The yellow and green lowest energetic transitions are dipole-forbidden, therefore we only observe the blue and violet series in the absorption spectrum.

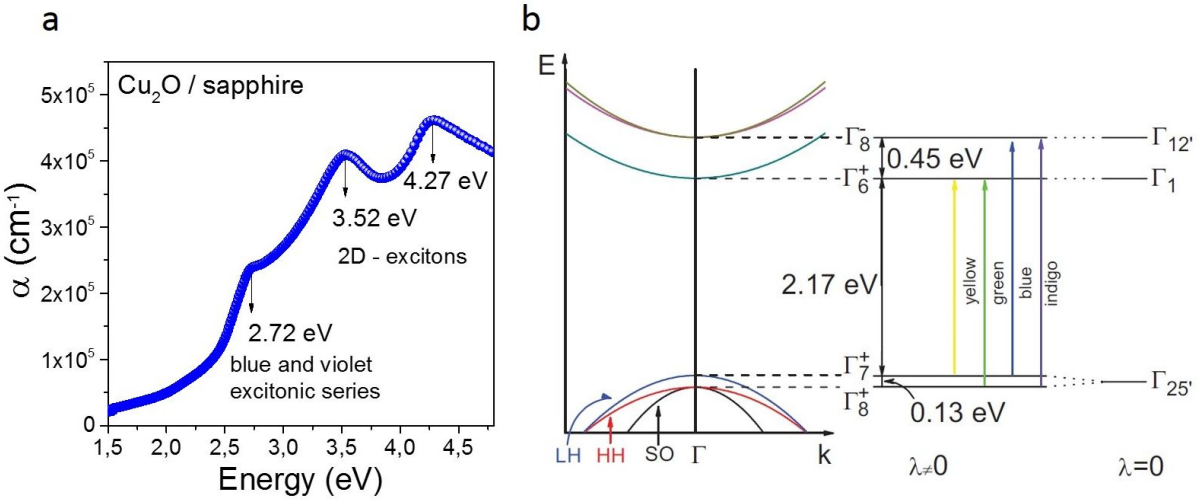

Figure 5.6. Absorption coefficient for the Cu_2O film deposited on α-Al_2O_3 (a). Schematic of the Cu_2O electronic band structure around the center of the Brillion zone (**Γ**-point), without (λ=0) and with (λ≠0) spin-orbit interaction. Transition from the $\boldsymbol{E_C}$ to the $\boldsymbol{E_V}$ leads to the four excitonic series represented in color lines (b).

Finally, the peaks located around 3.52 and 4.27 eV have been ascribed to the 2D excitonic transitions [237]. The possibility to observe the excitonic peaks at room temperature is due to the high exciton binding energy for Cu_2O (~150 meV). Furthermore, this is an evidence of the good quality of our Cu_2O films deposited by ALD. The band gap of the Cu_2O film was determined from the Tauc Plot (see Figure 5.7 a). A value of 2.44 eV is determined, in good agreement with the values obtained by ellipsometry.

The band gap of ZnO was also determined from transmittance measurements of ZnO films deposited on glass substrates. ZnO is a direct band gap semiconductor, therefore an exponent n=1/2 was used for the Tauc plot (see Figure 5.7 c). A value of 3.16 eV is obtained. This value is smaller compared with the typical values of ca. 3.37 eV reported for ZnO. However, a red shift of the optical band gap of ZnO films deposited by reactive magnetron sputtering has been reported when decreasing the oxygen partial pressure, related with the oxygen vacancies content in the film. Liu *et. al.* [238] reported ZnO band gap values ranging from 3.1 to 3.26 eV for oxygen partial pressures between 0.1 and 0.25 Pa. In our case an oxygen partial pressure of 0.07 Pa was employed, which results in low values for the ZnO band gap, in relatively good agreement with the results of Liu *et. al.*, and in agreement with the compositional profiles obtained by EDS that indicates a sub-stoichiometry in oxygen for the ZnO film.

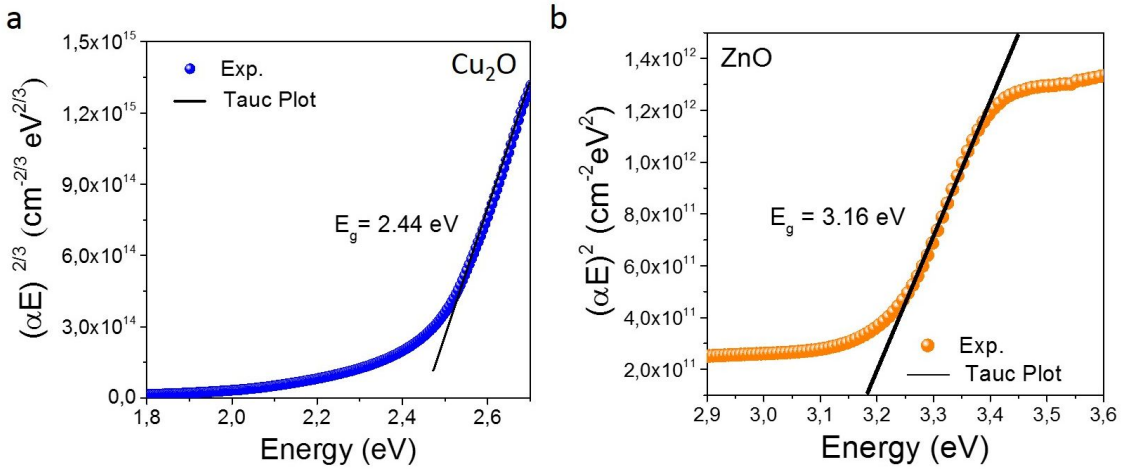

Figure 5.7. Tauc Plot for the Cu_2O (a) and ZnO (b) films deposited on α-Al_2O_3, and glass substrates, respectively.

5.4 Electrical Characterization of the Films

Four point probes measurements were performed in order to determine the resistivity of the Cu_2O films deposited on ZnO substrates. The typical values reported in the literature for this

material change widely depending on growth conditions and ranges from 10 to 10^5 Ω cm [239,240]. Values between 7-61 Ω cm have also been reported for sputtered Cu_2O samples after air-annealing (thicknesses ~ 820 nm) [16] and values around 125 Ω cm have been obtained for Cu_2O thin films (~100 nm) deposited by atmospheric ALD [28]. In our case, the resistivity values were in the range 9 – 150 Ω cm, in good agreement with the best ones described previously. Hall effect measurements were performed to the Cu_2O film of lowest resistivity and the values of carriers concentration and mobility are $4 \times 10^{16}\ cm^{-3}$ and $19\ cm^2/Vs$, respectively. This low resistivity and high mobility values are explained by the good crystalline quality of the Cu_2O film, confirmed by the HR-TEM micrographs. In fact, the local epitaxial relationship between the Cu_2O and the ZnO film favors the growth of a high quality Cu_2O layer, which results in higher mobility and higher carrier's diffusion length due to lower defect density in the Cu_2O layer and at the heterojunction interface. Furthermore, the large size of Cu_2O grains (~100-200 nm) observed in the top-view SEM micrograph also contributes to the high mobility, since electron scattering at grain boundaries is reduced [28,137,210].

For the ZnO films deposited on Si substrates, resistivity values change widely with the oxygen partial pressure and the position of the substrate in the substrate holder (see Chapter 3). In particular, the ZnO films used for the fabrication of the heterojunction (P_{O_2} = 0.07 Pa, d = 5 cm) show resistivity values of 150 – 200 Ω cm. The Hall measurements performed to this sample were very unstable and for this reason are not reported here.

5.5 Electrical and Optical Characterization of the Heterojunctions

For the optical and electrical characterization of the junctions, a Cu_2O (40 nm) / ZnO (250 nm) heterojunction was deposited on top of an ITO/glass substrate. The transmittance spectrum of the Cu_2O/ZnO heterojunction is displayed in Figure 5.8 a. The black line corresponds to the sputtered ZnO thin film and the blue line is after the deposition of Cu_2O by ALD. Oscillations are due to optical interference phenomena. The average transmittance (AVT) of the system was determined following the same approach that is employed in window technology and described by the following equation [89],

$$AVT = \frac{\int T(\lambda)P(\lambda)S(\lambda)d\lambda}{\int P(\lambda)S(\lambda)\,d\lambda} \qquad \textbf{(5.4)}$$

where λ is the wavelength, T the transmittance of the sample, P is the photopic response of the human eye [241] (Figure 5.8 a, violet line) and S the Solar flux (AM1.5G). For the Cu_2O/ZnO/ITO/glass sample an AVT of 73 % was obtained when integrating over the visible range of the electromagnetic spectrum (400 - 700 nm). A picture of the sample is shown at the

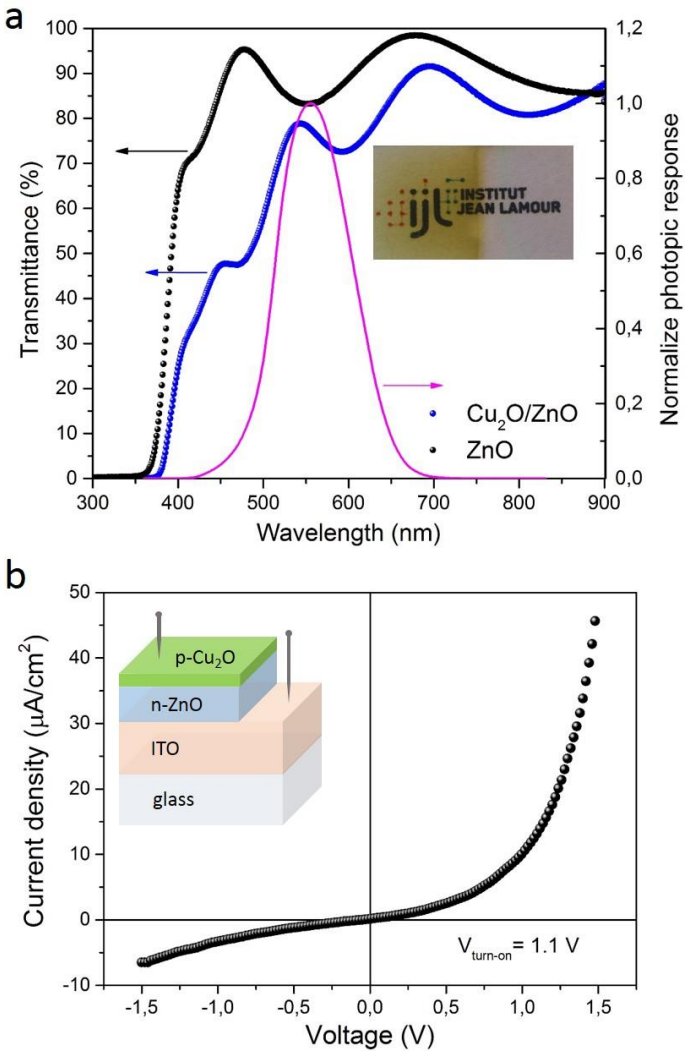

Figure 5.8. Transmittance of the ZnO film (black), Cu_2O/ZnO film (blue) and the normalized photopic response of the human eye (magenta) (a), at the inset a picture of the sample deposited on a glass substrate resting on a piece of paper with IJL logo to illustrate the transparency, the left side corresponds to the Cu_2O/ZnO junction and the right side to the ZnO film alone. Current density-voltage characteristics of the p-Cu_2O/n-ZnO/ITO junction (b), schematic of the sample configuration for the measurement at the inset.

inset of Figure 5.8 b. The left side (yellow-brown) corresponds to the Cu_2O/ZnO/glass and the right side is the uncovered ZnO film (this region was masked during ALD deposition).

To verify the rectifying behavior of the Cu_2O/ZnO heterojunctions, electrical measurements were performed to the samples. The contacts to the sample were done through two metallic needles as depicted in the schematic of Figure 5.8 b, inset. Figure 5.8 b, shows the current density – voltage (J-V) characteristics of the sample. A non-linear rectifying behavior is observed, demonstrating the formation of the p-n junction between the Cu_2O and the ZnO thin films. A turn-on voltage of 1.1 V was measured form the J-V curve.

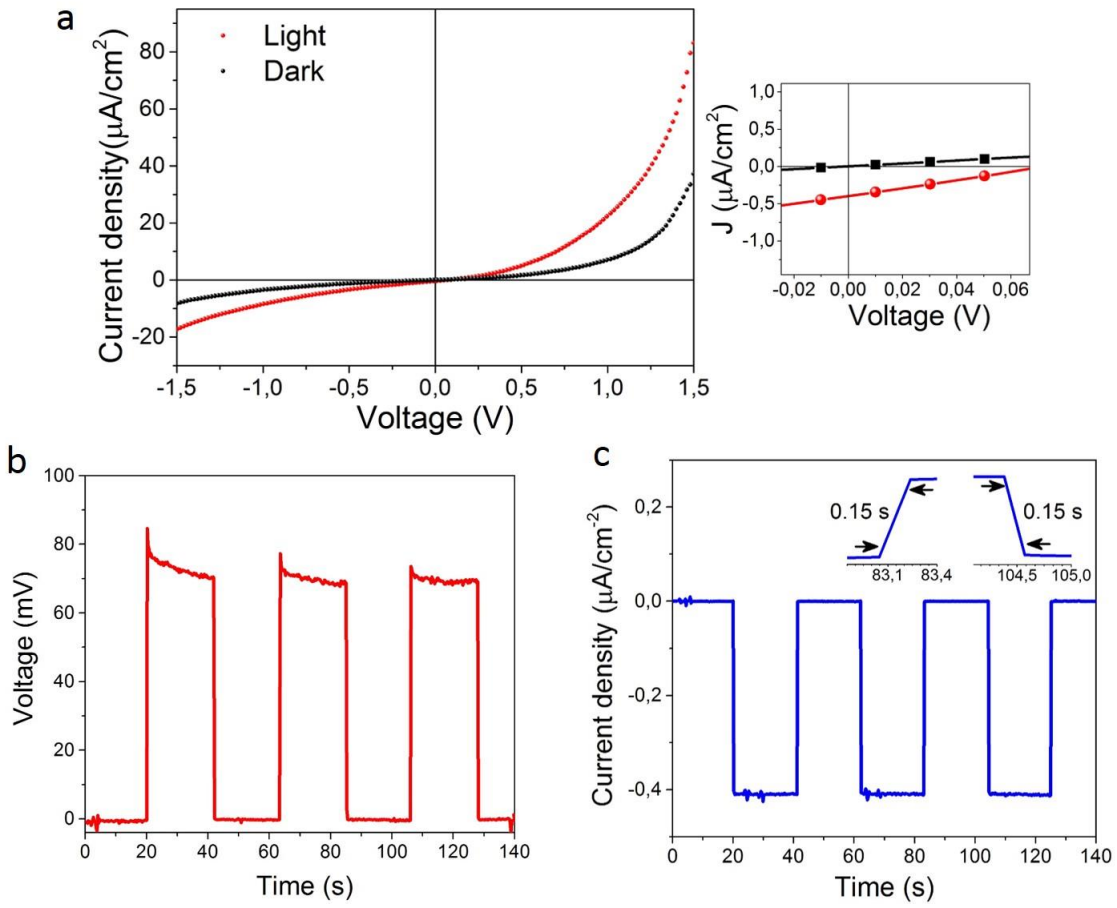

Figure 5.9. Current density characteristics of the Cu_2O/ZnO heterojunction in the dark and under 1 Sun illumination (a). Voltage (b) and current density (c) versus time during multiples dark/light cycles of 20 seconds.

In order to analyze the possible photo-response of the heterojunction, J-V characteristics were measured by exposing $0.16\ cm^2$ of the sample to 1 Sun (see Figure 5.9). As can be seen in Figure 5.9 a, there is an enhancement of the photocurrent under both forward and reverse voltages. Moreover, a clear photovoltaic effect is observed with open circuit voltage and short circuit current of $V_{OC} = 72\ mV$ and $I_{SC} = 0.44\ \mu A/cm^2$, respectively (see the inset of Figure 5.9 a). Typical values of V_{OC} and I_{SC} for traditional Cu_2O/ZnO-based heterojunctions has ranged from $0.2 - 0.7\ V$ and $1.8 - 11.4\ mA/cm^2$, respectively [94,242,243]. The small values obtained in this case are due to the very thin Cu_2O films which result in low absorption, and the absence of appropriate contacts at the Cu_2O film. In Figure 5.9 the voltage (b) and the current density (c) are reported during several dark/light cycles at 0 V bias voltage. As can be seen, the device can be switched on/off showing relatively good stability for V_{OC} and I_{SC}. The possibility of observing a photovoltaic effect in such small absorber layer is promising.

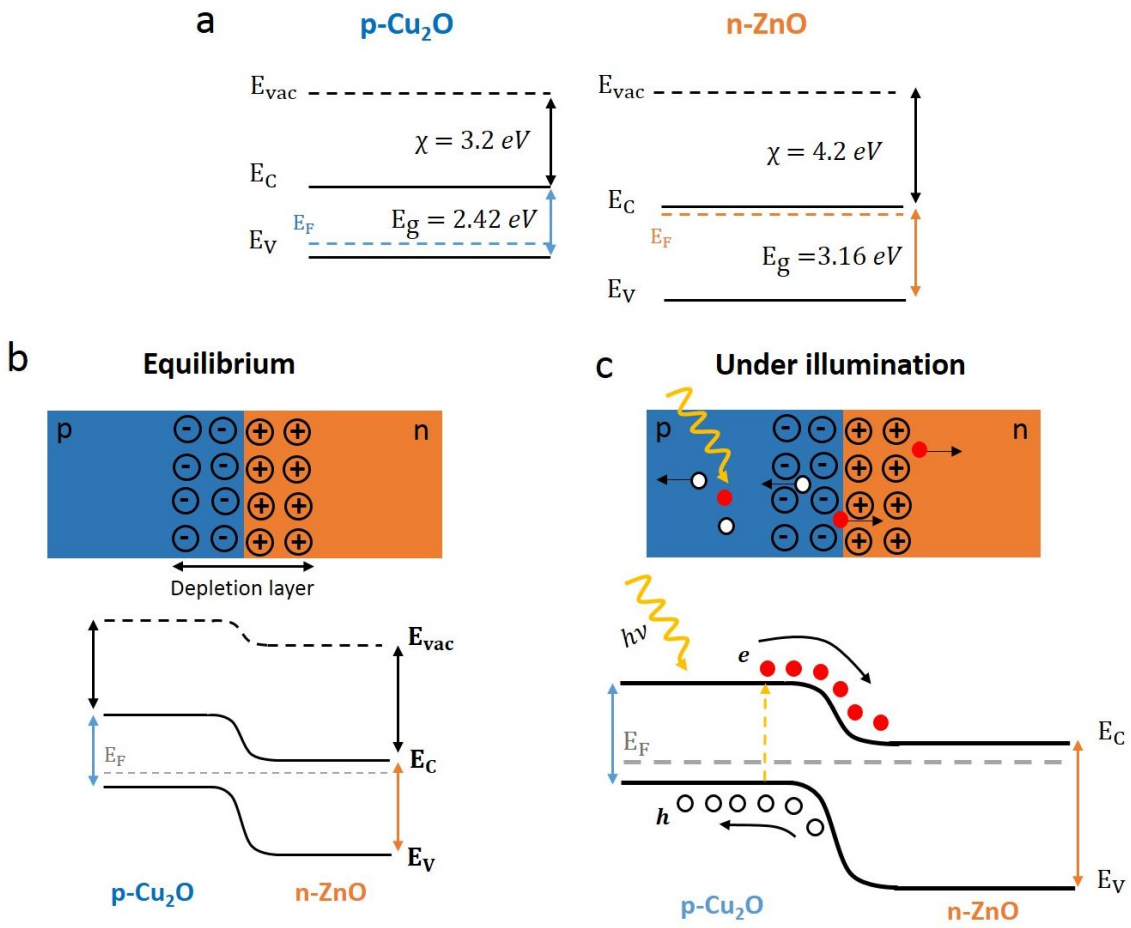

Figure 5.10. Band energy diagram of the isolated Cu_2O and ZnO semiconductor (a) and after the formation of the heterojunction under equilibrium (b) and under illumination at 0 bias voltage (c).

A simplified schematic of the band energy diagram for the isolated Cu_2O and ZnO semiconductors is depicted in Figure 5.10 a. The electron affinity values have been taken from the literature [48], and the bandgaps were determined from ellipsometry and UV-VIS spectroscopy for the samples obtained in this work. The band bending at the interface after the heterojunction formation is shown in Figure 5.10 b under equilibrium conditions. A schematic illustrating the photocurrent generation at 0 bias voltage under illumination is shown in Figure 5.10 c. Electron-hole pairs generated after light absorption in Cu_2O are separated in the space charge region (depletion layer) by the built-in electric field and collected by the electrodes, producing the photocurrent detected in Figure 5.9 c. It is worth to note that the diagram of Figure 5.10 c is valid for a solar cell in short circuit conditions and if the internal series resistance is neglected. If the device is connected to an external load, a potential drop is produced, reducing the electric field at the junction. In consequence, the Fermi level will be

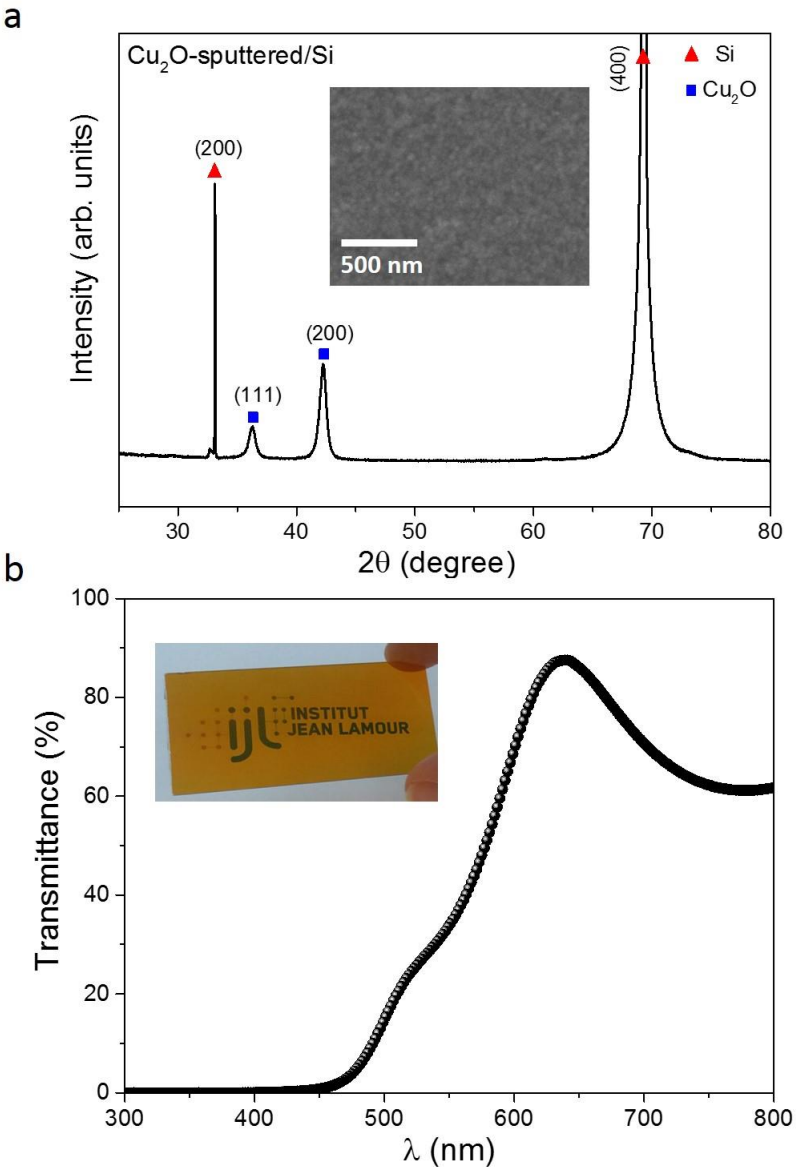

Figure 5.11. X-ray diffractogram of the Cu_2O film deposited on Si substrate (a), a top-view SEM micrograph is shown as inset. Transmittance spectrum of the Cu_2O film deposited on a glass substrate (b), a picture of the sample is shown as inset.

split into two quasi-Fermi levels (E_{f_n} for electrons and E_{f_p} for holes), and the band bending is modified with respect to the equilibrium conditions.

The photoconductive behavior of the device together with the observed self-powered photoresponse can be also interesting for UV-VIS photodetection. The maximum responsivity of the device was of 461 μA/W, obtained at a forward bias voltage of 1.5 V. Additionally, the response time of the system was calculated as the time required to go from 10 % to 90 % of maximum amplitude of the current pulse (Figure 5.9 c, inset). Values around 0.10 to 0.15 s were measured from several pulses, which are faster as compared with other similar oxide-

based visible photodetectors [244], and are in relatively good agreement with the values obtained for some nanostructured Cu_2O/ZnO photodetectors [9,86,92].

5.6 Characterization of the Sputtered Cu_2O films

One of the possibilities for improving the electrical parameters of the heterojunctions is increasing the thickness of the Cu_2O absorber layer. Cu_2O thin films deposited by ALD allow the formation of a high quality interface with the ZnO due to the local epitaxial growth described before. However, the slowness of the process makes unpractical the deposition of thicker films. Therefore, we decided to deposit a thin film of Cu_2O by ALD (~ 40 nm) and proceed with the deposition of a thicker Cu_2O layer by reactive magnetron sputtering on top of it. This process allows keeping a good interface and at the same time increasing the absorption of light. For semi-transparent heterojunctions there is always a compromise between transparency and electrical performance. The heterojunction studied before presented very high transparency (73 %), which means that there is still room for the improvement of the electrical parameters by increasing the thickness of the absorber layer, keeping a reasonable degree of transparency. The Cu_2O thin film interfacial layer, and the ZnO window layer were deposited by the same process already described before (see section 5.5). In the case of the Cu_2O layer deposited by reactive magnetron sputtering, Ar and O_2 flow rates of 30 and 6 sccm, respectively, were used for the deposition of single phase Cu_2O at a total pressure of 0.5 Pa (more details on the deposition parameters are given in Chapter 2). A Cu_2O film of 200 nm was obtained and it shows a preferential orientation in the [100] direction, as can be seen in the diffractogram of Figure 5.11 a. A top-view SEM micrograph is shown in Figure 5.11 b.

The resistivity of the film was measured by the 4-point probe technique and values of (13.6 ± 1.1) Ωcm were obtained. Hall effect measurements were also performed to the films which provide values for the mobility and carrier concentration of 1.5 cm^2/Vs and 8×10^{16} cm^{-3}, respectively. Figure 5.11 b shows the transmittance spectrum taken to the Cu_2O film grown on a glass substrate. At 200 nm, the film is still transparent with an orange-yellow appearance as can be seen in Figure 5.11 b. A bandgap of 2.45 eV was estimated from the Tauc Plot, close to the value determined for the Cu_2O films deposited by ALD.

5.7 Improving the Electrical Properties of the Heterojunction

In order to perform the electrical and optical characterization of the heterojunctions, the Cu_2O-200 nm-sputtered/ Cu_2O-40 nm-ALD/ ZnO-250 nm was deposited on an ITO/glass substrate, (see schematic in Figure 5.12 a). Figure 5.12 b shows the transmittance spectra of the

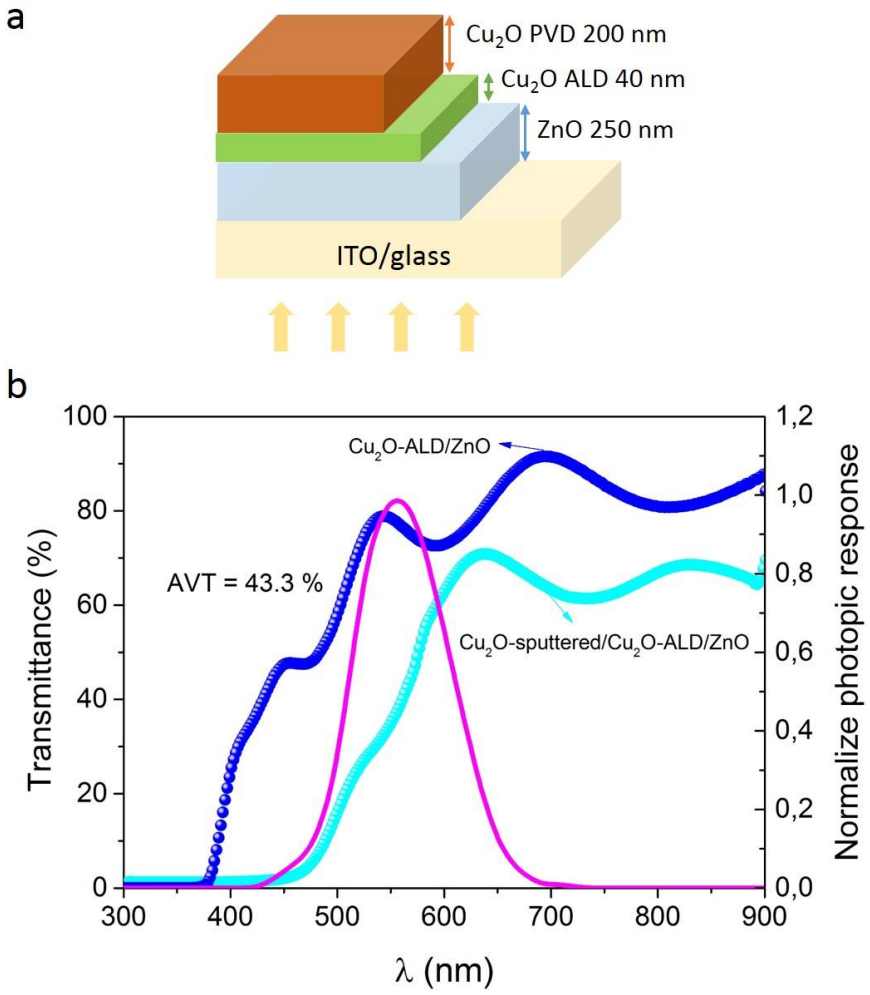

Figure 5.12. Schematic of the heterojunction with the addition of an uppermost Cu_2O layer growth by sputtering (a). Transmittance of the Cu_2O-ALD/ZnO (blue), Cu_2O-sputtered/Cu_2O-ALD/ZnO film (cyan) and the normalize photopic response of the human eye (violet) (b).

heterojunction with (cyan line) and without (blue line) the uppermost sputtered Cu_2O film, for comparison. The AVT was reduced from 73% to 43%, as thickness was increased from 40 to 240 nm. This AVT is still adequate for building-integrated photovoltaic applications, evidently the glass will be tinted and not as clear as for an AVT of 90%, but it is still possible to see through (see Figure 5.11 b, inset). It is generally accepted than AVT higher than 20% are acceptable for building integrate photovoltaics applications [245].

The J-V characteristics for the heterojunction in dark and under 1 Sun illumination are depicted in Figure 5.13 a. An enhancement of the forward and reverse current is observed when the device is illuminated. A photovoltaic effect is clearly observed, with $V_{OC} = 0.32$ V and $I_{SC} = 0.69\ \mu A/cm^2$, respectively. These values are considerably higher than those reported before for the thinner heterojunction (formed only by the 40-nm-Cu_2O-ALD layer), as can be seen in Figure 5.13 b, where the J-V characteristics for both samples are presented around the

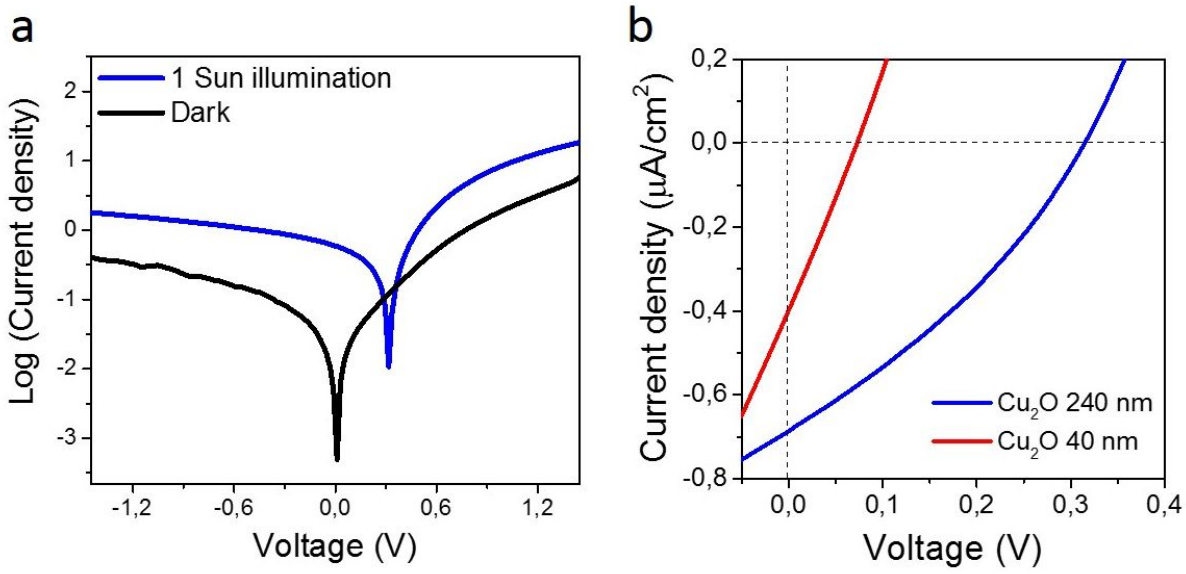

Figure 5.13. Current density characteristics of the heterojunction (in semi logarithmic scale) in dark (black line) and under 1 Sun illumination (blue line) (a). Current density characteristics amplified around the short-circuit current and open-circuit voltage points for the heterojunction with (blue line) and without (red line) the 240-nm-Cu_2O sputtered layer (b).

I_{SC} and V_{OC} points. Evidently, the addition of the 200-nm-Cu_2O-sputtered layer results in a considerable improvement of the junction performance, mainly due to an increase of the light absorption and, in consequence, of the number of photogenerated carriers.

However, the current density values are still very low, the main reason being the absence of an appropriate contact on the Cu_2O film. An Ag contact was deposited on top of the Cu_2O film. Unfortunately, when the electrical measurements were performed on the Ag contact, the cell was short-circuited. To overcome this problem, I-V measurements were done with the electrode directly on the Cu_2O film, with the drawback of low current collection.

Cu_2O films deposited by electrochemical routes typically show V_{OC} values of 0.2 – 0.6 V, for thickness of 2 – 3.5 μm [94,84,246]. The possibility of obtaining V_{OC} values of 0.32 V in our case, where the Cu_2O thickness is only 240 nm, is already promising since minority carrier lengths in Cu_2O have been estimated in the 0.4 – 1 μm range [247]. Therefore, only the carriers photogenerated at this distance from the junction interface will be collected, and carriers generated farther away will recombine before reaching the depletion layer. Thus, thicker absorbing Cu_2O layers result in recombination losses in the device. Therefore, achieving high V_{OC} values with thinner absorbing layers is desired.

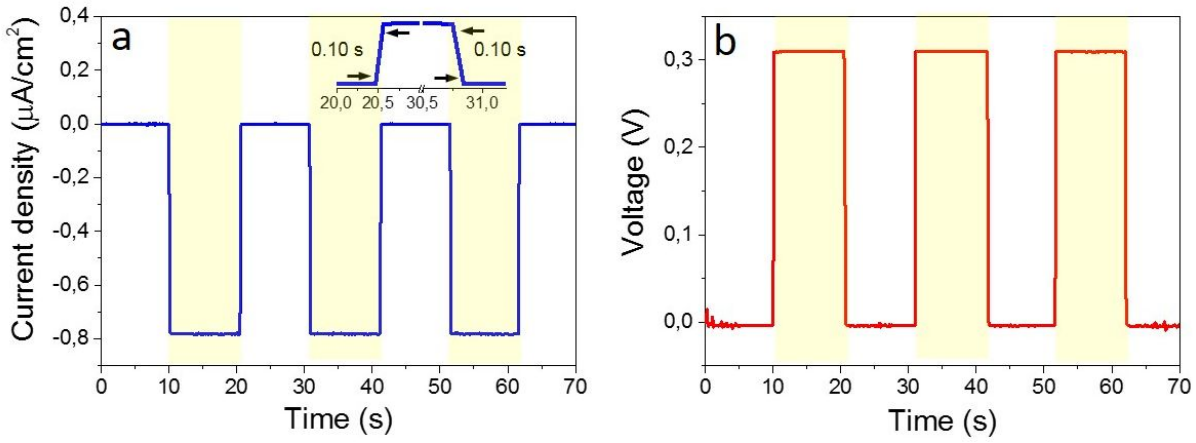

Figure 5.14. Current density (a) and voltage (b) versus time during multiples dark/light cycles of 20 seconds.

The relatively high V_{OC} obtained for our heterojunction can be explained as due to the higher carrier concentration of 10^{16} cm^{-3} in both Cu_2O films (those obtained by ALD and sputtering), compared with the values of the electrodeposited films, as will be discussed below.

The depletion layer thickness at the p-side (x_p) can be determined by,

$$x_p = \sqrt{\frac{2 * \varepsilon_r * \varepsilon_0 * V_{bi}(p)}{q * N_A}} \qquad \textbf{(5.5)}$$

where ε_r is the relative permittivity or dielectric constant of Cu_2O, ε_0 is the vacuum permittivity, N_A the doping density, and $V_{bi}(p)$ the built-in bias at the p-side. It is worth to note that if we consider typical electron concentrations for ZnO films of $10^{18} - 10^{20} cm^{-3}$, which are orders of magnitude higher than for the Cu_2O films, the entire built-in potential will be formed at the p-side, and there will be practically no depletion layer at the n-side [84,248]. From equation (5.5), for a typical built-in potential of 0.7 V (considering the position of the Fermi levels in both materials [34]) the depletion layer thickness at the Cu_2O side will be of 3 μm approximately (considering a carrier concentration of $\sim 10^{13}$ cm^{-3}, typical for electrodeposited films) [34,84]. In consequence, Cu_2O films of at least this thicknesses are required to achieve the full built-in bias and the maximum V_{OC}. If now we consider the hole concentration in our Cu_2O films of 4×10^{16} cm^{-3}, obtained from Hall measurements, and $\varepsilon_r = 8.2$, obtained from ellipsometric measurements (see Figure 5.5 c), from equation (5.5) the depletion layer thickness is considerably reduced to 125 nm [84]. This explain why V_{OC} values of 0.32 V can be attained with considerably thinner Cu_2O layers.

Figure 5.14 a shows the evolution of the current density vs. time during dark/light cycles of 20 s at 0 V bias voltage (short circuit conditions). Analogously, the evolution of the open

circuit voltage vs. time is depicted in Figure 5.14 b. The device shows a stable response with response times of 0.10 ± 0.03 s (see Figure 5.14 a, inset). The fastest response times obtained here, compared with those of others Cu_2O/ZnO visible photodetectors [244,249], can be due to the decrease in the depletion layer thickness at the Cu_2O side, as a result of the high carrier concentration obtained in our Cu_2O films. One of the factors influencing the response speed of a photodiode is the carrier drift transit time across the depletion layer. This time is directly proportional to the depletion layer thickness and inversely proportional to the carrier drift velocity. Therefore, a thinner depletion layer, as the one obtained for our films, results in faster response because the carrier diffusion in the neutral region can be neglected. Moreover, the possibility of developing the full built-in potential will also result in a strong electric field at the junction and a faster charge separation.

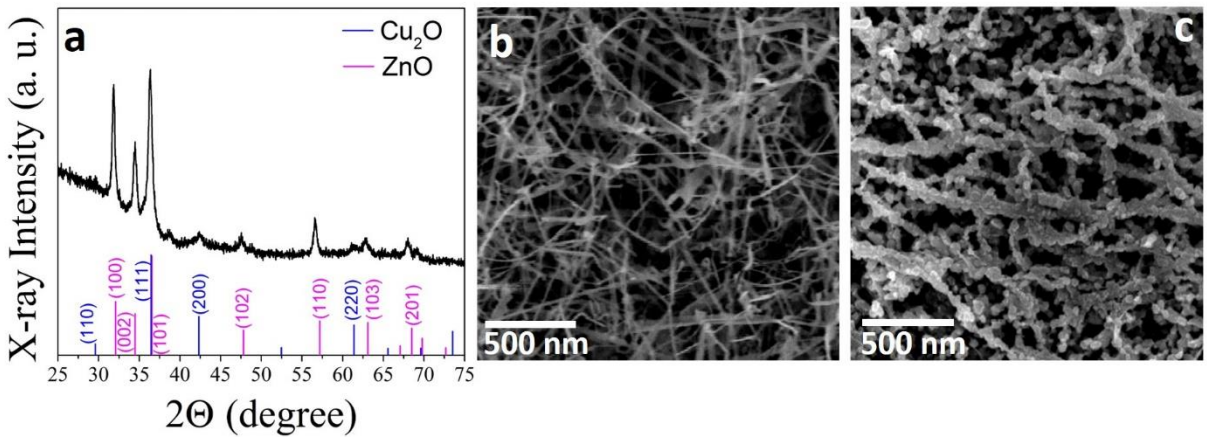

Figure 5.15. X-ray diffractogram of the Cu_2O/ZnO nanowires (a). SEM micrograph of the ZnO before (b) and after the Cu_2O deposition by ALD (c).

5.8 Preliminary Results in the Cu_2O Deposition on ZnO Nanowires

In order to test the possibility of depositing Cu_2O on high aspect ratio structures we employed a substrate formed by ZnO nanowires (the same type of substrates used for the deposition of Cu NP in chapter 4). Cu_2O films were grown by ALD on the nanowires, using the typical conditions employed for the deposition on ZnO thin film, except for the exposure time to $Cu(hfac)_2$ that was increased to 3s to allow the diffusion of $Cu(hfac)_2$ along the nanowires, favoring a conformal growth. The growth temperature was set to 250 °C to allow the growth of single phase Cu_2O, since at 280 °C we have metallic Cu deposition.

The ZnO nanowires obtained by this method are single-crystalline, but randomly oriented with average length of 750 nm [233]. Figure 5.15 a shows a X-ray diffractogram of the sample

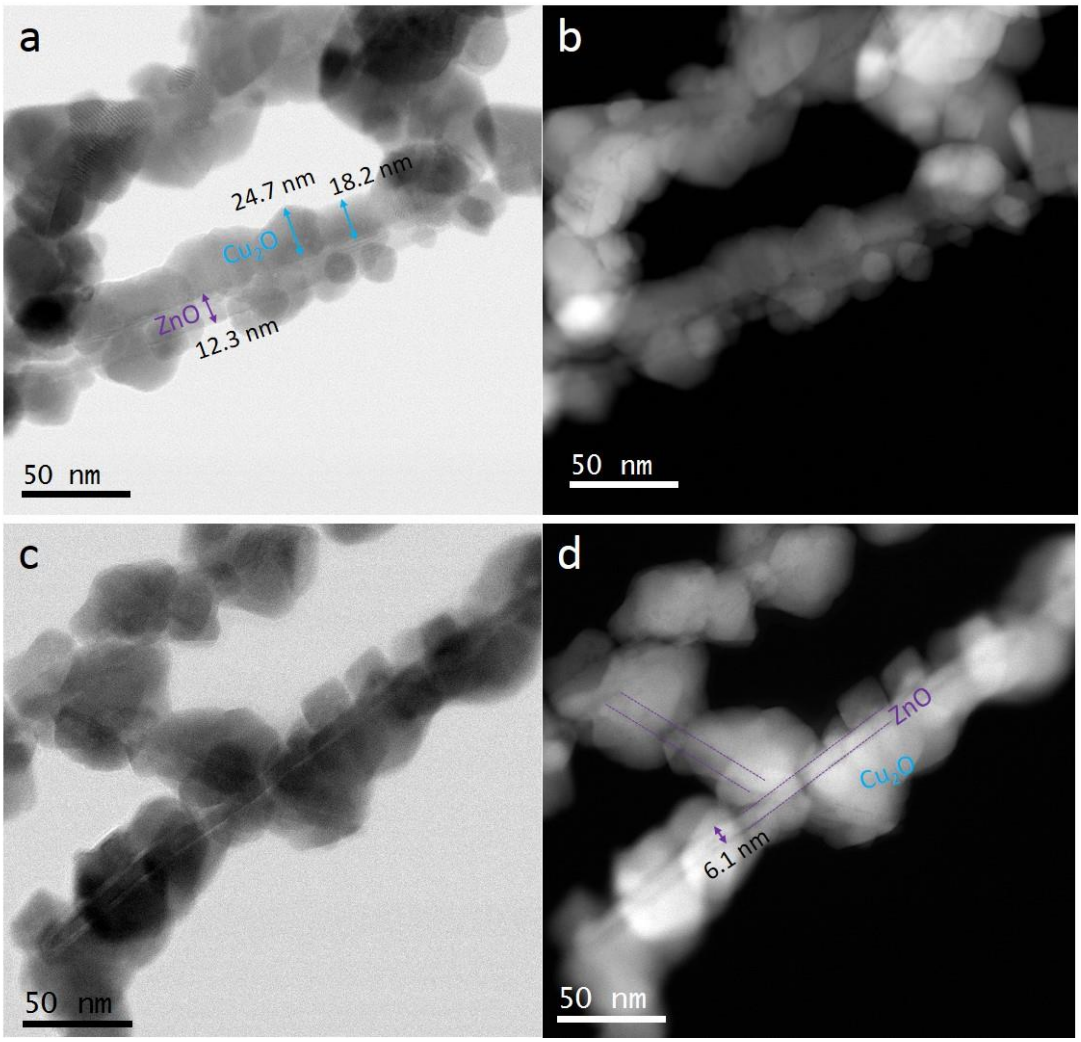

Figure 5.16. Bright Field (a, c) and Dark Field (b, d) TEM micrographs taken to different ZnO nanowires.

indexed to the wurtzite (PDF 00-036-1451) and cuprite (PDF 04-007-9767) phases for the ZnO and Cu_2O, respectively. No preferential orientation was observed neither for the ZnO nor for the Cu_2O. Figure 5.15 b, c shows the SEM micrographs of the pristine ZnO nanowires (b) and after the covering with the Cu_2O by ALD (c). The Cu_2O was deposited along the nanowires length down to the bottom. To perform TEM analysis to the sample, we scratched the sample surface with a diamond tip over a the TEM grid. Figure 5.16 shows bright and dark field micrographs of a few ZnO nanowires. The lateral nanowire size, measured from the TEM micrographs, ranged from 6 to 17 nm. As can be seen, large Cu_2O crystals were deposited on the ZnO nanowires walls, with a wide distribution of sizes ranging 10 to 50 nm. Most of the nanowires surface was covered by the Cu_2O, however there are few sites uncovered, which means that conformability needs to be improved by optimizing the growth parameters.

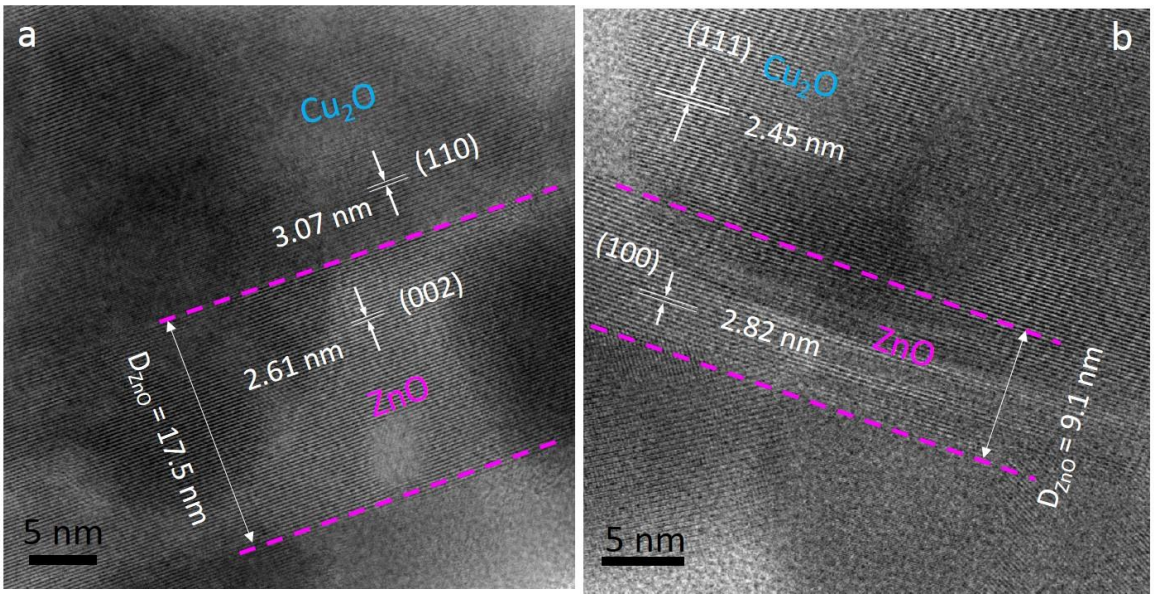

Figure 5.17. HR-TEM micrograph showing the orientation relationship between the Cu_2O and the ZnO nanowires.

Figure 5.17 shows a HR-TEM micrograph of two nanowires with different orientations. There is an area not covered by the Cu_2O for which it was possible to identify the ZnO crystallographic orientation. For ZnO nanowires with the (002) crystallographic planes perpendicular to the growth direction (Figure 5.17 a), the Cu_2O film grows with the (110) planes parallel to the (002) ZnO; that is, following the same orientation relationship observed for the Cu_2O on the c-axis ZnO polycrystalline thin films, and on the O-terminated ZnO monocrystalline substrates (see Chapter 3). On the other hand, for the nanowires oriented with the (100) planes perpendicular to the growth direction (Figure 5.17 b), the Cu_2O films grows with the (111) planes parallel to the (100) planes of ZnO, i. e. the same orientation relationship observed on the (100)-oriented ZnO monocrystalline substrates.

5.9 Chapter Conclusions

In this chapter we presented the results on the fabrication of semi-transparent thin film p-Cu_2O/n-ZnO heterojunctions. The morphology and structure of the films was studied by SEM, DRX and TEM, showing a high crystalline quality, and a good interface between both materials. The bandgap of the films was determined by ellipsometry and transmittance measurements, giving a value of 2.42 eV for Cu_2O and 3.16 eV for ZnO. Electrical characterization of the Cu_2O films show relatively high carrier concentration of $\sim 10^{16}$ cm^{-3}, very low resistivity of 9 - 150 Ω cm, and high mobility values of 19 cm^2 / Vs. In a first part of the study, the heterojunctions were made by growing a 40-nm Cu_2O film on a ZnO films deposited on ITO/glass substrates. I-V characteristics showed a non-linear rectifying behavior typical of a p-n junction, and a self-powered photoresponse was observed under 1-Sun illumination. Moreover, the heterojunctions showed high average transmittance of 73%. In a second part, the electrical properties of the heterojunctions were considerably improved by incorporating an uppermost 200-nm-Cu_2O film deposited by reactive magnetron sputtering. The heterojunction shows a stable photoresponse under several dark/light cycles. Particularly, relatively high V_{OC} values were achieved, considering the small thickness of the film, which is due to the high carrier concentration of the Cu_2O films. A faster response time of 0.10 s was determined from the current density vs. time curve, in comparison with similar oxide-based visible photodetectors. This fast response is due to the small depletion layer thickness and the possibility to develop the full built-in potential, providing a strong electric field at the junction interface and allowing a faster charge separation, and in consequence a fast response of the device.

Finally, preliminary results on the deposition of Cu_2O on ZnO nanowires are presented, which are promising for photovoltaic and photodetecting applications as a way of enhancing the absorption by the high surface-to-volume ratio of the junctions and by light trapping effects inside the nanostructured ZnO. Furthermore, this architecture can improve the charge collection efficiency, due to the small distance that photogenerated carriers need to travel before being collected.

The high average transmittance together with the self-powered photo-response of the heterojunctions presented here is promising in the field of all-oxide transparent electronics, semi-transparent photovoltaics and photodetection. Even if ALD is a slow process not suitable for growing thick Cu_2O films, it can serve to growth high quality buffer layers. Also, it could be interesting for growing Cu_2O in nanostructured solar cells where no thick layers of Cu_2O are required due to the high surface-to-volume ratio.

Conclusions and Outlook

Selective atomic layer deposition of Cu_2O and metallic Cu have been achieved on ZnO and AZO thin films, ZnO nanowires, and α-Al_2O_3 substrates, using $Cu(hfac)_2$ as Cu precursor and H_2O as oxidizer. This selective deposition process is temperature-dependent; Cu_2O deposition is favored at lower temperatures (200 - 250 °C), while metallic Cu is obtained at higher temperatures (280 – 310 °C).

A substrate-selective atomic layer deposition process is also demonstrated on ZnO and AZO substrates, in addition to the temperature-driven selectivity. The ZnO properties were modulated by varying the oxygen partial pressure in the reactive sputtering process, which allows tuning the ZnO conductivity/type of majority point defects over a very large range (10^{-4} to 10^{3} S/cm), influencing the nature of the final material deposited: Cu or Cu_2O. A phase diagram was presented showing the different phases formed as a function of the temperature and substrates conductivity. We proposed that the area-selective deposition is achieved thanks to the inherent selectivity of the $Cu(hfac)_2$ precursor toward the different ZnO substrates, with different conductivity/density of donor defects. Furthermore, in the case of Cu_2O deposition, the crystal orientation relationship between film and substrate strongly influences the film growth as was demonstrated on monocrystalline ZnO substrates of different orientations.

Area-selective atomic layer deposition (AS-ALD) process was demonstrated using a patterned bilayer structure made of low-conductive and highly-conductive regions. HR-TEM, EELS and EDS confirm the AS-ALD process, where Cu_2O is deposited on the low-conductive ZnO regions and metallic Cu on the highly-conductive AZO regions. AS-ALD has been verified on features of lateral dimensions ranging from 200 nm up to several centimeters. The "traditional" selectivity (deposition vs. no deposition) is also achieved by using highly-resistive ZnO films, to avoid local growth. Overall, a model explaining the temperature, substrate, and spatial selectivity have been proposed based on initial reduction of Cu^{2+} in $Cu(hfac)_2$, into Cu^{+} upon adsorption of the precursor, inducing the epitaxial growth of Cu_2O on ZnO of low density of donor defects (low-conductive) or further reduction of Cu^{+} into Cu^{0}, i.e. growth of metallic copper, on highly conductive ZnO surfaces.

Taking advantage of the AS-ALD process Cu_2O/ZnO/AZO microjunctions were successfully fabricated by a bottom-up approach. The deposition of the Cu_2O on ZnO was achieved at the same time that the deposition of the Cu metallic contact on the AZO film, thanks to AS-ALD. Furthermore, I-V measurements performed by C-AFM demonstrated the non-

linear rectifying behavior of the heterojunctions. Suitable patterning of the AZO/ZnO bilayer enables producing segmented microjunctions, which offers many opportunities for micro and nano-electronic applications.

A detailed study on the metallic Cu growth showed the formation of Cu nanoparticles (NP) on ZnO thin films, owing to the Volmer-Weber growth mode, at early stages of deposition. The NP lateral size, height, density and surface coverage was controlled by varying the number of ALD cycles. The NP exhibit localized surface plasmon resonance (LSPR), as was demonstrated by ellipsometric measurements. Furthermore, the LSPR signal was tuned from the visible to the near-infrared, depending on particles lateral size and inter-particle distance both controlled by the number of ALD cycles.

The deposition of plasmonic NP on ZnO thin films allows the fabrication of a highly responsive photodetector in the visible region, as was demonstrated by C-AFM measurements performed to the samples in dark and under white light illumination. By comparison with a Cu film/ZnO traditional Schottky junction, the Cu NP/ZnO device shows a considerable improvement of the photocurrent under reverse bias voltage that can be unequivocally attributed to the effect of the Cu NP. We propose that the photodetection mechanism here is the hot-electrons generation at the Cu NP surface, after LSPR non-radiative decay, and injection into the ZnO conduction band through the Schottky barrier formed at the interface between both materials. Different hot-electron plasmonic devices have been designed to improve the performance of multiple optoelectronic devices, however they are usually based on Au and Ag plasmonic nanostructures. Here, we have shown the potentialities of plasmonic Cu NP, in particular for photodetection, which have the advantage of low-cost and abundance of Cu in earth crust, compared with Au and Ag. On the other hand, the possibility of tuning the LSPR band between the visible and near-infrared, offers opportunities for application in light-emitting and photovoltaics devices.

In general, both the Cu and Cu_2O films deposited by ALD showed high crystalline quality, as was demonstrated by HR-TEM micrographs. Cu films exhibit relatively low resistivity values of $8 - 10$ μΩ cm, considering electron scattering at the film interfaces due to the small thickness of the films (45 - 50 nm). Cu_2O films showed excellent electrical performance with low resistivity values ranging from 9 to 150 Ω cm, relatively high carriers concentration of $\sim 10^{16}\ cm^{-3}$, and high mobility values of 19 cm^2 / Vs.

Semi-transparent thin film p-Cu_2O/n-ZnO heterojunctions were successfully fabricated by a combination of ALD and reactive magnetron sputtering. The heterojunctions showed a rectifying behavior, as was demonstrated by macroscopic electrical measurements. A stable

self-powered photoresponse was observed under 1 Sun illumination, with fast response times under several light/dark cycles. Furthermore, a high average transmittance of 73 %, was determined from transmittance measurements.

The electrical performance of the heterojunctions was considerably improved by the addition of a 200-nm-Cu_2O films deposited by sputtering (compared to solely ALD Cu_2O), essentially due to the increase in film thickness, which results in enhancements of light absorption and density of photogenerated carriers. Even with the addition of the 200 nm layer the transparency of the film was still high enough to allow visible light transmission.

We believe that the Cu_2O films deposited by ALD is fundamental to guarantee a good interface with ZnO and improve the device performance. Furthermore, the faster response time obtained here, compared with similar oxide-based photodetectors are the result of the excellent electrical properties of the Cu_2O films deposited by ALD. Even if ALD is not suitable for growing thick Cu_2O films, it can serve for the deposition of high quality buffer layers and also to deposit on nanostructured architectures, in which no thick film is required due to the large area-to-volume ratio of these devices. All in all, these results are promising for semi-transparent electronics, all-oxide photovoltaics, and photodetection applications.

Perspectives

The results reported in this thesis have opened an avenue toward multiple optoelectronic applications. In the following, we will present some aspect that can be of interest for future research:

- We have presented the area-selective atomic layer deposition of Cu_2O and Cu films on ZnO substrates. We proposed that the selectivity is driven by the evolution of conductivity/point defect density of the ZnO substrates. However, further experiments need to be performed in order to clarify this mechanism. Particularly, since the ALD reactor is connected under ultra-high vacuum with and XPS system it will be interesting to analyze the surface after each precursor exposure during the ALD process, which would give insight into the precursor absorption mechanisms and the reactions taking place on the different ZnO surfaces.
- Exploring the possibility of obtaining an area-selective deposition process on others materials in which the conductivity/defect density can be tuned as for the ZnO films. An interesting case of study will be, for example, MoO_x since a transition from the

insulating MoO_3 to the semi-metallic MoO_2 has been reported in the literature, with conductivities varying in more than ten orders of magnitude.

- We have presented in this thesis a highly responsive visible photodetector, based on Cu NP/ZnO, due to hot-electron generation at the plasmonic Cu NP. It will be interesting to perform the same study on the other Cu NP/ZnO systems that showed a LSPR signal in the near-infrared, to verify the hot-electron generation and injection into the ZnO, under excitation by infrared light, which will allow to expand the potential applications of the Cu NP/ZnO system.
- Regarding the Cu NP/ZnO device, a very interesting approach would be embedding the plasmonic Cu NP in the ZnO films, or sandwiching the Cu NP between ZnO thin films. The approach of embedding the plasmonic nanostructured into the semiconductor has already been employed in some hot-electron devices, and it has considerably increased the device performance due to a more efficient hot-electron injection into the semiconductor.
- We have demonstrated the possibility to deposit Cu NP on nanostructured ZnO (nanowires), which can result in a considerable enhancement of the photodetection capabilities of the device (compared with the planar architecture), due to the increase of surface area and, in consequence, the increase of light absorption and the hot-electron generation at the plasmonic NP. Therefore, it would be interesting to performe electrical characterization of this type of device, after the deposition of appropriate metallic electrodes.
- We have reported the formation of semi-transparent p-Cu_2O/n-ZnO heterojunctions that showed a self-powered photoresponse with fast response times, of interest for all-oxide photodetectors and photovoltaics. However, the photocurrent density was very small (in the order μA). This was due to manufacturing problems, since when measuring the I-V characteristics on the top Ag electrode a short-circuit was obtained. Therefore, the measurements were performed locally directly on the Cu_2O film, resulting in a low current collection. In the future, appropriate contacts need to be fabricated in order to avoid this issue and improve the current collection.
- We reported the deposition of Cu_2O on ZnO nanowires. As in the case of the Cu NP/ZnO device, it would be interesting to measure the electrical performance of the nanostructured heterojunctions since the deposition of Cu_2O on the ZnO nanowires can

considerably enhance the absorption and carrier collection efficiency, which hold promises for all-oxide photodetectors and photovoltaics.

Appendixes

Appendix A

Spectroscopic Ellipsometry Data

ZnO films

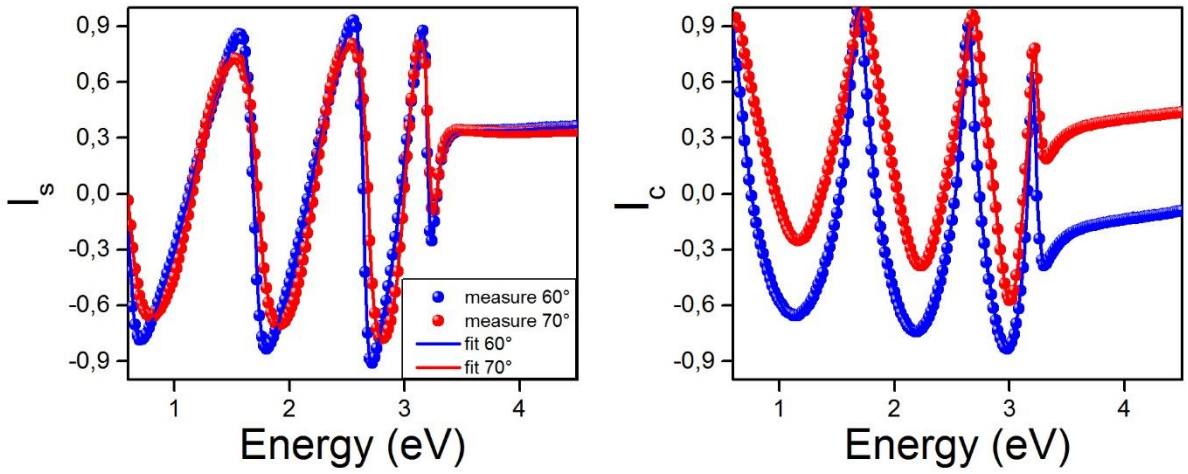

Figure I. Measured and simulated ellipsometric spectra for a typical ZnO substrate at 60° (blue) and 70° (red).

Cu nanoparticles and Cu film on ZnO

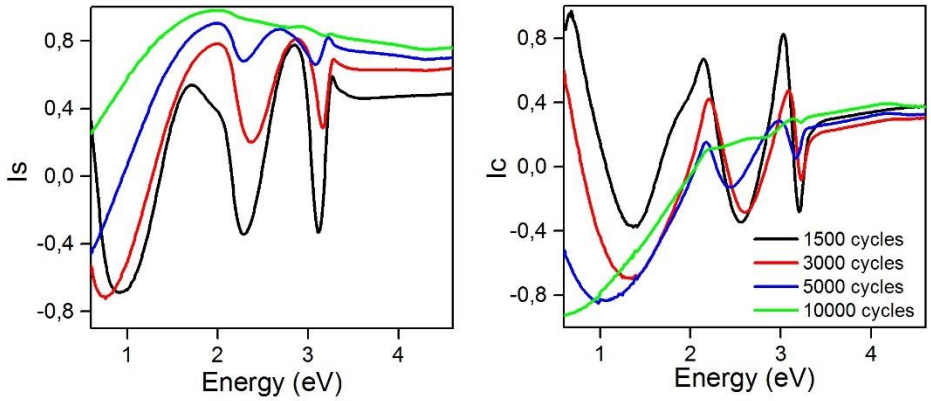

Figure II. Comparison of the ellipsometry measurements of the Cu nanoparticles/ZnO (1500, 3000 and 5000) and Cu film/ZnO (10000) at 70°.

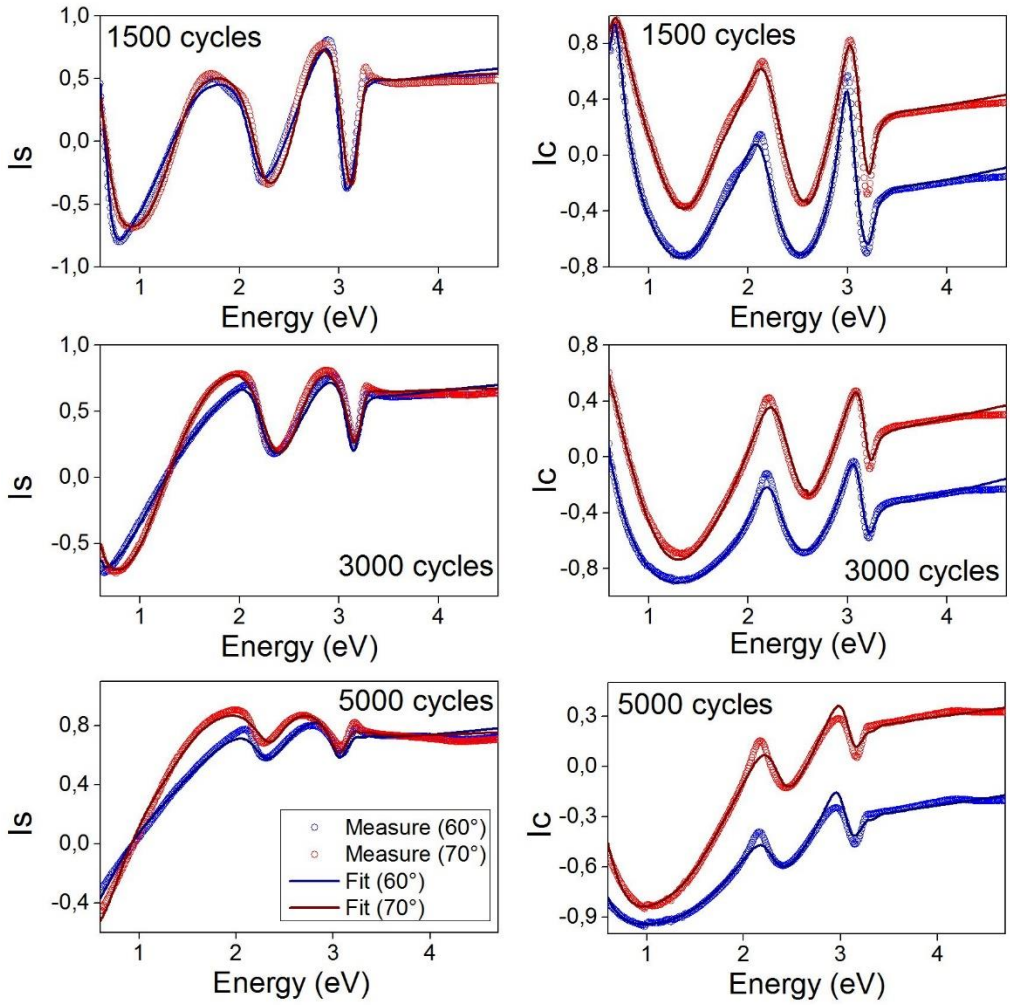

Figure III. Measured and simulated ellipsometric spectra for the Cu NPs/ZnO films deposited at 1500, 3000 and 5000 ALD cycles.

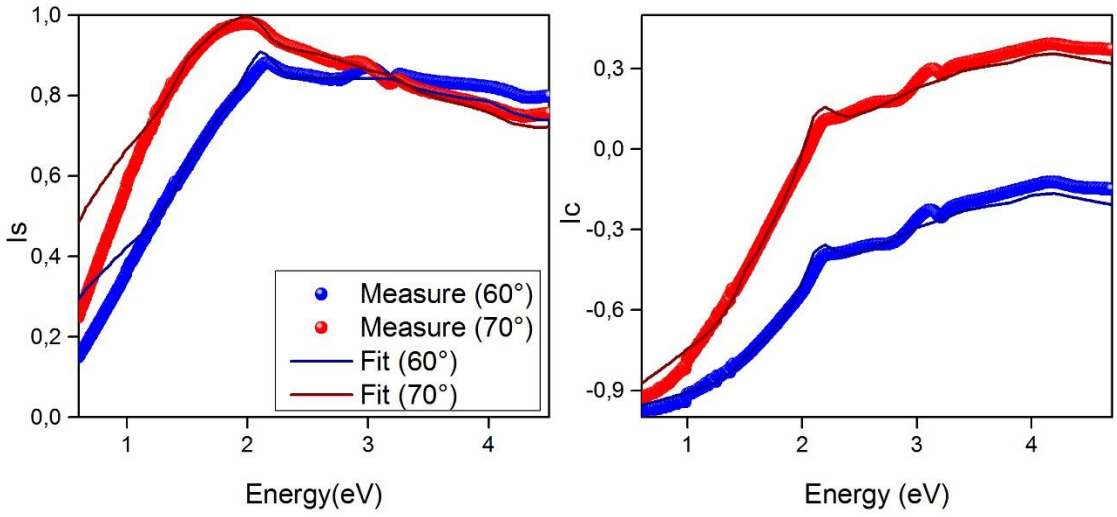

Figure IV. Measured and simulated ellipsometric spectra for the Cu/ZnO (10 000 ALD cycles) film at 60° (blue) and 70° (red).

Cu_2O on ZnO substrates

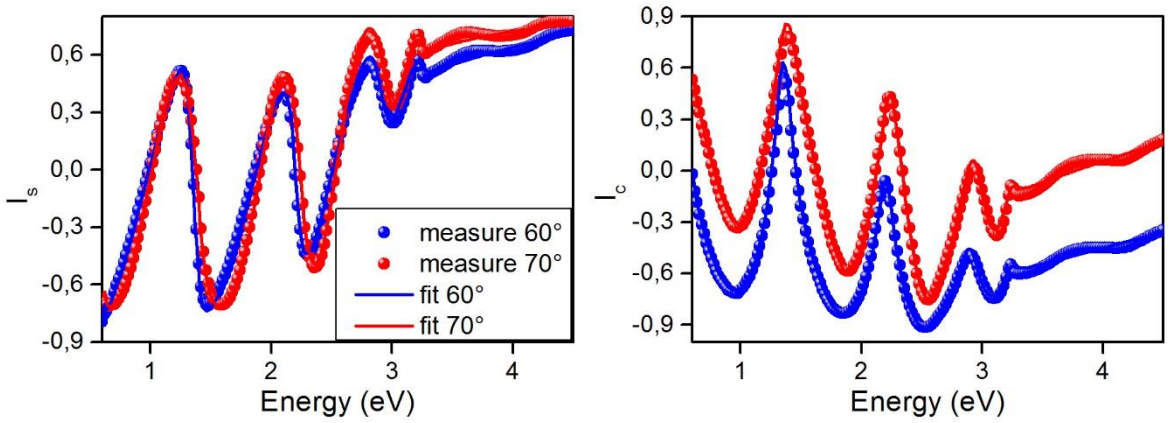

Figure V. Measured and simulated ellipsometric spectra for the Cu_2O/ZnO films at 60° (blue) and 70° (red).

Appendix B

AFM force curves

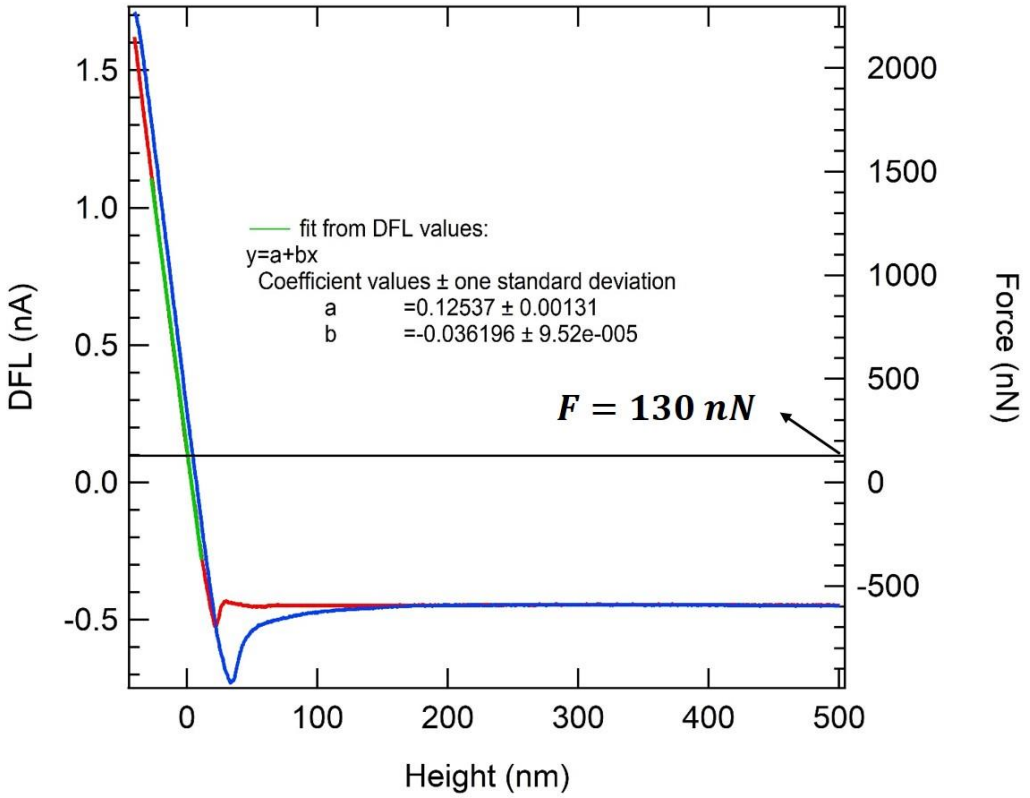

Figure VI. Typical AFM force curve taken to the Cu nanoparticles/ZnO sample.

The force applied (F) by the AFM tip (spring constant $k = 48\ N/m$), was calculated by the formula:

$$F = \frac{DFL * k}{b}$$

Where DFL is the tip deflection, and b the slope of the linear region in the plot DFL vs. height (see Figure VI, green line). Taking into account the set point ($DFL = 0.1\ nA$) the force applied to the samples was of $130\ nN$.

Bibliography

[1] A.J.M. Mackus, A.A. Bol, W.M.M. Kessels, The use of atomic layer deposition in advanced nanopatterning, Nanoscale. 6 (2014) 10941–10960. doi:10.1039/C4NR01954G.

[2] D. Bobb-Semple, K.L. Nardi, N. Draeger, D.M. Hausmann, S.F. Bent, Area-Selective Atomic Layer Deposition Assisted by Self-Assembled Monolayers: A Comparison of Cu, Co, W, and Ru, Chem. Mater. 31 (2019) 1635–1645. doi:10.1021/acs.chemmater.8b04926.

[3] C. Clavero, Plasmon-induced hot-electron generation at nanoparticle/metal-oxide interfaces for photovoltaic and photocatalytic devices, Nat. Photonics. 8 (2014) 95–103.

[4] H. Chalabi, D. Schoen, M.L. Brongersma, Hot-Electron Photodetection with a Plasmonic Nanostripe Antenna, Nano Lett. 14 (2014) 1374–1380. doi:10.1021/nl4044373.

[5] A. Pescaglini, A. Martín, D. Cammi, G. Juska, C. Ronning, E. Pelucchi, D. Iacopino, Hot-Electron Injection in Au Nanorod–ZnO Nanowire Hybrid Device for Near-Infrared Photodetection, Nano Lett. 14 (2014) 6202–6209. doi:10.1021/nl5024854.

[6] L.C. Olsen, F.W. Addis, W. Miller, Experimental and theoretical studies of Cu_2O solar cells, Sol. Cells. 7 (1982) 247–279. doi:10.1016/0379-6787(82)90050-3.

[7] T. Minami, Y. Nishi, T. Miyata, Efficiency enhancement using a $Zn_{1-x}Ge_x$-O thin film as an n-type window layer in Cu_2O-based heterojunction solar cells, Appl. Phys. Express. 9 (2016) 052301. doi:10.7567/APEX.9.052301.

[8] S. Rühle, A.Y. Anderson, H.-N. Barad, B. Kupfer, Y. Bouhadana, E. Rosh-Hodesh, A. Zaban, All-Oxide Photovoltaics, J. Phys. Chem. Lett. 3 (2012) 3755–3764. doi:10.1021/jz3017039.

[9] P. Ghamgosar, F. Rigoni, S. You, I. Dobryden, M.G. Kohan, A.L. Pellegrino, I. Concina, N. Almqvist, G. Malandrino, A. Vomiero, ZnO-Cu_2O core-shell nanowires as stable and fast response photodetectors, Nano Energy. 51 (2018) 308–316. doi:10.1016/j.nanoen.2018.06.058.

[10] B.K. Meyer, A. Polity, D. Reppin, M. Becker, P. Hering, P.J. Klar, T. Sander, C. Reindl, J. Benz, M. Eickhoff, C. Heiliger, M. Heinemann, J. Bläsing, A. Krost, S. Shokovets, C. Müller, C. Ronning, Binary copper oxide semiconductors: From materials towards devices, Phys. Status Solidi B. 249 (2012) 1487–1509. doi:10.1002/pssb.201248128.

[11] S.T. Omelchenko, Y. Tolstova, H.A. Atwater, N.S. Lewis, Excitonic Effects in Emerging Photovoltaic Materials: A Case Study in Cu_2O, ACS Energy Lett. 2 (2017) 431–437. doi:10.1021/acsenergylett.6b00704.

[12] T. Kazimierczuk, D. Fröhlich, S. Scheel, H. Stolz, M. Bayer, Giant Rydberg excitons in the copper oxide Cu_2O, Nature. 514 (2014) 343–347. doi:10.1038/nature13832.

[13] M. Saffman, T.G. Walker, K. Mølmer, Quantum information with Rydberg atoms, Rev. Mod. Phys. 82 (2010) 2313–2363. doi:10.1103/RevModPhys.82.2313.

[14] C. Malerba, F. Biccari, C. Leonor Azanza Ricardo, M. D'Incau, P. Scardi, A. Mittiga, Absorption coefficient of bulk and thin film Cu_2O, Sol. Energy Mater. Sol. Cells. 95 (2011) 2848–2854. doi:10.1016/j.solmat.2011.05.047.

[15] F. Schöne, H. Stolz, N. Naka, Phonon-assisted absorption of excitons in Cu_2O, Phys. Rev. B. 96 (2017) 115207. doi:10.1103/PhysRevB.96.115207.

[16] Y. Wang, P. Miska, D. Pilloud, D. Horwat, F. Mücklich, J.F. Pierson, Transmittance enhancement and optical band gap widening of Cu_2O thin films after air annealing, J. Appl. Phys. 115 (2014) 073505. doi:10.1063/1.4865957.

[17] F.S. Schweiner, Theory of excitons in cuprous oxide, PhD Thesis, Stuttgart University, 2017.

[18] A. Soon, X.-Y. Cui, B. Delley, S.-H. Wei, C. Stampfl, Native defect-induced multifarious magnetism in nonstoichiometric cuprous oxide: First-principles study of bulk and surface properties of $Cu_{2-\delta}O$, Phys. Rev. B. 79 (2009) 035205. doi:10.1103/PhysRevB.79.035205.

[19] D.O. Scanlon, B.J. Morgan, G.W. Watson, A. Walsh, Acceptor Levels in p-Type Cu_2O: Rationalizing Theory and Experiment, Phys. Rev. Lett. 103 (2009) 096405. doi:10.1103/PhysRevLett.103.096405.

[20] G.K. Paul, R. Ghosh, S.K. Bera, S. Bandyopadhyay, T. Sakurai, K. Akimoto, Deep level transient spectroscopy of cyanide treated polycrystalline p-Cu_2O/n-ZnO solar cell, Chem. Phys. Lett. 463 (2008) 117–120. doi:10.1016/j.cplett.2008.08.065.

[21] Y. Wang, J. Ghanbaja, D. Horwat, L. Yu, J.F. Pierson, Nitrogen chemical state in N-doped Cu_2O thin films, Appl. Phys. Lett. 110 (2017) 131902. doi:10.1063/1.4979140.

[22] D.O. Scanlon, G.W. Watson, Uncovering the Complex Behavior of Hydrogen in Cu_2O, Phys. Rev. Lett. 106 (2011) 186403. doi:10.1103/PhysRevLett.106.186403.

[23] Y. Wang, J. Ghanbaja, F. Soldera, P. Boulet, D. Horwat, F. Mücklich, J.F. Pierson, Controlling the preferred orientation in sputter-deposited Cu_2O thin films: Influence of the initial growth stage and homoepitaxial growth mechanism, Acta Mater. 76 (2014) 207–212. doi:10.1016/j.actamat.2014.05.008.

[24] S.B. Ogale, P.G. Bilurkar, N. Mate, S.M. Kanetkar, N. Parikh, B. Patnaik, Deposition of copper oxide thin films on different substrates by pulsed excimer laser ablation, J. Appl. Phys. 72 (1992) 3765–3769. doi:10.1063/1.352271.

[25] U.C. Bind, R.K. Dutta, G.K. Sekhon, K.L. Yadav, J.B.M. Krishna, R. Menon, P.Y. Nabhiraj, Ion implantation induced phase transformation and enhanced crystallinity of as deposited copper oxide thin films by pulsed laser deposition, Superlattices Microstruct. 84 (2015) 24–35. doi:10.1016/j.spmi.2015.03.064.

[26] Z. Zhang, P. Wang, Highly stable copper oxide composite as an effective photocathode for water splitting via a facile electrochemical synthesis strategy, J. Mater. Chem. 22 (2012) 2456–2464. doi:10.1039/C1JM14478B.

[27] H. Kim, M.Y. Lee, S.-H. Kim, S.I. Bae, K.Y. Ko, H. Kim, K.-W. Kwon, J.-H. Hwang, D.-J. Lee, Highly-conformal p-type copper (I) oxide (Cu_2O) thin films by atomic layer deposition using a fluorine-free amino-alkoxide precursor, Appl. Surf. Sci. 349 (2015) 673–682. doi:10.1016/j.apsusc.2015.05.062.

[28] D. Muñoz-Rojas, M. Jordan, C. Yeoh, A.T. Marin, A. Kursumovic, L.A. Dunlop, D.C. Iza, A. Chen, H. Wang, J.L. MacManus Driscoll, Growth of ~ 5 $cm^2 V^{-1} s^{-1}$ mobility, p-type Copper(I) oxide (Cu_2O) films by fast atmospheric atomic layer deposition (AALD) at 225°C and below, AIP Adv. 2 (2012) 042179. doi:10.1063/1.4771681.

[29] B.P. Rai, Cu_2O solar cells: a review, Sol. Cells. 25 (1988) 265–272. doi:10.1016/0379-6787(88)90065-8.

[30] K. Mizuno, M. Izaki, K. Murase, T. Shinagawa, M. Chigane, M. Inaba, A. Tasaka, Y. Awakura, Structural and Electrical Characterizations of Electrodeposited p-Type Semiconductor Cu_2O Films, J. Electrochem. Soc. 152 (2005) C179. doi:10.1149/1.1862478.

[31] Y.S. Lee, M.T. Winkler, S.C. Siah, R. Brandt, T. Buonassisi, Hall mobility of cuprous oxide thin films deposited by reactive direct-current magnetron sputtering, Appl. Phys. Lett. 98 (2011) 192115. doi:10.1063/1.3589810.

[32] M. Leskelä, M. Ritala, Atomic Layer Deposition Chemistry: Recent Developments and Future Challenges, Angew. Chem. Int. Ed. 42 (2003) 5548–5554. doi:10.1002/anie.200301652.

[33] P. Poodt, D.C. Cameron, E. Dickey, S.M. George, V. Kuznetsov, G.N. Parsons, F. Roozeboom, G. Sundaram, A. Vermeer, Spatial atomic layer deposition: A route towards further industrialization of atomic layer deposition, J. Vac. Sci. Technol. Vac. Surf. Films. 30 (2011) 010802. doi:10.1116/1.3670745.

[34] A.T. Marin, D. Muñoz-Rojas, D.C. Iza, T. Gershon, K.P. Musselman, J.L. MacManus-Driscoll, Novel Atmospheric Growth Technique to Improve Both Light Absorption and Charge Collection in ZnO/Cu_2O Thin Film Solar Cells, Adv. Funct. Mater. 23 (2013) 3413–3419. doi:10.1002/adfm.201203243.

[35] T. Wächtler, Thin films of copper oxide and copper grown by atomic layer deposition for applications in metallization systems of microelectronic devices, PhD Thesis, Technische Universität Chemnitz, 2010.

[36] P. Mårtensson, J.-O. Carlsson, Atomic Layer Epitaxy of Copper on Tantalum, Chem. Vap. Depos. 3 (1997) 45–50. doi:10.1002/cvde.19970030107.

[37] R. Solanki, B. Pathangey, Atomic Layer Deposition of Copper Seed Layers, Electrochem. Solid-State Lett. 3 (2000) 479–480. doi:10.1149/1.1391185.

[38] J. Huo, R. Solanki, J. McAndrew, Characteristics of copper films produced via atomic layer deposition, J. Mater. Res. 17 (2002) 2394–2398. doi:10.1557/JMR.2002.0350.

[39] Z. Li, A. Rahtu, R.G. Gordon, Atomic Layer Deposition of Ultrathin Copper Metal Films from a Liquid Copper(I) Amidinate Precursor, J. Electrochem. Soc. 153 (2006) C787. doi:10.1149/1.2338632.

[40] D. Dhakal, K. Assim, H. Lang, P. Bruener, T. Grehl, C. Georgi, T. Waechtler, R. Ecke, S.E. Schulz, T. Gessner, Atomic layer deposition of ultrathin Cu_2O and subsequent reduction to Cu studied by in situ x-ray photoelectron spectroscopy, J. Vac. Sci. Technol. A. 34 (2015) 01A111. doi:10.1116/1.4933088.

[41] T. Torndahl, Atomic Layer Deposition of Copper, Copper (I) Oxide, and Copper (I) Nitride on Oxide substrates, PhD Thesis, Uppsala University, 2004.

[42] T. Törndahl, M. Ottosson, J.-O. Carlsson, Growth of Copper(I) Nitride by ALD Using Copper(II) Hexafluoroacetylacetonate, Water, and Ammonia as Precursors, J. Electrochem. Soc. 153 (2006) C146. doi:10.1149/1.2160427.

[43] J.-D. Kwon, S.-H. Kwon, T.-H. Jung, K.-S. Nam, K.-B. Chung, D.-H. Kim, J.-S. Park, Controlled growth and properties of p-type cuprous oxide films by plasma-enhanced atomic layer deposition at low temperature, Appl. Surf. Sci. 285 (2013) 373–379. doi:10.1016/j.apsusc.2013.08.063.

[44] M.E. Alnes, E. Monakhov, H. Fjellvåg, O. Nilsen, Atomic Layer Deposition of Copper Oxide using Copper(II) Acetylacetonate and Ozone, Chem. Vap. Depos. 18 (2012) 173–178. doi:10.1002/cvde.201106959.

[45] A. Janotti, C.G. Van de Walle, Fundamentals of zinc oxide as a semiconductor, Rep. Prog. Phys. 72 (2009) 126501. doi:10.1088/0034-4885/72/12/126501.

[46] Z.L. Wang, Zinc oxide nanostructures: growth, properties and applications, J. Phys. Condens. Matter. 16 (2004) R829–R858. doi:10.1088/0953-8984/16/25/R01.

[47] E. Fortunato, P. Barquinha, R. Martins, Oxide Semiconductor Thin-Film Transistors: A Review of Recent Advances, Adv. Mater. 24 (2012) 2945–2986. doi:10.1002/adma.201103228.

[48] H. Lahmar, A. Azizi, G. Schmerber, A. Dinia, Effect of the thickness of the ZnO buffer layer on the properties of electrodeposited p-Cu_2O/n-ZnO/n-AZO heterojunctions, RSC Adv. 6 (2016) 68663–68674. doi:10.1039/C6RA04834J.

[49] S. Du, W. Tang, X. Lu, S. Wang, Y. Guo, P.-X. Gao, Methanol Production: Cu-Decorated ZnO Nanorod Array Integrated Structured Catalysts for Low-Pressure CO_2 Hydrogenation to Methanol, Adv. Mater. Interfaces. 5 (2018) 1870011. doi:10.1002/admi.201870011.

[50] S.K. Shaikh, V.V. Ganbavle, S.I. Inamdar, K.Y. Rajpure, Multifunctional zinc oxide thin films for high-performance UV photodetectors and nitrogen dioxide gas sensors, RSC Adv. 6 (2016) 25641–25650. doi:10.1039/C6RA01750A.

[51] C. Klingshirn, ZnO: From basics towards applications, Phys. Status Solidi B. 244 (2007) 3027–3073. doi:10.1002/pssb.200743072.

[52] F. Oba, A. Togo, I. Tanaka, J. Paier, G. Kresse, Defect energetics in ZnO: A hybrid Hartree-Fock density functional study, Phys. Rev. B. 77 (2008) 245202. doi:10.1103/PhysRevB.77.245202.

[53] D.G. Thomas, Interstitial zinc in zinc oxide, J. Phys. Chem. Solids. 3 (1957) 229–237. doi:10.1016/0022-3697(57)90027-6.

[54] Ü. Özgür, Y.I. Alivov, C. Liu, A. Teke, M.A. Reshchikov, S. Doğan, V. Avrutin, S.-J. Cho, H. Morkoç, A comprehensive review of ZnO materials and devices, J. Appl. Phys. 98 (2005) 041301. doi:10.1063/1.1992666.

[55] X.L. Chen, B.H. Xu, J.M. Xue, Y. Zhao, C.C. Wei, J. Sun, Y. Wang, X.D. Zhang, X.H. Geng, Boron-doped zinc oxide thin films for large-area solar cells grown by metal organic chemical vapor deposition, Thin Solid Films. 515 (2007) 3753–3759. doi:10.1016/j.tsf.2006.09.039.

[56] S. Ilican, Y. Caglar, M. Caglar, F. Yakuphanoglu, Structural, optical and electrical properties of F-doped ZnO nanorod semiconductor thin films deposited by sol–gel process, Appl. Surf. Sci. 255 (2008) 2353–2359. doi:10.1016/j.apsusc.2008.07.111.

[57] D. Horwat, M. Mickan, W. Chamorro, New strategies for the synthesis of ZnO and Al-doped ZnO films by reactive magnetron sputtering at room temperature, Phys. Status Solidi C. 13 (2016) 951–957. doi:10.1002/pssc.201600136.

[58] M. Mickan, U. Helmersson, H. Rinnert, J. Ghanbaja, D. Muller, D. Horwat, Room temperature deposition of homogeneous, highly transparent and conductive Al-doped ZnO films by reactive high power impulse magnetron sputtering, Sol. Energy Mater. Sol. Cells. 157 (2016) 742–749. doi:10.1016/j.solmat.2016.07.020.

[59] T. Minami, H. Nanto, S. Takata, Highly conductive and transparent ZnO thin films prepared by r.f. magnetron sputtering in an applied external d.c. magnetic field, Thin Solid Films. 124 (1985) 43–47. doi:10.1016/0040-6090(85)90026-4.

[60] M. Mickan, Deposition of Al-doped ZnO films by high power impulse magnetron sputtering, PhD Thesis, Linköping University Electronic Press, 2017.

[61] H. Agura, A. Suzuki, T. Matsushita, T. Aoki, M. Okuda, Low resistivity transparent conducting Al-doped ZnO films prepared by pulsed laser deposition, Thin Solid Films. 445 (2003) 263–267. doi:10.1016/S0040-6090(03)01158-1.

[62] A. Henni, A. Merrouche, L. Telli, A. Karar, Studies on the structural, morphological, optical and electrical properties of Al-doped ZnO nanorods prepared by electrochemical deposition, J. Electroanal. Chem. 763 (2016) 149–154. doi:10.1016/j.jelechem.2015.12.037.

[63] D.B. Potter, D.S. Bhachu, M.J. Powell, J.A. Darr, I.P. Parkin, C.J. Carmalt, Al-, Ga-, and In-doped ZnO thin films via aerosol assisted CVD for use as transparent conducting oxides, Phys. Status Solidi A. 213 (2016) 1346–1352. doi:10.1002/pssa.201532996.

[64] Ü. Özgür, V. Avrutin, H. Morkoç, Chapter 16 - Zinc Oxide Materials and Devices Grown by Molecular Beam Epitaxy, in: M. Henini (Ed.), Mol. Beam Epitaxy Second Ed., Elsevier, 2018: pp. 343–375. doi:10.1016/B978-0-12-812136-8.00016-5.

[65] W. Chamorro, D. Horwat, P. Pigeat, P. Miska, S. Migot, F. Soldera, P. Boulet, F. Mücklich, Near-room temperature single-domain epitaxy of reactively sputtered ZnO films, J. Phys. Appl. Phys. 46 (2013) 235107. doi:10.1088/0022-3727/46/23/235107.

[66] Fraunhofer Institute for Solar Energy Systems, ISE, Photovoltaics report 2018, Freiburg, Germany, 2018. https://www.ise.fraunhofer.de/content/dam/ise/de/documents/publications/studies/Photovoltaics-Report.pdf (accessed January 27, 2019).

[67] T. Minami, Y. Nishi, T. Miyata, J. Nomoto, High-Efficiency Oxide Solar Cells with ZnO/Cu_2O Heterojunction Fabricated on Thermally Oxidized Cu_2O Sheets, Appl. Phys. Express. 4 (2011) 062301. doi:10.1143/APEX.4.062301.

[68] Copper Indium Gallium Diselenide Solar Cells | Photovoltaic Research | NREL, (n.d.). https://www.nrel.gov/pv/copper-indium-gallium-diselenide-solar-cells.html (accessed January 27, 2019).

[69] K.L. Chopra, P.D. Paulson, V. Dutta, Thin-film solar cells: an overview, Prog. Photovolt. Res. Appl. 12 (2004) 69–92. doi:10.1002/pip.541.

[70] N. Amin, T. Isaka, A. Yamada, M. Konagai, Highly efficient 1μm thick CdTe solar cells with textured TCOs, Sol. Energy Mater. Sol. Cells. 67 (2001) 195–201. doi:10.1016/S0927-0248(00)00281-6.

[71] A. R. Uhl, J. K. Katahara, H. W. Hillhouse, Molecular-ink route to 13.0% efficient low-bandgap $CuIn(S,Se)_2$ and 14.7% efficient $Cu(In,Ga)(S,Se)_2$ solar cells, Energy Environ. Sci. 9 (2016) 130–134. doi:10.1039/C5EE02870A.

[72] Y.C. Lin, T.Y. Chen, L.C. Wang, S.Y. Lien, Comparison of AZO, GZO, and AGZO thin films TCOs applied for a-Si solar cells, J. Electrochem. Soc. 159 (2012) H599–H604. doi:10.1149/2.108206jes.

[73] S. Hegedus, B. Sopori, P.D. Paulson, Optical design and analysis of textured a-Si solar cells, in: Conf. Rec. Twenty-Ninth IEEE Photovolt. Spec. Conf. 2002, IEEE, New Orleans, LA, USA, 2002: pp. 1122–1125. doi:10.1109/PVSC.2002.1190803.

[74] P. Reinhard, A. Chirila, F. Pianezzi, S. Nishiwaki, S. Buecheler, A.N. Tiwari, High efficiency flexible $Cu(In,Ga)Se_2$ solar cells, in: 2013 Twent. Int. Workshop Act.-Matrix Flatpanel Disp. Devices AM-FPD, 2013: pp. 79–82.

[75] M.G. Panthani, J.M. Kurley, R.W. Crisp, T.C. Dietz, T. Ezzyat, J.M. Luther, D.V. Talapin, High Efficiency Solution Processed Sintered CdTe Nanocrystal Solar Cells: The Role of Interfaces, Nano Lett. 14 (2014) 670–675. doi:10.1021/nl403912w.

[76] T. Minami, Y. Nishi, T. Miyata, Heterojunction solar cell with 6% efficiency based on an n-type aluminum–gallium–oxide thin film and p-type sodium-doped Cu_2O sheet, Appl. Phys. Express. 8 (2015) 022301. doi:10.7567/APEX.8.022301.

[77] Y. Ievskaya, R.L.Z. Hoye, A. Sadhanala, K.P. Musselman, J.L. MacManus-Driscoll, Fabrication of ZnO/Cu_2O heterojunctions in atmospheric conditions: Improved interface quality and solar cell performance, Sol. Energy Mater. Sol. Cells. 135 (2015) 43–48. doi:10.1016/j.solmat.2014.09.018.

[78] M. Pavan, S. Rühle, A. Ginsburg, D.A. Keller, H.-N. Barad, P.M. Sberna, D. Nunes, R. Martins, A.Y. Anderson, A. Zaban, E. Fortunato, TiO_2/Cu_2O all-oxide heterojunction solar cells produced by spray pyrolysis, Sol. Energy Mater. Sol. Cells. 132 (2015) 549–556. doi:10.1016/j.solmat.2014.10.005.

[79] C. Zuo, L. Ding, Solution-Processed Cu_2O and CuO as Hole Transport Materials for Efficient Perovskite Solar Cells, Small. 11 (2015) 5528–5532. doi:10.1002/smll.201501330.

[80] Ø. Nordseth, R. Kumar, K. Bergum, L. Fara, S.E. Foss, H. Haug, F. Drăgan, D. Crăciunescu, P. Sterian, I. Chilibon, C. Vasiliu, L. Baschir, D. Savastru, E. Monakhov, B.G. Svensson, Optical Analysis of a ZnO/Cu_2O Subcell in a Silicon-Based Tandem Heterojunction Solar Cell, Green Sustain. Chem. 07 (2017) 57. doi:10.4236/gsc.2017.71005.

[81] A. Mittiga, E. Salza, F. Sarto, M. Tucci, R. Vasanthi, Heterojunction solar cell with 2% efficiency based on a Cu_2O substrate, Appl. Phys. Lett. 88 (2006) 163502. doi:10.1063/1.2194315.

[82] Y. Nishi, T. Miyata, T. Minami, The impact of heterojunction formation temperature on obtainable conversion efficiency in n-ZnO/p-Cu_2O solar cells, Thin Solid Films. 528 (2013) 72–76. doi:10.1016/j.tsf.2012.09.090.

[83] T. Minami, Y. Nishi, T. Miyata, Cu_2O-based solar cells using oxide semiconductors, J. Semicond. 37 (2016) 014002. doi:10.1088/1674-4926/37/1/014002.

[84] K.P. Musselman, A. Marin, L. Schmidt-Mende, J.L. MacManus-Driscoll, Incompatible Length Scales in Nanostructured Cu_2O Solar Cells, Adv. Funct. Mater. 22 (2012) 2202–2208. doi:10.1002/adfm.201102263.

[85] M. Abd-Ellah, J.P. Thomas, L. Zhang, K.T. Leung, Enhancement of solar cell performance of p-Cu_2O/n-ZnO-nanotube and nanorod heterojunction devices, Sol. Energy Mater. Sol. Cells. 152 (2016) 87–93. doi:10.1016/j.solmat.2016.03.022.

[86] M. Deo, S. Mujawar, O. Game, A. Yengantiwar, A. Banpurkar, S. Kulkarni, J. Jog, S. Ogale, Strong photo-response in a flip-chip nanowire p-Cu_2O/n-ZnO junction, Nanoscale. 3 (2011) 4706–4712. doi:10.1039/C1NR10665A.

[87] K.P. Musselman, A. Wisnet, D.C. Iza, H.C. Hesse, C. Scheu, J.L. MacManus-Driscoll, L. Schmidt-Mende, Strong Efficiency Improvements in Ultra-low-Cost Inorganic Nanowire Solar Cells, Adv. Mater. 22 (2010) E254–E258. doi:10.1002/adma.201001455.

[88] S. Rühle, Tabulated values of the Shockley–Queisser limit for single junction solar cells, Sol. Energy. 130 (2016) 139–147. doi:10.1016/j.solener.2016.02.015.

[89] C.J. Traverse, R. Pandey, M.C. Barr, R.R. Lunt, Emergence of highly transparent photovoltaics for distributed applications, Nat. Energy. 2 (2017) 849–860. doi:10.1038/s41560-017-0016-9.

[90] S. Nandy, A. Banerjee, E. Fortunato, R. Martins, A Review on Cu_2O and Cu^I-Based p-Type Semiconducting Transparent Oxide Materials: Promising Candidates for New Generation Oxide Based Electronics, Rev. Adv. Sci. Eng. 2 (2013) 273–304. doi:10.1166/rase.2013.1045.

[91] A.H. El-Amin, Investigation of semitransparent Cu_2O/ZnO based heterostructure diodes for memory and related applications, Master of Science, University of Toledo, 2014. https://etd.ohiolink.edu/.

[92] X. Liu, H. Du, P. Wang, T.-T. Lim, X. Wei Sun, A high-performance UV/visible photodetector of Cu_2O/ZnO hybrid nanofilms on SWNT-based flexible conducting substrates, J. Mater. Chem. C. 2 (2014) 9536–9542. doi:10.1039/C4TC01585A.

[93] H. Tanaka, T. Shimakawa, T. Miyata, H. Sato, T. Minami, Electrical and optical properties of TCO–Cu_2O heterojunction devices, Thin Solid Films. 469–470 (2004) 80–85. doi:10.1016/j.tsf.2004.06.180.

[94] M. Izaki, T. Shinagawa, K.-T. Mizuno, Y. Ida, M. Inaba, A. Tasaka, Electrochemically constructed p-Cu_2O/n-ZnO heterojunction diode for photovoltaic device, J. Phys. Appl. Phys. 40 (2007) 3326–3329. doi:10.1088/0022-3727/40/11/010.

[95] T. Minami, Y. Nishi, T. Miyata, High-Efficiency Cu_2O-Based Heterojunction Solar Cells Fabricated Using a Ga_2O_3 Thin Film as N-Type Layer, Appl. Phys. Express. 6 (2013) 044101. doi:10.7567/APEX.6.044101.

[96] Y.S. Lee, D. Chua, R.E. Brandt, S.C. Siah, J.V. Li, J.P. Mailoa, S.W. Lee, R.G. Gordon, T. Buonassisi, Atomic Layer Deposited Gallium Oxide Buffer Layer Enables 1.2 V Open-Circuit Voltage in Cuprous Oxide Solar Cells, Adv. Mater. 26 (2014) 4704–4710. doi:10.1002/adma.201401054.

[97] Z. Zang, Efficiency enhancement of ZnO/Cu_2O solar cells with well oriented and micrometer grain sized Cu_2O films, Appl. Phys. Lett. 112 (2018) 042106. doi:10.1063/1.5017002.

[98] K.A. Willets, R.P. Van Duyne, Localized Surface Plasmon Resonance Spectroscopy and Sensing, Annu. Rev. Phys. Chem. 58 (2007) 267–297. doi:10.1146/annurev.physchem.58.032806.104607.

[99] M. Losurdo, M.M. Giangregorio, G.V. Bianco, A. Sacchetti, P. Capezzuto, G. Bruno, Enhanced absorption in Au nanoparticles/a-Si:H/c-Si heterojunction solar cells exploiting Au surface plasmon resonance, Sol. Energy Mater. Sol. Cells. 93 (2009) 1749–1754. doi:10.1016/j.solmat.2009.06.002.

[100] F. Wu, X. Hu, J. Fan, E. Liu, T. Sun, L. Kang, W. Hou, C. Zhu, H. Liu, Photocatalytic Activity of Ag/TiO_2 Nanotube Arrays Enhanced by Surface Plasmon Resonance and Application in Hydrogen Evolution by Water Splitting, Plasmonics. 8 (2013) 501–508. doi:10.1007/s11468-012-9418-5.

[101] Z. Zhong, S. Patskovskyy, P. Bouvrette, J.H.T. Luong, A. Gedanken, The Surface Chemistry of Au Colloids and Their Interactions with Functional Amino Acids, J. Phys. Chem. B. 108 (2004) 4046–4052. doi:10.1021/jp037056a.

[102] R. Vajtai, ed., Springer Handbook of Nanomaterials, Springer Berlin Heidelberg, Berlin, Heidelberg, 2013. doi:10.1007/978-3-642-20595-8.

[103] M. Rycenga, C.M. Cobley, J. Zeng, W. Li, C.H. Moran, Q. Zhang, D. Qin, Y. Xia, Controlling the Synthesis and Assembly of Silver Nanostructures for Plasmonic Applications, Chem. Rev. 111 (2011) 3669–3712. doi:10.1021/cr100275d.

[104] S.K. Ghosh, T. Pal, Interparticle Coupling Effect on the Surface Plasmon Resonance of Gold Nanoparticles: From Theory to Applications, Chem. Rev. 107 (2007) 4797–4862. doi:10.1021/cr0680282.

[105] S. Link, M.A. El-Sayed, Size and Temperature Dependence of the Plasmon Absorption of Colloidal Gold Nanoparticles, J. Phys. Chem. B. 103 (1999) 4212–4217. doi:10.1021/jp984796o.

[106] K.L. Kelly, E. Coronado, L.L. Zhao, G.C. Schatz, The Optical Properties of Metal Nanoparticles: The Influence of Size, Shape, and Dielectric Environment, J. Phys. Chem. B. 107 (2003) 668–677. doi:10.1021/jp026731y.

[107] E. Hutter, J.H. Fendler, Exploitation of Localized Surface Plasmon Resonance, Adv. Mater. 16 (2004) 1685–1706. doi:10.1002/adma.200400271.

[108] S. Lin, M. Li, E. Dujardin, C. Girard, S. Mann, One-Dimensional Plasmon Coupling by Facile Self-Assembly of Gold Nanoparticles into Branched Chain Networks, Adv. Mater. 17 (2005) 2553–2559. doi:10.1002/adma.200500828.

[109] J. G. Hinman, A. J. Stork, J. A. Varnell, A. A. Gewirth, C. J. Murphy, Seed mediated growth of gold nanorods: towards nanorod matryoshkas, Faraday Discuss. 191 (2016) 9–33. doi:10.1039/C6FD00145A.

[110] M.W. Knight, H. Sobhani, P. Nordlander, N.J. Halas, Photodetection with Active Optical Antennas, Science. 332 (2011) 702–704. doi:10.1126/science.1203056.

[111] S. Linic, P. Christopher, D.B. Ingram, Plasmonic-metal nanostructures for efficient conversion of solar to chemical energy, Nat. Mater. 10 (2011) 911–921. doi:10.1038/nmat3151.

[112] X. Ren, E. Cao, W. Lin, Y. Song, W. Liang, J. Wang, Recent advances in surface plasmon-driven catalytic reactions, RSC Adv. 7 (2017) 31189–31203. doi:10.1039/C7RA05346K.

[113] J.K. Hyun, L.J. Lauhon, Spatially Resolved Plasmonically Enhanced Photocurrent from Au Nanoparticles on a Si Nanowire, Nano Lett. 11 (2011) 2731–2734. doi:10.1021/nl201021k.

[114] M.L. de Souza, P. Corio, A.G. Brolo, Cu nanoparticles enable plasmonic-improved silicon photovoltaic devices, Phys. Chem. Chem. Phys. 14 (2012) 15722–15728. doi:10.1039/C2CP43475J.

[115] M. Razeghi, ed., Photodetectors, in: Fundam. Solid State Eng., Springer US, Boston, MA, 2002: pp. 545–581. doi:10.1007/0-306-47567-7_16.

[116] D. Liu, D. Yang, Y. Gao, J. Ma, R. Long, C. Wang, Y. Xiong, Flexible Near-Infrared Photovoltaic Devices Based on Plasmonic Hot-Electron Injection into Silicon Nanowire Arrays, Angew. Chem. 128 (2016) 4653–4657. doi:10.1002/ange.201600279.

[117] L.-B. Luo, X.-L. Huang, M.-Z. Wang, C. Xie, C.-Y. Wu, J.-G. Hu, L. Wang, J.-A. Huang, The Effect of Plasmonic Nanoparticles on the Optoelectronic Characteristics of CdTe Nanowires, Small. 10 (2014) 2645–2652. doi:10.1002/smll.201303388.

[118] L.-B. Luo, W.-J. Xie, Y.-F. Zou, Y.-Q. Yu, F.-X. Liang, Z.-J. Huang, K.-Y. Zhou, Surface plasmon propelled high-performance CdSe nanoribbons photodetector, Opt. Express. 23 (2015) 12979. doi:10.1364/OE.23.012979.

[119] M.W. Knight, Y. Wang, A.S. Urban, A. Sobhani, B.Y. Zheng, P. Nordlander, N.J. Halas, Embedding Plasmonic Nanostructure Diodes Enhances Hot Electron Emission, Nano Lett. 13 (2013) 1687–1692. doi:10.1021/nl400196z.

[120] D.-D. Wang, C.-W. Ge, G.-A. Wu, Z.-P. Li, J.-Z. Wang, T.-F. Zhang, Y.-Q. Yu, L.-B. Luo, A sensitive red light nano-photodetector propelled by plasmonic copper nanoparticles, J. Mater. Chem. C. 5 (2017) 1328–1335. doi:10.1039/C6TC05117K.

[121] R.L. Puurunen, Surface chemistry of atomic layer deposition: A case study for the trimethylaluminum/water process, J. Appl. Phys. 97 (2005) 121301. doi:10.1063/1.1940727.

[122] M. Ritala, M. Leskelä, Deposition and Processing of Thin Films, in: H.S. Nalwa (Ed.), Handb. Thin Films Mater., Elsevier, 2001: pp. 103–159.

[123] R.W. Johnson, A. Hultqvist, S.F. Bent, A brief review of atomic layer deposition: from fundamentals to applications, Mater. Today. 17 (2014) 236–246. doi:10.1016/j.mattod.2014.04.026.

[124] Z. Zhu, E. Salmi, S. Virtanen, Residual stress study of thin films deposited by atomic layer deposition, in: 2017 IEEE 12th Int. Conf. ASIC ASICON, 2017: pp. 233–236. doi:10.1109/ASICON.2017.8252455.

[125] A. Yamada, B. Sang, M. Konagai, Atomic layer deposition of ZnO transparent conducting oxides, Appl. Surf. Sci. 112 (1997) 216–222. doi:10.1016/S0169-4332(96)01022-7.

[126] L. Lamagna, C. Wiemer, M. Perego, S. Spiga, J. Rodríguez, D. Santiago Coll, M.E. Grillo, S. Klejna, S.D. Elliott, Mechanisms for Substrate-Enhanced Growth during the Early Stages of Atomic Layer Deposition of Alumina onto Silicon Nitride Surfaces, Chem. Mater. 24 (2012) 1080–1090. doi:10.1021/cm203362d.

[127] H. Kim, S.M. Rossnagel, Growth kinetics and initial stage growth during plasma-enhanced Ti atomic layer deposition, J. Vac. Sci. Technol. Vac. Surf. Films. 20 (2002) 802–808. doi:10.1116/1.1469009.

[128] M. Junige, M. Geidel, M. Knaut, M. Albert, J.W. Bartha, Monitoring atomic layer deposition processes in situ and in real-time by spectroscopic ellipsometry, in: 2011 Semicond. Conf. Dresd., 2011: pp. 1–4. doi:10.1109/SCD.2011.6068739.

[129] A. Satta, J. Schuhmacher, C.M. Whelan, W. Vandervorst, S.H. Brongersma, G.P. Beyer, K. Maex, A. Vantomme, M.M. Viitanen, H.H. Brongersma, W.F.A. Besling, Growth mechanism and continuity of atomic layer deposited TiN films on thermal SiO_2, J. Appl. Phys. 92 (2002) 7641–7646. doi:10.1063/1.1522485.

[130] S. Jeong, E.S. Aydil, Heteroepitaxial growth of Cu_2O thin film on ZnO by metal organic chemical vapor deposition, J. Cryst. Growth. 311 (2009) 4188–4192. doi:10.1016/j.jcrysgro.2009.07.020.

[131] B. Lecohier, B. Calpini, J. -M. Philippoz, T. Stumm, H. van den Bergh, Selective low pressure chemical vapor deposition of copper: Effect of added water vapor in hydrogen or helium carrier gas, Appl. Phys. Lett. 60 (1992) 3114–3116. doi:10.1063/1.106769.

[132] N. Awaya, Y. Arita, Accelerated-Deposition Rate and High-Quality Film Copper Chemical Vapor Deposition Using a Water Vapor Addition to a Hydrogen and $Cu(HFA)_2$ Reaction System, Jpn. J. Appl. Phys. 32 (1993) 3915–3919. doi:10.1143/JJAP.32.3915.

[133] D. Depla, Magnetrons, reactive gases and sputtering, Diederik Depla, 2013. http://hdl.handle.net/1854/LU-4239033.

[134] A. Billard, F. Perry, Pulvérisation cathodique magnétron, Tech. Ing. Matér. Métalliques. (2005). https://www.techniques-ingenieur.fr.

[135] A. Billard, F. Perry, C. Frantz, Stable and unstable conditions of the sputtering mode by modulating at low frequency the current of a magnetron discharge, Surf. Coat. Technol. 94–95 (1997) 345–351. doi:10.1016/S0257-8972(97)00449-0.

[136] I. Safi, Recent aspects concerning DC reactive magnetron sputtering of thin films: a review, Surf. Coat. Technol. 127 (2000) 203–218. doi:10.1016/S0257-8972(00)00566-1.

[137] Horwat, D., Billard, A., Effects of substrate position and oxygen gas flow rate on the properties of ZnO: Al films prepared by reactive co-sputtering, Thin Solid Films. 515 (2007) 5444–5448. doi:10.1016/j.tsf.2006.12.188.

[138] Y. Wang, J. Ghanbaja, F. Soldera, S. Migot, P. Boulet, D. Horwat, F. Mücklich, J.F. Pierson, Tuning the structure and preferred orientation in reactively sputtered copper oxide thin films, Appl. Surf. Sci. 335 (2015) 85–91. doi:10.1016/j.apsusc.2015.02.028.

[139] V.K. Pecharsky, P.Y. Zavalij, Fundamentals of powder diffraction and structural characterization of materials, Springer, New York, 2005.

[140] J.I. Langford, A.J.C. Wilson, Scherrer after sixty years: a survey and some new results in the determination of crystallite size, J. Appl. Crystallogr. 11 (1978) 102–113.

[141] M. Ohring, Materials Science of Thin Films - 2nd Edition, Academic Press, 2001. https://www.elsevier.com/books/materials-science-of-thin-films/ohring/978-0-12-524975-1 (accessed October 21, 2018).

[142] C. de Melo, S. Larramendi, V. Torres-Costa, J. Santoyo-Salazar, M. Behar, J. Ferraz Dias, O. de Melo, Enhanced ZnTe infiltration in porous silicon by Isothermal Close Space Sublimation, Microporous Mesoporous Mater. 188 (2014) 93–98. doi:10.1016/j.micromeso.2013.12.036.

[143] Hiroyuki Fujiwara, Spectroscopic Ellipsometry. Principles and Applications, John Wiley & Sons Ltd, West Sussex, England, 2007.

[144] E.A. Davis, N.F. Mott, Conduction in non-crystalline systems V. Conductivity, optical absorption and photoconductivity in amorphous semiconductors, Philos. Mag. J. Theor. Exp. Appl. Phys. 22 (1970) 0903–0922. doi:10.1080/14786437008221061.

[145] J. Orloff, ed., Handbook of charged particle optics, 2. ed, CRC Press/ Taylor & Francis, Boca Raton, Fla., 2009.

[146] C.S. Campos, M.A.Z. Vasconcellos, J.C. Trincavelli, S. Segui, Analytical expression for *K* - and *L* -shell cross sections of neutral atoms near ionization threshold by electron impact, J. Phys. B At. Mol. Opt. Phys. 40 (2007) 3835–3841. doi:10.1088/0953-4075/40/19/004.

[147] A.J. Garratt-Reed, D.C. Bell, Energy-dispersive X-ray analysis in the electron microscope, BIOS, Oxford, 2003. http://site.ebrary.com/id/10162910 (accessed January 14, 2019).

[148] F. Hofer, F.-P. Schmidt, W. Grogger, G. Kothleitner, Fundamentals of electron energy-loss spectroscopy, IOP Conf. Ser. Mater. Sci. Eng. 109 (2016) 012007. doi:10.1088/1757-899x/109/1/012007.

[149] V.J. Keast, A.J. Scott, R. Brydson, D.B. Williams, J. Bruley, Electron energy-loss near-edge structure–a tool for the investigation of electronic structure on the nanometre scale, J. Microsc. 203 (2001) 135–175. doi:10.1046/j.1365-2818.2001.00898.x.

[150] D.B. Williams, C.B. Carter, Transmission electron microscopy: a textbook for materials science, 2nd ed, Springer, New York, 2008.

[151] Moulder, John F., Stickle, William F., Sobol, Peter E., Bomben, Kenneth D., Handbook of X-ray Photoelectron Spectroscopy, Physical Electronics, Inc., Jill Chastain and Roger C. King, Jr., Minnesota 55344, 1995.

[152] C. Ionescu-Zanetti, A. Mechler, Applications of Conductive Atomic Force Microscopy, Microsc. Anal. 19 (2005) 9–11.

[153] T. Fukuma, M.J. Higgins, Dynamic-Mode AFM in Liquid, in: At. Force Microsc. Liq., John Wiley & Sons, Ltd, 2012: pp. 87–119. doi:10.1002/9783527649808.ch4.

[154] F.J. Giessibl, Atomic Force Microscopy in Ultrahigh Vacuum, Jpn. J. Appl. Phys. 33 (1994) 3726. doi:10.1143/JJAP.33.3726.

[155] J.M. Mativetsky, Y.-L. Loo, P. Samorì, Elucidating the nanoscale origins of organic electronic function by conductive atomic force microscopy, J Mater Chem C. 2 (2014) 3118–3128. doi:10.1039/C3TC32050B.

[156] L. Heng, D. Tian, L. Chen, J. Su, J. Zhai, D. Han, L. Jiang, Local photoelectric conversion properties of titanyl-phthalocyanine (TiOPc) coated aligned ZnO nanorods, Chem. Commun. 46 (2010) 1162. doi:10.1039/b916026d.

[157] P. Deb, H. Kim, Y. Qin, R. Lahiji, M. Oliver, R. Reifenberger, T. Sands, GaN Nanorod Schottky and p−n Junction Diodes, Nano Lett. 6 (2006) 2893–2898. doi:10.1021/nl062152j.

[158] O.A. Bârsan, G.G. Hoffmann, L.G.J. van der Ven, G. de With, Quantitative Conductive Atomic Force Microscopy on Single-Walled Carbon Nanotube-Based Polymer Composites, ACS Appl. Mater. Interfaces. 8 (2016) 19701–19708. doi:10.1021/acsami.6b06201.

[159] C. de Melo, M. Jullien, Y. Battie, A. En Naciri, J. Ghanbaja, F. Montaigne, J.-F. Pierson, F. Rigoni, N. Almqvist, A. Vomiero, S. Migot, F. Mücklich, D. Horwat, Tunable Localized Surface Plasmon Resonance and Broadband Visible Photoresponse of Cu Nanoparticles/ZnO Surfaces, ACS Appl. Mater. Interfaces. 10 (2018) 40958–40965. doi:10.1021/acsami.8b17194.

[160] L.S.C. Pingree, O.G. Reid, D.S. Ginger, Imaging the Evolution of Nanoscale Photocurrent Collection and Transport Networks during Annealing of Polythiophene/Fullerene Solar Cells, Nano Lett. 9 (2009) 2946–2952. doi:10.1021/nl901358v.

[161] L.D. Partain, L.M. Fraas, eds., Solar cells and their applications, 2nd ed, Wiley, Hoboken, N.J, 2010.

[162] P.S. Priambodo, D. Sukoco, W. Purnomo, H. Sudibyo, D. Hartanto, Electric Energy Management and Engineering in Solar Cell System, in: Sol. Cells - Res. Appl. Perspect., Arturo Morales - Arcevedo, 2013. https://www.intechopen.com/books/solar-cells-research-and-application-perspectives/electric-energy-management-and-engineering-in-solar-cell-system (accessed May 22, 2019).

[163] J. Mulkens, M. Hanna, H. Wei, V. Vaenkatesan, H. Megens, D. Slotboom, Overlay and edge placement control strategies for the 7nm node using EUV and ArF lithography, in: Extreme Ultrav. EUV Lithogr. VI, International Society for Optics and Photonics, 2015: p. 94221Q. doi:10.1117/12.2085761.

[164] R. Vallat, R. Gassilloud, O. Salicio, K. El Hajjam, G. Molas, B. Pelissier, C. Vallée, Area selective deposition of TiO_2 by intercalation of plasma etching cycles in PEALD process: A bottom up approach for the simplification of 3D integration scheme, J. Vac. Sci. Technol. A. 37 (2019) 020918. doi:10.1116/1.5049361.

[165] R. Chen, H. Kim, P.C. McIntyre, D.W. Porter, S.F. Bent, Achieving area-selective atomic layer deposition on patterned substrates by selective surface modification, Appl. Phys. Lett. 86 (2005) 191910. doi:10.1063/1.1922076.

[166] A. Mameli, M.J.M. Merkx, B. Karasulu, F. Roozeboom, W. (Erwin) M.M. Kessels, A.J.M. Mackus, Area-Selective Atomic Layer Deposition of SiO_2 Using Acetylacetone as a Chemoselective Inhibitor in an ABC-Type Cycle, ACS Nano. 11 (2017) 9303–9311. doi:10.1021/acsnano.7b04701.

[167] M.H. Park, Y.J. Jang, H.M. Sung-Suh, M.M. Sung, Selective Atomic Layer Deposition of Titanium Oxide on Patterned Self-Assembled Monolayers Formed by Microcontact Printing, Langmuir. 20 (2004) 2257–2260. doi:10.1021/la035760c.

[168] F.S. Minaye Hashemi, B.R. Birchansky, S.F. Bent, Selective Deposition of Dielectrics: Limits and Advantages of Alkanethiol Blocking Agents on Metal–Dielectric Patterns, ACS Appl. Mater. Interfaces. 8 (2016) 33264–33272. doi:10.1021/acsami.6b09960.

[169] S. Seo, B.C. Yeo, S.S. Han, C.M. Yoon, J.Y. Yang, J. Yoon, C. Yoo, H. Kim, Y. Lee, S.J. Lee, J.-M. Myoung, H.-B.-R. Lee, W.-H. Kim, I.-K. Oh, H. Kim, Reaction Mechanism of Area-Selective Atomic Layer Deposition for Al_2O_3 Nanopatterns, ACS Appl. Mater. Interfaces. 9 (2017) 41607–41617. doi:10.1021/acsami.7b13365.

[170] R. Chen, H. Kim, P.C. McIntyre, S.F. Bent, Self-assembled monolayer resist for atomic layer deposition of HfO_2 and ZrO_2 high-κ gate dielectrics, Appl. Phys. Lett. 84 (2004) 4017–4019. doi:10.1063/1.1751211.

[171] H.-B.-R. Lee, W.-H. Kim, J.W. Lee, J.-M. Kim, K. Heo, I.C. Hwang, Y. Park, S. Hong, H. Kim, High Quality Area-Selective Atomic Layer Deposition Co Using Ammonia Gas as a Reactant, J. Electrochem. Soc. 157 (2010) D10–D15. doi:10.1149/1.3248002.

[172] W.-H. Kim, H.-B.-R. Lee, K. Heo, Y.K. Lee, T.-M. Chung, C.G. Kim, S. Hong, J. Heo, H. Kim, Atomic Layer Deposition of Ni Thin Films and Application to Area-Selective Deposition, J. Electrochem. Soc. 158 (2011) D1–D5. doi:10.1149/1.3504196.

[173] J. Hong, D.W. Porter, R. Sreenivasan, P.C. McIntyre, S.F. Bent, ALD Resist Formed by Vapor-Deposited Self-Assembled Monolayers, Langmuir. 23 (2007) 1160–1165. doi:10.1021/la0606401.

[174] S.L. Cohen, M. Liehr, S. Kasi, Mechanisms of copper chemical vapor deposition, Appl. Phys. Lett. 60 (1992) 50–52. doi:10.1063/1.107370.

[175] P.C. Lemaire, M. King, G.N. Parsons, Understanding inherent substrate selectivity during atomic layer deposition: Effect of surface preparation, hydroxyl density, and metal oxide composition on nucleation mechanisms during tungsten ALD, J. Chem. Phys. 146 (2016) 052811. doi:10.1063/1.4967811.

[176] D. Horwat, M. Dehmas, A. Gutiérrez, J.-F. Pierson, A. Anders, F. Soldera, J.-L. Endrino, Efficient, Low Cost Synthesis of Sodium Platinum Bronze $Na_XPt_3O_4$, Chem. Mater. 24 (2012) 2429–2432. doi:10.1021/cm301179x.

[177] K. Sivaramakrishnan, N.D. Theodore, J.F. Moulder, T.L. Alford, The role of copper in ZnO/Cu/ZnO thin films for flexible electronics, J. Appl. Phys. 106 (2009) 063510. doi:10.1063/1.3213385.

[178] M. Behrens, F. Studt, I. Kasatkin, S. Kühl, M. Hävecker, F. Abild-Pedersen, S. Zander, F. Girgsdies, P. Kurr, B.-L. Kniep, M. Tovar, R.W. Fischer, J.K. Nørskov, R. Schlögl, The

Active Site of Methanol Synthesis over $Cu/ZnO/Al_2O_3$ Industrial Catalysts, Science. 336 (2012) 893–897. doi:10.1126/science.1219831.

[179] T. Lunkenbein, J. Schumann, M. Behrens, R. Schlögl, M.G. Willinger, Formation of a ZnO Overlayer in Industrial $Cu/ZnO/Al_2O_3$ Catalysts Induced by Strong Metal–Support Interactions, Angew. Chem. 127 (2015) 4627–4631. doi:10.1002/ange.201411581.

[180] S.S. Jeong, A. Mittiga, E. Salza, A. Masci, S. Passerini, Electrodeposited ZnO/Cu_2O heterojunction solar cells, Electrochimica Acta. 53 (2008) 2226–2231. doi:10.1016/j.electacta.2007.09.030.

[181] K. Tominaga, T. Yuasa, M. Kume, O. Tada, Influence of Energetic Oxygen Bombardment on Conductive ZnO Films, Jpn. J. Appl. Phys. 24 (1985) 944–949.

[182] M. Jullien, D. Horwat, F. Manzeh, R. Escobar Galindo, P. Bauer, J.F. Pierson, J.L. Endrino, Influence of the nanoscale structural features on the properties and electronic structure of Al-doped ZnO thin films: An X-ray absorption study, Sol. Energy Mater. Sol. Cells. 95 (2011) 2341–2346. doi:10.1016/j.solmat.2011.04.003.

[183] J. Gan, S. Gorantla, H.N. Riise, Ø.S. Fjellvåg, S. Diplas, O.M. Løvvik, B.G. Svensson, E.V. Monakhov, A.E. Gunnæs, Structural properties of Cu_2O epitaxial films grown on c-axis single crystal ZnO by magnetron sputtering, Appl. Phys. Lett. 108 (2016) 152110. doi:10.1063/1.4945985.

[184] J. Narayan, B.C. Larson, Domain epitaxy: A unified paradigm for thin film growth, J. Appl. Phys. 93 (2002) 278. doi:10.1063/1.1528301.

[185] A. Trampert, K. h. Ploog, Heteroepitaxy of Large-Misfit Systems: Role of Coincidence Lattice, Cryst. Res. Technol. 35 (2000) 793–806. doi:10.1002/1521-4079(200007)35:6/7<793::AID-CRAT793>3.0.CO;2-3.

[186] P. Zaumseil, High-resolution characterization of the forbidden Si 200 and Si 222 reflections, J. Appl. Crystallogr. 48 (2015) 528–532. doi:10.1107/S1600576715004732.

[187] A.E. Gunnæs, S. Gorantla, O.M. Løvvik, J. Gan, P.A. Carvalho, B.G. Svensson, E.V. Monakhov, K. Bergum, I.T. Jensen, S. Diplas, Epitaxial Strain-Induced Growth of CuO at Cu_2O/ZnO Interfaces, J. Phys. Chem. C. 120 (2016) 23552–23558. doi:10.1021/acs.jpcc.6b07197.

[188] S.L. Cohen, M. Liehr, S. Kasi, Selectivity in copper chemical vapor deposition, Appl. Phys. Lett. 60 (1992) 1585–1587. doi:10.1063/1.107259.

[189] N. ul H. Alvi, S. Hussain, J. Jensen, O. Nur, M. Willander, Influence of helium-ion bombardment on the optical properties of ZnO nanorods/p-GaN light-emitting diodes, Nanoscale Res. Lett. 6 (2011) 628. doi:10.1186/1556-276X-6-628.

[190] L.J. Brillson, H.L. Mosbacker, D.L. Doutt, Y. Dong, Z.-Q. Fang, D.C. Look, G. Cantwell, J. Zhang, J.J. Song, Nanoscale depth-resolved cathodoluminescence spectroscopy of ZnO surfaces and metal interfaces, Superlattices Microstruct. 45 (2009) 206–213. doi:10.1016/j.spmi.2008.11.008.

[191] S.A. French, A.A. Sokol, S.T. Bromley, C.R.A. Catlow, P. Sherwood, Identification and Characterization of Active Sites and Their Catalytic Processes—the Cu/ZnO Methanol Catalyst, Top. Catal. 24 (2003) 161–172. doi:10.1023/B:TOCA.0000003087.47073.de.

[192] K. Henzler, A. Heilemann, J. Kneer, P. Guttmann, H. Jia, E. Bartsch, Y. Lu, S. Palzer, Investigation of reactions between trace gases and functional CuO nanospheres and octahedrons using NEXAFS-TXM imaging, Sci. Rep. 5 (2015) 17729. doi:10.1038/srep17729.

[193] W. Chamorro, T.S. Shyju, P. Boulet, S. Migot, J. Ghanbaja, P. Miska, P. Kuppusami, J.F. Pierson, Role of Cu+ on ZnS:Cu p-type semiconductor films grown by sputtering: influence of substitutional Cu in the structural, optical and electronic properties, RSC Adv. 6 (2016) 43480–43488. doi:10.1039/C6RA05819A.

[194] Y. Wang, S. Lany, J. Ghanbaja, Y. Fagot-Revurat, Y.P. Chen, F. Soldera, D. Horwat, F. Mücklich, J.F. Pierson, Electronic structures of Cu_2O, Cu_4O_3, and CuO: A joint experimental and theoretical study, Phys. Rev. B. 94 (2016) 245418. doi:10.1103/PhysRevB.94.245418.

[195] R.D. Leapman, L.A. Grunes, P.L. Fejes, Study of the L_{23} edges in the 3d transition metals and their oxides by electron-energy-loss spectroscopy with comparisons to theory, Phys. Rev. B. 26 (1982) 614–635. doi:10.1103/PhysRevB.26.614.

[196] A.B. Gurevich, B.E. Bent, A.V. Teplyakov, J.G. Chen, A NEXAFS investigation of the formation and decomposition of CuO and Cu_2O thin films on Cu(100), Surf. Sci. 442 (1999) L971–L976. doi:10.1016/S0039-6028(99)00913-9.

[197] R. Stanley, Plasmonics in the mid-infrared, Nat. Photonics. 6 (2012) 409–411. doi:10.1038/nphoton.2012.161.

[198] T. Jiang, C. Jia, L. Zhang, S. He, Y. Sang, H. Li, Y. Li, X. Xu, H. Liu, Gold and gold–palladium alloy nanoparticles on heterostructured TiO_2 nanobelts as plasmonic photocatalysts for benzyl alcohol oxidation, Nanoscale. 7 (2015) 209–217. doi:10.1039/C4NR05905K.

[199] C.-H. Chou, F.-C. Chen, Plasmonic nanostructures for light trapping in organic photovoltaic devices, Nanoscale. 6 (2014) 8444–8458. doi:10.1039/C4NR02191F.

[200] P. Liu, H. Wang, X. Li, M. Rui, H. Zeng, Localized surface plasmon resonance of Cu nanoparticles by laser ablation in liquid media, RSC Adv. 5 (2015) 79738–79745. doi:10.1039/C5RA14933A.

[201] Z. Han, L. Wei, Z. Zhang, X. Zhang, H. Pan, J. Chen, Visible-Light Photocatalytic Application of Hierarchical Au-ZnO Flower-Rod Heterostructures via Surface Plasmon Resonance, Plasmonics. 8 (2013) 1193–1202. doi:10.1007/s11468-013-9531-0.

[202] N. Gogurla, A.K. Sinha, S. Santra, S. Manna, S.K. Ray, Multifunctional Au-ZnO Plasmonic Nanostructures for Enhanced UV Photodetector and Room Temperature NO Sensing Devices, Sci. Rep. 4 (2014) 6483–6492. doi:10.1038/srep06483.

[203] G.H. Chan, J. Zhao, E.M. Hicks, G.C. Schatz, R.P. Van Duyne, Plasmonic Properties of Copper Nanoparticles Fabricated by Nanosphere Lithography, Nano Lett. 7 (2007) 1947–1952. doi:10.1021/nl070648a.

[204] C. Wei, Q. Liu, Shape-, size-, and density-tunable synthesis and optical properties of copper nanoparticles, CrystEngComm. 19 (2017) 3254–3262. doi:10.1039/C7CE00750G.

[205] A. Khan, A. Rashid, R. Younas, R. Chong, A chemical reduction approach to the synthesis of copper nanoparticles, Int. Nano Lett. 6 (2016) 21–26. doi:10.1007/s40089-015-0163-6.

[206] C. de Melo, M. Jullien, J. Ghanbaja, F. Montaigne, J.-F. Pierson, F. Soldera, F. Rigoni, N. Almqvist, A. Vomiero, F. Mücklich, D. Horwat, Local Structure and Point-Defect-Dependent Area-Selective Atomic Layer Deposition Approach for Facile Synthesis of p-Cu_2O/n-ZnO Segmented Nanojunctions, ACS Appl. Mater. Interfaces. 10 (2018) 37671–37678. doi:10.1021/acsami.8b12584.

[207] P. Shrestha, D. Gu, N. Tran, K. Tapily, H. Baumgart, G. Namkoong, Investigation of Volmer-Weber Growth during the Nucleation Phase of ALD Platinum Thin Films and Template Based Platinum Nanotubes, ECS Trans. 33 (2010) 127–134. doi:10.1149/1.3485249.

[208] R.L. Puurunen, W. Vandervorst, Island growth as a growth mode in atomic layer deposition: A phenomenological model, J. Appl. Phys. 96 (2004) 7686–7695. doi:10.1063/1.1810193.

[209] J.W.C. de Vries, F.J.A. den Broeder, Influence of interface scattering on the resistance of polycrystalline Au/Pd multilayered thin films, J. Phys. F Met. Phys. 18 (1988) 2635–2647. doi:10.1088/0305-4608/18/12/014.

[210] D. Gall, Electron mean free path in elemental metals, J. Appl. Phys. 119 (2016) 085101.

[211] Y. Battie, A. En Naciri, M. Vergnat, Plasmonic and metallic optical properties of Au/SiO_2 metal-insulator films, J. Appl. Phys. 122 (2017) 213101. doi:10.1063/1.5003302.

[212] R.S. Moirangthem, Y.-C. Chang, P.-K. Wei, Ellipsometry study on gold-nanoparticle-coated gold thin film for biosensing application, Biomed. Opt. Express. 2 (2011) 2569–2576. doi:10.1364/BOE.2.002569.

[213] B.M. Reinhard, M. Siu, H. Agarwal, A.P. Alivisatos, J. Liphardt, Calibration of Dynamic Molecular Rulers Based on Plasmon Coupling between Gold Nanoparticles, Nano Lett. 5 (2005) 2246–2252. doi:10.1021/nl051592s.

[214] J.J. Mock, M. Barbic, D.R. Smith, D.A. Schultz, S. Schultz, Shape effects in plasmon resonance of individual colloidal silver nanoparticles, J. Chem. Phys. 116 (2002) 6755–6759. doi:10.1063/1.1462610.

[215] J. Vieaud, J. Gao, J. Cane, M. Stchakovsky, A. En Naciri, K. Ariga, R. Oda, E. Pouget, Y. Battie, Gold Nanoparticle Chains: Synthesis, Characterization, and Modeling Using Spectroscopic Ellipsometry, J. Phys. Chem. C. 122 (2018) 11973–11984. doi:10.1021/acs.jpcc.8b01614.

[216] A. Ziashahabi, T. Ghodselahi, M. Heidari saani, Localized Surface Plasmon Resonance properties of copper nano-clusters: A theoretical study of size dependence, J. Phys. Chem. Solids. 74 (2013) 929–933. doi:10.1016/j.jpcs.2013.02.009.

[217] A. Khan, M. Hussain, M.A. Abbasi, Z.H. Ibupoto, O. Nur, M. Willander, Study of transport properties of copper/zinc-oxide-nanorods-based Schottky diode fabricated on textile fabric, Semicond. Sci. Technol. 28 (2013) 125006. doi:10.1088/0268-1242/28/12/125006.

[218] L.J. Brillson, Y. Lu, ZnO Schottky barriers and Ohmic contacts, J. Appl. Phys. 109 (2011) 121301. doi:10.1063/1.3581173.

[219] K. Muhammed Shafi, R. Vinodkumar, R.J. Bose, V.N. Uvais, V.P. Mahadevan Pillai, Effect of Cu on the microstructure and electrical properties of Cu/ZnO thin films, J. Alloys Compd. 551 (2013) 243–248. doi:10.1016/j.jallcom.2012.10.032.

[220] H.B. Michaelson, The work function of the elements and its periodicity, J. Appl. Phys. 48 (1977) 4729–4733. doi:10.1063/1.323539.

[221] I. Lange, S. Reiter, M. Pätzel, A. Zykov, A. Nefedov, J. Hildebrandt, S. Hecht, S. Kowarik, C. Wöll, G. Heimel, D. Neher, Tuning the Work Function of Polar Zinc Oxide Surfaces using Modified Phosphonic Acid Self-Assembled Monolayers, Adv. Funct. Mater. 24 (2014) 7014–7024. doi:10.1002/adfm.201401493.

[222] M. Wei, C.-F. Li, X.-R. Deng, H. Deng, Surface Work Function of Transparent Conductive ZnO Films, Energy Procedia. 16 (2012) 76–80. doi:10.1016/j.egypro.2012.01.014.

[223] A. Kahn, Fermi level, work function and vacuum level, Mater. Horiz. 3 (2016) 7–10. doi:10.1039/C5MH00160A.

[224] L. Hu, L. Zhu, H. He, Y. Guo, G. Pan, J. Jiang, Y. Jin, L. Sun, Z. Ye, Colloidal chemically fabricated ZnO:Cu-based photodetector with extended UV-visible detection waveband, Nanoscale. 5 (2013) 9577–9581. doi:10.1039/C3NR01979A.

[225] E. Kus¸demir, D. Özkendir, V. Fırat, C. Çelebi, Epitaxial graphene contact electrode for silicon carbide based ultraviolet photodetector, J. Phys. Appl. Phys. 48 (2015) 095104. doi:10.1088/0022-3727/48/9/095104.

[226] S. Samanta, K. Das, A.K. Raychaudhuri, Junction Effect on Transport Properties of a Single Si Nanowire Metal–Semiconductor–Metal Device, IEEE Trans. Nanotechnol. 12 (2013) 1089–1093. doi:10.1109/TNANO.2013.2279838.

[227] J. Osvald, Back-to-back connected asymmetric Schottky diodes with series resistance as a single diode, Phys. Status Solidi A. 212 (2015) 2754–2758. doi:10.1002/pssa.201532374.

[228] W.M.H. Sachtler, G.J.H. Dorgelo, A.A. Holscher, The work function of gold, Surf. Sci. 5 (1966) 221–229. doi:10.1016/0039-6028(66)90083-5.

[229] E.H. Rhoderick, Metal-semiconductor contacts, IEE Proc. - Solid State Electron Devices. 129 (1982) 1–14. doi:10.1049/ip-i-1.1982.0001.

[230] I. Goykhman, U. Sassi, B. Desiatov, N. Mazurski, S. Milana, D. de Fazio, A. Eiden, J. Khurgin, J. Shappir, U. Levy, A.C. Ferrari, On-Chip Integrated, Silicon–Graphene Plasmonic Schottky Photodetector with High Responsivity and Avalanche Photogain, Nano Lett. 16 (2016) 3005–3013. doi:10.1021/acs.nanolett.5b05216.

[231] N. Kouklin, Cu-Doped ZnO Nanowires for Efficient and Multispectral Photodetection Applications, Adv. Mater. 20 (2008) 2190–2194. doi:10.1002/adma.200701071.

[232] T.-F. Zhang, G.-A. Wu, J.-Z. Wang, Y.-Q. Yu, D.-Y. Zhang, D.-D. Wang, J.-B. Jiang, J.-M. Wang, L.-B. Luo, A sensitive ultraviolet light photodiode based on graphene-on-zinc oxide Schottky junction, Nanophotonics. 6 (2017) 1073–1081. doi:10.1515/nanoph-2016-0143.

[233] A. Altaweel, A. Imam, J. Ghanbaja, D. Mangin, P. Miska, T. Gries, T. Belmonte, Fast synthesis of ultrathin ZnO nanowires by oxidation of Cu/Zn stacks in low-pressure afterglow, Nanotechnology. 28 (2017) 085602. doi:10.1088/1361-6528/28/8/085602.

[234] K. Kardarian, D. Nunes, P. Maria Sberna, A. Ginsburg, D.A. Keller, J. Vaz Pinto, J. Deuermeier, A.Y. Anderson, A. Zaban, R. Martins, E. Fortunato, Effect of Mg doping on Cu_2O thin films and their behavior on the TiO_2/Cu_2O heterojunction solar cells, Sol. Energy Mater. Sol. Cells. 147 (2016) 27–36. doi:10.1016/j.solmat.2015.11.041.

[235] Y. Nishi, T. Miyata, T. Minami, Effect of inserting a thin buffer layer on the efficiency in n-ZnO/p-Cu_2O heterojunction solar cells, J. Vac. Sci. Technol. A. 30 (2012) 04D103. doi:10.1116/1.3698596.

[236] L. Olivieri, E. Caamaño-Martin, F. Olivieri, J. Neila, Integral energy performance characterization of semi-transparent photovoltaic elements for building integration under real operation conditions, Energy Build. 68 (2014) 280–291. doi:10.1016/j.enbuild.2013.09.035.

[237] T. Ito, T. Kawashima, H. Yamaguchi, T. Masumi, S. Adachi, Optical Properties of Cu_2O Studied by Spectroscopic Ellipsometry, J. Phys. Soc. Jpn. 67 (1998) 2125–2131. doi:10.1143/JPSJ.67.2125.

[238] H. Liu, F. Zeng, Y. Lin, G. Wang, F. Pan, Correlation of oxygen vacancy variations to band gap changes in epitaxial ZnO thin films, Appl. Phys. Lett. 102 (2013) 181908. doi:10.1063/1.4804613.

[239] L. De Los Santos Valladares, D.H. Salinas, A.B. Dominguez, D.A. Najarro, S.I. Khondaker, T. Mitrelias, C.H.W. Barnes, J.A. Aguiar, Y. Majima, Crystallization and electrical resistivity of Cu_2O and CuO obtained by thermal oxidation of Cu thin films on SiO_2/Si substrates, Thin Solid Films. 520 (2012) 6368–6374. doi:10.1016/j.tsf.2012.06.043.

[240] C.-L. Chu, H.-C. Lu, C.-Y. Lo, C.-Y. Lai, Y.-H. Wang, Physical properties of copper oxide thin films prepared by dc reactive magnetron sputtering under different oxygen partial pressures, Phys. B Condens. Matter. 404 (2009) 4831–4834. doi:10.1016/j.physb.2009.08.185.

[241] Gunter Wyszecki, W. S. Stiles, Color Science: Concepts and Methods, Quantitative Data and Formulae, 2nd ed., John Wiley and Sons, New York, 1982. https://onlinelibrary-wiley-com/doi/abs/10.1002/col.5080080421.

[242] T. Dimopoulos, A. Peić, S. Abermann, M. Postl, E.J.W. List-Kratochvil, R. Resel, Effect of thermal annealing in vacuum on the photovoltaic properties of electrodeposited Cu_2O-absorber solar cell, EPJ Photovolt. 5 (2014) 50301. doi:10.1051/epjpv/2014005.

[243] S. Jeong, S.H. Song, K. Nagaich, S.A. Campbell, E.S. Aydil, An analysis of temperature dependent current–voltage characteristics of Cu_2O–ZnO heterojunction solar cells, Thin Solid Films. 519 (2011) 6613–6619. doi:10.1016/j.tsf.2011.04.241.

[244] J. Lv, J. Xu, M. Zhao, P. Yan, S. Mao, F. Shang, G. He, M. Zhang, Z. Sun, Effect of seed layer on optical properties and visible photoresponse of ZnO/Cu_2O composite thin films, Ceram. Int. 41 (2015) 13983–13987. doi:10.1016/j.ceramint.2015.07.010.

[245] M. Saifullah, S. Ahn, J. Gwak, S. Ahn, K. Kim, J. Cho, J.H. Park, Y.J. Eo, A. Cho, J.-S. Yoo, J.H. Yun, Development of semitransparent CIGS thin-film solar cells modified with a sulfurized-AgGa layer for building applications, J. Mater. Chem. A. 4 (2016) 10542–10551. doi:10.1039/C6TA01909A.

[246] Y. Liu, H.K. Turley, J.R. Tumbleston, E.T. Samulski, R. Lopez, Minority carrier transport length of electrodeposited Cu_2O in ZnO/Cu_2O heterojunction solar cells, Appl. Phys. Lett. 98 (2011) 162105. doi:10.1063/1.3579259.

[247] T. Gershon, K.P. Musselman, A. Marin, R.H. Friend, J.L. MacManus-Driscoll, Thin-film ZnO/Cu_2O solar cells incorporating an organic buffer layer, Sol. Energy Mater. Sol. Cells. 96 (2012) 148–154. doi:10.1016/j.solmat.2011.09.043.

[248] P. Würfel, Physics of solar cells: from principles to new concepts, Wiley-VCH, Weinheim, 2005.

[249] P. Lin, X. Chen, X. Yan, Z. Zhang, H. Yuan, P. Li, Y. Zhao, Y. Zhang, Enhanced photoresponse of Cu_2O/ZnO heterojunction with piezo-modulated interface engineering, Nano Res. 7 (2014) 860–868. doi:10.1007/s12274-014-0447-6.

Resume

Place and date of birth: August 28th, Havana, Cuba, 1989 claudiadem@gmail.com

Address: 240 Rue Jeanne d'Arc, 54000 Nancy, France + 33 6 10 44 30 50

Language skills: Spanish (mother tong), English (fluent), French (fluent)

Education

PhD in Materials Science. University of Lorraine, Nancy, France/ Saarland University, Saarbrucken, Germany. (Novemeber 2015 – May 2019)

MSc. in Physics. School of Physics, University of Havana, Cuba (September 2012 – January 2015)

Bachelor of Science in Physics. School of Physics, University of Havana, Cuba (September 2007 – July 2012)

Experience

PhD student. Institute Jean Lamour, University of Lorraine and Chair of Functional Materials, Saarland University (November 2015 – Mai 2019).

Research project: *Selective growth of metallic Cu, Cu_2O thin films and Cu nanoparticles by atomic layer deposition on ZnO films deposited by reactive magnetron sputtering for photodetecion and photovoltaics*.

Junior Assistant Professor and Researcher. School of Physics, University of Havana, Cuba (September 2012- July 2015).

Research project: *Studying the modification of the optical properties of porous Si by embedding II-VI semiconductors (ZnTe, CdTe and ZnO) using the isothermal closed space vaporization technique.*

Awards

Best Oral Presentation Award, RAFALD 2018, November 6 – 8, Lyon, France

Erasmus mundus fellowship 2015 to participate in the DocMASE Doctoral Programme.

National Award of the Sciences Academy of Cuba 2015. *Physics vapor transport for the preparation of photovoltaic materials,* O. de Melo, G. Santana, G. Contreras, P. Gutierrez, C. de Melo.

Best Poster Mention presented by a Junior Researcher. 8th Symposium of the Cuban Physics Society, Havana, March 2014.

Best Graduate of the School of Physics in the academic year 2011-2012.

Publications

1. C. de Melo, M. Jullien, Y. Battie, A. En Naciri, J. Ghanbaja, F. Montaigne, J. F. Pierson, F. Rigoni, N. Almqvist, A. Vomiero, S. Migot, F. Mücklich, D. Horwat, Self-powered visible photoresponse of semi-transparent p-Cu_2O/n-ZnO heterojunctions, ACS Appl. Nano Mater. (under review).

2. C. de Melo, M. Jullien, Y. Battie, A. En Naciri, J. Ghanbaja, F. Montaigne, J. F. Pierson, F. Rigoni, N. Almqvist, A. Vomiero, S. Migot, F. Mücklich, D. Horwat. Tunable Localized Surface Plasmon Resonance and Broadband Visible Photo-response of Cu Nanoparticles/ZnO Surfaces, ACS Applied Materials & Interfaces, 10, 40958 (2018).

3. C. de Melo, M. Jullien, J. Ghanbaja, F. Montaigne, J. F. Pierson, F. Soldera, F. Rigoni, N. Almqvist, A. Vomiero, F. Mücklich, D. Horwat, Local structure and point defects-dependent Area-Selective Atomic Layer Deposition Approach for Facile Synthesis of p-Cu_2O/n-ZnO Segmented Nano-junctions, ACS Applied Materials & Interfaces 10, 37671 (2018).

4. O. de Melo, M. Sánchez, A. Borroto, **C. de Melo**, B. J. García, J. L. Pau, and D. Horwat, WTe_2 Synthesis by Tellurization of W Precursors Using Isothermal Close Space Vapor Transport Annealing, Phys. Status Solidi A 215, 1800425 (2018).

5. C. de Melo, G. Santana, V. Torres-Costa, M Behar, J. Ferraz Dias, J. L. Colaux, G. Contreras-Puente, O. de Melo, Infiltration of ZnO in mesoporous silicon by isothermal Zn annealing and oxidation, ECS Journal of Solid State Science and Technology 5, 6 (2016).

6. C. de Melo, G. Santana, J. Santoyo and O. de Melo, White luminescence in porous silicon embedded with II-VI semiconductors, Revista Cubana de Física 31, 29 (2014).

7. C. de Melo, S. Larramendi, V. Torres- Costa, J. Santoyo-Salazar, M. Behar, J. Ferraz Dias, O. de Melo, Enhanced ZnTe infiltration in porous silicon by Isothermal Close Space Sublimation, Microporous and Mesoporous Materials 188, 93 (2014).

8. V. Torres – Costa, **C. de Melo**, A. Climent – Font, F. Argulló – Rueda and O. de Melo, Isothermal close space sublimation for II-VI semiconductor filling of porous matrices, Nanoscale Research Letters 7, 409 (2012).

9. O. de Melo, **C. de Melo**, G. Santana, J. Santoyo, O. Zelaya – Angel, J. G. Mendoza – Álvarez, V. Torres – Costa, Intense white luminescence in ZnTe embedded porous silicon, Applied Physics Letters 100, 263110 (2012).

Scientific Meetings

Oral Communications

1. Workshop RAFALD 2018, November 6 – 8, Lyon, France, *Fabrication of p-Cu_2O / n-ZnO micro-junctions by area-selective atomic layer deposition*. **C. de Melo**, M. Jullien, J. Ghanbaja, F. Montaigne, J. F. Pierson, F. Soldera, F. Rigoni, N. Almqvist, A. Vomiero, F. Mücklich, D. Horwat.

2. EMN Meetings 2018, September 10-14, 2018, Barcelona, Spain, *Area-selective atomic layer deposition of copper oxide and metallic copper thin films for facile synthesis of p-Cu_2O/n-ZnO junctions* **(INVITED CONFERENCE)**. **C. de Melo**, M. Jullien, J. Ghanbaja, F. Montaigne, J. F. Pierson, F. Soldera, F. Rigoni, N. Almqvist, A. Vomiero, F. Mücklich, D. Horwat.

3. MRS Fall Meeting and Exhibit, November 26 - December 1, 2017, Boston, Massachusetts, United States, *Epitaxial growth of copper oxide on c-axis oriented ZnO films by atomic layer deposition*. **C. de Melo**, M. Jullien, J. F. Pierson, Y. Battie, A. En Naciri, F. Mücklich, D. Horwat.

4. European congress and exhibition on advanced materials and processes EUROMAT 2017, September 17 – 22, Thessaloniki, Greece, *Atomic layer deposition of copper oxide and metallic copper thin films*. **C. de Melo**, M. Jullien, J. F. Pierson, F. Mücklich, D. Horwat.

5. 8th International Conference on Innovations in Thin Film Processing and Characterization, October 23-27, 2017, Nancy, France, *Atomic layer deposition of copper oxide and metallic*

copper thin films on ZnO. **C. de Melo**, M. Jullien, J. F. Pierson, Y. Battie, A. En Naciri, F. Mücklich, D. Horwat.

6. Workshop RAFALD 2017, November 7 – 9, Montpellier, France, *Selective deposition of Cu and Cu_2O by atomic layer deposition using $Cu(hfac)_2$*. **C. de Melo**, M. Jullien, J. F. Pierson, Y. Battie, A. En Naciri, F. Montaigne, S. Migot, J. Ghanbaja, T. Gries, F. Mücklich, D. Horwat.

7. VIII International Conference on Surfaces, Materials and Vacuum, Puebla, September 21-25, 2015, *Structure and luminescence of CdTe embedded porous silicon*, **C. de Melo**, G. Romero, G. Santana, J. Santoyo-Salazar, J. Ferraz Dias, M. Behar, O. de Melo.

8. Scientific Conferences of the Institute of Science and Materials Technology, Havana, June 17-18, 2014, *White luminescence in porous silicon infiltrated with II-VI semiconductors*, **C. de Melo**, G. Santana, J. Santoyo-Salazar, M. Behar, J. Ferraz-Dias, O. de Melo.

Poster

1. Seminar of the EMMA doctoral school 2017, May 4th, 2017, Nancy, France, *Atomic layer deposition of copper oxide and metallic copper thin films on ZnO*, **C. de Melo**, M. Jullien, J.F. Pierson, Y. Battie, A. En Naciri, F. Mücklich, D. Horwat.

2. RAFALD: Journée du Réseau des Acteurs Français de l'ALD, November 14 – 16, 2016, Chatou/Paris, France, *Atomic layer deposition of copper oxide thin films using copper (II) hexafluoro-acetyl-acetonate and water as precursors*, **C. de Melo**, M. Jullien, J. F. Pierson, F. Mücklich, D. Horwat.

3. International Materials Research Meeting in the Greater Region: Current Trends in the Characterization of Materials and Surface Modification, April 6 – 7, 2017, Saarbrücken, Germany, *Atomic layer deposition of copper oxide and metallic copper thin films on ZnO*, **C. de Melo**, M. Jullien, J. F. Pierson, F. Mücklich, D. Horwat.

4. International Conference Material Science in the Age of Sustainability, Havana, June 29-July 1, 2015. *Infiltration of ZnO in mesoporous silicon by isothermal Zn annealing and oxidation*, **C. de Melo**, G. Santana, V. Torres-Costa, M. Behar, J. Ferraz Dias, O. de Melo

5. 13th Symposium and 11th Congress of the Cuban Physics Society, Havana, March 17 – 21, 2014. *White luminescence in porous silicon infiltrated with II-VI semiconductors*, **C. de Melo**, G. Santana, J. Santoyo, M. Behar, J. Ferraz-Dias, O. de Melo.

6. Porous Semiconductors Science and Technology, PSST 2014, Benidorm, March 3, 2014, *Enhancing ZnTe infiltration into porous silicon by ICSS for white luminescence structures*, C. de Melo, **V. Torres-Costa**, J. Santoyo-Salazar, M. Behar, J. Ferraz-Dias, G. Santana, O. de Melo.

7. 8th International Congress on Chemistry, Chemical Engineering and Biochemistry, October 9 – 12, 2012, Havana, *Infiltration of II-VI semiconductors into porous silicon*, **C. de Melo**, V. Torres-Costa, A. Climent-Font, O. de Melo.

8. 5th International Conference on Surfaces, Materials and Vacuum, September 24 – 28, 2012, Tuxtla Gutiérrez, Chiapas, *White luminescence in ZnTe embedded porous silicon*, **O. de Melo**, C. de Melo, J. Santoyo, O. Zelaya- Angel, Julio German Mendoza- Alvarez, V. Torres- Costa.

9. 8th International Conference on Porous Semiconductors, Málaga, March 25 – 30, 2012, *Isothermal close space sublimation for II-VI semiconductor filling of porous matrices*, **V. Torres- Costa**, C. de Melo, A. Climent- Font, O. de Melo.

10. 12th Symposium of the Cuban Physics Society, Havana, March 7 – 11, 2011, *Infiltration of ZnTe into porous silicon*, **C. de Melo**, V. Torres- Costa, G. Santana, M. Behar, E. Pedrero, O. de Melo

Croissance sélective de Cu_2O et Cu métallique par dépôt par couche atomique sur ZnO et leur application en optoélectronique

Résumé : Dans ce travail, après l'état de l'art et la présentation de méthodes de synthèse et d'analyse, nous présentons des résultats sur la croissance sélective de Cu_2O et Cu métallique par dépôt par couche atomique (ALD) sur ZnO, ZnO dopé à l'Al (AZO) et α-Al_2O_3. Nous mettons en évidence la possibilité de déposer de façon sélective Cu métallique ou Cu_2O, en contrôlant la température de dépôt et la conductivité ou la densité des défauts ponctuels au sein du substrat. Un procédé sélectif local de dépôt par couche atomique (AS-ALD) a été mis en évidence sur une bicouche à motifs composée de zones de ZnO de faible conductivité et de régions d'AZO de forte conductivité. De plus, l'AS-ALD permet la fabrication de nano-jonctions à base de Cu_2O/ZnO /AZO/Cu, dont le comportement de jonction p-n a été confirmé par microscopie à force atomique à pointe conductrice (C-AFM). Les mécanismes liés à la croissance sélective locale sont également discutés. Dans la seconde partie de cette thèse, des nanoparticules de Cu (NP) ont été déposées par ALD sur des couches minces de ZnO. Les NP de Cu présentent une résonance plasmon de surface localisée caractérisée par ellipsométrie. La position de la bande de résonance plasmon est ajustable entre les régions visible et infrarouge du spectre électromagnétique en gérant la taille des particules et leur espacement par l'intermédiaire du temps de dépôt. Le système Cu NP/ZnO montre une photo-réponse dans le visible grâce à la génération d'électrons chauds à la surface des NP de Cu et l'injection dans la bande de conduction de ZnO. Finalement, des hétérojonctions Cu_2O/ZnO semi-transparentes ont été fabriquées par ALD et pulvérisation cathodique. Les hétérojonctions présentent une photo-réponse autoalimentée sous éclairement, des temps de réponse rapides et une transparence élevée dans le visible, ce qui est prometteur pour des applications dans les domaines de l'électronique transparente, la photo-détection et le photovoltaïque.

Mots-clés : *oxyde de cuivre, dépôt sélectif local par couche atomique, nanoparticules de cuivre, résonance plasmon de surface localisée, jonctions p-n*

Selective growth of Cu_2O and metallic Cu by atomic layer deposition on ZnO and their application in optoelectronics

Abstract: In this work we present the results on the selective growth of Cu_2O and metallic Cu by atomic layer deposition (ALD) on ZnO, Al-doped ZnO (AZO) and α-Al_2O_3 substrates. It was possible to tune the deposited material (Cu or Cu_2O) by controlling the deposition temperature, and the substrate conductivity/density of donor defects. An area-selective atomic layer deposition (AS-ALD) process was demonstrated on a patterned bi-layer structure composed of low-conductive ZnO, and highly-conductive AZO regions. Furthermore, the AS-ALD allows the fabrication of Cu_2O/ZnO/AZO/Cu-back-electrode microjunctions, as confirmed by conductive atomic force microscopy (C-AFM). The mechanism behind the temperature and spatial selectivities is discussed. In a second part of this thesis, Cu nanoparticles (NP) were deposited by ALD on ZnO thin films. The Cu NP exhibit a localized surface plasmon resonance, tunable from the visible to the near-infrared regions, as confirmed by spectroscopic ellipsometry. An enhanced visible photo-response was observed in the Cu NP/ZnO device thanks to the hot-electron generation at the surface of the plasmonic Cu NP and transfer into the conduction band of ZnO. Finally, semi-transparent Cu_2O/ZnO heterojunctions were fabricated by ALD and reactive magnetron sputtering. The heterojunctions present a stable self-powered photo-response under 1 Sun illumination, fast response times and high transparency in the visible region, which is promising for all-oxide transparent electronics, photodetection and photovoltaics.

Keywords: *copper oxide, area-selective atomic layer deposition, copper nanoparticles, localized surface plasmon resonance, p-n junctions*